BEILSTEIN JOURNAL OF NANOTECHNOLOGY

Scanning probe microscopy for energy-related materials

Edited by Philippe Leclère, Rüdiger Berger, Benjamin Grévin and Yi Zhang



Generated on 12 November 2026, 11:30

Imprint

Beilstein Journal of Nanotechnology
www.bjnano.org
ISSN 2190-4286
Email: journals-support@beilstein-institut.de

The *Beilstein Journal of Nanotechnology* is published by the Beilstein-Institut zur Förderung der Chemischen Wissenschaften.

Beilstein-Institut zur Förderung der Chemischen Wissenschaften
Trakehner Straße 7–9
60487 Frankfurt am Main
Germany
www.beilstein-institut.de

The copyright to this document as a whole, which is published in the *Beilstein Journal of Nanotechnology*, is held by the Beilstein-Institut zur Förderung der Chemischen Wissenschaften. The copyright to the individual articles in this document is held by the respective authors, subject to a Creative Commons Attribution license.

The cover art was sketched by Rüdiger Berger and drawn by Xue Zhang. The image is licensed under the terms of the CC BY 4.0 license copyright 2019 Berger and Zhang.

BEILSTEIN JOURNAL OF NANOTECHNOLOGY

Scanning probe microscopy for energy-related materials

Rüdiger Berger[*1], Benjamin Grévin[*2], Philippe Leclère[*3] and Yi Zhang[*4]

Editorial

Open Access

Address:
[1]Max Planck Institute for Polymer Research, Mainz, Germany, [2]UMR5819 CEA-CNRS-UGA, CEA-Grenoble INAC/SYMMES, Grenoble, France, [3]CIRMAP, University of Mons (UMONS), Mons, Belgium and [4]Shanghai Institute of Applied Physics, Chinese Academy of Sciences, Shanghai, PR of China

Email:
Rüdiger Berger[*] - berger@mpip.mainz.mpg.de; Benjamin Grévin[*] - benjamin.grevin@cea.fr; Philippe Leclère[*] - philippe.leclere@umons.ac.be; Yi Zhang[*] - zhangyi@sinap.ac.cn

* Corresponding author

Keywords:
energy conversion and storage, in-operando, Scanning Probe Microscopy, Scanning Force Microscopy

Beilstein J. Nanotechnol. **2019,** *10,* 132–134.
doi:10.3762/bjnano.10.12

Received: 12 November 2018
Accepted: 18 November 2018
Published: 10 January 2019

This article is part of the Thematic Series "Scanning probe microscopy for energy-related materials".

Editor-in-Chief: T. Schimmel

© 2019 Berger et al.; licensee Beilstein-Institut.
License and terms: see end of document.

In order to stimulate, bundle and strengthen the activities in the field of scanning probe microscopy for energy applications, we have organized a symposium at the European Material Research Society (E-MRS) fall meeting held in Warsaw in 2017. We were impressed by the high quality of the presentations and decided to create this thematic issue published in the Beilstein Journal of Nanotechnology based on these results. We feel that the manuscripts perfectly reflect the current activities and advances in the field of scanning probe microscopy for energy applications.

The term “energy applications” refers to materials that are used for energy conversion, energy transport and energy storage. In these fields, intensive basic and applied research is ongoing to address requirements of today and the future. These requirements are, for example, high power conversion efficiency, loss-free transport of energy, fast charging rates and high charging capacity. In order to fulfil these requirements, specific functional materials are being developed, investigated and optimized. Energy-related materials often include electrochemical reactions and (opto-)electronic transport phenomena at their interfaces. In particular, material properties on the nanometer scale play a major role. The understanding of these nanoscale phenomena occurring at material interfaces is therefore essential. Furthermore, these interface phenomena are strongly linked to material properties such as grain size, roughness, mechanical properties and work function. In an attempt to address the diversity of phenomena on the nanoscale, scanning probe microscopy (SPM) methods play an significant role for the in-operando characterization. SPM methods offer a plethora of operation modes beyond topography imaging, which is well reflected in the articles of this thematic issue.

The majority of contributions stem from research on photovoltaic materials. Here, electrical conductive atomic force microscopy (cAFM) and Kelvin probe force microscopy (KPFM) are the major methods that enable the study of the movement of charge carriers and their pathways [1]. We note that the KPFM method is rapidly becoming a tool capable of time-resolved studies. In this context, Yann Almadori and co-workers discuss the time-dependent changes of the surface potential occurring under illumination. This work also unravels

lattice expansion phenomena under illumination in perovskite structure forming photo-absorbing materials [2]. Pablo A. Fernández Garrillo and co-workers go one step further by addressing photocarrier dynamics in order to study charge carrier lifetimes. This contribution focuses on a mathematical model to calculate time constants [3]. Such a model is critical for understanding the photophysics at the nanometer scale. Amelie Axt and co-workers discuss the applicability and reliability of different ways of performing KPFM measurements on nanoscale electrical devices [4]. In particular, the knowledge of the true potential of surfaces is required for the analysis of cross-sections of solar cell devices [5,6]. Thus, this work is the basis for future quantitative analysis of nanoscale devices even beyond the scope of solar cells. Katherine Atamanuk and co-workers impressively demonstrate that SPM methods can also be used to perform tomography [7]. They apply photoconducting scanning force microscopy for mapping the open-circuit voltage of cadmium telluride (CdTe) polycrystalline thin film solar cells. Tomography is achieved by gradually removing surface material during continuous high-load topographic imaging. For photovoltaic materials, the interface between materials accepting electrons or holes is of crucial importance. Laurie Letertre and co-workers study a nanocolumnar TiO_2 surface covalently grafted with a monolayer of poly(3-hexylthiophene) functionalized with carboxylic groups [8]. Their study unravels the physical mechanisms taking place locally during the photovoltaic process and its correlation to the nanoscale morphology.

Electrochemical energy storage (i.e., in a battery) is a major topic in our daily life. Jonathan Op de Beeck and co-workers identify the ionic processes occurring inside Li-ion composites in order to understand the impact on the entire battery cell [9]. In particular, the authors combine cAFM and secondary-ion mass spectrometry to correlate the presence of nanometer-sized conductive paths with the Li concentration. This study exemplifies that SPM combined with complementary methods providing information on the chemistry or atomic composition of materials is very beneficial for understanding the performance of devices. Nino Schön and co-workers study the relationship between Li-ion conductivity and the microstructure of the solid-state electrolyte lithium aluminum titanium phosphate films [10]. Furthermore, dielectric properties play a role for the storage of electrochemical energy. Ying Wang and co-workers report on a novel method for the characterization of the local dielectric distribution based on surface adhesion mapping by SPM [11]. This method is evidently easy in terms of operation and thus has the potential to be widely used. Finally, we want to highlight the contribution “Electrostatic force spectroscopy revealing the degree of reduction of individual graphene oxide sheets” by Yue Shen and co-workers. Yue Shen won the prize for the best presentation during the E-MRS conference [12]. Electrostatic force spectroscopy (EFS) is used here to characterize the degree of reduction of uniformly reduced one-atom-thick graphene oxide (GO) sheets at the nanoscale. The identification and chemical control of the degree of reduction of GO sheets is highly desired to realize nanoscale electronic devices in the future.

We thank all authors for participating with their contribution to this thematic issue. The published manuscripts will be a significant contribution to the advancement of the field of understanding energy materials on the nanometer scale. In addition, we acknowledge the expertise of the reviewers who provided helpful reports to us and the authors. Finally, we acknowledge the valuable support of Wendy Patterson and her team working for the Beilstein Journal of Nanotechnology.

Rüdiger Berger, Benjamin Grévin, Philippe Leclère and Yi Zhang

Mainz, Grenoble, Mons and Shanghai, October 2018

ORCID® iDs

Rüdiger Berger - https://orcid.org/0000-0002-4084-0675
Benjamin Grévin - https://orcid.org/0000-0002-6494-8138
Philippe Leclère - https://orcid.org/0000-0002-5490-0608

References

1. Berger, R.; Domanski, A. L.; Weber, S. A. L. *Eur. Polym. J.* **2013,** *49,* 1907–1915. doi:10.1016/j.eurpolymj.2013.03.005
2. Almadori, Y.; Moerman, D.; Martinez, J. L.; Leclère, P.; Grévin, B. *Beilstein J. Nanotechnol.* **2018,** *9,* 1695–1704. doi:10.3762/bjnano.9.161
3. Fernández Garrillo, P. A.; Grévin, B.; Borowik, Ł. *Beilstein J. Nanotechnol.* **2018,** *9,* 1834–1843. doi:10.3762/bjnano.9.175
4. Axt, A.; Hermes, I. M.; Bergmann, V. W.; Tausendpfund, N.; Weber, S. A. L. *Beilstein J. Nanotechnol.* **2018,** *9,* 1809–1819. doi:10.3762/bjnano.9.172
5. Bergmann, V. W.; Weber, S. A. L.; Javier Ramos, F.; Nazeeruddin, M. K.; Grätzel, M.; Li, D.; Domanski, A. L.; Lieberwirth, I.; Ahmad, S.; Berger, R. *Nat. Commun.* **2014,** *5,* 5001. doi:10.1038/ncomms6001
6. Weber, S. A. L.; Hermes, I. M.; Turren-Cruz, S.-H.; Gort, C.; Bergmann, V. W.; Gilson, L.; Hagfeldt, A.; Graetzel, M.; Tress, W.; Berger, R. *Energy Environ. Sci.* **2018,** *11,* 2404–2413. doi:10.1039/c8ee01447g
7. Atamanuk, K.; Luria, J.; Huey, B. D. *Beilstein J. Nanotechnol.* **2018,** *9,* 1802–1808. doi:10.3762/bjnano.9.171
8. Letertre, L.; Roche, R.; Douhéret, O.; Kassa, H. G.; Mariolle, D.; Chevalier, N.; Borowik, Ł.; Dumas, P.; Grévin, B.; Lazzaroni, R.; Leclère, P. *Beilstein J. Nanotechnol.* **2018,** *9,* 2087–2096. doi:10.3762/bjnano.9.197

9. Op de Beeck, J.; Labyedh, N.; Sepúlveda, A.; Spampinato, V.; Franquet, A.; Conard, T.; Vereecken, P. M.; Vandervorst, W.; Celano, U. *Beilstein J. Nanotechnol.* **2018,** *9,* 1623–1628. doi:10.3762/bjnano.9.154
10. Schön, N.; Gunduz, D. C.; Yu, S.; Tempel, H.; Schierholz, R.; Hausen, F. *Beilstein J. Nanotechnol.* **2018,** *9,* 1564–1572. doi:10.3762/bjnano.9.148
11. Wang, Y.; Shen, Y.; Wang, X.; Shen, Z.; Li, B.; Hu, J.; Zhang, Y. *Beilstein J. Nanotechnol.* **2018,** *9,* 900–906. doi:10.3762/bjnano.9.84
12. Shen, Y.; Wang, Y.; Zhou, Y.; Hai, C.; Hu, J.; Zhang, Y. *Beilstein J. Nanotechnol.* **2018,** *9,* 1146–1155. doi:10.3762/bjnano.9.106

License and Terms

This is an Open Access article under the terms of the Creative Commons Attribution License (http://creativecommons.org/licenses/by/4.0). Please note that the reuse, redistribution and reproduction in particular requires that the authors and source are credited.

The license is subject to the *Beilstein Journal of Nanotechnology* terms and conditions: (https://www.beilstein-journals.org/bjnano)

The definitive version of this article is the electronic one which can be found at: doi:10.3762/bjnano.10.12

BEILSTEIN JOURNAL OF NANOTECHNOLOGY

Nanoscale mapping of dielectric properties based on surface adhesion force measurements

Ying Wang[1], Yue Shen[2], Xingya Wang[1,3], Zhiwei Shen[1,3], Bin Li[1], Jun Hu[1] and Yi Zhang[*1]

Full Research Paper

Open Access

Address:
[1]Key Laboratory of Interfacial Physics and Technology and Laboratory of Physical Biology, Shanghai Institute of Applied Physics, Chinese Academy of Sciences, Shanghai 201800, China, [2]Key Laboratory of Salt Lake Resources Chemistry of Qinghai Province, Qinghai Institute of Salt Lakes, Chinese Academy of Sciences, Xining, Qinghai 810008, China and [3]University of Chinese Academy of Sciences, Beijing 100049, China

Email:
Yi Zhang[*] - zhangyi@sinap.ac.cn

* Corresponding author

Keywords:
adhesion; atomic force microscopy (AFM); graphene oxide (GO); nanoscale dielectric properties; reduced graphene oxide (RGO)

Beilstein J. Nanotechnol. **2018,** *9,* 900–906.
doi:10.3762/bjnano.9.84

Received: 22 November 2017
Accepted: 16 February 2018
Published: 16 March 2018

This article is part of the Thematic Series "Scanning probe microscopy for energy-related materials".

Guest Editor: P. Leclère

© 2018 Wang et al.; licensee Beilstein-Institut.
License and terms: see end of document.

Abstract

The detection of local dielectric properties is of great importance in a wide variety of scientific studies and applications. Here, we report a novel method for the characterization of local dielectric distributions based on surface adhesion mapping by atomic force microscopy (AFM). The two-dimensional (2D) materials graphene oxide (GO), and partially reduced graphene oxide (RGO), which have similar thicknesses but large differences in their dielectric properties, were studied as model systems. Through direct imaging of the samples with a biased AFM tip in PeakForce Quantitative Nano-Mechanics (PF-QNM) mode, the local dielectric properties of GO and RGO were revealed by mapping their surface adhesion forces. Thus, GO and RGO could be conveniently differentiated. This method provides a simple and general approach for the fast characterization of the local dielectric properties of graphene-based materials and will further facilitate their applications in energy generation and storage devices.

Introduction

The local dielectric distribution is a key factor that influences the physical properties and functionalities of various materials such as polymer nanocomposites [1-4], carbon nanotube compounds [5-8], metal–dielectric films [9-12], and biomembranes [13-15]. Understanding the behaviour of these complex nanostructured systems requires precise morphological and dielectric characterization approaches on the nanometre scale. Atomic force microscopy (AFM), which analyses the interactions between a sharp tip and samples with very high spatial resolution, is a good candidate to carry out the aforementioned tasks. In the last two decades, many AFM-based techniques have been developed for qualitatively or quantitatively detecting the local dielectric properties of nanomaterials, such as electrostatic force microscopy [16-19], scanning polarization force microscopy

(SPFM) [20-23], local dielectric spectroscopy [24-26], and nanoscale capacitance microscopy [27-29]. Most of the proposed techniques are based on long-range electrostatic interactions between the sample and a biased AFM tip, which in turn is closely related to the intrinsic dielectric properties of materials. In this regard, one of the primary disadvantages of these dielectric-related AFM measurements is their lower lateral resolution compared to the conventional AFM modes, which is attributed to the larger tip–sample distance [30]. Moreover, in ambient electrical AFM scanning, relative humidity usually has a strong impact on image resolution and contrast [31,32].

We propose that fast mapping of the local dielectric distribution on a sample surface can be achieved with high lateral resolution by combining the advantages of the electrowetting (EW) effect [33] and an AFM imaging mode, PeakForce Quantitative Nano-Mechanics (PF-QNM) [34]. Electrowetting is a phenomenon in which the wetting properties of a dielectric surface are modified using an external electric field [33]. At the nanometre scale, EW has also been observed to modify the adhesion force [35-37]. The adhesion force between an AFM tip with radius R and a flat surface with liquid absorbed on it can be expressed as [35-38]:

$$F_{\text{adh}} = 4\pi R\gamma\cos\theta_0 + \frac{2\pi R\varepsilon_r\varepsilon_0}{d}\cdot V^2, \qquad (1)$$

where V is the voltage applied on the AFM tip, γ is the liquid interfacial tension, θ_0 is the contact angle at zero external voltage, and d, ε_r and ε_0 are the thickness, relative permittivity of the dielectric layer, and the absolute dielectric permittivity of vacuum, respectively. Hence, the adhesion force between the AFM tip and the sample is affected by both of the wetting and dielectric properties of the sample. Based on this principle, a quantitative analysis on the dielectric constant of macroscopic film has been realized by measuring the surface–water contact angle and adhesion force between the dielectric layer and a biased AFM tip [38].

Recently, the newly-developed PF-QNM mode of AFM made it possible to simultaneously map the adhesion property as well as topography of the sample with high spatial resolution. In PF-QNM mode, force–distance curves between the AFM tip and the sample are measured at each pixel, so the force where the tip finally breaks free of the surface attraction in the withdraw direction can be extracted for adhesion mapping. This offers an opportunity to directly image the adhesion over the whole scanning area rather than only record force–distance curves at specific points on the sample.

In this letter, a method to qualitatively characterize the local dielectric distribution by adhesion mapping between a dielectric layer and a biased AFM probe is described. With this method we can simultaneously obtain the topographic and dielectric properties of the sample surface under ambient conditions without requiring reference samples [39] or lifting of the AFM tip to scan for a second time [40], which may result in a lower spatial resolution. The method was validated by local dielectric mapping of graphene oxide (GO) and reduced graphene oxide (RGO), which have similar thicknesses but large differences in their dielectric properties [21]. This approach is expected to provide a simple and convenient method to characterize the dielectric distribution of graphene-based materials, and will further facilitate their application in energy generation and storage devices, i.e., super-capacitor, lithium ion battery, solar cells, and fuel cells [41,42].

Results and Discussion

A schematic diagram indicating the working principle of dielectric property mapping based on the adhesion force in the PF-QNM mode is shown in Figure 1. A dc voltage can be applied to the AFM tip in the PF-QNM mode under ambient

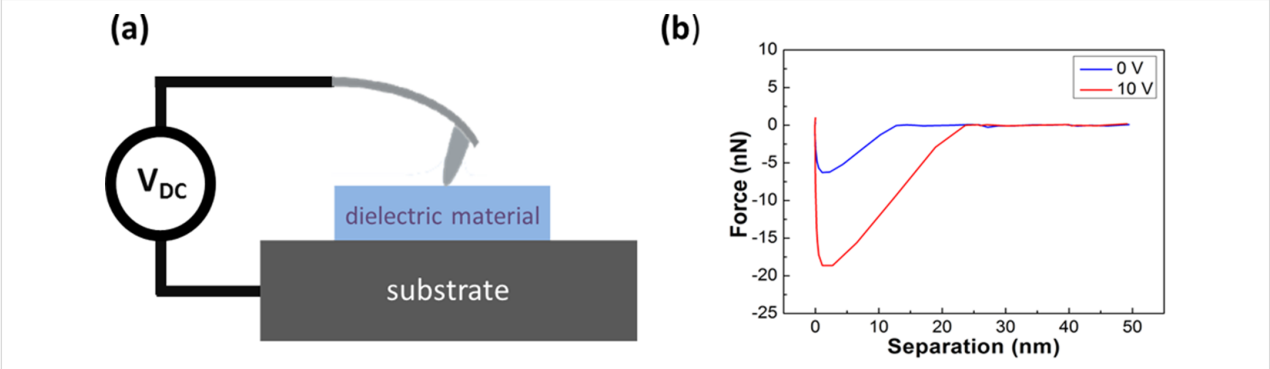


Figure 1: Schematic representation of the experimental principle. (a) A dc voltage can be applied to the AFM tip in PF-QNM mode under ambient conditions. (b) Representative retracting lines of force–distance curves under tip biases of 0 V and 10 V. The adhesion force between the tip and the sample will increase due to polarization of the sample when the tip is biased at 10 V.

conditions (Figure 1a). The force–distance curves are measured at every pixel in the scan range, and the peak forces below the baselines in the retracting line of the force–distance curves are then used for adhesion mapping. According to Equation 1, once the AFM tip is biased, the adhesion force between the tip and the sample, F_{adh}, will increase due to sample polarization (Figure 1b), which is positively correlated to its dielectric constant. Therefore, adhesion force mapping under a biased AFM tip can be expected to characterize the local dielectric property distribution.

An example of adhesion force mapping with a biased AFM tip in PF-QNM mode is shown in Figure 2. The height images of a single-layered GO sheet, which was chemically reduced (thus named as CRGO) by saturated hydrazine vapour on a mica surface, showed little change when the AFM tip bias increased from 0 to 10 V under ambient conditions (room temperature 18–25 °C, and relative humidity (RH) 35–60%) (Figure 2a,c). However, the contrast of the corresponding adhesion images increases significantly (Figure 2b,d). When the tip bias was lowered back to 0 V, both height and adhesion images returned to the original state before the dc voltage was applied (Figure 2e,f). Figure 2g and Figure 2h display the cross-sectional profiles along the blue, red, and green lines in Figure 2a,c,e and Figure 2b,d,f, respectively. The section profiles reveal that the change of the apparent heights was very small (ca. 0.2 nm) as the tip bias increased from 0 to 10 V and then dropped back to 0 V. Meanwhile, the adhesion force increased from −2.7 nN to 16.6 nN when the tip bias increased from 0 V to 10 V, and then returned to −2.7 nN when the tip bias was set back to zero. All measured values of the adhesion forces of the CRGO sheets are relative to that of the mica substrate. This result indicates the increase in the adhesion force when the AFM tip is biased is due to the greater degree of polarization of CRGO with respect to the mica substrate, rather than charge injection into the CRGO sheets [43]. In this case, the apparent height of the CRGO sheet under the biased AFM tip changed very little, which is quite different from the result in our previous SPFM experiment, in which the apparent height of RGO sheets under a biased tip usually increased sharply when RH was lower than 40% [32]. This is because the set point of the force, which is used as the feedback signal for AFM imaging, is quite different in PF-QNM mode and SPFM mode. Specifically, the set point of force for SPFM imaging is usually selected in the long-range attraction region of the force–distance curve, so a higher apparent height than the real value of the sample is normally observed [30]. In contrast, the set point of force for PF-QNM imaging is the peak value of the force–distance curve, which is usually in the repulsive region. Therefore, the effect of long-range attraction between a biased tip and the sample can be eliminated in PF-QNM height images, which leads to a true height of the sample in the height image. In addition, by comparing Figure 2a and Figure 2e, we can see the RGO sheet was not damaged by the biased AFM tip. This is because the increase of adhesion caused by the applied tip bias is no more than 20 nN, which is about two orders of magnitude lower than the threshold force to destruct GO and RGO in our previous study [44]. Therefore, this method is not more destruc-

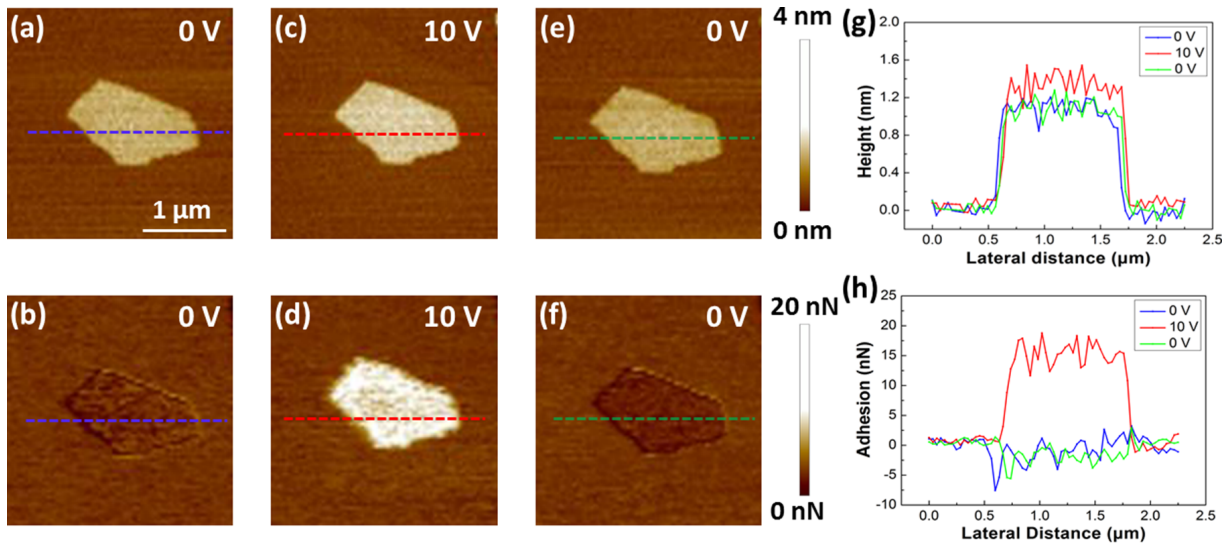


Figure 2: AFM height and adhesion images of single-layered CRGO sheets under different tip biases obtained in PF-QNM mode. (a,c,e) Height images obtained with an AFM tip biased at 0 V, 10 V, and 0 V, respectively. (b,d,f) Adhesion images corresponding to (a), (c), and (e), respectively. All of the images were taken with a peakforce set point of 5 nN. (g) Cross-sectional profiles along the blue, red, and green dashed lines in (a), (c), and (e), respectively. (h) Cross sectional profiles of the blue, red, and green lines in (b), (d), and (f), respectively.

tive compared to the standard peak force mode without tip bias. This result shows that imaging in PF-QNM mode with a biased AFM tip can be used to simultaneously characterize topographic and dielectric properties under ambient conditions.

In addition, adhesion force mapping with a biased AFM tip can be used to distinguish between different dielectric materials at the nanoscale. In order to prove this, a mixed sample of GO and CRGO sheets was studied as a model system (Figure 3). CRGO is a product of GO after being chemically reduced by removing some oxygen-containing groups and has a similar thickness but a larger dielectric constant than GO [21,45]. Figure 3a shows a representative height image of a mixture of GO and CRGO on a mica substrate under the tip biased at 0 V under ambient conditions (room temperature 18–25 °C, RH 35–60%). All of the sheets in the height image have similar contrast (Figure 3a) but are quite different in the adhesion force images (Figure 3b,c). When the tip bias was 0 V, although the contrast of all sheets is darker than that of the mica substrate, the sheets can still be divided into two types, with one having a slightly smaller adhesion than the other (Figure 3b). However, we cannot infer which one has the larger dielectric constant from this image. When the tip bias increased to 10 V, the contrast of one type increased sharply and became much brighter than that of the mica substrate. The contrast for the other increased only slightly and remained darker than that of the mica substrate (Figure 3c). Two sheets in the centre of Figure 3b, which are marked as 1 and 2, were studied as representative of these two types. The cross-sectional profile (Figure 3d) reveals that the mean thicknesses of sheets 1 and 2 are 1 nm and 1.2 nm, respectively. Figure 3e indicates that the mean adhesion force of sheet 1 increased from −2.7 to 16.6 nN along with the increase in the tip bias from 0 to 10 V. In the meantime, the mean adhesion force of sheet 2 increased from −9.4 to −5.1 nN under the same conditions. The statistical average adhesion force from over 100 sheets in the mixed sample, the areas of which ranged from 0.01 to 4 μm^2, showed that the increase in adhesion force was from −2.2 ± 0.6 nN to 12.8 ± 4.0 nN for type 1, and from −11.0 ± 2.9 nN to −8.3 ± 2.3 nN for type 2 (Figure 3f). According to Equation 1, the increase in the adhesion force caused by the external voltage, which is rooted in the polarization of the sample, is positively related to the dielectric constant of the sample. Therefore, type 1, which displayed a larger increase in adhesion force, is CRGO. That is, GO and CRGO in the mixed sample can be distinguished clearly by this method. It is worth noting that the contact potential differences between the AFM tip and GO/RGO are about three orders of magnitude lower than the tip bias in adhesion mapping (Supporting Information File 1, Figure S1). So the effect of the contact potential difference between the tip and our sample was ignored in our experiments.

A comparison study of dielectric property mapping by adhesion force and SPFM was also carried out. Figure 3g shows an in situ SPFM image of Figure 3c taken with an AFM tip biased at 10 V at RH 10% [32]. All of the sheets with increased adhesion forces in Figure 3c have increased apparent heights in the corresponding SPFM image, and the apparent heights of the

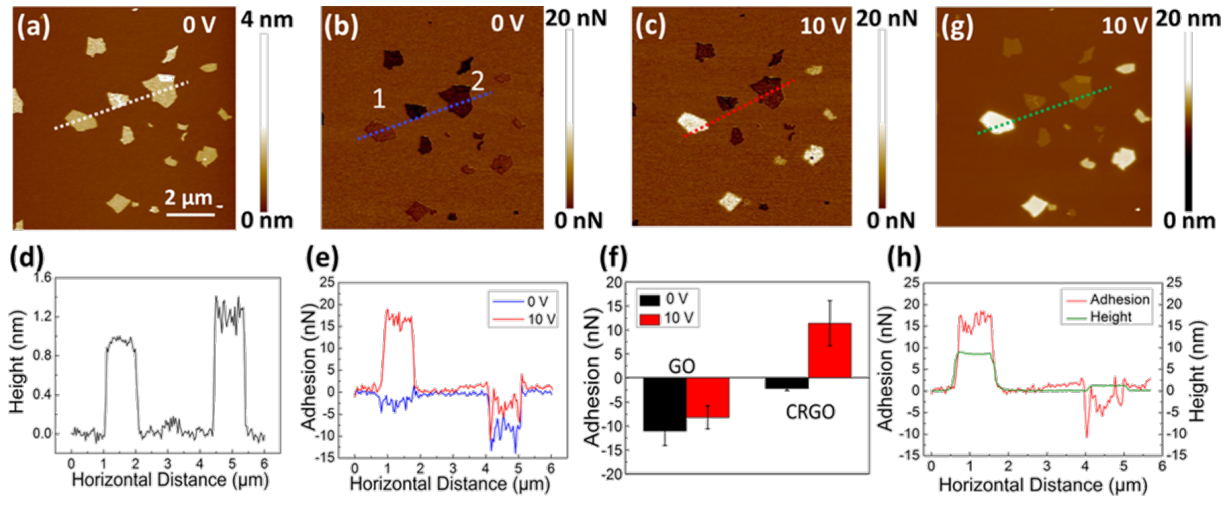


Figure 3: Discrimination of GO and CRGO on mica by adhesion mapping with a biased AFM tip. (a) Height and (b) adhesion force images taken simultaneously under an AFM tip bias of 0 V in PQ-QNM mode. (c) Adhesion force image taken under an AFM tip bias of 10 V. All of the images were taken with the peakforce set point at 5 nN under ambient conditions. (d) Cross-sectional profiles of the white dotted line in (a). (e) Cross sectional profiles of the blue and red dotted lines in (b) and (c), respectively. (f) The average adhesion forces of GO and RGO sheets under AFM tip biases of 0 and 10 V, respectively. (g) An in situ SPFM image of (c) taken under an AFM tip bias of 10 V with RH 10%. (h) Cross-sectional profiles of the red and green dotted lines in (c) and (g).

other sheets remain unchanged. That is, adhesion mapping under a biased AFM tip in PF-QNM mode is in good agreement with SPFM imaging in local dielectric property detection. Figure 3h shows the cross-sectional profiles along the red and green dotted lines in Figure 3c and Figure 3g, respectively. It indicates that the surfaces of the sheets in SPFM images are quite smooth in comparison with those in the adhesion image. The small grainy structures with a lateral size of less than dozens of nanometres on the basal planes of GO and RGO sheets, which are regarded as oxygen-containing functional groups [21,31], cannot be observed in the SPFM image but can be seen in the adhesion image. This is because SPFM works in the long-range electrostatic interaction region, but the adhesion mapping in PF-QNM mode works on the sample surface all the time, no matter if the AFM tip is biased or not. This result proves that adhesion force mapping under a biased AFM tip has the same capacity as SPFM to distinguish local dielectric distribution, but has a higher lateral resolution comparable to the conventional AFM modes.

The dependence of the adhesion force under a biased AFM tip on the reduction degree of GO was also studied through X-ray photoelectron spectroscopy (XPS) experiments. Figure 4a shows the average adhesion forces of the three samples plotted against different biases of the AFM tip. For GO, the mean value of the adhesion force initially increased from −11.0 ± 2.9 nN to −7.2 ± 2.2 nN when the tip bias increased from 0 V to 2.5 V, and then decreased slightly to −8.3 ± 2.3 nN along with the tip bias rising to 10 V. For CRGO and thermally reduced GO (TRGO), the initial values of the adhesion force with a tip bias of 0 V were −2.2 ± 0.4 nN and −2.3 ± 0.3 nN, respectively. The values subsequently increased monotonically with almost exactly the same trend to 11.2 ± 4.7 nN and 11.0 ± 2.5 nN until the tip bias reached 10 V. Since all of the adhesion forces mentioned in this paper are relative values to mica, the effect of system drift on force–distance curves during the imaging process can be eliminated (Supporting Information File 1, Figure S2). The increases in the adhesion forces of CRGO and TRGO when the tip bias increased from 0 to 10 V are 13.4 nN and 13.3 nN, respectively, which are very similar and almost five times larger than that of GO. Figure 4b–d shows XPS spectra of single-layered GO, CRGO, and TRGO, respectively, which reveal that the C/O ratios of GO increased from 1:1 to 3.3:1 and 3.2:1 after being chemically and thermally reduced, respectively. In general, the reduction degree of GO is positively related to its dielectric properties [21,46]. This result further confirms that the reduction degree of GO is positively related to the adhesion force caused by the biased AFM tip.

Conclusion

In summary, it was found that the adhesion force between a dielectric sample and a biased AFM tip was affected by sample polarization. The increase in the adhesion force caused by an external voltage is positively related to the dielectric properties of the sample. Based on this principle, GO and its reduction products can be precisely distinguished by adhesion mapping using a biased AFM tip. This experiment, in principle, proves that imaging in the PF-QNM mode with a biased AFM tip can

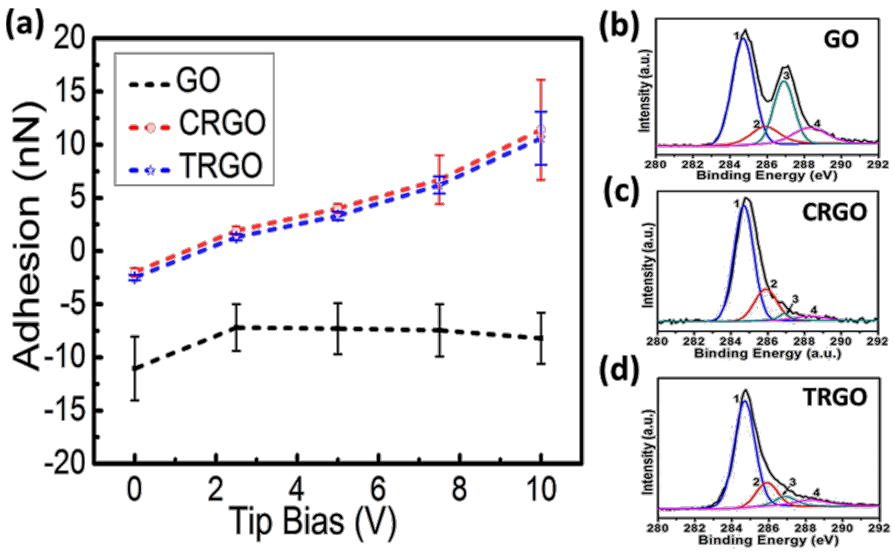


Figure 4: The dependence of the adhesion force on the AFM tip bias for three types of single-layered GO and RGO. (a) The average adhesion forces of the GO, CRGO (chemically reduced by saturated hydrazine vapor at 80 °C for 1 h) and TRGO (thermally reduced at 180 °C for 15 min) plotted against different biases of the AFM tip. XPS spectra of (b) GO, (c) CRGO and (d) TRGO. The peaks 1, 2, 3, and 4 in the coloured curves correspond to C=C/C–C in aromatic rings, C–O (epoxy and alkoxy), C=O, and COOH groups, respectively. The C/O ratios for these samples are 1:1, 3.3:1, and 3.2:1, respectively.

be used to simultaneously characterize topographic and dielectric properties in the nanoscale under ambient conditions with a high lateral resolution that is comparable to the conventional AFM modes. This method provides a general but simple approach for the fast characterization of the local dielectric properties of graphene-based materials and will facilitate their future applications in the energy generation and storage devices.

Experimental

Sample preparation

An aqueous solution of single-layered GO sheets was prepared from graphite powder following a modified Hummer's method [47-49]. A drop of 10 μL of as-prepared GO solution (50 ng/μL) was placed onto a mica substrate. Chemical reduction of GO was performed by exposure to a saturated vapour of hydrazine monohydrate (85 wt % in water, Sinopharm) in a sealed Petri dish at 80 °C for 1 h. Thermal reduction of GO was carried out in a vacuum oven at 180 °C for 15 min. A hybrid GO/RGO sample was made by depositing another drop of GO solution onto the substrate on which reduced GO had been deposited.

Characterization

The samples were characterized by using a MultiMode 8 AFM (Bruker) equipped with a J scanner. Silicon cantilevers coated with a 30 nm Pt layer with a nominal spring constant of 2.8 $N \cdot m^{-1}$ and oscillating frequencies of 60–90 kHz (NSC18/Pt, MikroMasch Co.) were used. Height and adhesion mapping were conducted in PeakForce Quantitative Nano-Mechanics (PF-QNM) mode, in which the maximum force (peak force) applied to the sample by the tip was directly regulated through the peak force setpoint and kept constant throughout the whole scan. In this mode, the peak force amplitude was set at 150 nm, the *Z*-piezo oscillation frequency at 2.0 kHz, and the scan rate at 1 Hz. Voltage to the tip was applied using the scan parameter "tip bias". All AFM experiments were conducted under ambient conditions at a room temperature of 18–25 °C and relative humidity of 35–60%. AFM images of the samples were processed using the software Nanoscope Analysis v1.7. For each image, a first-order flatten correction was applied to remove sample inclination. The reduction extent of the GO was characterized by X-ray photoelectron spectroscopy (XPS, AXIS Ultra DLD, Kratos).

Supporting Information

Supporting Information File 1

Additional experimental data.
[https://www.beilstein-journals.org/bjnano/content/supplementary/2190-4286-9-84-S1.pdf]

Acknowledgments

This work is supported by a grant from the National Natural Science Foundation of China (NSFC Nos. 11604358, 11674344 and 31670871), the Youth Innovation Promotion Association, Chinese Academy of Sciences (No. 2017469), and Key Research Program of Frontier Sciences, Chinese Academy of Sciences (No. QYZDJ-SSW-SLH019).

ORCID® iDs

Ying Wang - https://orcid.org/0000-0002-7128-6988
Yue Shen - https://orcid.org/0000-0001-9163-5148

References

1. Tanaka, T.; Montanari, G. C.; Mulhaupt, R. *IEEE Trans. Dielectr. Electr. Insul.* **2004,** *11,* 763–784. doi:10.1109/TDEI.2004.1349782
2. Tanaka, T. *IEEE Trans. Dielectr. Electr. Insul.* **2005,** *12,* 914–928. doi:10.1109/TDEI.2005.1522186
3. Yang, C.; Hao, S.-J.; Dai, S.-L.; Zhang, X.-Y. *Carbon* **2017,** *117,* 301–312. doi:10.1016/j.carbon.2017.03.004
4. Dang, Z.-M.; Yuan, J.-K.; Zha, J.-W.; Zhou, T.; Li, S.-T.; Hu, G.-H. *Prog. Mater. Sci.* **2012,** *57,* 660–723. doi:10.1016/j.pmatsci.2011.08.001
5. Dang, Z.-M.; Wang, L.; Yin, Y.; Zhang, Q.; Lei, Q.-Q. *Adv. Mater.* **2007,** *19,* 852–857. doi:10.1002/adma.200600703
6. Spitalsky, Z.; Tasis, D.; Papagelis, K.; Galiotis, C. *Prog. Polym. Sci.* **2010,** *35,* 357–401. doi:10.1016/j.progpolymsci.2009.09.003
7. Yang, C.; Lin, Y.; Nan, C. W. *Carbon* **2009,** *47,* 1096–1101. doi:10.1016/j.carbon.2008.12.037
8. Lu, W.; Xiong, Y.; Hassanien, A.; Zhao, W.; Zheng, M.; Chen, L. *Nano Lett.* **2009,** *9,* 1668–1672. doi:10.1021/nl900194j
9. Genov, D. A.; Sarychev, A. K.; Shalaev, V. M. *Phys. Rev. E* **2003,** *67,* 056611. doi:10.1103/PhysRevE.67.056611
10. Cai, W.; Genov, D. A.; Shalaev, V. M. *Phys. Rev. B* **2005,** *72,* 193101. doi:10.1103/PhysRevB.72.193101
11. Moulin, E.; Sukmanowski, J.; Schulte, M.; Gordijn, A.; Royer, F. X.; Stiebig, H. *Thin Solid Films* **2008,** *516,* 6813–6817. doi:10.1016/j.tsf.2007.12.018
12. Grésillon, S.; Aigouy, L.; Boccara, A. C.; Rivoal, J. C.; Quelin, X.; Desmarest, C.; Gadenne, P.; Shubin, V. A.; Sarychev, A. K.; Shalaev, V. M. *Phys. Rev. Lett.* **1999,** *82,* 4520–4523. doi:10.1103/PhysRevLett.82.4520
13. Warshel, A.; Sharma, P. K.; Kato, M.; Parson, W. W. *Biochim. Biophys. Acta, Proteins Proteomics* **2006,** *1764,* 1647–1676. doi:10.1016/j.bbapap.2006.08.007
14. Coster, H. G. L. *J. Biol. Phys.* **2003,** *29,* 363–399. doi:10.1023/A:1027362704125
15. Kimura, Y.; Ikegami, A. *J. Membr. Biol.* **1985,** *85,* 225–231. doi:10.1007/BF01871517
16. Riedel, C.; Arinero, R.; Tordjeman, P.; Lévêque, G.; Schwartz, G. A.; Alegria, A.; Colmenero, J. *Phys. Rev. E* **2010,** *81,* 010801. doi:10.1103/PhysRevE.81.010801
17. Gramse, G.; Dols-Perez, A.; Edwards, M. A.; Fumagalli, L.; Gomila, G. *Biophys. J.* **2013,** *104,* 1257–1262. doi:10.1016/j.bpj.2013.02.011
18. Peng, S.; Zeng, Q.; Yang, X.; Hu, J.; Qiu, X.; He, J. *Sci. Rep.* **2016,** *6,* 38978. doi:10.1038/srep38978

19. Van der Hofstadt, M.; Fabregas, R.; Millan-Solsona, R.; Juarez, A.; Fumagalli, L.; Gomila, G. *ACS Nano* **2016,** *10,* 11327–11336. doi:10.1021/acsnano.6b06578
20. Hu, J.; Xiao, X.-D.; Salmeron, M. *Appl. Phys. Lett.* **1995,** *67,* 476–478. doi:10.1063/1.114541
21. Shen, Y.; Zhang, Y.; Hu, J. *J. Chin. Electron Microsc. Soc.* **2013,** *32,* 95–100.
22. Villares, A.; Martin, S.; Giner, I.; Diaz, J.; Lydon, D. P.; Low, P. J.; Cea, P. *Soft Matter* **2008,** *4,* 1508–1514. doi:10.1039/b716798a
23. Verdaguer, A.; Sacha, G. M.; Luna, M.; Ogletree, D. F.; Salmeron, M. *J. Chem. Phys.* **2005,** *123,* 124703. doi:10.1063/1.1996568
24. Crider, P. S.; Majewski, M. R.; Zhang, J.; Oukris, H.; Israeloff, N. E. *Appl. Phys. Lett.* **2007,** *91,* 013102. doi:10.1063/1.2753539
25. Crider, P. S.; Majewski, M. R.; Zhang, J.; Oukris, H.; Israeloff, N. E. *J. Chem. Phys.* **2008,** *128,* 044908. doi:10.1063/1.2825301
26. Fumagalli, L.; Ferrari, G.; Sampietro, M.; Gomila, G. *Nano Lett.* **2009,** *9,* 1604–1608. doi:10.1021/nl803851u
27. Fumagalli, L.; Ferrari, G.; Sampietro, M.; Gomila, G. *Appl. Phys. Lett.* **2007,** *91,* 243110. doi:10.1063/1.2821119
28. Erickson, A.; Sadwick, L.; Neubauer, G.; Kopanski, J.; Adderton, D.; Rogers, M. *J. Electron. Mater.* **1996,** *25,* 301–304. doi:10.1007/BF02666260
29. Gomila, G.; Toset, J.; Fumagalli, L. *J. Appl. Phys.* **2008,** *104,* 024315. doi:10.1063/1.2957069
30. Salmeron, M. *Oil Gas Sci. Technol.* **2001,** *56,* 63–75. doi:10.2516/ogst:2001008
31. Kulkarni, D. D.; Kim, S.; Chyasnavichyus, M.; Hu, K.; Fedorov, A. G.; Tsukruk, V. V. *J. Am. Chem. Soc.* **2014,** *136,* 6546–6549. doi:10.1021/ja5005416
32. Shen, Y.; Zhou, Y.; Sun, Y.; Zhang, L.; Wang, Y.; Hu, J.; Zhang, Y. *Appl. Surf. Sci.* **2017,** *412,* 497–504. doi:10.1016/j.apsusc.2017.03.291
33. Mugele, F.; Baret, J.-C. *J. Phys.: Condens. Matter* **2005,** *17,* R705–R774. doi:10.1088/0953-8984/17/28/R01
34. Zhao, B.; Song, Y.; Wang, S.; Dai, B.; Zhang, L.; Dong, Y.; Lü, J.; Hu, J. *Soft Matter* **2013,** *9,* 8837–8843. doi:10.1039/c3sm50942g
35. Revilla, R. I.; Guan, L.; Zhu, X.-Y.; Quan, B.-G.; Yang, Y.-L.; Wang, C. *J. Phys. Chem. C* **2012,** *116,* 14311–14317. doi:10.1021/jp301549p
36. Revilla, R.; Guan, L.; Zhu, X.-Y.; Yang, Y.-L.; Wang, C. *Langmuir* **2011,** *27,* 7603–7608. doi:10.1021/la200983y
37. Guan, L.; Qi, G.; Liu, S.; Zhang, H.; Zhang, Z.; Yang, Y.; Wang, C. *J. Phys. Chem. C* **2009,** *113,* 661–665. doi:10.1021/jp806538r
38. Revilla, R. I. *J. Adhes. Sci. Technol.* **2016,** *30,* 1479–1486. doi:10.1080/01694243.2016.1155877
39. Revilla, R. I.; Li, X.-J.; Yang, Y.-L.; Wang, C. *J. Phys. Chem. C* **2014,** *118,* 5556–5562. doi:10.1021/jp411951h
40. Riedel, C.; Arinero, R.; Tordjeman, P.; Ramonda, M.; Lévêque, G.; Schwartz, G. A.; de Oteyza, D. G.; Alegria, A.; Colmenero, J. *J. Appl. Phys.* **2009,** *106,* 024315. doi:10.1063/1.3182726
41. Zhu, J.; Yang, D.; Yin, Z.; Yan, Q.; Zhang, H. *Small* **2014,** *10,* 3480–3498. doi:10.1002/smll.201303202
42. Mao, S.; Lu, G.; Chen, J. *Nanoscale* **2015,** *7,* 6924–6943. doi:10.1039/c4nr06609j
43. Shen, Y.; Guo, S.; Hu, J.; Zhang, Y. *Appl. Phys. Lett.* **2012,** *101,* 183109. doi:10.1063/1.4765359
44. Wang, Y.; Shen, Y.; Li, B.; Wang, S.; Zhang, J.; Zhang, Y.; Hu, J. *J. Phys. Chem. B* **2018,** *122,* 612–617. doi:10.1021/acs.jpcb.7b05175
45. Wang, Y.; Shen, Y.; Zhang, X.; Zhang, Y.; Hu, J. *Appl. Phys. Lett.* **2014,** *105,* 233107. doi:10.1063/1.4903836
46. Liu, H.; Xu, P.; Yao, H.; Chen, W.; Zhao, J.; Kang, C.; Bian, Z.; Gao, L.; Guo, H. *Appl. Surf. Sci.* **2017,** *420,* 390–398. doi:10.1016/j.apsusc.2017.05.181
47. He, H.; Klinowski, J.; Forster, M.; Lerf, A. *Chem. Phys. Lett.* **1998,** *287,* 53–56. doi:10.1016/S0009-2614(98)00144-4
48. Schniepp, H. C.; Li, J.-L.; McAllister, M. J.; Sai, H.; Herrera-Alonso, M.; Adamson, D. H.; Prud'homme, R. K.; Car, R.; Saville, D. A.; Aksay, I. A. *J. Phys. Chem. B* **2006,** *110,* 8535–8539. doi:10.1021/jp060936f
49. Zhang, J.; Yang, H.; Shen, G.; Cheng, P.; Zhang, J.; Guo, S. *Chem. Commun.* **2010,** *46,* 1112–1114. doi:10.1039/b917705a

License and Terms

This is an Open Access article under the terms of the Creative Commons Attribution License (http://creativecommons.org/licenses/by/4.0), which permits unrestricted use, distribution, and reproduction in any medium, provided the original work is properly cited.

The license is subject to the *Beilstein Journal of Nanotechnology* terms and conditions: (https://www.beilstein-journals.org/bjnano)

The definitive version of this article is the electronic one which can be found at: doi:10.3762/bjnano.9.84

BEILSTEIN JOURNAL OF NANOTECHNOLOGY

Electrostatic force spectroscopy revealing the degree of reduction of individual graphene oxide sheets

Yue Shen[1,2,3], Ying Wang[3], Yuan Zhou[1,2], Chunxi Hai[1,2], Jun Hu[*3] and Yi Zhang[*3]

Full Research Paper

Open Access

Address:
[1]Key Laboratory of Comprehensive and Highly Efficient Utilization of Salt Lake Resources, Qinghai Institute of Salt Lakes, Chinese Academy of Sciences, Xining, Qinghai 810008, China, [2]Key Laboratory of Salt Lake Resources Chemistry of Qinghai Province, Xining 810008, China and [3]Key Laboratory of Interfacial Physics and Technology, Shanghai Institute of Applied Physics, Chinese Academy of Sciences, Shanghai 201800, China

Email:
Jun Hu[*] - hujun@sinap.ac.cn; Yi Zhang[*] - zhangyi@sinap.ac.cn

* Corresponding author

Keywords:
degree of reduction; dielectric property; electrostatic force microscopy; electrostatic force spectroscopy; graphene oxide

Beilstein J. Nanotechnol. **2018,** *9,* 1146–1155.
doi:10.3762/bjnano.9.106

Received: 14 December 2017
Accepted: 09 March 2018
Published: 11 April 2018

This article is part of the Thematic Series "Scanning probe microscopy for energy-related materials".

Guest Editor: P. Leclère

© 2018 Shen et al.; licensee Beilstein-Institut.
License and terms: see end of document.

Abstract

Electrostatic force spectroscopy (EFS) is a method for monitoring the electrostatic force microscopy (EFM) phase with high resolution as a function of the electrical direct current bias applied either to the probe or sample. Based on the dielectric constant difference of graphene oxide (GO) sheets (reduced using various methods), EFS can be used to characterize the degree of reduction of uniformly reduced one-atom-thick GO sheets at the nanoscale. In this paper, using thermally or chemically reduced individual GO sheets on mica substrates as examples, we characterize their degree of reduction at the nanoscale using EFS. For the reduced graphene oxide (rGO) sheets with a given degree of reduction (sample n), the EFS curve is very close to a parabola within a restricted area. We found that the change in parabola opening direction (or sign the parabola opening value) indicates the onset of reduction on GO sheets. Moreover, the parabola opening value, the peak bias value (tip bias leads to the peak or valley EFM phases) and the EFM phase contrast at a certain tip bias less than the peak value can all indicate the degree of reduction of rGO samples, which is positively correlated with the dielectric constant. In addition, we gave the ranking of degree for reduction on thermally or chemically reduced GO sheets and evaluated the effects of the reducing conditions. The identification of the degree of reduction of GO sheets using EFS is important for reduction strategy optimization and mass application of GO, which is highly desired owing to its mechanical, thermal, optical and electronic applications. Furthermore, as a general and quantitative technique for evaluating the small differences in the dielectric properties of nanomaterials, the EFS technique will extend and facilitate its nanoscale electronic devices applications in the future.

Introduction

Graphene is a two dimensional (2D) crystal with superior mechanical [1], thermal [2], electrical [3,4] and optical [5] properties. It can be produced using graphene oxide (GO) as a precursor through cost-effective reduction methods with high yield. Reducing GO to reduced graphene oxide (rGO) is a key step toward the large-scale use of graphene [6]. Different reduction processes that partially restore the structure and properties result in different properties of rGO, which in turn affect the final performance of rGO-based devices [6].

Because the microstructure and properties of GO sheets can be greatly manipulated during the reduction process, it is important to characterize and evaluate the reducing effect of different reduction processes. Microelectrode-based electrical conductivity measurements [7] and spectral methods, such as X-ray photoelectron spectroscopy (XPS) [8,9], Raman spectroscopy [10], and UV–vis absorption spectra [11,12], reflect the average information of rGO materials. However, they cannot characterize an isolated rGO sheet at the nanoscale. Optical observation [13] and transmission electron microscopy (TEM) [14] has shown color changes and atomic scale feature changes, respectively, in GO sheets after reduction. However, any changes in performance are not identified, and differentiating rGO sheets with a similar degree of reduction is difficult. Based on the changes in the electrical properties of rGO, scanning probe microscopy (SPM) has also been employed recently to study the reduction of GO sheets at the nanoscale. Conductive atomic force microscopy (CAFM) [15,16] can be used to verify the reduced nanostructures on GO sheets. However, because CAFM relies on contact with the sample, the electrically induced reduction or oxidation may affect the degree of reduction of rGO sheets [17]. Scanning polarization force microscopy (SPFM), also called dielectric force microscopy, was developed firstly by Hu et al. in 1995 [18,19] to measure the dielectric properties of soft or weakly bound materials on a substrate that could be easily damaged by a scanning tip. In the SPFM operation, a direct current (DC) or alternating current (AC) bias is applied to a conductive probe, polarizing the sample below and generating a long-range electrostatic attractive force. This electrostatic attractive force superposes on the van der Waals force between the tip and sample so that both forces contribute to the imaging. In recent years, its applications have been extended to study the local dielectric properties of semiconductor nanomaterials such as GO sheets or partially reduced rGO sheets [20-22], graphene sheets [23], carbon nanotubes (CNTs) [24] and so on. SPFM [25] and electrostatic force microscopy (EFM) [26] have revealed a step-by-step reduction process in GO sheets. However, when the reduction reactions are completed, it is hard for these methods to identify the small difference between GO sheets reduced with different methods.

Although the reduction process of GO sheets has been studied with EFM, little attention has been paid to the use of electrostatic force spectroscopy (EFS) to reveal uniformly reduced GO sheets with various degree of reduction. Previously, EFS was proposed to distinguish graphene domains and optimize EFM imaging [27]. The EFS is a method monitoring the EFM phases with high resolution as a function of the electrical DC bias applied either to the probe or sample. Based on the dielectric constant difference of rGO sheets reduced using various methods, EFS can characterize the degree of reduction of uniformly reduced GO sheets at the nanoscale. Thus, the EFS, which combines imaging and spectroscopy, can be used to supplement SPFM and EFM to further reveal the reducing effects of rGO after the reduction reactions have completed. In this paper, using thermally or chemically reduced GO sheets for examples, we aim to evaluate the degree of reduction of individual rGO sheets at the nanoscale using EFS.

Results and Discussion

The thermal or chemical reduction of GO sheets was verified with XPS, UV–vis absorption spectra, and SPFM, as shown in Figure 1. The sample labels and the corresponding descriptions are shown in Table 1. The deconvoluted peaks A–D in Figure 1a centered at the binding energies of 284.5, 285.5, 286.9, and 288.5 eV, respectively, correspond to C=C/C–C in aromatic rings, C–O (epoxy and alkoxy), C=O, and COOH groups, respectively [20]. After reduction (sample 5), the XPS peak magnitudes for carbon atoms bonded to oxygen have decreased, indicating that most of the oxygen groups have been removed [8,9,20]. From the XPS data, we observed an increase in the ratio of the carbon atoms in aromatic rings (C=C/C–C) to those bonded to oxygen after the chemical reduction [20] from 1.1:1 to 6.3:1 (Figure 1a). However, the degree of reduction of samples 1–5 cannot be characterized from the almost coincident XPS spectrum in Figure 1b. In the normalized UV–vis absorption spectra (Figure 1c), the red-shift of the main absorbance peak from 226 nm to 264 nm the absorption increment in the visible region as well as the disappearance of the broad shoulder at 300 nm for samples 1–5 compared to sample 0 imply the removal of the oxygen-containing groups and the restoration of the π-conjugation network within the graphene nanosheets [11,12]. Nevertheless, except for the transparency injury in sample 2 caused by high temperature (450 °C) and oxidation in the atmosphere, no other differences amongst samples 1–5 were observed.

In addition, the increased apparent height in the SPFM images compared with the height in the topography images (Figure 1d–n) indicates that the GO sheets are reduced [21]. We can know whether the reduction is homogeneous (Figure 1f,g,i,

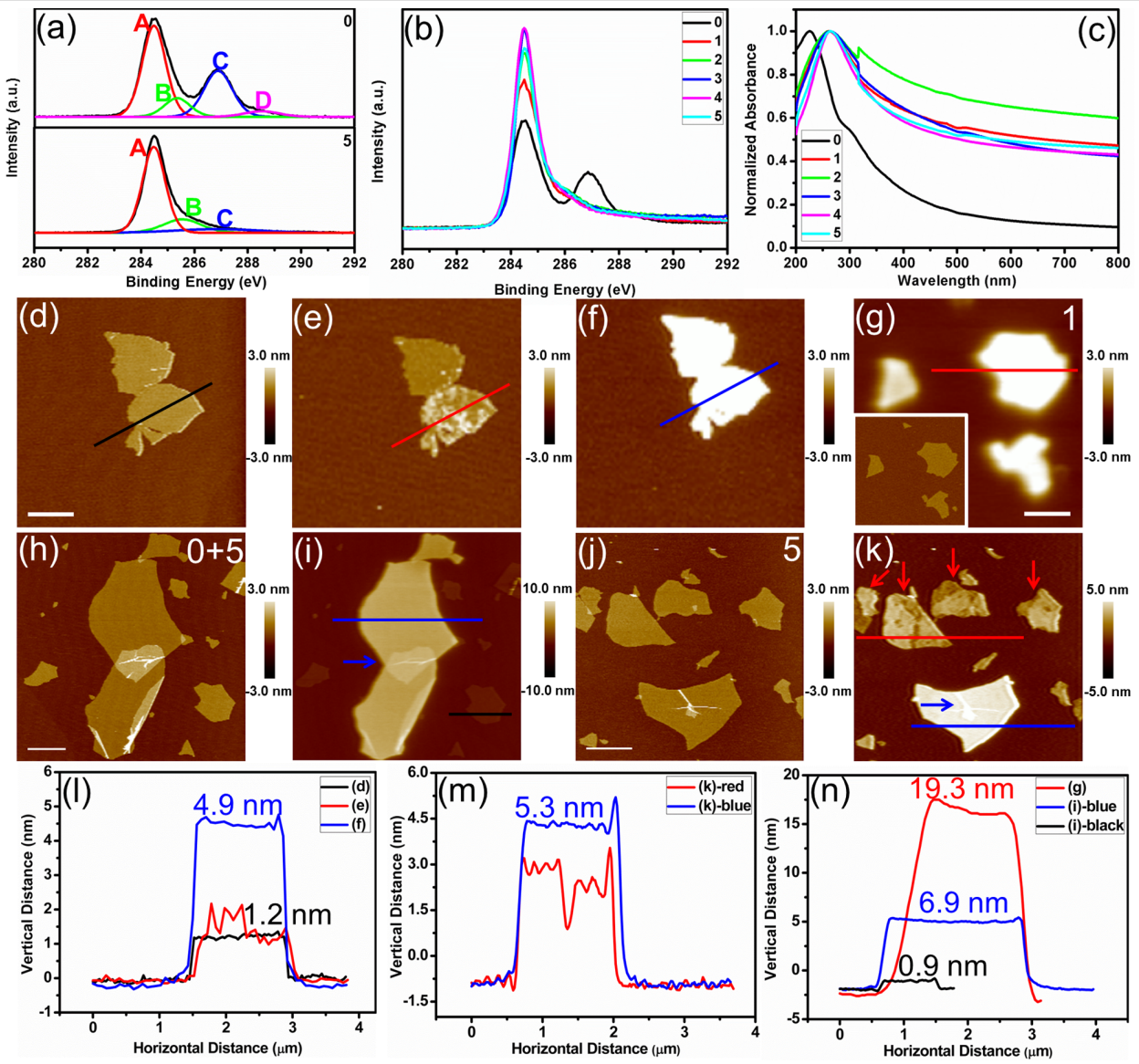


Figure 1: Characterizing the degree of reduction of GO sheets reduced using various methods. C 1s XPS spectra of (a, top) sample 0, (a, bottom) sample 5, and (b) samples 0–5; (c) normalized UV–vis absorption spectra of samples 0–5; in situ SPFM images of GO sheets thermally reduced at 150 °C for (d) 0 min, (e) 15 min, and (f) 75 min; (g) SPFM image of sample 1 (the in situ tapping AFM image is highlighted by the white rectangle); (h) tapping AFM and (i) in situ SPFM images of the mixture of sample 0 and 5; (j) tapping AFM and (k) in situ SPFM images of sample 5; cross-sectional profiles along (l) the lines in (d–f), (m) the lines in (k) and (n) the lines in (g, i). The numbers in the top right corners of the images (g, h, j) represent the sample numbers. The white scale bars represent 1000 nm. The *z*-scale bar is shown to the right of each SPM image.

Table 1: Sample labels and corresponding descriptions.

Sample label “n”	Sample description
0	GO sheets
1	thermally reduced GO sheets at 200 °C for 15 min
2	thermally reduced GO sheets at 450 °C for 15 min
3	chemically reduced GO sheets with hydrazine monohydrate at 80 °C for 1 h and then thermally reduced at 450 °C for 15 min
4	chemically reduced GO sheets with hydrazine monohydrate at 80 °C for 1 h and then thermally reduced at 200 °C for 15 min
5	chemically reduced GO sheets with hydrazine monohydrate at 80 °C for 1 h

blue line shown in Figure 1l, red and blue lines shown in Figure 1n) or heterogeneous (Figure 1e, red arrows marked in Figure 1k, and red lines shown in Figure 1l,m). Thus the initial stage of the reduction process (the reduction occurred on some domains on the GO sheets) can be characterized with SPFM [25]. However, when the GO sheets are reduced uniformly, evaluating the degree of reduction of samples 1–5 from the apparent height is difficult. The SPFM images contain both the dielectric properties and the morphology information (blue arrows marked in Figure 1i,k), indicating the contributions from the polarization force (dielectric properties) and the van der Waals force (topography) between the tip and sample. As we can see in the Figure 1l,m,n, the apparent height of samples 1 and 5 are 19.3 nm (Figure 1n) and 6.9 nm (Figure 1n) or 5.3 nm (Figure 1m), respectively. This inconsistency comes from the apparent height in SPFM imaging being influenced by the changed imaging force (amplitude set point). Considering the deficiencies in the above methods, we further explored EFS to characterize the homogeneously reduced GO samples 1–5 at the nanoscale.

In order to further characterize the degree of reduction of samples 1–5 at the nanoscale, we tested the EFS of each sample, as shown in Figure 2. EFS is based on measurements of the EFM

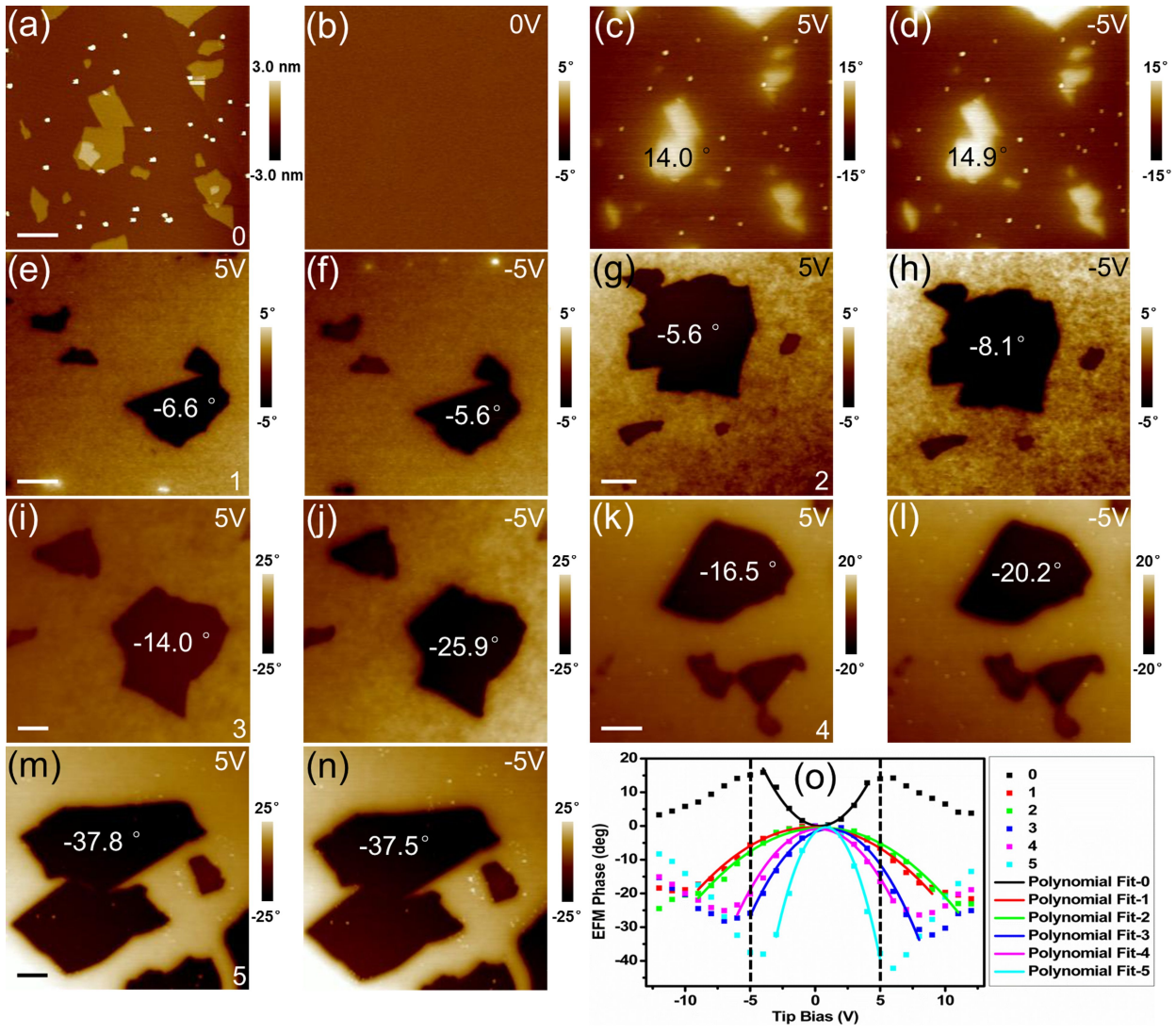


Figure 2: Characterizing the degree of reduction of GO sheets using EFM imaging and EFS: (a) tapping AFM image and in situ EFM images with tip biases of (b) 0 V, (c) 5 V and (d) −5 V of sample 0; EFM images of (e, f) sample 1, (g, h) sample 2, (i, j) sample 3, (k, l) sample 4, and (m, n) sample 5; (o) EFM spectra and the corresponding polynomial fits of samples 0–5 (the dashed vertical lines show the position of the biases at which images (c–n) were recorded). The number in the bottom right corner of the images represents the sample number. The upper right corner shows the tip bias used in the EFM imaging. The EFM phase contrast of the samples is labelled on the corresponding positions. The scale bars represent 1000 nm. The *z*-scale bar is shown to the right of each image.

phase contrast of the sample compared to the mica substrate as a function of different tip biases ranging from −12 V to 12 V. Then, the EFS can be obtained by plotting the EFM phase contrast versus the tip bias.

The principle of using EFS to evaluate the degree of reduction of rGO samples is shown in Figure 3. In a typical EFM measurement, a DC bias voltage is applied to the conductive cantilever (Figure 3a). Because of polarization, opposing charges are induced at the vicinity of the sample surface, causing an attractive force between the tip and the sample, which leads to a phase shift of the cantilever. In the absence of electrical forces, the cantilever has a resonant frequency, f_0. However, the tip bias causes an attractive (or repulsive) electrostatic force, making the cantilever effectively "softer" ("stiffer"), reducing (increasing) the resonant frequency [28,29]. The phase curve then correctly reflects the phase lag between the drive and the cantilever response (Figure 3b) [29]. This correspondingly results in a negative (or positive) phase shift of the cantilever, as labelled with red (or blue) in the Figure 3b. The case of repulsive electrostatic forces (in the parentheses) usually occurs when the sample itself is charged [21]. However, in the experiments here, electrostatic forces between the biased tip and the induced charges on sample surface are only attractive. Thus, in EFM imaging (Figure 3a,c–d), the electrostatic attraction causes a phase shift of the cantilever, leading to a dark color in the contrast (marked with red in Figure 3b).

In the EFS experiments, the probe is biased. The sample, however, which is adhered to the sample holder with insulating double-sided adhesive, is not connected to ground. Thus the tip material has a capacitance similar to an isolated conductor and the rGO sheets or mica act as a dielectric in its electrostatic field, rather than having a capacitance related to the tip–substrate. The tip can be approximated as a spherical conductor with a radius of R_{Tip}. The tip capacitance C_{Tip} can be expressed as:

$$C_{\text{Tip}} \cong 4\pi\varepsilon_0 R_{\text{Tip}}. \tag{1}$$

The tip charge, Q_{Tip}, and the induced charge at the vicinity of the sample surface, Q_{Sam}, can be expressed respectively as:

$$Q_{\text{Tip}} = C_{\text{Tip}} V \tag{2}$$

$$Q_{\text{Sam}} \cong -Q_{\text{Tip}}\left(1-\frac{1}{\varepsilon_{\text{Sam}}}\right), \tag{3}$$

where V is the DC voltage applied to the probe, and ε_{Sam} is the dielectric constant of the sample. The forces between the probe and the sample can be expressed as a Coulomb contribution:

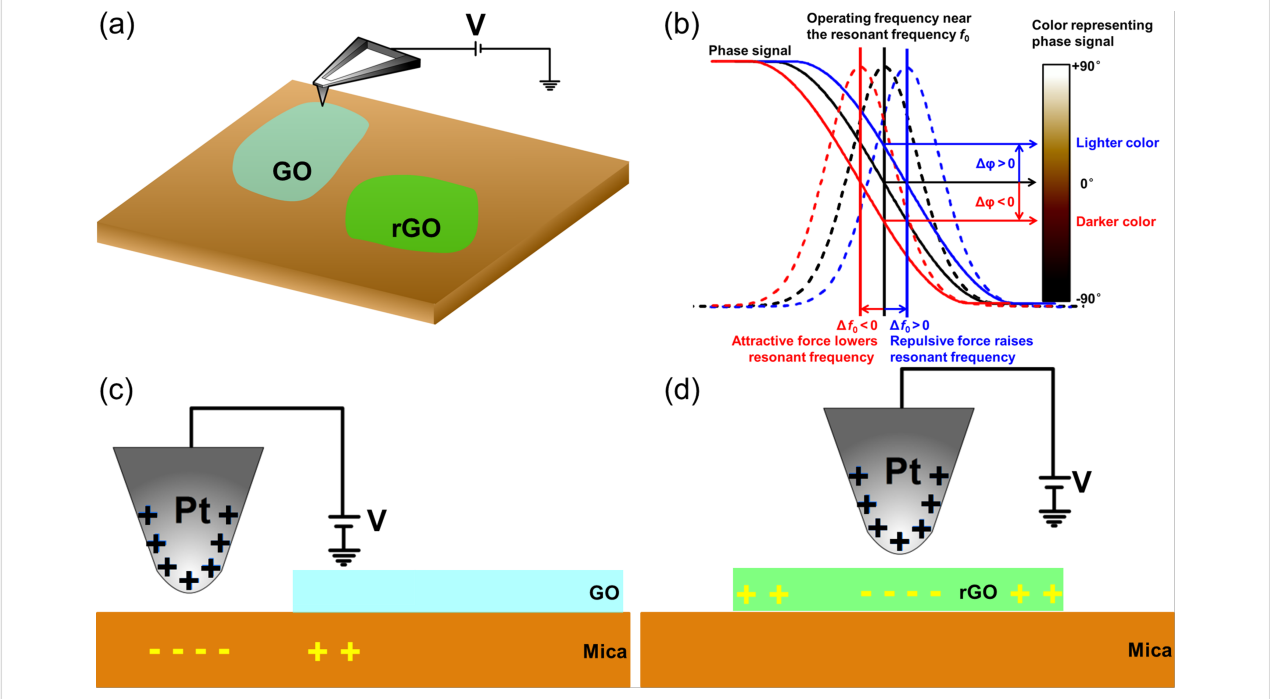


Figure 3: Illustrative diagram of EFM imaging and EFS: (a) schematic depiction of EFM, (b) electrostatic force between the biased tip and sample, causing a phase shift of the cantilever; EFM imaging of (c) GO or (d) rGO on mica substrate.

$$F = \frac{1}{4\pi\varepsilon_0}\frac{Q_{\text{Tip}}\,Q_{\text{Sam}}}{z^2} = -\frac{4\pi\varepsilon_0 {R_{\text{Tip}}}^2}{z^2}V^2\left(1-\frac{1}{\varepsilon_{\text{Sam}}}\right), \quad (4)$$

where z is the tip–sample distance. By differentiating Equation 4 we obtain the electric force gradients:

$$F' = \frac{\mathrm{d}F}{\mathrm{d}z} = \frac{8\pi\varepsilon_0 {R_{\text{Tip}}}^2}{z^3}V^2\left(1-\frac{1}{\varepsilon_{\text{Sam}}}\right). \quad (5)$$

The electric force gradients cause shifts of Δf_0 in the resonance frequency with a proportional relationship [30]:

$$f_0 \cong -\frac{F'}{2k}f_0 = -\frac{4\pi\varepsilon_0 {R_{\text{Tip}}}^2 f_0}{k\,z^3}V^2\left(1-\frac{1}{\varepsilon_{\text{Sam}}}\right), \quad (6)$$

where k is the stiffness (or spring constant) of the cantilever. Resonance shifts also give rise to phase shifts, Δφ, used to generate an image of the electric force gradients. In EFM imaging, the frequency shifts are detected through phase detection, which measures the cantilever's phase of oscillation relative to the piezo drive [29]. In a small resonant frequency shift range (at low biases), small phase shifts, Δφ, are proportional to the resonance frequency shifts, Δf_0:

$$\Delta\varphi \cong A\,\Delta f_0 = -\frac{4\pi\varepsilon_0 A {R_{\text{Tip}}}^2 f_0}{k\,z^3}V^2\left(1-\frac{1}{\varepsilon_{\text{Sam}}}\right), \quad (7)$$

where A is a coefficient of proportionality. The contrast between the phase shifts of probe imaging on mica and sample n can be expressed as:

$$\Delta\varphi^{\text{n}} - \Delta\varphi^{\text{Mica}} = \frac{4\pi\varepsilon_0 A {R_{\text{Tip}}}^2 f_0}{k\,z^3}V^2\left(\frac{1}{\varepsilon_{\text{n}}}-\frac{1}{\varepsilon_{\text{Mica}}}\right). \quad (8)$$

In EFM imaging, the lift mode is used. Topography data recorded during the main pass is used to keep the tip at a constant distance from the surface (lift scan height was 15 nm here) during the interleave trace and retrace, allowing imaging of the long-range electric interactions while minimizing the influence of topography [29]. So the tip–surface distance z is a constant, R_{Tip}, and f_0 and k are also kept constant provided that the same cantilever is used. Thus the differences between the phase of the probe on mica and sample n are only related to the tip bias and the local dielectric constant of sample n. For the case of $V = 0$ V for sample 0 (Figure 2b), there is no contrast in the EFM images, consistent with Equation 8 and indicating topographical features virtually absent from the EFM image by using lift mode.

For an rGO sample, when the tip bias increases from 0 V, the EFM contrast is enhanced by the increasing electrostatic attraction gradients. As represented in Figure 2o, within a restricted area, the curve of EFM phase contrast ($Y_{\text{Phase}} = \Delta\varphi^{\text{n}} - \Delta\varphi^{\text{Mica}}$) versus tip bias for each sample is very close to a parabola, and fits to the data are expressed respectively as:

$$\text{Sample 0}: Y_{\text{Phase}} = 0.9057V^2 - 0.6050V + 0.1173 \quad (9)$$

$$\text{Sample 1}: Y_{\text{Phase}} = -0.2364V^2 - 0.0697V - 0.3495 \quad (10)$$

$$\text{Sample 2}: Y_{\text{Phase}} = -0.2293V^2 + 0.2466V - 0.6107 \quad (11)$$

$$\text{Sample 3}: Y_{\text{Phase}} = -0.6909V^2 + 1.5238V - 1.7547 \quad (12)$$

$$\text{Sample 4}: Y_{\text{Phase}} = -0.6500V^2 + 0.3395V - 0.9410 \quad (13)$$

$$\text{Sample 5}: Y_{\text{Phase}} = -2.2320V^2 + 3.6350V - 1.8730 \quad (14)$$

These results provide the parabola opening values (listed later in the article in the Table 2). The parabola opening direction of sample 0 and sample 1–5 is upward (positive parabola opening value) and downward (negative parabola opening values), respectively. The EFM phase of sample 0 is positive (Figure 2c,d,o), whereas samples 1–5 have negative values (Figure 2e–o). We can thus draw the conclusion that $\varepsilon_{\text{GO}} < \varepsilon_{\text{Mica}}$ and $\varepsilon_{\text{rGO}} > \varepsilon_{\text{Mica}}$ from Equation 8. When $\varepsilon_{\text{Mica}} > \varepsilon_{\text{GO}}$, then $(\Delta\varphi^{\text{n}} - \Delta\varphi^{\text{Mica}}) > 0$, and the more attractive force gradients between the tip and mica cause the mica substrate to appear darker than the GO sample (Figure 3c). Thus, the GO sample (sample 0) in the EFM images has a lighter color than the mica substrate (Figure 2c,d,o). When $\varepsilon_{\text{Mica}} < \varepsilon_{\text{rGO}}$, then $(\Delta\varphi^{\text{n}} - \Delta\varphi^{\text{Mica}}) < 0$, and the greater attractive force between the tip and the rGO sample causes the rGO sample to appear darker than the mica substrate (Figure 3d). Thus, the rGO samples (samples 1–5) in the EFM images have a darker color than the mica substrate (Figure 2e–o). Therefore, the sign change (the parabola opening direction change, or color change from lighter to darker) indicates the occurrence of reduction on the GO sheets.

The parabola opening values are negatively correlated with the dielectric constant of the sample on a mica substrate (Equation 8). Thus, according to the parabola opening values, we can deduce the ranking of dergree of the samples' reduction as: sample 0 < sample 1 ≈ sample 2 < sample 4 < sample 3 < sample 5. The parabola of $\Delta\varphi^{n} - \Delta\varphi^{Mica}$ versus tip bias (Equation 8) is consistent with the previous results [31] that the small phase shifts Δφ can be approximated by

$$\Delta\varphi \cong -\frac{Q}{2k}F' = -\frac{4\pi\varepsilon_0 {R_{\mathrm{Tip}}}^2 Q}{z^3 k}V^2\left(1-\frac{1}{\varepsilon_{\mathrm{Sam}}}\right), \quad (15)$$

where Q is the quality factor of the cantilever. We can obtain the difference between phase shifts of probe imaging on mica and sample n as:

$$\Delta\varphi^{n} - \Delta\varphi^{\mathrm{Mica}} = \frac{4\pi\varepsilon_0 {R_{\mathrm{Tip}}}^2 Q}{k z^3}V^2\left(\frac{1}{\varepsilon_{\mathrm{n}}}-\frac{1}{\varepsilon_{\mathrm{Mica}}}\right). \quad (16)$$

Comparing Equation 16 with Equation 8, the difference is just $A{\cdot}f_0$ is replaced with Q. Therefore, the two expressions are consistent considering both the parameters related to the cantilever. However, the above equation is only valid for the small phase shift angles due to the nonlinearity of the phase shifts with respect to the resonance frequency shifts [31]. The spectroscopic curves deviate strongly from an ideal parabolic shape at high bias Figure 2o.

For a tip bias lower than the peak tip bias values (tip biases lead to the peak or valley EFM phases), the EFM phase contrast is significantly enhanced by the reduction methods used on samples 1–5 (Figure 2e–n, and dashed vertical lines in Figure 2o). This also indicates that the dielectric constant increases from sample 0 to sample 5, improving the electrostatic attraction gradients at certain tip bias. When the tip bias is sufficiently large, the influence of the substrate under the sample will be coupled into the measurement such that the contrast between the sample and mica (after coupling) decreases. For rGO sheets with a strong degree of reduction (high dielectric constants), a small tip bias is sufficient to induce enough local charge in the rGO sheets, polarizing the substrate below, further reducing the electrostatic attraction between the tip and rGO sheets. Thus, a sample with a stronger degree of reduction requires a smaller tip bias to reach the peak EFM phase. The peak tip bias values of each sample (Table 2) gradually decrease from sample 1 to sample 5, indicating a gradually enhanced degree of reduction. Therefore, both the peak tip bias value and the EFM phase contrast at a certain tip bias less than the peak value can indicate the degree of reduction of rGO sheets, which is positively correlated with the dielectric constant. A larger phase contrast and a smaller peak tip bias together indicate a higher degree of reduction. From this logic, we can deduce the ranking of degree of the samples' reduction as: sample 0 < sample 1 ≈ sample 2 < sample 3 ≈ sample 4 < sample 5, which is almost consistent with the quantitative results shown by the parabola opening values. Therefore, chemical reduction with hydrazine monohydrate can reach a higher degree of reduction than thermal reduction without inert atmosphere protection. Moreover, it is not necessary to continue raising the reducing temperature when the GO sheets can be thermally reduced uniformly. For the chemically reduced GO sample (sample 5), further heat treatment in air would oxidize it. Ultimately, to supplement SPFM for characterization of the initial stage of the reduction process, EFS can be used to further identify the degree of reduction of uniformly reduced GO sheets, advancing our understanding of the effects of various reduction methods.

Conclusion

We used EFS to evaluate the degree of reduction of GO sheets that were uniformly reduced by thermal or chemical methods, or through a combination thereof. For the rGO sheets with given degree of reduction (sample n), the EFS curve is very close to a parabola within a restricted area. The sign change of

Table 2: Peak EFM phase, the corresponding tip biases used in EFM imaging, and parabola opening values (from the EFS measurements in Figure 2o).

Sample	Positive tip bias (V)	EFM phase (°)	Negative tip bias (V)	EFM phase (°)	Parabola opening
0	6	14.2	−4	15.9	0.9057
1	12	−21.6	−11	−19.2	−0.2364
2	12	−23.1	−12	−24.5	−0.2293
3	9	−32.3	−7	−28.2	−0.6909
4	8	−26.4	−7	−25.1	−0.6500
5	6	−42.2	−4	−38.0	−2.2320

the phase contrast (the parabola opening direction change, or sign change of parabola opening value) indicates the occurrence of reduction on GO sheets. Furthermore, the parabola opening values, the peak tip bias value and the EFM phase contrasts at a certain tip bias less than the peak value can all indicate the degree of reduction of rGO samples, which is positively correlated with the dielectric constant. A smaller parabola opening value, a larger EFM phase contrast and a smaller peak tip bias together indicate a higher degree of reduction. From this logic, we could deduce the ranking of degree of the samples' reduction as: sample 0 < sample 1 ≈ sample 2 < sample 4 < sample 3 < sample 5. From the EFS measurements, we found that chemical reduction with hydrazine monohydrate can enable a higher degree of reduction than thermal reduction without inert atmosphere protection. Additionally, it was found that a further increase in the reduction temperature was not necessary when the GO sheets can be thermally reduced uniformly. For the chemically reduced GO sample, further heat treatment in atmosphere resulted in oxidization. To supplement SPFM for the characterization of heterogeneously reduced GO sheets in the initial stage of the reduction process, EFS can be employed to further identify the degree of reduction of the individual uniformly reduced GO sheets and aids in advancing our understanding of the effects of various reduction methods on GO sheets. The characterization of the degree of reduction of GO sheets using EFS is important for the reduction strategy optimization and mass application of GO material, whose use is strongly desired for its mechanical, thermal, optical and electronic applications. Moreover, we believe that this advanced SPM method provides a general and quantitative approach for characterizing the small differences in the dielectric properties of nanomaterials, which is critically important for further device applications.

Experimental

The samples under study were GO sheets prepared from graphite powder following a modified Hummers' method [9,32-35]. Thermal reduction of GO sheets deposited on a substrate was carried out in an oven at 200 °C or 450 °C for 15 min. Chemical reduction of GO was achieved by exposure to a saturated vapor of hydrazine monohydrate in a sealed petri dish at 80 °C for 1 h [36]. Mica substrates were used in this work. The reduction of the GO sheets was verified with XPS (AXIS ULTRA^{DLD}, Kratos Analytical, Ltd., Manchester, UK), UV–vis absorption spectra (Lambda 750 UV/VIS/NIR spectrometer, PerkinElmer, Inc., Waltham, MA, USA) and SPFM.

In the SPFM, a DC or AC bias is applied to a tapping mode AFM tip, generating an electrostatic attractive force (polarization force) between the biased tip and the polarized charge on the sample surface. The electrostatic attractive force superposes on the van der Waals force between the tip and sample so that the SPFM imaging gives a higher apparent height than the topographic height of nanomaterials when the dielectric constant of the nanomaterials is larger than the substrate. The apparent height (polarization height) of nanomaterials in SPFM images are an indication of the local dielectric constant difference between the sample and substrate [20,37]. However, when a DC bias is applied, a local net charge (or the surface charge for nanomaterials) would affect the apparent height in SPFM imaging [21,22]. In order to reflect the local variation of the dielectric constant more accurately, we used an AC tip bias (10 V for 100 kHz) instead of a DC one for the SPFM operations in the experiments here.

Tapping AFM, SPFM and EFM were all performed using a commercial AFM instrument (Multimode Nanoscope V, Bruker, previously Veeco) which was installed in an in-house environment-controlled box. The in-house environment-controlled box used here was jointly developed by Shanghai Espec Environmental Equipment Corp. with us. The system uses a compressor and a heater to control the ambient temperature, and uses a compressor and a humidifier to control the humidity of the environment. In order to eliminate the influence of noise from the system, the temperature and humidity generator are physically separated from the AFM. The humidity generator and the AFM are connected with adiabatic hoses, forming the gas transmission loop. The temperature fluctuations were below 0.2 °C and the error of humidity control was about 2% relative humidity (RH). To avoid influences on EFM or SPFM imaging from the dielectric constant change of the mica substrate, all the SPM-based operations were carried out under room temperature at 23 °C and at a relative humidity of 15% in order to ensure constant substrate surface properties (especially regarding the dielectric constant of the mica surface) [20]. In all the SPM operations, the NSC18/Ti-Pt (MikroMasch Co.) tip was used, which employed a silicon cantilever coating with a 10 nm Pt layer on a 20 nm Ti sublayer with a nominal spring constant of ≈3.5 Nm^{-1} and oscillating frequencies of 60–90 kHz. The lift start height and lift scan height in EFM imaging were 20 nm and 15 nm, respectively.

Acknowledgements

We thank Professor Zhenghui Liu from Suzhou Institute of Nano-Tech and Nano-bionics (Chinese Academy of Sciences) for helpful discussions. This work was supported by the Joint Funds of the National Natural Science Foundation of China [grant nos. U1707603 and U1407105], the National Natural Science Foundation of China [grant nos. 11604358 and 11674344], the Natural Science Foundation of Qinghai Province [grant no. 2015-ZJ-930Q], the Hundred-Talent Program (Chinese academy of Sciences), the Youth Innovation

Promotion Association CAS [grant nos. 2017469 and 2016376] and the Qinghai Provincial Thousand Talents Program for High-Level Innovative Professionals.

ORCID® iDs

Yue Shen - https://orcid.org/0000-0001-9163-5148
Ying Wang - https://orcid.org/0000-0002-7128-6988
Yuan Zhou - https://orcid.org/0000-0002-0655-0391

References

1. Lee, C.; Wei, X.; Kysar, J. W.; Hone, J. *Science* **2008,** *321,* 385–388. doi:10.1126/science.1157996
2. Balandin, A. A.; Ghosh, S.; Bao, W.; Calizo, I.; Teweldebrhan, D.; Miao, F.; Lau, C. N. *Nano Lett.* **2008,** *8,* 902–907. doi:10.1021/nl0731872
3. Orlita, M.; Faugeras, C.; Plochocka, P.; Neugebauer, P.; Martinez, G.; Maude, D. K.; Barra, A. L.; Sprinkle, M.; Berger, C.; de Heer, W. A.; Potemski, M. *Phys. Rev. Lett.* **2008,** *101,* 267601. doi:10.1103/PhysRevLett.101.267601
4. Castro Neto, A. H.; Guinea, F.; Peres, N. M. R.; Novoselov, K. S.; Geim, A. K. *Rev. Mod. Phys.* **2009,** *81,* 109–162. doi:10.1103/RevModPhys.81.109
5. Kim, K. S.; Zhao, Y.; Jang, H.; Lee, S. Y.; Kim, J. M.; Kim, K. S.; Ahn, J.-H.; Kim, P.; Choi, J.-Y.; Hong, B. H. *Nature* **2009,** *457,* 706–710. doi:10.1038/nature07719
6. Pei, S. F.; Cheng, H. M. *Carbon* **2012,** *50,* 3210–3228. doi:10.1016/j.carbon.2011.11.010
7. López, V.; Sundaram, R. S.; Gómez-Navarro, C.; Olea, D.; Burghard, M.; Gómez-Herrero, J.; Zamora, F.; Kern, K. *Adv. Mater.* **2009,** *21,* 4683–4686. doi:10.1002/adma.200901582
8. Yang, D.; Velamakanni, A.; Bozoklu, G.; Park, S.; Stoller, M.; Piner, R. D.; Stankovich, S.; Jung, I.; Field, D. A.; Ventrice, C. A., Jr.; Ruoff, R. S. *Carbon* **2009,** *47,* 145–152. doi:10.1016/j.carbon.2008.09.045
9. Zhang, J.; Yang, H.; Shen, G.; Cheng, P.; Zhang, J.; Guo, S. *Chem. Commun.* **2010,** *46,* 1112–1114. doi:10.1039/B917705A
10. Shen, Y.; Guo, S.; Hu, J.; Zhang, Y. *Appl. Phys. Lett.* **2012,** *101,* 183109. doi:10.1063/1.4765359
11. Zhou, Y.; Bao, Q.; Tang, L. A. L.; Zhong, Y.; Loh, K. P. *Chem. Mater.* **2009,** *21,* 2950–2956. doi:10.1021/cm9006603
12. Kumar, P. V.; Bardhan, N. M.; Tongay, S.; Wu, J.; Belcher, A. M.; Grossman, J. C. *Nat. Chem.* **2014,** *6,* 151–158. doi:10.1038/nchem.1820
13. Gao, L.; Ren, W.; Li, F.; Cheng, H.-M. *ACS Nano* **2008,** *2,* 1625–1633. doi:10.1021/nn800307s
14. Gómez-Navarro, C.; Meyer, J. C.; Sundaram, R. S.; Chuvilin, A.; Kurasch, S.; Burghard, M.; Kern, K.; Kaiser, U. *Nano Lett.* **2010,** *10,* 1144–1148. doi:10.1021/nl9031617
15. Wei, Z.; Wang, D.; Kim, S.; Kim, S.-Y.; Hu, Y.; Yakes, M. K.; Laracuente, A. R.; Dai, Z.; Marder, S. R.; Berger, C.; King, W. P.; de Heer, W. A.; Sheehan, P. E.; Riedo, E. *Science* **2010,** *328,* 1373–1376. doi:10.1126/science.1188119
16. Zhang, K.; Fu, Q.; Pan, N.; Yu, X.; Liu, J.; Luo, Y.; Wang, X.; Yang, J.; Hou, J. *Nat. Commun.* **2012,** *3,* No. 1194. doi:10.1038/ncomms2200
17. Ekiz, O. Ö.; Ürel, M.; Güner, H.; Mizrak, A. K.; Dâna, A. *ACS Nano* **2011,** *5,* 2475–2482. doi:10.1021/nn1014215
18. Hu, J.; Xiao, X.-D.; Salmeron, M. *Appl. Phys. Lett.* **1995,** *67,* 476–478. doi:10.1063/1.114541
19. Hu, J.; Xiao, X.-D.; Ogletree, D. F.; Salmeron, M. *Science* **1995,** *268,* 267–269. doi:10.1126/science.268.5208.267
20. Shen, Y.; Zhou, Y.; Sun, Y.; Zhang, L.; Wang, Y.; Hu, J.; Zhang, Y. *Appl. Surf. Sci.* **2017,** *412,* 497–504. doi:10.1016/j.apsusc.2017.03.291
21. Shen, Y.; Wang, Y.; Zhang, J.; Hai, C.; Zhou, Y.; Hu, J.; Zhang, Y. *J. Appl. Phys.* **2014,** *115,* No. 244302. doi:10.1063/1.4883538
22. Shen, Y.; Wang, Y.; Zhou, Y.; Shi, A.; Hu, J.; Zhang, Y. *J. Phys. D: Appl. Phys.* **2016,** *49,* 415303. doi:10.1088/0022-3727/49/41/415303
23. Verdaguer, A.; Cardellach, M.; Segura, J. J.; Sacha, G. M.; Moser, J.; Zdrojek, M.; Bachtold, A.; Fraxedas, J. *Appl. Phys. Lett.* **2009,** *94,* 233105. doi:10.1063/1.3149770
24. Lu, W.; Wang, D.; Chen, L. *Nano Lett.* **2007,** *7,* 2729–2733. doi:10.1021/nl071208m
25. Shen, Y.; Zhang, Y.; Hu, J. *J. Chin. Electron Microsc. Soc.* **2013,** *32,* 95–100. doi:10.3969/j.1000-6281.2013.02.001
26. Kulkarni, D. D.; Kim, S.; Chyasnavichyus, M.; Hu, K.; Fedorov, A. G.; Tsukruk, V. V. *J. Am. Chem. Soc.* **2014,** *136,* 6546–6549. doi:10.1021/ja5005416
27. Burnett, T.; Yakimova, R.; Kazakova, O. *Nano Lett.* **2011,** *11,* 2324–2328. doi:10.1021/nl200581g
28. Kurra, N.; Prakash, G.; Basavaraja, S.; Fisher, T. S.; Kulkarni, G. U.; Reifenberger, R. G. *Nanotechnology* **2011,** *22,* 245302. doi:10.1088/0957-4484/22/24/245302
29. Electric Techniques on MultiMode Systems, Support Note 231, Revision E, Digital Instruments Veeco Metrology Group (now Bruker).
30. El Khoury, D.; Arinero, R.; Laurentie, J. C.; Castellon, J. *AIP Adv.* **2016,** *6,* 035318. doi:10.1063/1.4944953
31. de Tournadre, G.; Reisdorffer, F.; Rödel, R.; Simonetti, O.; Klauk, H.; Giraudet, L. *J. Appl. Phys.* **2016,** *119,* 125501. doi:10.1063/1.4944884
32. He, H.; Klinowski, J.; Forster, M.; Lerf, A. *Chem. Phys. Lett.* **1998,** *287,* 53–56. doi:10.1016/S0009-2614(98)00144-4
33. Schniepp, H. C.; Li, J.-L.; McAllister, M. J.; Sai, H.; Herrera-Alonso, M.; Adamson, D. H.; Prud'homme, R. K.; Car, R.; Saville, D. A.; Aksay, I. A. *J. Phys. Chem. B* **2006,** *110,* 8535–8539. doi:10.1021/jp060936f
34. Hummers, W. S., Jr.; Offeman, R. E. *J. Am. Chem. Soc.* **1958,** *80,* 1339. doi:10.1021/ja01539a017
35. Zhou, X.; Lu, G.; Qi, X.; Wu, S.; Li, H.; Boey, F.; Zhang, H. *J. Phys. Chem. C* **2009,** *113,* 19119–19122. doi:10.1021/jp9079298
36. Eda, G.; Mattevi, C.; Yamaguchi, H.; Kim, H.; Chhowalla, M. *J. Phys. Chem. C* **2009,** *113,* 15768–15771. doi:10.1021/jp9051402
37. Kendall, T. A.; Martin, S. T. *J. Phys. Chem. A* **2006,** *111,* 505–514. doi:10.1021/jp0647129

License and Terms

This is an Open Access article under the terms of the Creative Commons Attribution License (http://creativecommons.org/licenses/by/4.0), which permits unrestricted use, distribution, and reproduction in any medium, provided the original work is properly cited.

The license is subject to the *Beilstein Journal of Nanotechnology* terms and conditions: (https://www.beilstein-journals.org/bjnano)

The definitive version of this article is the electronic one which can be found at: doi:10.3762/bjnano.9.106

BEILSTEIN JOURNAL OF NANOTECHNOLOGY

Correlative electrochemical strain and scanning electron microscopy for local characterization of the solid state electrolyte $Li_{1.3}Al_{0.3}Ti_{1.7}(PO_4)_3$

Nino Schön[1,2], Deniz Cihan Gunduz[1,2], Shicheng Yu[1,2], Hermann Tempel[1], Roland Schierholz[1] and Florian Hausen[*1,2,3]

Full Research Paper

Open Access

Address:
[1]Forschungszentrum Jülich, Institute of Energy and Climate Research, IEK-9, 52425 Jülich, Germany, [2]RWTH Aachen University, Institute of Physical Chemistry, 52074 Aachen, Germany and [3]Jülich-Aachen Research Alliance, section JARA-Energy, 52425 Jülich, Germany

Email:
Florian Hausen* - f.hausen@fz-juelich.de

* Corresponding author

Keywords:
correlative microscopy; electrochemical strain microscopy (ESM); $Li_{1.3}Al_{0.3}Ti_{1.7}(PO_4)_3$ (LATP); scanning electron microscopy (SEM); solid state electrolytes (SSE)

Beilstein J. Nanotechnol. **2018,** *9,* 1564–1572.
doi:10.3762/bjnano.9.148

Received: 05 January 2018
Accepted: 23 April 2018
Published: 28 May 2018

This article is part of the Thematic Series "Scanning probe microscopy for energy-related materials".

Guest Editor: P. Leclère

© 2018 Schön et al.; licensee Beilstein-Institut.
License and terms: see end of document.

Abstract

Correlative microscopy has been used to investigate the relationship between Li-ion conductivity and the microstructure of lithium aluminum titanium phosphate ($Li_{1.3}Al_{0.3}Ti_{1.7}(PO_4)_3$, LATP) with high spatial resolution. A key to improvement of solid state electrolytes such as LATP is a better understanding of interfacial and ion transport properties on relevant length scales in the nanometer to micrometer range. Using common techniques, such as electrochemical impedance spectroscopy, only global information can be obtained. In this work, we employ multiple microscopy techniques to gain local chemical and structural information paired with local insights into the Li-ion conductivity based on electrochemical strain microscopy (ESM). Scanning electron microscopy (SEM) and energy-dispersive X-ray spectroscopy (EDX) have been applied at identical regions to identify microstructural components such as an $AlPO_4$ secondary phase. We found significantly lower Li-ion mobility in the secondary phase areas as well as at grain boundaries. Additionally, various aspects of signal formation obtained from ESM for solid state electrolytes are discussed. We demonstrate that correlative microscopy is an adjuvant tool to gain local insights into interfacial properties of energy materials.

Introduction

Solid state electrolytes (SSE) of the NASICON-type exhibit a high ionic conductivity and are in this respect becoming comparable to conventional organic electrolytes commonly used in lithium-ion batteries (LIBs) [1-5]. SSEs have gained much interest in recent years for replacing the flammable liquid electrolyte in LIBs, especially in safety-related environments like automotive applications [6,7]. Furthermore, the increased electrochemical window in the case of SSEs opens the path to use

advanced electrode materials with improved volumetric and gravimetric energy density [1,8-10]. Lithium aluminum titanium phosphate $Li_{1.3}Al_{0.3}Ti_{1.7}(PO_4)_3$ (LATP), a ceramic with NASICON-type structure, is especially considered as a beneficial solid state electrolyte due to its superior lithium-ion conductivity in the range of 2 mS cm^{-1} in the "bulk" and 2 µS cm^{-1} at grain boundaries with an overall conductivity of 0.2 mS cm^{-1} [11] and has therefore attracted much research within the last decade [12-15]. In classical electrochemical impedance spectroscopy (EIS), the ionic conductivity is measured through the entire sample and over the full electrode contact area (typically in the range of 1 cm^2). Hence, only averaged values are obtained whilst locally the ion mobility can still be inhomogeneous [11]. Translating local ion migration into global conductivity is part of ongoing research. First approaches for small-scale impedance measurements have been reported to gain adequate EIS resolution by coupling with AFM [16]. The authors reported experiments on silver-ion conducting glasses and found good agreement between the mean value of local conductivities and the macroscopic conductivity. It has been found that the electrochemical characteristics of LATP correlate with the microstructure of the material [17-19]. The microstructure describes the relationship between density, porosity and particle size, grain structure and phase composition. These attributes are primarily defined by the sintering process [20] and have been analyzed macroscopically. But, as it can already be seen from the results of different lithium-ion conductivities for grain and grain boundary structures in comparison to the overall ionic conductivity, it is of utmost importance to understand the electrochemical and ion-transport properties of promising SSEs such as LATP at the length scale of the grain size, local defects and structural inhomogeneities, that is, on the nanometer to low-micrometer scale [10,11].

Reports on local behavior and properties of SSEs are scarce. Very recently, Sasano et al. have reported about the qualitative relation between grain orientation and Li-ion mobility in $Li_{0.33}La_{0.56}TiO_3$ using scanning electron microscopy (SEM) with electron backscatter diffraction (EBSD) and electrochemical strain microscopy (ESM) [21]. The authors correlate variations in the Li-ion mobility detected by ESM with limitations in the Li-ion migration pathway. ESM is a relatively new technique based on atomic force microscopy (AFM): An AC voltage with the same frequency as the contact resonance frequency of the tip–sample contact is applied to a conductive tip. [22,23]. The induced electrical field in the material under investigation is extremely localized due to the small tip radius on the order of 15 nm. Hence, the interaction between the electric field and the local structure of the material can be studied with high spatial resolution. Mobile ions are accelerated by the electric field towards or away from the tip. Consequently, the concentration of ions changes within a small volume under the tip, leading to a deformation of the surface. The resulting strain is measured by the system and reflected in the ESM amplitude signal. For electrode materials, the strain is supposed to be directly proportional to the Li-ion mobility [24-27].

In this work we combine the strengths of two microscopy techniques: SEM in combination with energy-dispersive X-ray spectroscopy (EDX) and ESM as an AFM-based technique. Both techniques are consecutively employed at identical regions of interest on LATP samples. Hence, chemical information, as detected by EDX, and information about the local mobility of ions, extracted from ESM measurements, are available with very high spatial resolution. Such a correlative microscopy approach allows for direct comparison of microstructure and ionic mobility, enabling unique local insights into the structural, chemical and electrochemical characteristics of solid state electrolytes.

Results and Discussion

The grain structure of a typical region of hand-polished $Li_{1.3}Al_{0.3}Ti_{1.7}(PO_4)_3$ (LATP), as observed by SEM, is shown in Figure 1a. A large variation in grain size and shape is clearly

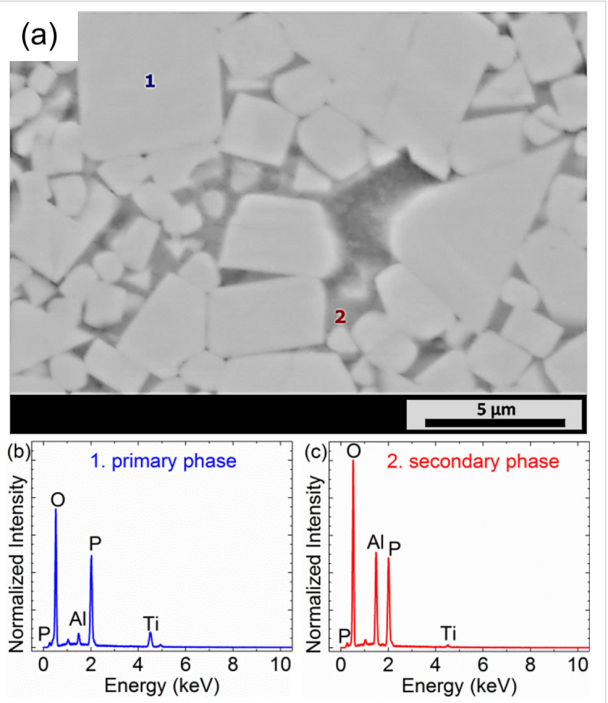


Figure 1: (a) Typical SEM back scattered electron (BSE) image of a LATP pellet sintered at 1000 °C and polished by hand; the markings 1 and 2 denote regions where EDX was performed. (b) Micro-area EDX spectra of a brighter grain of the material as denoted by the marking 1 in (a). The spectrum contains characteristic peaks corresponding to Al, Ti, O and P with intensities as expected for $Li_{1.3}Al_{0.3}Ti_{1.7}(PO_4)_3$. (c) Micro-area EDX spectrum of a darker region of the material as denoted by the marking 2 in (a).

visible, with a preference for cubic structures. The largest grains are about 20 μm^2 in size while the typical grain size is on the order of 1 μm^2. As the surface was polished, the observed contrast in color cannot be related to topographical effects, but rather indicates the existence of a secondary phase. This finding becomes evident in EDX measurements, depicted in Figure 1b,c, revealing the existence of two separate phases inside the material. The primary phase (denoted as 1 in Figure 1a) appears brighter in the SEM image and consists of Al, Ti, P and O (Li is not detectable by EDX) while the secondary phase (denoted as 2 in Figure 1a) appears darker and contains the elements Al, P and O but only minor Ti content. Based on this observation, the primary phase is attributed to LATP while the secondary phase can be related to aluminum phosphate ($AlPO_4$). As the stoichiometry of the EDX analysis matches that of LATP and aluminum phosphate, respectively, the assignment of the individual phases to their chemical composition is further supported. Additionally, the occurrence of a secondary phase of $AlPO_4$ has been previously observed [1,4]. No changes based on the different composition in phase images of tapping-mode AFM, nor in peak-force tapping quantitative nanomechanical property mapping have been observed. The insignificant amount of detected titanium is due to the resolution limit of the EDX measurements. The volume from which characteristic X-ray peaks can escape is largest for Ti at Kα at 4510 eV, and therefore, contributions from the surrounding material should also be considered for Ti. For P (Kα at 2010 eV) and Al (Kα at 1486 eV) this volume becomes smaller and for O (Kα at 525 eV) only regions close to the surface contribute.

Recently, a very similar microstructure of LATP has been published and discussed in further detail [11,17]. Information about the behavior of the material as a solid state electrolyte cannot be derived based on SEM and EDX mappings alone, hence we performed ESM.

Figure 2 shows correlative images of SEM and AFM topography as well as ESM on identical regions of LATP sintered at 1050 °C. The SEM image (Figure 2a) illustrates the grain structure of the sample and reveals the existence of primary phase and secondary phase represented by different colors. In accordance with Figure 1 and the EDX spectra, such regions are attributed to LATP (brighter contrasts) and aluminum phosphate (darker contrasts), respectively. Additionally, the presence of

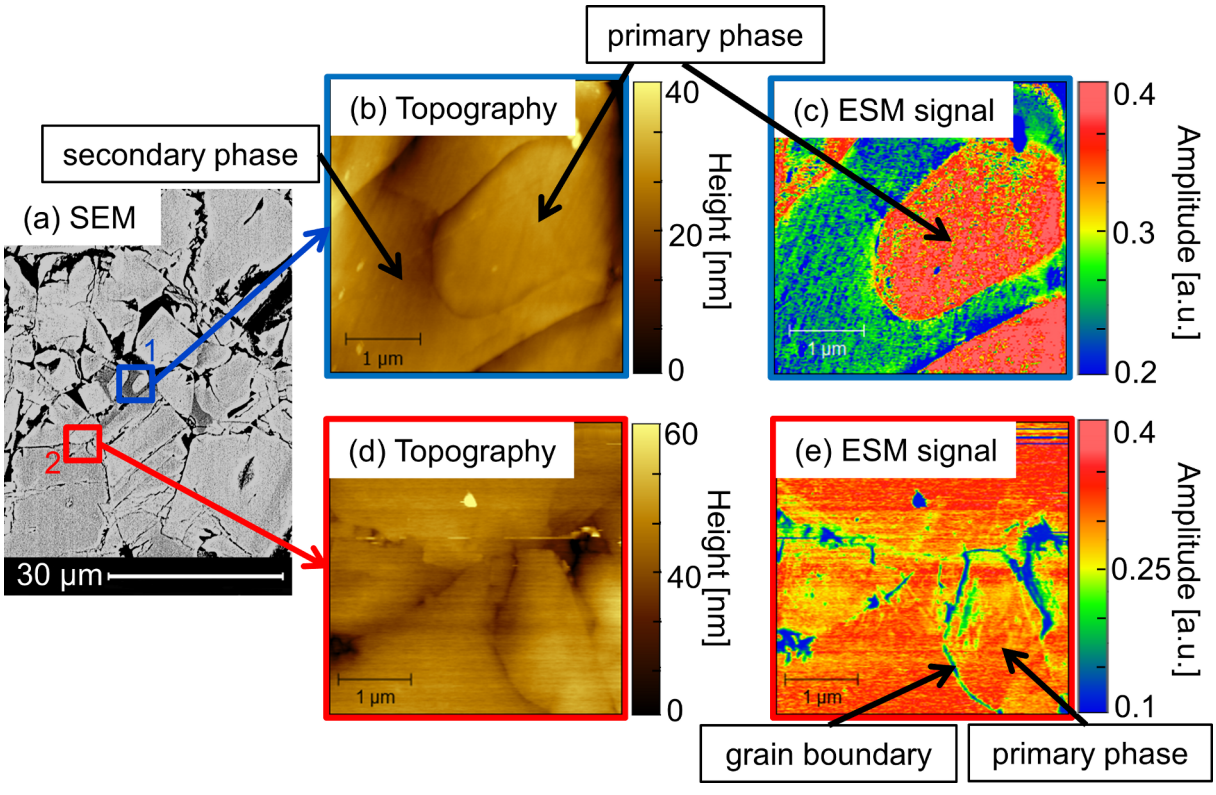


Figure 2: Correlative microscopy of selected areas on LATP sintered at 1050 °C and polished by hand. (a) SEM is used to identify grains of LATP and aluminum phosphate, respectively. (b) and (d) are topographical AFM images of the regions marked by blue and red squares in (a). (c) and (e) are ESM amplitude signals and exhibit a strong contrast between primary and secondary phase. The contact resonance frequency of the tip–sample system was at 281 kHz for (c) and 285 kHz for (e).

several small pores is very likely as can be seen by the dark regions in Figure 2a, but these are mainly excluded for the regions selected for ESM measurements (except the upper-right corner in Figure 2b and the pore in Figure 2d). Correlative AFM and ESM images were obtained from two different areas indicated by the blue (1) and red (2) markings in Figure 2a. In the topography images illustrated in Figure 2b,d, minor amounts of residue originating from the polishing procedure are observed in the form of elevated particles. Apart from this, the AFM images reflect the same surface features as observed by SEM, providing evidence that both methods can be applied complementary. The same pores as those observed via SEM can be found in the AFM topography image and the topography reveals some preferential etching at the grain boundaries and interfaces. Differentiation between the primary and secondary phase is not possible based on the topography images as no isolated terraces with differing heights are formed.

As small pores often resemble a similar color as the secondary phase in SEM images, and are therefore difficult to distinguish from one another, correlative microscopy offers the advantage to unambiguously verify small-sized pores due to the high *z*-contrast of the AFM, as depicted in Figure 2d.

Next to the topography, the ESM amplitude signal for the regions indicated by blue and red squares in Figure 2a is recorded and depicted in Figure 2c,e. A change in the amplitude can be correlated to local interactions between the applied electrical field and the SSE material in the respective areas. While no differentiation between the primary and secondary phase of LATP could be derived from topography images, the simultaneously recorded ESM amplitude signal exhibits clear contrast between the different phases. According to the SEM image, it is possible to identify the grains as LATP and aluminum phosphate as labeled in Figure 2. It becomes apparent that LATP shows a strong ESM amplitude signal. In contrast, the amplitude is significantly smaller for regions consisting of aluminum phosphate. The residual particles on the top of the sample exhibit very low amplitude. In line with reports by Balke et al. and Sasano et al. [21,22,24] we correlate a larger ESM amplitude signal to higher Li content or Li mobility. A thorough discussion about signal formation follows later in the manuscript.

The selected regions of interest have been chosen as in area 1 (blue square) where grains of both LATP and aluminum phosphate are present, and hence, different Li-ion transport properties are to be expected. This assumption is verified by the larger ESM amplitude signal for the primary phase in comparison to the secondary phase, as demonstrated in Figure 2c. In spot 2 (red square), only LATP is present, but well-separated into several grains. A similar finding as for area 1 is obtained for the amplitude from spot 2 as demonstrated in Figure 2e. A strong amplitude signal was found for grains consisting of LATP. Interestingly, the grain boundaries exhibit significantly smaller amplitudes comparable to that of aluminum phosphate in area 1.

This is examined in more detail for the region of grain boundary marked by the arrow in Figure 2e. Figure 3 shows AFM topography and ESM images with higher resolution. Various effects are observed in the ESM amplitude signal, depicted in

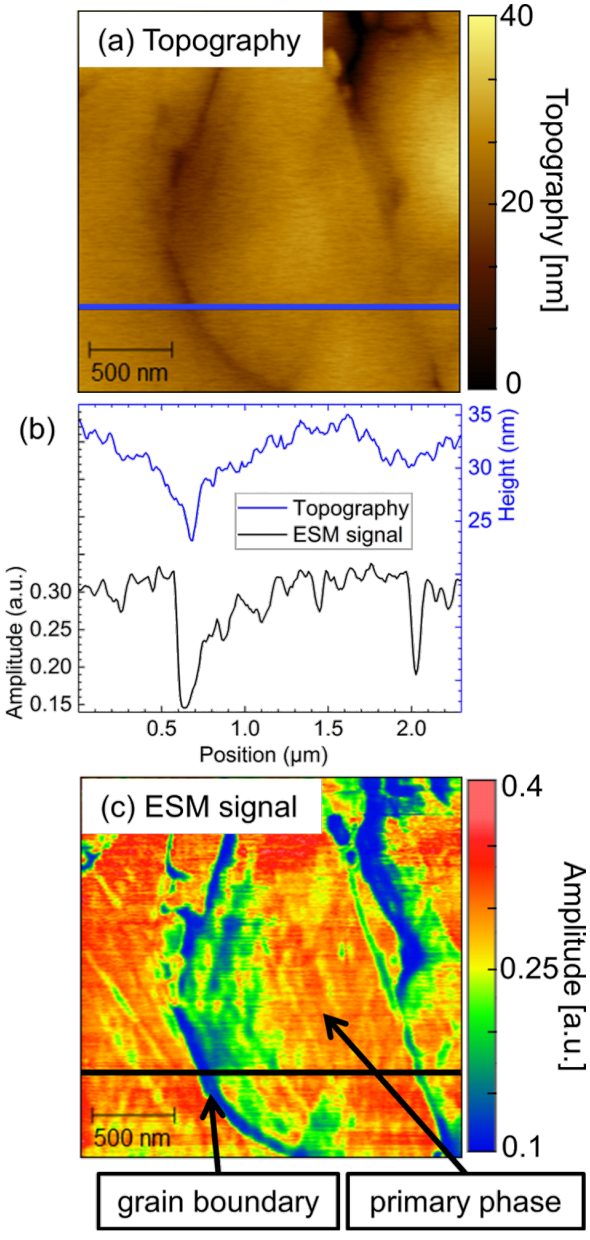


Figure 3: Higher resolution images of part of the area shown in Figure 2d and Figure 2e. (a) Topography, (c) ESM amplitude, and (b) line scans along the topography (blue) and the ESM amplitude signal (black) as indicated in the corresponding images. The contact resonance frequency of the tip–sample system was 299 kHz.

Figure 3c: Firstly, minor variations in the magnitude of the ESM amplitude signal are recognizable in Figure 3c in comparison to Figure 2e on the left side of the central grain. The image in Figure 3c was recorded about twenty minutes after Figure 2e. Such alterations demonstrate the dynamic nature of the system. Secondly, it is apparent from Figure 3c that the ESM amplitude signal shows differentiations inside individual grains of the primary phase. The origin of the effect of variations in the observed ESM amplitude intensity might be related to deviations in the lithium content within single grains. Besides, variations in crystal orientation might be accountable for the observed effect, as was discussed recently for LLTO [21]. However, both assumptions need further experimental evidence and cannot be answered based on the present data.

Finally, Figure 3c demonstrates that the grain boundaries between three grains of primary phase exhibit significantly smaller ESM amplitude signal than the grains themselves. The influence of the topography can be elucidated by the line sections as indicated in Figure 3a for topography and in Figure 3c for the ESM amplitude signal and shown in Figure 3b. From left to right three grains and correspondingly two grain boundaries can be identified in the topography image (Figure 3a). An overall height difference of about 8 nm for the left grain boundary and of 3 nm for the right grain boundary can be extracted from the line section illustrated in Figure 3b. For both grain boundaries, sharp peaks with significantly lowered magnitude of the ESM amplitude signal with respect to the overall grain are obtained at the point of lowest topography, i.e. the grain boundary. From the line section, it becomes clear that this observation cannot be related to an image or tip artifact as the simultaneously recorded topography exhibits a different and well-resolved response. While the ESM signal amplitude stays rather homogeneous across the grains, the topography shows a smoother transition from one grain to the other over a distance of about 0.7 μm to 0.8 μm. This finding indicates low crosstalk between the topography of the sample and the ESM amplitude signal. However, it is conceivable that the surface topography influences the observed ESM amplitude signal in some way. Topographical features lead to a change in contact area between tip and sample, which is likely to influence the signal formation process and therefore induce crosstalk as a change in contact area influences the contact resonance conditions. In order to investigate this effect in more detail, a different preparation method has been employed to obtain a significantly smoother LATP surface.

Figure 4 shows an SEM picture of the area on LATP sintered at 1000 °C that was polished by means of a focused ion beam (FIB). Please note that the color contrast is inverted in this case as the SEM signal is detected by secondary electrons (SEM-SE) rather than back-scattered electrons (SEM-BSE). Therefore, darker regions correspond to LATP and brighter contrasts can be attributed to aluminum phosphate. Correlative microscopy was performed in a region of 10 μm × 10 μm in the selected area depicted in Figure 4b. AFM topography as well as ESM amplitude signal is shown in Figure 4c,d, respectively. In comparison with hand polished samples (see Figure 2b,d) a smoother surface finish was obtained. Nevertheless, the Ga-ion beam produced some trenches due to the curtaining effect. The hand-polished LATP sample exhibits an RMS roughness of 4.4 nm and 2.7 nm for the regions depicted in Figure 2b and Figure 2d, respectively. However, the sample shown in Figure 4c prepared by FIB exhibits an RMS roughness of only 1.8 nm for a comparable size.

Regardless of the curtaining effect, grain boundaries and individual grains can hardly be seen in the topography image (Figure 4c), using the same color scale as in Figure 2. This means, preparation with the ion beam almost parallel to the surface introduces less preferential etching of the grain boundaries. However, the ESM amplitude signal, as shown in Figure 4d, possesses a stark contrast between the primary and secondary phase. A considerably larger signal is observed for the primary phase that corresponds to LATP in comparison with aluminum phosphate, the secondary phase. The variation of the AFM scanning angle affected the observed lines, providing evidence that the effect results from a physical deformation of the sample surface induced by the FIB preparation.

As expected, grain boundaries display an ESM amplitude signal that is larger than for the secondary phase but smaller than for the primary phase. Significantly more “noise” is observed in Figure 4d and seems to appear in horizontal lines, which was the direction of the ion beam during preparation and therefore is introduced by the curtaining effect. However, at similar positions in the SEM image (Figure 4b), the curtaining effect is visible, which is a consequence of the FIB polishing and caused by local inhomogeneities in the material, leading to uneven erosion. This points to an influence due to the preparation method on the obtained ESM amplitude signal and should be considered for further experiments.

Topography as well as variations in the ESM amplitude signal with respect to grain boundary, primary and secondary phase on a higher magnification region for the FIB-polished sample are demonstrated in Figure 5. As observed before, a difference between the primary and secondary phase cannot be deduced by only topographical data from AFM. On the other hand, the ESM amplitude signal shows a pronounced contrast between different phases, whereas grain boundaries and the secondary phase are hardly distinguishable. This observation can be explained by

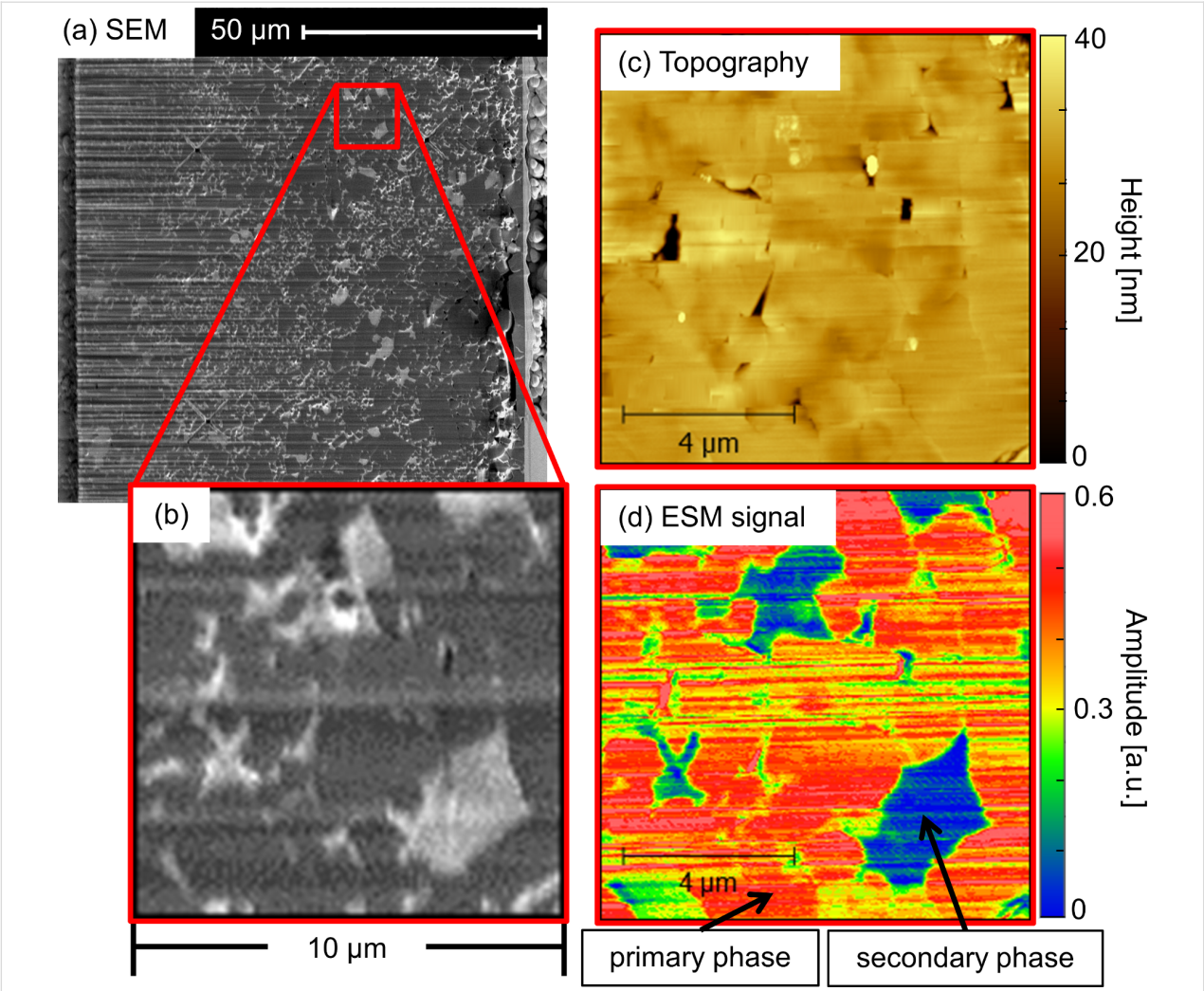


Figure 4: Correlative microscopy images from LATP sintered at 1000 °C and polished by a focused-ion beam. (a) SEM image of the polished area on the LATP pellet. In the left part of the image, a curtaining effect is observed. (b) Cut-out area of interest of 10 × 10 µm indicated by the red square revealing primary and secondary phases. (c) Topography and (d) ESM amplitude signal of the selected area shown in (b). The contact resonance frequency of the tips–sample system was 331 kHz.

a partial incorporation of $AlPO_4$ into the grain boundaries. A similar effect has been recently reported as a function of sintering temperature, supporting the argumentation [17]. Of note is that at certain positions in the grain boundary a high ESM amplitude signal is also observed, suggesting a locally heterogeneous composition of the grain boundary. The negligible difference in ESM amplitude signal between the grain boundary and secondary phase also indicates what was previously demonstrated in Figure 2 and Figure 3, that is, significant contributions of the surface topography on the ESM amplitude signal are not likely to influence the results for the material studied here.

Assuming that a larger ESM amplitude signal corresponds directly to an increased Li-ion mobility in the sample, as predicted for Li-ion battery electrodes [22], the conclusion drawn in this manuscript is that Li-ion conductivity through the grains is favorable [11]. We want to emphasize that additional effects, such as a change in tip contact radius as well as changes in the crystal orientation, might also relate to the observed reduced ionic conductivity in grain boundaries. Correlative microscopy was successfully implemented to determining the influence of secondary phases on ion conductivity by enabling clear chemical analyses of each grain probed by ESM.

However, it is currently discussed to what extent the ESM amplitude signal can be attributed to an increased molar volume induced by the electric field in the vicinity of the tip, as proposed by Balke et al. [22]. This mechanism implies that the mobile ions in the material are attracted towards the surface, causing a strain of the material according to Vegard's Law [25]. In the case of a solid state electrolyte, with its inherently low

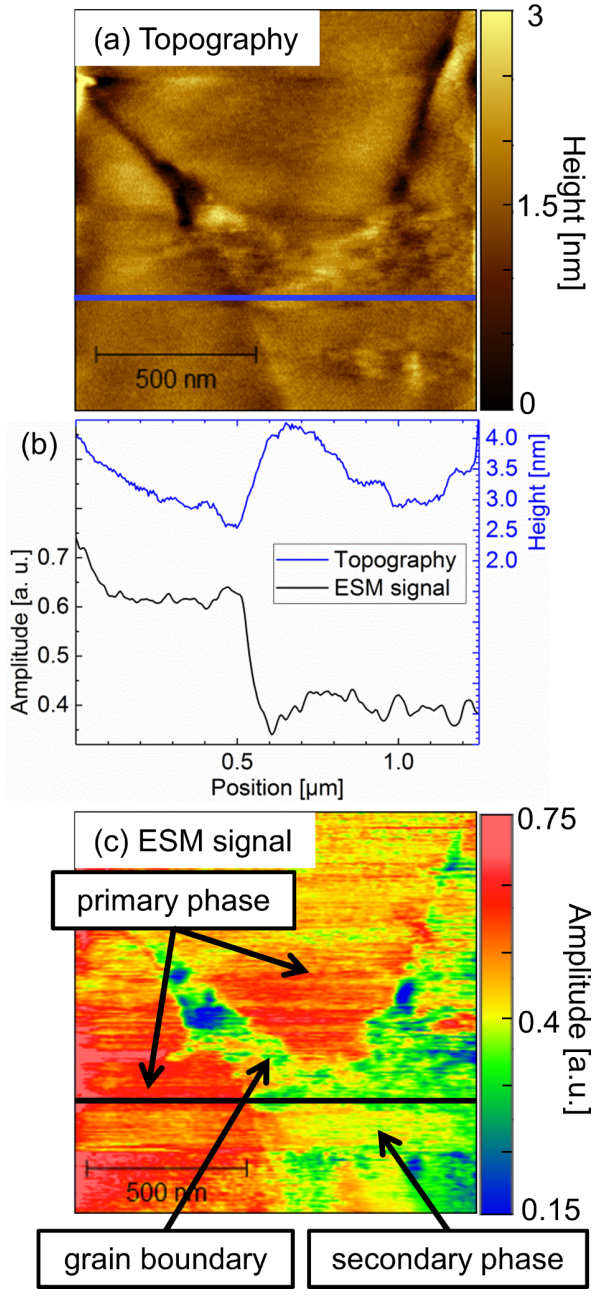


Figure 5: High magnification image of LATP polished by focused-ion beam showing the (a) topography and (c) ESM amplitude signal of the primary phase (LATP), secondary phase ($AlPO_4$) and grain boundaries. (b) Line scans (average of ten lines) along the topography (blue) and the ESM amplitude signal (black) as indicated in the corresponding images. The contact resonance frequency of the tip–sample system was 292 kHz.

electronic conductivity, it remains arguable if the ESM amplitude signal is predominantly caused by ion migration. Very recently, Lushta et al. [28] presented ESM measurements on a commercially available Li-ion conducting glass ceramic (LICGC) using dual AC resonance tracking (DART) and band excitation (BE) as excitation methods. Furthermore, the authors calculated the diffusion constant and diffusion time of the commercially available LICGC, taking into account the density of the ceramic and the electronic conductivity. The idea behind this approach is that for reasons of charge neutrality, the mobility of cations is also linked to the electronic conductivity of the material. The authors came to the conclusion that the observed ESM signal cannot be based on Vegard's strain, but rather on ion diffusion because the calculated diffusion processes are too slow to follow the applied AC frequency. As the calculations are independent of the exact excitation method we calculated diffusion coefficients for the LATP pellets used in this study according to equation 6 in [28] of 3.1×10^{-16} m² s^{-1} for pellets sintered at 1000 °C and of 3.0×10^{-16} m² s^{-1} for pellets sintered at 1050 °C. For the calculations a Li-ion conductivity of 2 mS cm^{-1}, an electronic conductivity of 10^{-10} S cm^{-1} (as found in [29]), a temperature of 298 K as well as a density of 2.61 g cm^{-3} for pellets sintered at 1000 °C and 2.65 g cm^{-3} for pellets sintered at 1050 °C (both values taken from [16]), leading to a lithium ion density of 5.2×10^{21} cm^{-3} and 5.4×10^{21} cm^{-3}, respectively, were considered. Assuming a diffusion length of 50 nm (as suggested in [28]) this leads to diffusion times of 8.1 s and 8.5 s, respectively. Even for a diffusion length of only 10 nm, a diffusion time of about 0.3 s is expected, which is far above the applied AC frequency on the order of 300 kHz. Based on these calculations, we also expect that effects other than Vegard's Law contribute substantially to the observed ESM amplitude signal. Electrostatic interactions are discussed to be an important additional parameter that can influence ESM experiments [28,30,31] and will be the subject of future research. Additionally, LATP is known to have a strong anisotropic thermal expansion [3]. LTP, which has the same structure, exhibits an anisotropic reaction upon lithium intercalation; the *a*-axis contracts while the *c*-axis expands with the transformation from $LiTi_2(PO_4)_3$ to $Li_3Ti_2(PO_4)_3$ [32]. Hence, LATP might show similar behavior upon (de)-lithiation and its electrostatic interaction can be expected to be strongly anisotropic. A simple interpretation of the ESM amplitude signal solely based on Vegard's Law is therefore demanding and would require a correlative EBSD analysis of the area to retrieve the actual crystallographic orientation [21]. However, a thorough analysis is out of the scope of the current study but is part of ongoing research.

Conclusion

We have presented correlative microscopy experiments by means of SEM and AFM-based techniques of the solid state electrolyte lithium aluminum titanium phosphate (LATP). In the SEM images, a primary and a secondary phase have been identified and could be attributed to LATP as the primary phase and $AlPO_4$ as the secondary. ESM was employed to locally identify

regions of increased interaction of the material with an applied alternating electric field. It was found that the secondary phase exhibits significantly lower interaction than the primary phase. It was discussed whether the interaction could be directly linked to Li-ion mobility. Furthermore, grain boundaries have been analyzed and show only weak response in ESM amplitude signal. This result is explained by incorporation of $AlPO_4$ into the grain boundary structure, as suggested in the literature [11,17]. It has been proven that correlative microscopy leads to improved understanding of the microstructure–property relationship of solid state electrolytes on a process-relevant scale. Increased knowledge in this respect is of utmost importance in order to develop SSEs with better functionalities.

Experimental

Synthesis of $Li_{1.3}Al_{0.3}Ti_{1.7}(PO_4)_3$ (LATP)

The synthesis of $Li_{1.3}Al_{0.3}Ti_{1.7}(PO_4)_3$ (LATP) has been described in detail elsewhere [17] and consists of an oxalic acid supported sol–gel process. Binder-free dense LATP pellets as used in this study were obtained by an improved route involving preannealing, shaping, pressing and sintering in air at 1000 °C or 1050 °C for 8 h as indicated. For both AFM as well as SEM measurements, the pellets were subject to a polishing step by hand polishing or by focused-ion beam.

Hand polishing

Smooth LATP surfaces suitable for SEM and AFM analysis were achieved by oil-based polishing to minimize exposure of LATP to water. For the first grinding step, silicon carbide paper of 800 grit was used with a particle size of about 20 µm. Stepwise, finer grit sandpapers were used: 1200 (15 µm), 2400 (10 µm) and ending with 4000 (5 µm). At each step, the sample was ground for 10 to 15 minutes at 150 rpm. This was followed by polishing the samples for 4 to 8 minutes at 300 rpm in four steps. In the first two steps, a diamond suspension with 3 µm and 2 µm particles was used. Finally, two finishing steps were performed with a 0.2 µm silica suspension and a 0.05 µm master polish. Afterwards, the pellets were rinsed thoroughly with isopropanol.

Focused-ion beam polishing

For comparison, a second sample was additionally polished using a focused-ion beam (FEI (now Thermo-Fisher) Helios 460F1) [33]. For this, a polished SEM sample was used. A protective Pt-layer the size of the final polished surface (90 µm × 90 µm) was deposited by the ion beam. Around this protective layer, wedge-shaped trenches were cut and from the edge of the polished pellet material was removed with the cleaning cross-section pattern until the protective Pt-layer was reached. Then, the sample was rotated and tilted for perpendicular ion polishing. For this purpose again, a protective Pt-layer was deposited on the new cross-section before removing the initially deposited protective Pt-layer of 90 µm × 90 µm size as well as parts of the material beneath it, to form the ion-polished surface. Due to the large area, curtaining is present in the left part of the ion-polished area in Figure 4a. The protective Pt-layer and an incidence angle smaller than 1.5° precludes the material from being doped by gallium.

Scanning electron microscopy

A SEM (Quanta FEG 650; FEI part of Thermo-Fischer, Hillsboro, Oregon, USA) equipped with a field emission gun (FEG) and EDX (Octane 60 mm^2, EDAX Inc., Mahwah, NJ, USA) was employed to visualize the grain structure of LATP samples. Chemical information from the various regions of interest was obtained by means of EDX.

Atomic force microscopy and electrochemical strain microscopy

An AFM (Bruker, Santa Barbara, USA, Dimension Icon Microscope) operating inside a glovebox (MBraun, Stratham, USA) was used to record AFM images. Electrochemical strain microscopy (ESM) is a special mode of the AFM, suitable to qualitatively detect local variations in ionic mobility [22]. As cantilevers, Bruker SCM-PIT-V2 (Bruker, Camarillo, USA) cantilevers with a conductive Pt/Ir coating and a nominal spring constant of 3 $N \cdot m^{-1}$ were employed. The contact resonance frequency and the amplitude were tracked with a phase-locked loop (HF2LI, Zurich Instruments, Switzerland) [34]. Further information on how to connect this instrument to a Bruker Dimension Icon AFM is described in [35]. The applied AC frequency must match the contact resonance frequency of the cantilever used, and is exactly given in the respective figure caption. To ensure a stable tip–sample interaction, a slow scanning speed of about 0.2 Hz was applied. Topographical images as well as the change in amplitude signal were recorded simultaneously. The samples were first investigated using SEM and subsequently using AFM.

Acknowledgements

The FEI Helios 460 F1 used in this work was funded by the Bundesministerium für Bildung und Forschung (BMBF) under project SABLE 03EK3543. FH and NS thank Nina Balke for fruitful discussions. The authors thank R.-A. Eichel, L.G.J. de Haart and H. Kungl for continuous support of the project.

ORCID® iDs

Nino Schön - https://orcid.org/0000-0002-1411-7264
Deniz Cihan Gunduz - https://orcid.org/0000-0002-3252-3792
Hermann Tempel - https://orcid.org/0000-0002-9794-6403
Roland Schierholz - https://orcid.org/0000-0002-2298-4405
Florian Hausen - https://orcid.org/0000-0001-5712-6761

References

1. Hupfer, T.; Bucharsky, E. C.; Schell, K. G.; Senyshyn, A.; Monchak, M.; Hoffmann, M. J.; Ehrenberg, H. *Solid State Ionics* **2016,** *288,* 235–239. doi:10.1016/j.ssi.2016.01.036
2. Janek, J.; Zeier, W. G. *Nat. Energy* **2016,** *1,* 16141. doi:10.1038/nenergy.2016.141
3. Monchak, M.; Hupfer, T.; Senyshyn, A.; Boysen, H.; Chernyshov, D.; Hansen, T.; Schell, K. G.; Bucharsky, E. C.; Hoffmann, M. J.; Ehrenberg, H. *Inorg. Chem.* **2016,** *55,* 2941–2945. doi:10.1021/acs.inorgchem.5b02821
4. Arbi, K.; Bucheli, W.; Jiménez, R.; Sanz, J. *J. Eur. Ceram. Soc.* **2015,** *35,* 1477–1484. doi:10.1016/j.jeurceramsoc.2014.11.023
5. Yan, Y.; Kühnel, R.-S.; Remhof, A.; Duchêne, L.; Reyes, E. C.; Rentsch, D.; Łodziana, Z.; Battaglia, C. *Adv. Energy Mater.* **2017,** *7,* 1700294. doi:10.1002/aenm.201700294
6. Aono, H.; Imanaka, N.; Adachi, G.-y. *Acc. Chem. Res.* **1994,** *27,* 265–270. doi:10.1021/ar00045a002
7. Sun, C.; Liu, J.; Gong, Y.; Wilkinson, D. P.; Zhang, J. *Nano Energy* **2017,** *33,* 363–386. doi:10.1016/j.nanoen.2017.01.028
8. Yang, Z.; Zhang, J.; Kintner-Meyer, M. C. W.; Lu, X.; Choi, D.; Lemmon, J. P.; Liu, J. *Chem. Rev.* **2011,** *111,* 3577–3613. doi:10.1021/cr100290v
9. Tarascon, J.-M.; Armand, M. *Nature* **2001,** *414,* 359–367. doi:10.1038/35104644
10. Kerman, K.; Luntz, A.; Viswanathan, V.; Chiang, Y.-M.; Chen, Z. *J. Electrochem. Soc.* **2017,** *164,* A1731–A1744. doi:10.1149/2.1571707jes
11. Mertens, A.; Yu, S.; Schön, N.; Gunduz, D. C.; Tempel, H.; Schierholz, R.; Hausen, F.; Kungl, H.; Granwehr, J.; Eichel, R.-A. *Solid State Ionics* **2017,** *309,* 180–186. doi:10.1016/j.ssi.2017.07.023
12. Aono, H.; Sugimoto, E.; Sadaoka, Y.; Imanaka, N.; Adachi, G.-y. *Chem. Lett.* **1991,** *20,* 1567–1570. doi:10.1246/cl.1991.1567
13. Aono, H.; Sugimoto, E.; Sadaoka, Y.; Imanaka, N.; Adachi, G.-y. *Solid State Ionics* **1991,** *47,* 257–264. doi:10.1016/0167-2738(91)90247-9
14. Aono, H.; Sugimoto, E.; Sadaoka, Y.; Imanaka, N.; Adachi, G.-y. *Solid State Ionics* **1990,** *40–41,* 38–42. doi:10.1016/0167-2738(90)90282-V
15. Arbi, K.; Mandal, S.; Rojo, J. M.; Sanz, J. *Chem. Mater.* **2002,** *14,* 1091–1097. doi:10.1021/cm010528i
16. Kruempelmann, J.; Balabajew, M.; Gellert, M.; Roling, B. *Solid State Ionics* **2011,** *198,* 16–21. doi:10.1016/j.ssi.2011.07.008
17. Yu, S.; Mertens, A.; Gao, X.; Gunduz, D. C.; Schierholz, R.; Benning, S.; Hausen, F.; Mertens, J.; Kungl, H.; Tempel, H.; Eichel, R.-A. *Funct. Mater. Lett.* **2016,** *9,* 1650066. doi:10.1142/S1793604716500661
18. Fu, J. *Solid State Ionics* **1997,** *96,* 195–200. doi:10.1016/S0167-2738(97)00018-0
19. Narváez-Semanate, J. L.; Rodrigues, A. C. M. *Solid State Ionics* **2010,** *181,* 1197–1204. doi:10.1016/j.ssi.2010.05.010
20. Duluard, S.; Paillassa, A.; Puech, L.; Vinatier, P.; Turq, V.; Rozier, P.; Lenormand, P.; Taberna, P.-L.; Simon, P.; Ansart, F. *J. Eur. Ceram. Soc.* **2013,** *33,* 1145–1153. doi:10.1016/j.jeurceramsoc.2012.08.005
21. Sasano, S.; Ishikawa, R.; Sugiyama, I.; Higashi, T.; Kimura, T.; Ikuhara, Y. H.; Shibata, N.; Ikuhara, Y. *Appl. Phys. Express* **2017,** *10,* 061102. doi:10.7567/APEX.10.061102
22. Balke, N.; Jesse, S.; Morozovska, A. N.; Eliseev, E.; Chung, D. W.; Kim, Y.; Adamczyk, L.; Garcia, R. E.; Dudney, N.; Kalinin, S. V. *Nat. Nanotechnol.* **2010,** *5,* 749–754. doi:10.1038/nnano.2010.174
23. Kalinin, S.; Balke, N.; Jesse, S.; Tselev, A.; Kumar, A.; Arruda, T. M.; Guo, S.; Proksch, R. *Mater. Today* **2011,** *14,* 548–558. doi:10.1016/S1369-7021(11)70280-2
24. Balke, N.; Jesse, S.; Kim, Y.; Adamczyk, L.; Tselev, A.; Ivanov, I. N.; Dudney, N. J.; Kalinin, S. V. *Nano Lett.* **2010,** *10,* 3420–3425. doi:10.1021/nl101439x
25. Jesse, S.; Kumar, A.; Arruda, T. M.; Kim, Y.; Kalinin, S. V.; Ciucci, F. *MRS Bull.* **2012,** *37,* 651–658. doi:10.1557/mrs.2012.144
26. Morozovska, A. N.; Eliseev, E. A.; Balke, N.; Kalinin, S. V. *J. Appl. Phys.* **2010,** *108,* 053712. doi:10.1063/1.3460637
27. Morozovska, A. N.; Eliseev, E. A.; Kalinin, S. V. *Appl. Phys. Lett.* **2010,** *96,* 222906. doi:10.1063/1.3446838
28. Lushta, V.; Bradler, S.; Roling, B.; Schirmeisen, A. *J. Appl. Phys.* **2017,** *121,* 224302. doi:10.1063/1.4984831
29. Ling, Q.; Ye, Z.; Xu, H.; Zhu, G.; Zhang, X.; Zhao, Y.; Yu, A. *Mater. Lett.* **2016,** *169,* 42–45. doi:10.1016/j.matlet.2016.01.089
30. Balke, N.; Jesse, S.; Yu, P.; Carmichael, B.; Kalinin, S. V.; Tselev, A. *Nanotechnology* **2016,** *27,* 425707. doi:10.1088/0957-4484/27/42/425707
31. Balke, N.; Maksymovych, P.; Jesse, S.; Kravchenko, I. I.; Li, Q.; Kalinin, S. V. *ACS Nano* **2014,** *8,* 10229–10236. doi:10.1021/nn505176a
32. Aatiq, A.; Ménétrier, M.; Croguennec, L.; Suard, E.; Delmas, C. *J. Mater. Chem.* **2002,** *12,* 2971–2978. doi:10.1039/B203652P
33. Kruth, M.; Meertens, D.; Tillmann, K. *J. Large-Scale Res. Facil. JLSRF* **2016,** *2,* A59. doi:10.17815/jlsrf-2-105
34. Gardner, F. M. Anomalous Locking. *Phaselock Techniques,* 3rd ed.; John Wiley: Hoboken, NJ, 2005; pp 336–379. doi:10.1002/0471732699
35. Zurich Instruments, Connecting an HF2PLL to a Bruker Dimension Icon AFM / Nanoscope V Controller, Technical Note, 2012. https://www.zhinst.com/sites/default/files/zi_hf2pll_technote_bruker_icon.pdf (accessed March 22, 2018).

License and Terms

This is an Open Access article under the terms of the Creative Commons Attribution License (http://creativecommons.org/licenses/by/4.0), which permits unrestricted use, distribution, and reproduction in any medium, provided the original work is properly cited.

The license is subject to the *Beilstein Journal of Nanotechnology* terms and conditions: (https://www.beilstein-journals.org/bjnano)

The definitive version of this article is the electronic one which can be found at: doi:10.3762/bjnano.9.148

BEILSTEIN JOURNAL OF NANOTECHNOLOGY

Nanoscale electrochemical response of lithium-ion cathodes: a combined study using C-AFM and SIMS

Jonathan Op de Beeck[*1,2], Nouha Labyedh[1,3], Alfonso Sepúlveda[1], Valentina Spampinato[1], Alexis Franquet[1], Thierry Conard[1], Philippe M. Vereecken[1,3], Wilfried Vandervorst[1,2] and Umberto Celano[*1]

Letter

Open Access

Address:
[1]IMEC, Kapeldreef 75, 3001 Leuven, Belgium, [2]KU Leuven, Department of Physics and Astronomy, Celestijnenlaan 200D, B-3001 Leuven, Belgium and [3]KU Leuven, Department of Microbial and Molecular Systems, Celestijnenlaan 200D, B-3001 Leuven, Belgium

Email:
Jonathan Op de Beeck[*] - jonathan.opdebeeck@imec.be;
Umberto Celano[*] - celano@imec.be

* Corresponding author

Keywords:
all-solid-state microbatteries (ASB); conductive atomic force microscopy (C-AFM); Li-ion kinetics; secondary ion mass spectrometry (SIMS); 3D thin-film batteries

Beilstein J. Nanotechnol. **2018,** *9,* 1623–1628.
doi:10.3762/bjnano.9.154

Received: 18 December 2017
Accepted: 25 April 2018
Published: 04 June 2018

This article is part of the Thematic Series "Scanning probe microscopy for energy-related materials".

Guest Editor: P. Leclère

© 2018 Op de Beeck et al.; licensee Beilstein-Institut.
License and terms: see end of document.

Abstract

The continuous demand for improved performance in energy storage is driving the evolution of Li-ion battery technology toward emerging battery architectures such as 3D all-solid-state microbatteries (ASB). Being based on solid-state ionic processes in thin films, these new energy storage devices require adequate materials analysis techniques to study ionic and electronic phenomena. This is key to facilitate their commercial introduction. For example, in the case of cathode materials, structural, electrical and chemical information must be probed at the nanoscale and in the same area, to identify the ionic processes occurring inside each individual layer and understand the impact on the entire battery cell. In this work, we pursue this objective by using two well established nanoscale analysis techniques namely conductive atomic force microscopy (C-AFM) and secondary ion mass spectrometry (SIMS). We present a platform to study Li-ion composites with nanometer resolution that allows one to sense a multitude of key characteristics including structural, electrical and chemical information. First, we demonstrate the capability of a biased AFM tip to perform field-induced ionic migration in thin (cathode) films and its diagnosis through the observation of the local resistance change. The latter is ascribed to the internal rearrangement of Li-ions under the effect of a strong and localized electric field. Second, the combination of C-AFM and SIMS is used to correlate electrical conductivity and local chemistry in different cathodes for application in ASB. Finally, a promising starting point towards quantitative electrochemical information starting from C-AFM is indicated.

Findings

Conventional Li-ion battery technology is undergoing continuous improvements in order to fulfil the increasing demands from modern society on autonomous electronics, such as portable devices, internet-of-things applications and implants [1]. A multitude of studies have already indicated that nanotechnology, nanostructured designs and nanocomposite materials will play an important role for future Li-ion batteries [1-3]. The 3D all-solid-state microbattery (ASB) is a promising new architecture built using processing techniques compatible with semiconductor processing, which provides more power and more capacity compared to conventional planar designs [4]. In this kind of battery, the electrolyte is generally a solid and dense material while crystalline conductive oxides are used for the anode and cathode. As a solid electrolyte is significantly safer compared to its flammable organic liquid counterparts, its use does represent a clear advantage [2]. Moreover, the presence of crystalline ordering in the anode and cathode, creates high-mobility channels for the lithium migration, thus significantly enhancing the ionic conductivity of these materials [5].

However, being based on diffusion in a solid versus a liquid, the success of ASB will depend on the capability to address the nanoscale ionic processes in the thin films, at their interfaces and the combined electronic–ionic transport. It goes without saying that in sub-micrometer films thickness, the nanoionic properties of the system become more dominant and, similarly, the interfaces between layers represent a higher (compared to bulk) volume fraction in the final cell. This represents a criticality for virtually all battery technologies. However, as we focus on ASB technology the solid–solid interaction creates new challenges due to the different nature of the established interfaces. Uncontrolled side reactions and phase decomposition between the electrodes and the electrolyte, which are complex to characterize, give rise to failure and reduced performance of cells. This puts the outcome of our work in context of a wide range of applications. These pending problems pose severe challenges for the physical characterization of battery materials such as the local correlation between a nanoscale stimulus and the resulting dynamically evolving material response [6].

In this letter, we propose a solution to study the nanoscale characteristics of ASB materials by a combinatorial approach that uses two established analysis techniques such as conductive atomic force microscopy (C-AFM) and secondary ion mass spectrometry (SIMS). As model systems, we focus on $LiMn_2O_4$ (LMO) as cathode material [7] deposited by wet electrodeposition (thickness 260 nm) and RF-sputtered (thickness 100 nm) and compare their properties on a local (sub-100 nm) scale. In addition, a comparison is made with pristine electrodeposited MnO_2 (thickness roughly 250 nm) before conversion to LMO by solid-state reaction; this is done to have a reference sample that does not contain lithium.

The general structure of our samples and the C-AFM setup are schematically shown in Figure 1a. The three samples mentioned above are all deposited on a metallic current collector (Ni or Pt) on top of a silicon wafer. Spatially resolved electrical properties are observed with nanometer resolution by scanning a biased conductive AFM tip across the top surface. Unless specified otherwise, we apply always the bias to the sample (i.e., the metallic Ni/Pt layer) while the C-AFM tip is grounded. By measuring the current (using the tip as a nanoscale electrode) and the tip deflection as a function of the AFM tip position, two-dimensional maps of the local conductivity and the topography can be formed. For instance, Figure 1b shows the topography and current distribution map when performing such measurements in the case of the electrodeposited LMO. This basic concept was extended with the development of various scanning probe microscopy (SPM) techniques [8-12] dedicated to probe ionic dynamics such as the observation of motion of ions in mixed ionic–electronic conductors using the electrical current sensed by the AFM tip [6].

However, these techniques all probe the electrical, structural or ionic properties of the film and do not provide any direct information on the local chemistry, which is an important (missing) piece of information. For this reason, inspired by the work of E. Strelcov et al. [10] on the first-order reversal curve current–voltage (FORC-IV) method on ferroelectrics, we will investigate the fundamentals behind tip-induced sensing in Li-ion cathodes using a hybrid metrology approach combining SPM with SIMS, this is a technique able to observe the actual Li concentration.

Using the C-AFM tip as a nanoscaled electrode, we can now stress films at different bias values by scanning over the surface (8.5 min) and subsequently observe the induced conductivity changes. In Figure 1c–f we show the impact of different (tip-induced) voltage stresses applied under ambient conditions on two electrodeposited cathodes, i.e., MnO_2 before (Figure 1c,d) and after lithium insertion (LMO, Figure 1e,f). From the resulting modifications of the current maps (Figure 1d,f) it is clear that both films behave very differently. As visible in Figure 1d, MnO_2 shows no significant changes in conductivity after stressing with a positive sample bias of 3 V and 5 V. On the contrary, LMO shows a strong increase in the conductivity after the application of 3 V and 5 V relative to the map for its pristine state (Figure 1b). The different conductivity changes between MnO_2 and LMO can be attributed to the pres-

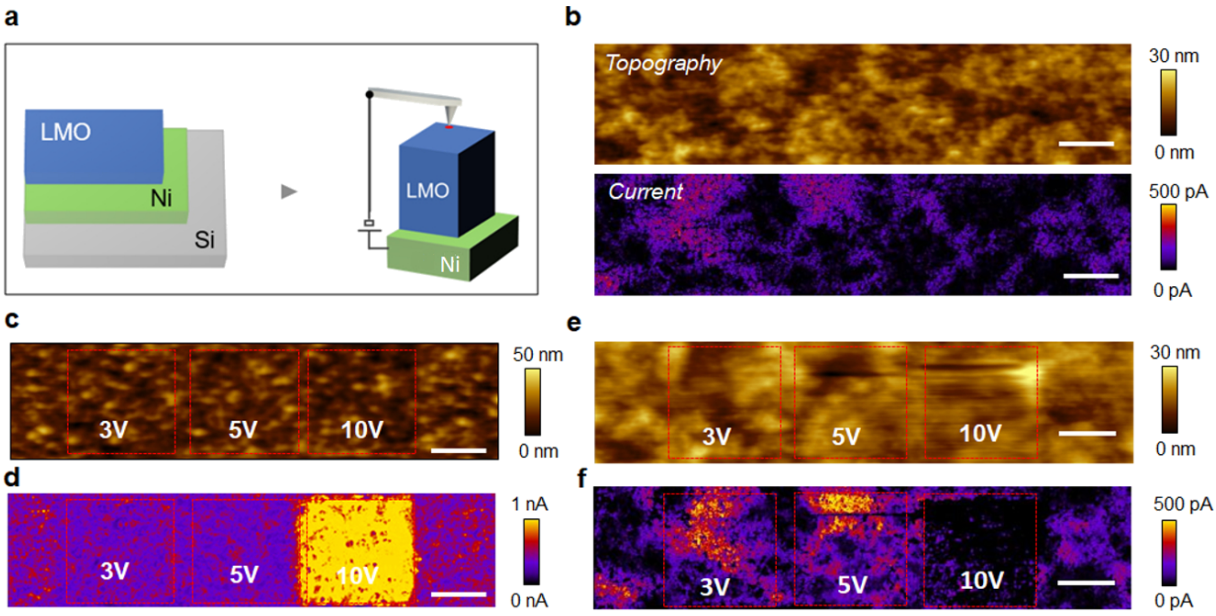


Figure 1: C-AFM configuration and study of the influence of an applied voltage stress on MnO_2 and LMO. (a) Schematic of the C-AFM setup and sample structure. The tip is grounded while the dc bias is applied to the sample. (b) Topography and current maps as collected by C-AFM on the electrodeposited LMO sample applying 1.5 V. (c) MnO_2 morphology and (d) current map reporting three areas previously stressed at different dc bias values applying 1.5 V. (e) Electrodeposited LMO morphology and (f) current map reporting three areas previously stressed at different dc bias values applying 1.5 V (scale bar 1 µm for all images).

ence of lithium in LMO as this can migrate and locally accumulate at the surface driven by the applied electric field. The impact of the 10 V stress is described later in the text, as it involves a dedicated interpretation due to the relatively high voltage involved. A more quantitative comparison of the regions is shown in Figure S1 (Supporting Information File 1). The line graph indicates clearly the increasing conductivity change (69%, 160%) with increasing stress (3 V, 5 V). Worth noting is that also regions outside of our intended stress have slightly changed in local conductivity due to the readout bias (1.5 V).

We also observed that the conductivity in the layer is not entirely uniform after lithium insertion, indicating that the LMO is not achieving maximum cathode utilization. The latter could be representative of the known fact that lithium shows a strong tendency to be localized and often is trapped at grain boundaries [13]. However, while C-AFM proves to be very useful to sense the electrical properties of the cathode materials, including the areal distribution and density of highly conductive paths, it does not provide any information about the chemical composition of such regions. For this purpose, the combination C-AFM with SIMS is needed.

It is important to mention that when working in air, a nanosized electrolytic half-cell is formed at the tip–sample system due to the presence of a water meniscus on all the surfaces. As shown elsewhere, this water layer can act as a Li-ion reservoir and in combination with an applied electric field at the AFM tip it can induce multiple oxidation processes leading to the formation of insulating Li-compounds (e.g., Li_2O and Li_2CO_3) [14]. This has a large influence on the C-AFM measurement as the insulating compounds on the top surface impact on the observed conductivity, up to preventing all electrical contact to the underlying film. We believe such oxide formation can also be observed in the present work since after stressing at 10 V, a net drop in conductivity (or observed current) is visible (10 V box Figure 1f). Since the observed morphology hardly changes (only a small effect is visible in case of a 10 V bias), taking tip wear into account, we believe that our bias stress up to 5 V does not induce modifications to the surface. These undesired side reactions between the tip and sample can be drastically reduced by performing the measurements under ultra-high vacuum conditions instead of normal ambient air. In the case of the 10 V bias stress applied to the MnO_2, a drastic increase of the conductivity is observed, which can be attributed to the dielectric breakdown of the film. High vacuum condition can be achieved (see below in Figure 3a) by working with a dedicated tool combining AFM and time-of-flight SIMS (TOF-SIMS) in the same apparatus (10^{-6} mbar or lower, TOF-SIMS V, ION-TOF GmbH, Münster, Germany). The advantage of this concept is that it allows one to perform electrical analysis (using

C-AFM) and chemical analysis (using TOF-SIMS) on exactly the same area with C-AFM offering a much higher spatial resolution (ca. 3–5 nm) than TOF-SIMS (50–100 nm).

The schematic of the experiment to perform TOF-SIMS (detecting the Li concentration at the surface) and C-AFM (local conductivity) in succession in the same area for the case of the RF-sputtered LMO cathode is shown in Figure 2a. The static SIMS analysis is performed using a Bi_3 cluster beam (spot size ca. 70 nm) in the area previously studied by C-AFM. Static SIMS is known to be probing only the outermost monolayer with minimal disturbance ensuring the information we obtain is only the surface chemical composition [15]. In essence, the SIMS results provide the 2D distribution map of the Li concentration at the surface with a clear distinction between Li-rich and Li-deficient areas. A striking correspondence (for example in Figure 2a, boxes 1–3) between the highly conductive regions and the high Li-concentration regions can be observed indicating the relation between electrical properties the chemical composition of that area. In other words, our results show that highly lithiated domains are localized within sub-micrometer clusters, which also represent a low-resistance path for the electronic current in the cathode layer. It is worth noting that besides the regions with a clear electrical and chemical correlation, conductive spots without high Li concentration are also visible. In addition, (partial) relaxation after bias stress can lead to modifications of the surface deviating from the original C-AFM image. Figure 2 demonstrates that with our method we can distinguish two extreme material phases and their respective electrical properties. This can be interesting in studying uncomplete cathode utilization, which is often considered as one of the main bottlenecks for ASB cathodes [2,4]. For example, for the system presented in our work, we show that the material is not yet fully optimised for maximal cathode utilization, as on a local scale, the LMO shows strong variations in Li concentration and conductivity (Figure 1 and Figure 2).

C-AFM does not allow any differentiation between the ionic and the electronic current contribution in the current map, but rather it shows the sum of both. Therefore, in this section, we discuss an approach to separate both components. Figure 1e,f proves that we can induce a local change in the conductivity of the layer when the tip is scanned with a negative polarity, which we relate to the presence of mobile Li ions in the LMO film. This effect, which has been already shown for other mixed ionic–electronic conductors, represents an interesting starting point to obtain local electrochemical information from the sample using C-AFM [6]. Indeed, the biased tip induces a strong electric field (localized under the tip) inside the material, thus triggering a field-induced ionic migration of the Li ions which, if mobile, start to accumulate at the tip–sample interface. As

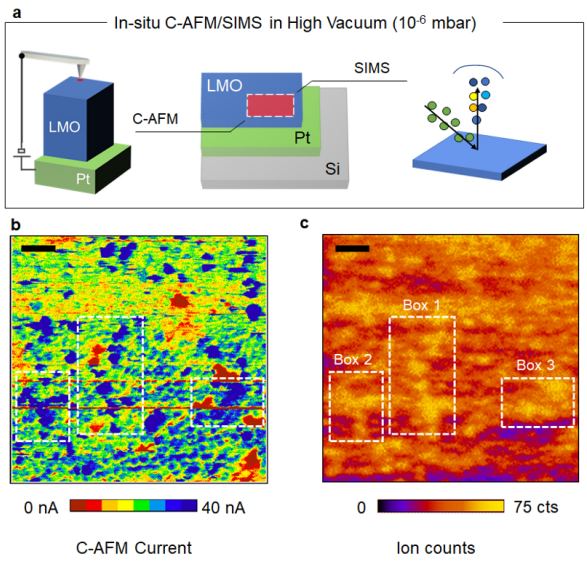


Figure 2: Combined C-AFM and SIMS analysis of a RF-sputtered LMO film. (a) Schematic of the measurement setup. The system is in high vacuum (10^{-6} mbar). (b) Local current map as probed by C-AFM (sample bias −8 V) and corresponding (c) local chemical profile of lithium as measured by SIMS on the same area (scale bar 2 µm). Both C-AFM and SIMS indicate the segregation of the film in phases with different local chemistry and electrical conduction. Additionally, their strong correlation reveals the inherent link between the varying Li content and electrical conductivity as highly lithiated regions show enhanced electrical conductivity.

shown in Figure 2, such local accumulation of Li locally induces a non-volatile change in resistance under the tip. While this effect is visible in Figure 1 for the (squared) regions we show the effect in a local point-contact *I*–*V* spectroscopy measurement in Figure 3. Here the tip is held fixed in contact with the sample while the dc bias is applied to the sample (inset Figure 3a). A decrease in the local tip–sample resistance resulting from applying a bias is visible from the hysteresis in the *I*–*V* curves, which is consistently observed between the trace (1) and retrace (2) dc bias sweeps. The amplitude of the hysteresis depends on the local concentration and mobility of Li under the tip. Figure 3a shows the example of two *I*–*V* curves acquired (1) in a pristine area (green trace) and (2) in a region that was previously scanned with the tip positively biased at 10 V (red trace). The large hysteresis observed in the second case, demonstrates that by stressing the sample surface with a negative dc sample bias a strong depletion of Li ions occurs such that a higher resistance change can be obtained under the tip while attracting the Li ions back during the following positive sample bias sweep. This effect is qualitatively shown in Figure 3a. We compare a more relevant statistical population in Figure 3b, where the comparison is done evaluating 145 *I*–*V* spectroscopy curves in which the negative dc sample bias stress was performed before every single measurement for roughly half of the data set. These results indicate that although the approach dis-

torts the initial state of the material and the Li-ion distribution, it can be an effective way of obtaining a higher response for the same applied bias, thus improving the sensitivity of a potential ion-modulated C-AFM measurement. This can be particularly useful for fundamental studies on the role of materials, grain boundaries and interfaces that provide a low bias induced response.

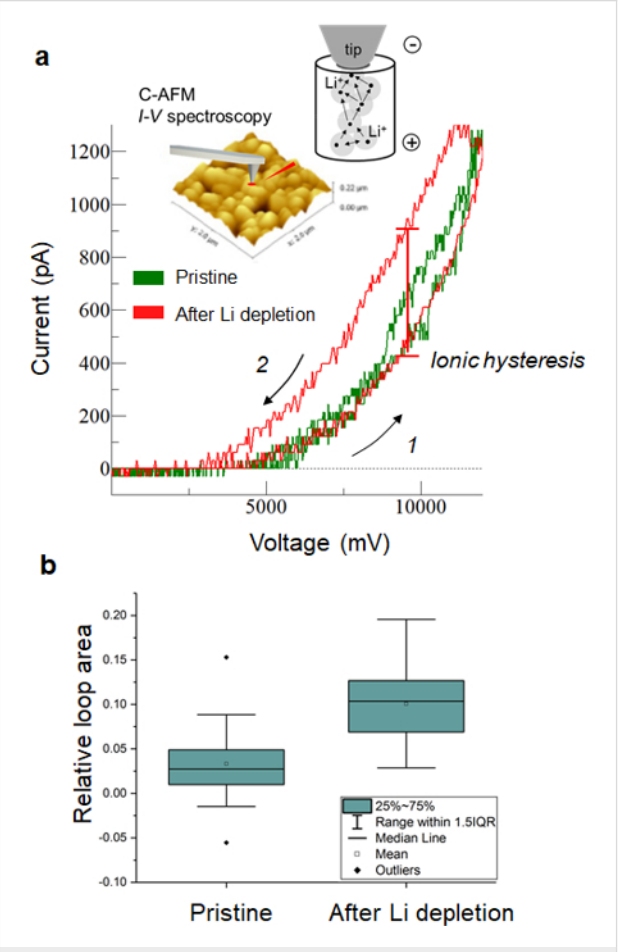


Figure 3: Appearance of the ionic hysteresis and influence of Li depletion during preconditioning. (a) The hysteresis loop visible in the *I–V* curves is indicating the local change in resistance under the tip induced by the Li modulation. The inset shows a schematic of the migration of Li ions towards the AFM tip. The measurements were performed on RF-sputtered LMO under high vacuum at a sweep rate of 0.2 Hz. (b) An enhanced hysteresis loop opening, i.e., electrochemical response, can be observed due to a preconditioning dc scan (10 V) performed to deplete the lithium before the *I–V* curves are measured. The boxplot shows the distribution of the relative loop area (area enclosed by the loop and divided by the peak current magnitude).

It is important to consider the formation of a thin local oxidized interface at the tip–sample junction as another possible origin of modified transport characteristics. Especially in air, local anodic oxidation is well known to limit C-AFM capabilities and complicate the results interpretation in the case of silicon [16]. For this reason, UHV conditions have been investigated in order to increase the reproducibility and quantitative interpretation of C-AFM [17]. At the same time, we do not expect the high-vacuum environment to be completely free from humidity. Therefore, in these measurements the formation of any Li composites such as Li_2O and Li_2CO_3 cannot be excluded as also considered by others [14]. However, a local oxidation effect is a non-reversible process, while in our observation the reversibility of the conductive changes (visible in Figure 3a red curve) proves that the local formation of these compounds (although not excluded) is not the main cause for the observation.

More work is required in particular for a quantitative interpretation of the information contained in the ionic hysteresis (Figure 3a), especially the conversion of the *I–V* resistance shift in relevant ionic parameters, e.g., local ionic mobility or diffusivity. This is an ongoing activity and represents the topic of state-of-the-art studies [18]. However, the observations reported in Figure 3a,b combined with the results of C-AFM and SIMS of Figure 1 and Figure 2 clearly represent an important starting point toward the development of a C-AFM/SIMS-based analysis framework for battery materials.

In summary, using MnO_2 and LMO as cathode model systems for ASB, we have demonstrated the use of combined scanning probe and beam analysis techniques to investigate electrical, structural and electrochemical properties at the nanoscale. C-AFM was used for comparing the local electrical conductivity of the two materials and shows the impact of the Li incorporation on the layer resistance. Second, by alternating on the same area C-AFM and SIMS, a direct correlation between the presence of nanosized conductive paths and Li concentration could be established. Moreover, we show the capability of a biased AFM tip to locally accumulate and deplete Li ions on/below the surface thus representing an interesting starting point towards the C-AFM-based analysis of electrochemical properties in mixed ionic–electronic conductors. These concepts can be extended to the other constituents of Li-ion batteries, such as the anode and the solid electrolyte, which share the same open issues for their nanoscale physical characterization. All-solid-state lithium batteries are considered as promising energy storage devices to meet the requirements of a low-carbon society, therefore the development of a dedicated material metrology platform is key to unlock the potentials of ASB.

Supporting Information

Supporting Information File 1

Additional experimental data.
[https://www.beilstein-journals.org/bjnano/content/supplementary/2190-4286-9-154-S1.pdf]

Acknowledgements

A. Sepúlveda acknowledges the EU Horizon 2020 research and innovation program under the MSCA grant agreement No 658057. This project has received funding from the European Union's Horizon 2020 research and innovation program under grant agreement No 688225 (Metro4-3D - Metrology for future 3D-technologies).

ORCID® iDs

Thierry Conard - https://orcid.org/0000-0002-4298-5851
Umberto Celano - https://orcid.org/0000-0002-2856-3847

References

1. Deng, D. *Energy Sci. Eng.* **2015,** *3,* 385–418. doi:10.1002/ese3.95
2. Vereecken, P. M.; Huyghebaert, C. *ECS Trans.* **2013,** *58,* 111–118. doi:10.1149/05810.0111ecst
3. Liu, C.; Gillette, E. I.; Chen, X.; Pearse, A. J.; Kozen, A. C.; Schroeder, M. A.; Gregorczyk, K. E.; Lee, S. B.; Rubloff, G. W. *Nat. Nanotechnol.* **2014,** *9,* 1031–1039. doi:10.1038/nnano.2014.247
4. Talin, A. A.; Ruzmetov, D.; Kolmakov, A.; McKelvey, K.; Ware, N.; El Gabaly, F.; Dunn, B.; White, H. S. *ACS Appl. Mater. Interfaces* **2016,** *8,* 32385–32391. doi:10.1021/acsami.6b12244
5. Yuan, Y.; Zhan, C.; He, K.; Chen, H.; Yao, W.; Sharifi-Asl, S.; Song, B.; Yang, Z.; Nie, A.; Luo, X.; Wang, H.; Wood, S. M.; Amine, K.; Islam, M. S.; Lu, J.; Shahbazian-Yassar, R. *Nat. Commun.* **2016,** *7,* 13374. doi:10.1038/ncomms13374
6. Strelcov, E.; Yang, S. M.; Jesse, S.; Balke, N.; Vasudevan, R. K.; Kalinin, S. V. *Nanoscale* **2016,** *8,* 13838–13858. doi:10.1039/C6NR01524G
7. Thackeray, M. M. *Prog. Solid State Chem.* **1997,** *25,* 1–71. doi:10.1016/S0079-6786(97)81003-5
8. Yang, S.; Yan, B.; Lu, L.; Zeng, K. *RSC Adv.* **2016,** *6,* 94000–94009. doi:10.1039/C6RA17681J
9. Guo, S.; Jesse, S.; Kalnaus, S.; Balke, N.; Daniel, C.; Kalinin, S. V. *J. Electrochem. Soc.* **2011,** *158,* A982–A990. doi:10.1149/1.3604759
10. Strelcov, E.; Kim, Y.; Jesse, S.; Cao, Y.; Ivanov, I. N.; Kravchenko, I. I.; Wang, C.-H.; Teng, Y.-C.; Chen, L.-Q.; Chu, Y. H.; Kalinin, S. V. *Nano Lett.* **2013,** *13,* 3455–3462. doi:10.1021/nl400780d
11. Zhu, J.; Lu, L.; Zeng, K. *ACS Nano* **2013,** *7,* 1666–1675. doi:10.1021/nn305648j
12. Jesse, S.; Balke, N.; Eliseev, E.; Tselev, A.; Dudney, N. J.; Morozovska, A. N.; Kalinin, S. V. *ACS Nano* **2011,** *5,* 9682–9695. doi:10.1021/nn203141g
13. Sui, T.; Song, B.; Dluhos, J.; Lu, L.; Korsunsky, A. M. *Nano Energy* **2015,** *17,* 254–260. doi:10.1016/j.nanoen.2015.08.013
14. Luchkin, S. Yu.; Amanieu, H.-Y.; Rosato, D.; Kholkin, A. L. *J. Power Sources* **2014,** *268,* 887–894. doi:10.1016/j.jpowsour.2014.06.143
15. van der Heide, P. *Secondary ion mass spectrometry : an introduction to principles and practices;* John Wiley & Sons, Inc.: Hoboken, NJ, USA, 2014. doi:10.1002/9781118916780
16. Vetushka, A.; Fejfar, A.; Ledinský, M.; Rezek, B.; Stuchlík, J.; Kočka, J. *Phys. Status Solidi C* **2010,** *7,* 728–731. doi:10.1002/pssc.200982777
17. Kyuno, K.; Kita, K.; Toriumi, A. *Appl. Phys. Lett.* **2005,** *86,* 063510. doi:10.1063/1.1862779
18. Alikin, D. O.; Ievlev, A. V.; Luchkin, S. Yu.; Turygin, A. P.; Shur, V. Ya.; Kalinin, S. V.; Kholkin, A. L. *Appl. Phys. Lett.* **2016,** *108,* 113106. doi:10.1063/1.4943944

License and Terms

This is an Open Access article under the terms of the Creative Commons Attribution License (http://creativecommons.org/licenses/by/4.0), which permits unrestricted use, distribution, and reproduction in any medium, provided the original work is properly cited.

The license is subject to the *Beilstein Journal of Nanotechnology* terms and conditions: (https://www.beilstein-journals.org/bjnano)

The definitive version of this article is the electronic one which can be found at: doi:10.3762/bjnano.9.154

BEILSTEIN JOURNAL OF NANOTECHNOLOGY

Multimodal noncontact atomic force microscopy and Kelvin probe force microscopy investigations of organolead tribromide perovskite single crystals

Yann Almadori[1], David Moerman[2], Jaume Llacer Martinez[2], Philippe Leclère[2] and Benjamin Grévin[*1]

Full Research Paper

Open Access

Address:
[1]Université Grenoble Alpes, CNRS, CEA, INAC-SyMMES, 38000 Grenoble, France, and [2]Laboratory for Chemistry of Novel Materials, Center of Innovation and Research in Materials & Polymers (CIRMAP), University of Mons, Place du Parc 20, B7000 Mons, Belgium

Email:
Benjamin Grévin[*] - benjamin.grevin@cea.fr

* Corresponding author

Keywords:
carrier lifetime; ion migration; Kelvin probe force microscopy (KPFM); noncontact atomic force microscopy (nc-AFM); organic–inorganic hybrid perovskites; photostriction; single crystals; surface photovoltage (SPV); time-resolved surface photovoltage

Beilstein J. Nanotechnol. **2018,** *9,* 1695–1704.
doi:10.3762/bjnano.9.161

Received: 15 December 2017
Accepted: 15 May 2018
Published: 07 June 2018

This article is part of the Thematic Series "Scanning probe microscopy for energy-related materials".

Associate Editor: T. Glatzel

© 2018 Almadori et al.; licensee Beilstein-Institut.
License and terms: see end of document.

Abstract

In this work, methylammonium lead tribromide ($MAPbBr_3$) single crystals are studied by noncontact atomic force microscopy (nc-AFM) and Kelvin probe force microscopy (KPFM). We demonstrate that the surface photovoltage and crystal photostriction can be simultaneously investigated by implementing a specific protocol based on the acquisition of the tip height and surface potential during illumination sequences. The obtained data confirm the existence of lattice expansion under illumination in $MAPbBr_3$ and that negative photocarriers accumulate near the crystal surface due to band bending effects. Time-dependent changes of the surface potential occurring under illumination on the scale of a few seconds reveal the existence of slow ion-migration mechanisms. Lastly, photopotential decay at the sub-millisecond time scale related to the photocarrier lifetime is quantified by performing KPFM measurements under frequency-modulated illumination. Our multimodal approach provides a unique way to investigate the interplay between the charges and ionic species, the photocarrier-lattice coupling and the photocarrier dynamics in hybrid perovskites.

Introduction

Organic–inorganic hybrid perovskites (RMX_3, where R = methylammonium or formamidinium, M = Pb or Sn, and X = halogen) have become a new platform for the development of next-generation light harvesting and optoelectronic devices in the past years [1]. Indeed, they exhibit an exceptional combination of optoelectronic properties, including a direct band gap,

high absorption coefficient, large and balanced carrier mobility, high diffusion length, long carrier lifetime and high photoluminescence quantum yield. Within a few years of their discovery, these materials were successfully used to develop photovoltaic cells [2] with power conversion efficiencies exceeding 20% and several kinds of optoelectronic devices, including efficient light-emitting diodes [3], laser devices [4] and high-gain photodetectors [5].

Recently, Kelvin probe force microscopy (KPFM) has been used to investigate the impact of grain boundaries (GBs) on the internal electric field distribution and photocarrier recombination mechanisms in polycrystalline perovskite thin films [6,7]. However, considering the results of earlier works shows that it is sometimes difficult to draw definitive conclusions about the detrimental (or beneficial) impact of the GBs on the photocarrier transport on the sole basis of KPFM data. This uncertainty is largely due to the contributions of the ionic species to the surface potential contrasts [6,8-10]. Time-resolved measurements have especially shown that intra-grain ion-migration mechanisms [9] can significantly impact the surface potential probed by KPFM. It is now clear that a complex interplay exists between the charge carrier populations, traps, and mobile ions. Despite all the progress made, interpreting the surface potential (SP) and surface photovoltage (SPV) contrasts recorded by KPFM on polycrystalline lead halide perovskite thin films remains a difficult task.

Over the last few years single crystals [11,12] have constituted an interesting alternative for basic research on hybrid perovskites. Thanks to the absence of grain boundaries (and noncrystalline domains) they can be advantageously used to probe the intrinsic material optoelectronic properties. Performing KPFM measurements on single crystals may therefore facilitate the interpretation of the SP and SPV data. Moreover, scanning probe microscopy measurements may help in distinguishing the properties of the bulk from the surface [13]. However, so far, KPFM investigations of hybrid perovskite single crystals remain rather limited [14,15].

Another important point to consider is the existence of photostriction effects, which have actually been observed in $MAPbI_3$ and $MAPbBr_3$ single crystals [16,17]. In the most general terms, photostriction can be defined as a nonthermal sample deformation under illumination. This effect is widely documented for ferroelectrics, polar and nonpolar semiconductors, and organic polymers, and it differs in origin depending on the class of material under consideration [18]. For instance, in the case of ferroelectric oxides, it originates indirectly from the superposition of photovoltaic and converse piezoelectricity effects (we refer the reader to review articles [18] for a more comprehensive introduction to the field of photostrictive materials). The photostriction observed by a few teams in organolead trialides is most probably related to the photovoltaic effect [16,17] and strong photon–lattice coupling [16], but its exact mechanism remains to be clarified.

In principle, the photostrictive response of any material can be simply probed by recording the height variation of an AFM tip as a function of the illumination state [16]. However, one can arguably invoke the existence of artefacts prone to affect this kind of measurement [17]. In recent work, Zhou et al. carried out a comprehensive series of experiments on $MAPbI_3$ single crystals (and thin films), providing strong evidence that the height changes probed by AFM under illumination originate mainly from the intrinsic material deformation [16]. More precisely, thanks to a rigorous experimental protocol, they demonstrated that it is possible to discriminate between the intrinsic material deformation and the extrinsic effects related to the AFM cantilever light-induced perturbation and thermal relaxation. In addition, by monitoring the sample temperature and analyzing the temporal evolution of the height change probed by AFM they were able to rule out possible contributions from the thermal expansion of the sample (we refer the reader to [16] and the related supporting information for more details).

Now, the question that presents itself is whether the photostriction can influence the results of SPV measurements by KPFM. In addition, valuable information about the light–matter interaction process may be gained by simultaneously measuring the light-induced SP and lattice changes. Lastly, the tip–sample height measured in dynamic AFM is prone to be affected by variations of the electrostatic forces, which in turn, vary as a function of the illumination state of the photovoltaic sample. Thus, for accurate photostrictive measurements, it is highly desirable to nullify (or a least minimize) the electrostatic forces by using an active KPFM compensation potential loop.

In this work, the photovoltaic and optomechanical properties of a methylammonium lead tribromide ($CH_3NH_3PbBr_3$, also referred to as $MAPbBr_3$) single crystal are investigated by noncontact AFM (nc-AFM) combined with KPFM. $MAPbBr_3$ has been selected for these experiments since its absorption band edge [12] falls well below the wavelength of the AFM light source (840 nm for the Omicron VT-AFM setup used here). A specific protocol allowing simultaneous recording of the spectroscopic curves as a function of time for the AFM tip height relative to the surface ($z(t)$) and of the surface potential (SP(t)) during pulsed illumination sequences is implemented. The AFM/KPFM signals are moreover investigated as a function of the optical excitation wavelength and fluence (with an optical power variation covering several decades). The analysis

of the full data set allows the confirmation that the height and SP variations under illumination originate from intrinsic photostriction and photovoltaïc effects, respectively. Furthermore, we show that the surface photovoltage decay can be probed by performing KPFM measurements under frequency-modulated illumination. These results establish that nc-AFM/KPFM can be effectively used to investigate both the photocarrier dynamics and the photon–lattice coupling in organic–inorganic hybrid perovskites.

Methods

Sample preparation

Methylammonium lead tribromide single crystals (millimeter- to centimeter-sized) were grown from *N*-dimethylformamide (DMF) solution at constant temperature. In this process [12] CH_3NH_3Br and $PbBr_2$ precursors are used that are soluble in DMF at room temperature, and the crystallization occurs between 90 °C and 100°C due to inverse temperature solubility. The single crystal investigated under ultrahigh vacuum (UHV) was fixed on a stainless steel sample UVH holder with a compatible electrically conductive silver epoxy paste (EPO-TEK E4110), which was cured at room temperature (RT) over 24 hours. The sample was subsequently cleaved with a scalpel just before being introduced in the load-lock of the VT-AFM (after cleavage, the sample thickness was estimated to be on the order of 1 mm).

Noncontact AFM and Kelvin probe force microscopy

The nc-AFM experiments were carried out with an Omicron VT-AFM setup in ultrahigh vacuum (UHV) at room temperature (RT) with in situ annealed Pt/Ir-coated silicon cantilevers (EFM, Nanosensors, resonance frequency in the 45–115 kHz range). Topographical imaging was performed in frequency modulation mode (FM-AFM) with negative frequency shifts of a few Hz and vibration amplitudes of a few tens of nanometers. KPFM measurements were carried out in single-pass mode under frequency modulation (FM-KPFM) with the modulation bias, V_{AC} (typically 0.5 V peak-to-peak at 1200 Hz), and the compensation voltage, V_{DC}, applied to the cantilever (tip bias $V_{tip} = V_{DC}$). The contact potential difference (CPD = $W_{tip} - W_{sample}$, where W is the work function divided by the elementary charge in absolute value) is thus the opposite of V_{DC} (more details about these polarity conventions can be found in [19]). In the following, the KPFM data are presented as compensation bias ($V_{tip} = -CPD$) images (also called the KPFM potential or surface potential images for simplicity).

Sample illumination

External fiber-coupled laser sources (Omicron Laserage GmBH, LuxX modules operated at 405, 515 and 685 nm or a PhoxXplus unit operated at 515 nm) were used for sample illumination (front side geometry, i.e., from the top) through an optical viewport of the UHV AFM chamber. For each measurement, the optical power P_{opt} (defined per unit of surface by taking into account the laser beam diameter) and wavelength λ are indicated in the corresponding figure caption. Note that the optical beam makes a 30° angle with respect to the sample plane (for simplicity P_{opt} was given at the output of the laser module fiber, without correction for the incidence angle).

The modules were calibrated prior to the KPFM measurements by measuring the power at the fiber output with a power meter. With these laser systems, the power regulation is inaccurate within a few percent of the maximum operating power (typically a few tens of milliwatts for our modules). A series of optical density filters (OD, with 1, 2 and 4 attenuation factors in log scale) were used to attenuate the illumination power, which allowed variation of the illumination power over several decades. For each optical density filter, the exact attenuation factor was calibrated at 405, 515 and 685 nm prior to the experiments. The curves of the photo-physical parameters (SPV and photostriction) as a function of the illumination power were reconstructed by merging the data acquired with different densities. Different symbols (indicated in the figure captions) corresponding to each density are used hereafter to plot the curves.

Spectroscopic and time-resolved measurements

An arbitrary waveform generator (AWG, Keysight 33622A) was used to operate the laser sources in digital modulation mode. Logic signals generated by the scanning probe microscope controller were used to trigger the generation of illumination pulse sequences by the AWG operated in "burst" mode. Spectroscopic data were acquired by simultaneously recording the temporal evolution of the surface potential (SP(t)) and the AFM tip height ($z(t)$) as the sample is subjected to an illumination sequence. Time-resolved measurements of the sub-millisecond SPV decays were performed by recording spectroscopic curves of the average surface potential as a function of the modulation frequency of the illumination source. By analyzing the dependency of the average potential with respect to the modulation frequency, it is possible to extract time constants characterizing the photopotential decay dynamics between the light pulses. More information about KPFM operations under frequency-modulated illumination (FMI-KPFM) can be found in our previous report [20].

Results and Discussion

The topographic nc-AFM images of the single crystal surface (Figure 1a) feature smooth terraces a few hundreds of nanometers wide. The step height deduced from z-level histograms

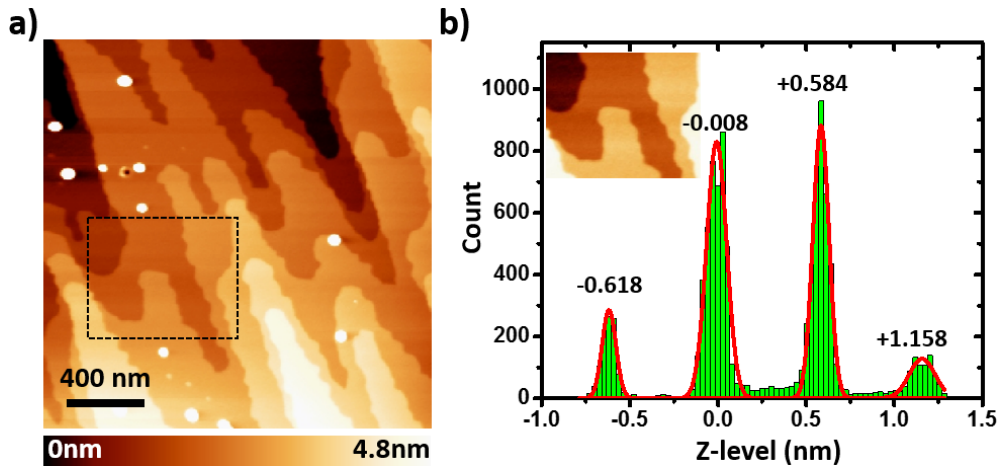


Figure 1: (a) nc-AFM topographic image (2 × 2 µm) of the $MAPbBr_3$ single crystal surface. The dotted rectangle highlights the area used to calculate the *z*-level histogram. (b) Height histogram of the image in the inset (numeric zoom from the image in (a)). The red line shows the result of a multiple Gaussian peak fit. The average step height deduced from the peak positions is equal to 0.59 ± 0.01 nm.

(Figure 1b) is exactly equal to the cubic perovskite unit cell (0.59 nm for $MAPbBr_3$ [1,21]). This confirms that the surface investigated corresponds to the (100) plane of the $MAPbBr_3$ crystal. Several features appearing as white spots in the topographic images indicate moreover the likelihood of defects, which could be attributed to surface contamination upon exposure to ambient atmosphere during the cleaving process. Alternatively, one may also hypothesize that intrinsic defects are formed during the solution process crystal growth. Addressing the origin of these defects is beyond the scope of the current work, and will require development of in situ cleaving facilities (enabling discrimination between extrinsic surface contamination and intrinsic defect formation). Here, our primary goal is to check if the surface photovoltage and crystal photostriction can be simultaneously and reliably probed by nc-AFM/KPFM. The discussion will be thus focused on the analysis of the single crystal response on the basis of spectroscopic curves acquired in point mode (i.e., at selected locations on the surface).

Figure 2a,b shows the KPFM surface potential (SP) and the tip height curves recorded during two successive single-pulse illumination sequences separated by a time interval of a few tens of seconds (at an excitation wavelength of 515 nm and with an optical power of 2.95 mW/cm^2). First, we note that the SP exhibits a quasi-instantaneous response (at the timescale of the KPFM regulation loop integration time, which was set to a few tens of ms for these experiments) in the form of a negative shift of ≈240 mV after switching the light pulse on. This fast change

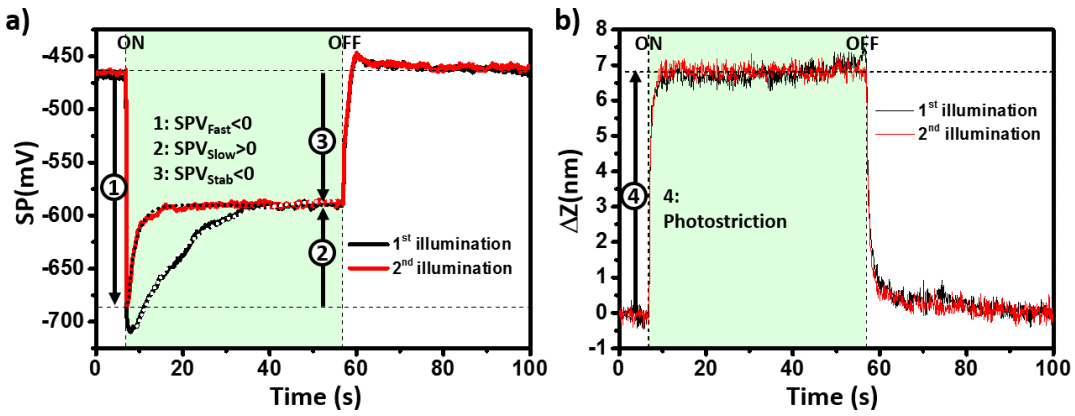


Figure 2: Plots of the (a) KPFM surface potential (b) and the tip height change relative to its initial position as a function of time during two successive illumination sequences (λ = 515 nm, P_{opt} = 2.95 mW/cm^2). The arrows labelled 1, 2, 3 in (a) and 4 in (b) highlight the fast (1), slow (2) and stabilized (3) components of the surface photovoltage and the photostriction signal (4), respectively. The dotted curves in (a) show the results of curve adjustments with functions based on a single exponential, yielding time constants for the SPV dynamics of 11.4 s and 2.1 s during the 1st and 2nd illumination sequences, respectively.

is followed by a slower evolution and a subsequent stabilization of the SP under illumination at a timescale of a few tens of seconds. The surface photovoltage (SPV) at equilibrium (or "stabilized SPV", SPV_{Stab}) is therefore equal to the sum of a negative and a positive term, which will be referred to hereafter as "fast" and "slow" SPV components (SPV_{Fast} and SPV_{Slow}, see Figure 2a) with regards to their different photoresponse dynamics. After switching the light off, the SP displays a fast positive shift followed by a slow stabilization towards its initial level. Remarkably, the tip height also displays a fast photoresponse, but shows almost no noticeable evolution under continuous illumination at this optical power. In other words, the maximum height photoresponse is quasi-instantaneous (at the time scale of our measurement) and does not scale with the illumination time. Consistent with the conclusions of the former work by Zhou et al. [16], this strongly supports the idea that the "fast" cantilever height photoresponse originates from an intrinsic photostriction effect (and not from a thermally induced sample dilatation).

Another significant difference is that the *z*-curves recorded during the first and the second illumination sequences are perfectly identical; in turn, the SP stabilizes more quickly under illumination during the second sequence. Time constants characterizing the SPV evolution under illumination can be deduced from the curve adjustments (shown as the dotted curves in Figure 2a) with single exponential based functions. They are equal to 11.4 s and 2.1 s for the first and second illumination sequence, respectively. Actually, complementary measurements performed by applying a series of successive pulses (see Figure S1 in Supporting Information File 1) demonstrate that the SP stabilization time constant under illumination does not evolve further after the second illumination pulse. In the following, the methodology used to calculate the SPV values consists of applying a first "initialization" light pulse. The data are then calculated from curves that are recorded during subsequent illumination sequences.

The different SP and height photoresponses already indicate that the surface photovoltage and photostriction effect probed in our experiment do not result from crosstalk between the *z* and KPFM regulation loops. In addition, two simple tests have been carried out to definitely exclude the existence of artefacts (see Figures S2 and S3 in Supporting Information File 1). First, the influence of the light pulse on the *z* regulation has been checked by recording spectroscopic curves of the frequency shift with the AFM tip in full backward position (i.e., retracted 1 μm away from the sample surface and kept at a fixed position with the topographic regulation disengaged). By comparing the frequency detuning induced by the light pulse with curves of the tip height (recorded in the interaction with an active regulation) as a function of the frequency set point (Figure S2, Supporting Information File 1), it can be simply shown that the cantilever detuning can at maximum (i.e., for the largest optical power applied in this study) induce a *z*-shift of 0.15 nm. Secondly, spectroscopic curves were acquired under the same illumination conditions and with the same cantilever on a highly oriented pyrolytic graphite (HOPG) substrate (Figure S3, Supporting Information File 1). The surface potential displays no shift under illumination (which also confirms the absence of any carrier photogeneration due to the cantilever tip itself), and the fast component of the *z* photoresponse is negligible compared to the one measured on the $MAPbBr_3$ single crystal with the same fluence. This reinforces the conclusion that the fast component of the *z* photoresponse detected on the $MAPbBr_3$ crystal does not originate from a thermal expansion effect. Note here that the HOPG substrate displays a thermal expansion coefficient [22] in the out-of-plane direction close to that of the $MAPbBr_3$ crystal [23] and that both samples are relatively similar in terms of size (0.5 mm thick for the HOPG vs ≈1 mm for the $MAPbBr_3$ crystal).

These comparative measurements on HOPG show that at high fluence, the thermal detuning of the cantilever can induce a slow evolution of the *z* level under illumination and a subsequent slow return to equilibrium in dark conditions. Nevertheless, this extrinsic *z*-change has no impact on the SP measurement, as demonstrated by the data acquired on the HOPG substrate. Finally, both the SPV and the photostrictive response show a clear dependence as a function of the photon energy (as shown in Figure S4, Supporting Information File 1). For equivalent optical powers, much smaller height variations and SP shifts are observed when the wavelength falls below the $MAPbBr_3$ bandgap ($E_G \approx 2.2$eV [12]). This confirms that the measured height changes originate from the intrinsic photostriction of the $MAPbBr_3$ crystal. However, an almost identical photoresponse is observed under 405 nm and 515 nm illumination, which seems different from the case of $MAPbI_3$ (for which a wavelength-dependent photostriction was observed [16] above the bandgap). Here, it is noteworthy that the wavelength of our green laser falls within an absorption peak due to a strong excitonic transition [24,25]. Further measurements at intermediate wavelengths (currently unavailable in our setup) would be necessary to draw a definitive conclusion about the wavelength dependency of the photoresponse above the bandgap.

The fast surface photovoltage polarity implies that negative charges accumulate quickly under illumination beneath the surface of the single crystal. This observation is fully consistent with the results of recent work by et Liu et al., who proposed [15] that a downward band bending occurs at the surface of p-type $MAPbBr_3$ crystals. This p-type conductivity has been

documented by numerous studies on $MAPbBr_3$ thin films [26,27] and single crystals [28]. Here, the band bending is due to the existence of surface states which are filled by forming a charge-depleted layer (also called a space-charge layer) beneath the surface [15]. The resulting internal built-in electric field induces a spatial separation of the photogenerated carriers of opposite sign in the space charge region (Figure 3a). On the other hand, the opposite polarity of the slow SPV component implies that charge redistribution occurs in the system within a few seconds, which is highly likely to originate from photoinduced ion-migration mechanisms. As mentioned above, there is nowadays overwhelming evidence that hybrid perovskites should be treated (at least to some extent) as mixed electronic–ionic semiconductors [29]. Ion migration occurs in these materials due to the existence of anion and cation vacancies [30] and is already known to induce changes in the surface potential recorded by KPFM at time scales ranging from seconds to minutes [6,8,9]. Here, we assume that the excess of negative photocarriers at the surface attracts methyl ammonium cations (while bromide anions are repelled from the surface), resulting in an effective reduction of the surface photovoltage after a few seconds. In that time frame, the difference observed between the SP curves acquired during the initial and subsequent illumination sequences may indicate that the ion-migration process is not fully reversible (at least at the scale of the time interval between the illumination sequences). However, we also note that the surface potential returns fully to its initial value after the first illumination sequence. A plausible scenario (yet to be definitely confirmed) would be that negative charge carriers remain trapped in the space charge area with a counter cation partner, resulting in a neutral electrostatic balance before and after the first illumination pulse. Actually, the return to the dark state occurs most likely through a two-step process involving firstly the photocarriers, and secondly, the ionic species. Indeed, a closer look at the SP(t) curves in Figure 2a reveals that the SP is slightly more positive than initially just after switching the light pulse off. This SP overshoot becomes much more pronounced at higher fluence (as shown in Figure 3c and Figure S3d in Supporting Information File 1). Our interpretation is that most of the photocarriers recombine quickly after the pulse extinction, leaving an excess of positive cations near the surface. Then, a reverse migration of the cations towards the bulk occurs at a slower time scale (however, some of the cations remain eventually trapped with a counter electric charge after the first illumination sequence as suggested above). A schematic representation illustrating the full sequence of photocarrier generation and spatial separation, the ion migration, the photocarrier recombination, and finally, the reverse ion migration is given in Figure 3b.

The picture which emerges from the above discussion is remarkably consistent with the conclusions that can be drawn from former KPFM works performed on perovskite single crystals (band bending induced accumulation of negative photocarriers at the surface of $MAPbBr_3$) and thin films (SPV time evolution resulting from an interplay between photocarrier and

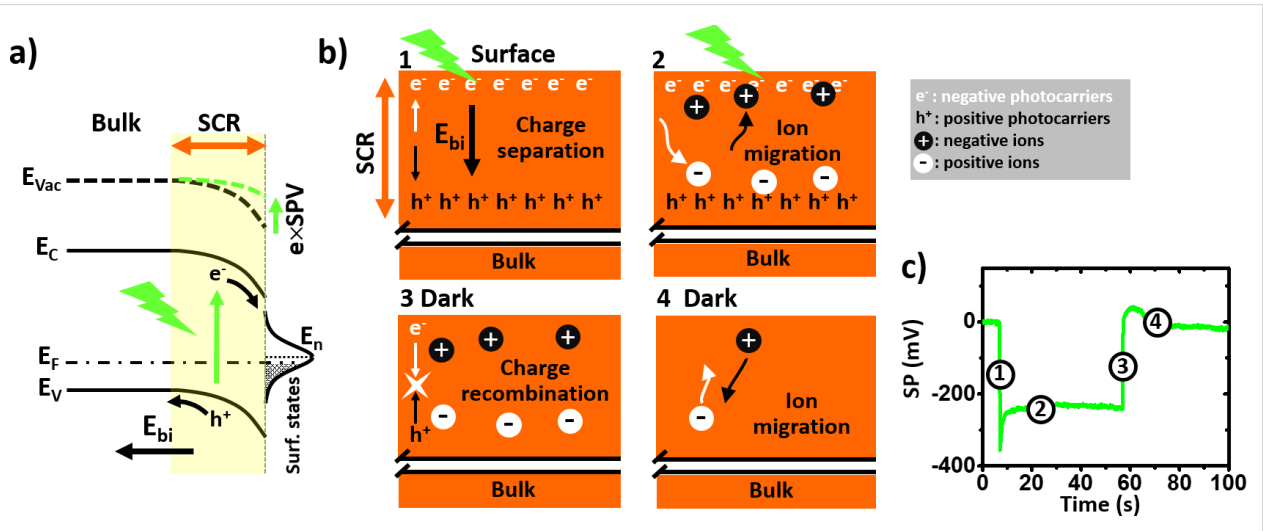


Figure 3: (a) Scheme illustrating how charge transfer from surface states bends the energy bands of p-type $MAPbBr_3$. The built-in electric field (resulting from the existence of permanent charges) induces a spatial separation of the photocarriers on both sides of the space charge area. SCR: space charge region. E_F: Fermi level. E_n: surface states charge neutrality level. (b) Schematic representation illustrating the photocarrier generation and spatial separation by drift under the built-in electric field (step 1), the ion migration under illumination (step 2), the photocarrier recombination (step 3), and finally, the reverse ion migration under dark conditions (step 4). Note that the whole crystal volume is not represented in this sketch, which depicts only the processes occurring near the surface in the space charge area. (c) Plot of the surface potential as a function of time during an illumination sequence (λ = 515 nm, P_{opt} = 65.54 mW·cm^{-2}). The curve has been rescaled by shifting the y-values in such a way that the SP at t = 0 is equal to 0 mV. The timing of the four steps depicted in b) is highlighted in c) by numbered circles.

ionic species). Equally remarkable is the simultaneous observation of a photostrictive response very similar to the one reported from AFM measurements performed on $MAPbI_3$ single crystals [16]. In particular, contrary to the conclusions of recent work based on Raman spectroscopy measurements [17], our data demonstrate that the crystal lattice also undergoes a dilatation under illumination in the case of the bromide compound. As shown hereafter, the photostrictive response displayed by our $MAPbBr_3$ single crystal is moreover comparable in magnitude with the one reported by Zhou et al. for $MAPbI_3$ in its cubic phase [16].

To carry out a quantitative comparison, it is mandatory to analyze the light intensity dependence on the photostrictive effect. Here, the crystal photostriction is defined as the "fast component" of the height change under illumination (see Figure S3c, Supporting Information File 1). The height change appears in first analysis proportional to the light intensity (see Figure 4a) and displays no saturation up to ≈350 mW/cm^2 under monochromatic illumination at 515 nm.The relative height change (i.e., height change divided by the sample thickness, here approximately 1 mm) under 100 mW/cm^2 is equal to 18 ppm. This last value is remarkably close to the one reported [16] for the cubic phase of $MAPbI_3$ (keeping in mind that our measurements are not performed under white light illumination, contrary to that reported for $MAPbI_3$ single crystals). However, we note that the photostriction does not scale perfectly linearly with the fluence over the full measurement range. The photostriction data acquired in the low fluence regime (i.e., for optical powers below 10 mW/cm^2) strongly deviates from a linear function, as clearly shown by the semi-logarithmic plot (inset in Figure 4a).

Further insight on the crystal photoresponse can be gained by analyzing the dependence of the SPV as a function of the optical power (Figure 4b). The fast component of the SPV displays a logarithmic dependence as a function of the illumination intensity. In principle, the slope of this curve (calculated with a natural logarithm) should fall between k_BT/q and $2k_BT/q$ (where k_BT/q is the thermal voltage) depending of the strength of trap-delayed recombination processes [31]. A pure bimolecular recombination process cannot explain the anomalously low value deduced from our measurements. Such deviations have already been observed in small-molecule bulk-heterojunction solar cells [32], and have been recently explained by considering the contribution of interface recombination processes [33]. More precisely, this recent model predicts that slopes lower than the thermal voltage can be observed in the presence of surface recombination for systems where the bulk recombination is purely (or almost completely) bimolecular. This scenario is remarkably consistent with our previous deduction about the existence of surface states (which are here a key ingredient at the origin of the built-in electric field and photocarrier spatial separation), and with the fact that according to the literature [11] the trap density level should be quite low in the bulk of the perovskite single crystals.

To probe the photocarrier dynamics, an alternative approach consists of performing the KPFM measurements under frequency modulated illumination (Figure 5a). In the last years, several works have indeed shown that the effective carrier lifetime in photovoltaic thin films can be quantified by analyzing the dependence of the time-averaged surface potential (SP_{av}) with respect to the modulation frequency (f) of the illumination source [20,34-36]. In short, if the system is characterized by a

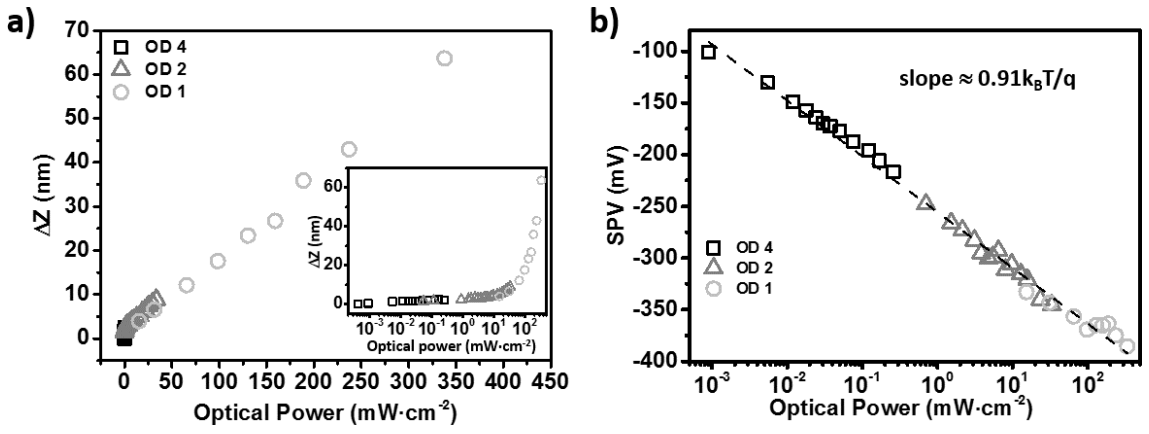


Figure 4: (a) Photostrictive signal as a function of the optical power at λ = 515 nm. Inset: plot in semi-logarithmic scale. (b) Fast component of the surface photovoltage as a function of the optical power (plot in semi-logarithmic scale) at λ = 515 nm. The slope of the linear fit (dotted line) is equal to ≈23.5 mV (calculation performed with the natural logarithm).Three optical densities (OD 1, 2 and 4) have been used to sweep the optical power over more than five decades (the data plotted with squares, triangles and circles have been acquired by using OD 4, OD 2 and OD 1 optical density filters, respectively).

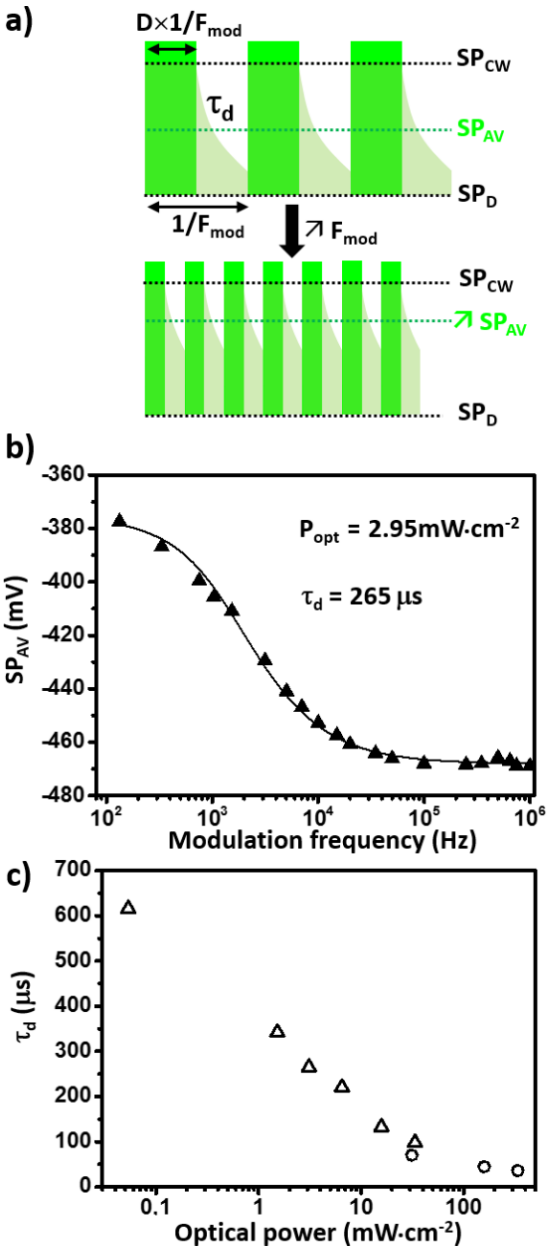


Figure 5: (a) Scheme of the surface potential time response under frequency modulated illumination. The SPV decay dynamics (characterized by a time constant τ_d) determine the frequency evolution of the average potential, SP_{av}, probed by KPFM. SP_D and SP_{CW} represent the in-dark surface potential and the maximum surface potential that would be measured under continuous wave illumination. Note that in this scheme the surface photovoltage (SPV = SPcw − SP_D) is positive; in the case of our experiment, it displays an opposite polarity. (b) Experimental curves of the average surface potential as a function of the illumination modulation frequency F_{mod} acquired at 515 nm with an optical peak power of 2.95 mWcm^{-2}. The result of the numerical fit performed to extract the SPV decay time constant is displayed by a solid line. (c) Plot of the SPV decay time constant as a function of the optical power.

single photopotential decay process in the dark state (related to the photocarrier recombination), SP_{av} will increase with the modulation frequency and saturate when the time between the pulses becomes shorter than the photopotential time decay. If one uses simple exponential functions characterized by a unique time constant τ_d to account for the SPV decay between the light pulse, $SPV_{av}(f)$ curves can be fitted by Equation 1 [20]:

$$SP_{av}(f) = SP_D + SPV_{cw} \cdot D + \tau_d \cdot f \cdot SPV_{cw}\left(1 - e^{-\frac{(1-D)}{\tau_d \cdot f}}\right) \quad (1)$$

where SP_D is the "in-dark" surface potential, SPV_{CW} the surface photovoltage that would be measured under continuous wave illumination (which is equal to SP_{av} in the high frequency limit) and D is the illumination duty ratio.

As seen in Figure 5b the agreement between this fitting law and the experimental curves acquired on the $MAPbBr_3$ single crystal is excellent, which confirms that the SPV dynamics can be properly accounted for on the basis of a single time constant decay. In addition, the time-resolved measurements have been carried out as a function of the fluence. As expected, the increase in charge carrier density (for increasing optical powers) leads to a decrease in the decay time (Figure 5c). More precisely, τ_d displays a linear decrease as a function of the optical power when plotted in semi-logarithmic scale in the 50 µW/cm^2 to 20 mW/cm^2 range. Although FMI-KPFM measurements are not performed in a nonperturbative regime [20], this observation seems consistent with former results of macroscopic transient photovoltage (TPV) measurements reported for $MAPb(I_{1-x},Br_x)_3$ perovskite thin films [37]. Besides, the similarity with the decay time values obtained by TPV measurements on $MAPbI_3$ single crystals [38] is remarkable (e.g., τ_d = 175 µs under 10 mW/cm^2 illumination for FMI-KPFM measurements on MAPbBr3, and τ_d = 234 µs under 0.1 sun in TPV measurements on $MAPbI_3$).

Strikingly, the carrier lifetime and photostriction curves display slope changes occurring in the same optical power range (to ease the comparison, these data are presented side by side with the photostriction curve in log–log scale in Figure S5, Supporting Information File 1). For a fluence greater than a few 10 mW/cm^2, the effective carrier lifetime decreases, and indeed less steeply when raising the optical power, while the photostriction displays an opposite trend. This photostrictive behavior indicates that the photocarrier coupling with the lattice becomes somehow "more efficient" in the high carrier density regime. It remains however difficult at this stage to draw a definitive conclusion about the origin of the photocarrier lifetime evolution in the high fluence regime. More specifically, the difficulty here is that the carrier density (in first approximation inversely proportional to the illumination intensity) remains a hidden parameter that cannot be directly deduced from our

data (contrary to conventional macroscopic measurements where transient photovoltage can be combined with charge extraction [37]).

Here, we stress that the carrier recombination dynamics in the bulk may strongly differ from the SPV decays probed by time-resolved KPFM. Let us remind the reader here that the SPV originates from spatially separated carriers due to the existence of a built-in electric field at the vicinity of the surface. In the future, it would be highly desirable to quantify the vertical extension of the space charge area at the origin of the spatial separation of the photocarrier and to check how it compares with the light absorption depth, and more importantly, with the photocarrier diffusion length. Regarding the photostrictive effect, it has been indeed argued that the responsive layer is much thicker that the light penetration depth due to the diffusion of photocarriers in the bulk [16]. In turn, the SPV (more precisely its fast component) originates from the contributions of oppositely charged photocarriers located on either side of the space charge region. Thus, the photostriction signal may originate from a much thicker part of the crystal beneath the surface than the SPV.

Further experiments are in progress to map two-dimensional images of the SPV decay. Revealing the existence (or observing the absence) of time-decay contrasts related to surface (or subsurface) defects could help in assessing the relative weight of photocarriers localized near the surface and deeper in the bulk to the SPV recombination dynamics.

Conclusion

In summary, we presented the results of a study intended to test if the optomechanical and optoelectronic properties of hybrid organic–inorganic perovskite single crystals can be investigated simultaneously by nc-AFM and KPFM. We successfully demonstrated that the height change and the surface potential shift under illumination originate from the crystal photostriction and the contributions of photogenerated charge carriers, respectively. The measurements revealed that, similar to the case of methylammonium lead triiodide, the photostrictive response of $MAPbBr_3$ consists of a lattice expansion. Moreover, we have shown that our methodology based on the acquisition of spectroscopic curves in the time domain allows disentangling the contributions of the photocarriers to the surface photovoltage from the ones due to the light-induced migration of ionic species. Lastly, the effective carrier lifetime has been quantified by analyzing the dependence of the surface potential as a function of the frequency modulation of the illumination source. Thus, it has been possible to analyze both the photostriction and carrier lifetime as a function of the optical power. Our multimodal approach opens up new possibilities to investigate a wide range of photo-physical process and dynamical phenomena in organic–inorganic perovskites and related materials.

Supporting Information

Supporting Information File 1

Additional experimental data.
Surface potential time evolution recorded during several successive illumination sequences. Measurements of the cantilever frequency shift as a function of the optical power and of the *z* variation as a function of the frequency shift set point. Curves of the relative height and surface potential recorded during illumination sequences on a highly oriented pyrolytic graphite substrate and on the $MAPbBr_3$ single crystal for various optical powers. Photostrictive response and fast component of the surface photovoltage as a function of the optical power for 685 nm, 515 nm and 405 nm illumination. Curves of the SPV time decay and photostriction as a function of the optical power.
[https://www.beilstein-journals.org/bjnano/content/supplementary/2190-4286-9-161-S1.pdf]

Acknowledgements

The nc-AFM/KPFM experiments were carried out thanks to the financial support (Y.A. post-doctoral fellowship) by the Agence Nationale de la Recherche (France) with the J2D (ANR-15-CE24-0017) project. The single crystal synthesis was supported by the European Commission and Région Wallonne FEDER Program, the Science Policy Office of the Belgian Federal Government (BELSPO-PAI VII/5), the FRS-FNRS PDR Project “Hybrid Organic/Inorganic Nanomaterials for Energy COnversion and STOrage Devices on FLEXible and Stretchable Substrates (ECOSTOFLEX)”, and MP 1307 COST Action “Stable Next-Generation Photovoltaics: Unraveling Degradation Mechanisms of Organic and Perovskite Solar Cells by Complementary Characterization Techniques (StableNextSol)”. D.M. is grateful to FRS-FNRS for a post-doctoral fellowship. Ph.L. is a Senior Research Associate of FRS-FNRS (Belgium).

ORCID® iDs

Jaume Llacer Martinez - https://orcid.org/0000-0002-3348-7295
Philippe Leclère - https://orcid.org/0000-0002-5490-0608

References

1. Chen, Q.; De Marco, M.; Yang, Y. M.; Song, T.-B.; Chen, C.-C.; Zhao, H.; Hong, Z.; Zhou, H.; Yang, Y. *Nano Today* **2015,** *10,* 355–396. doi:10.1016/j.nantod.2015.04.009
2. Correa-Baena, J.-P.; Abate, A.; Saliba, M.; Tress, W.; Jacobsson, T. J.; Grätzel, M.; Hagfeldta, A. *Energy Environ. Sci.* **2017,** *10,* 710–727. doi:10.1039/C6EE03397K

3. Zhang, L.; Yang, X.; Jiang, Q.; Wang, P.; Yin, Z.; Zhang, X.; Tan, H.; Yang, Y. M.; Wei, M.; Sutherland, B. R.; Sargent, E. H.; You, J. *Nat. Commun.* **2017,** *8,* 15640. doi:10.1038/ncomms15640
4. Sutherland, B. R.; Sargent, E. H. *Nat. Photonics* **2016,** *10,* 295–302. doi:10.1038/nphoton.2016.62
5. Wang, X.; Li, M.; Zhang, B.; Wang, H.; Zhao, Y.; Wang, B. *Org. Electron.* **2018,** *52,* 172–183. doi:10.1016/j.orgel.2017.10.027
6. Yun, J. S.; Ho-Baillie, A.; Huang, S.; Woo, S. H.; Heo, Y.; Seidel, J.; Huang, F.; Cheng, Y.-B.; Green, M. A. *J. Phys. Chem. Lett.* **2015,** *6,* 875–880. doi:10.1021/acs.jpclett.5b00182
7. Li, J.-J.; Ma, J.-Y.; Hu, J.-S.; Wang, D.; Wan, L.-J. *ACS Appl. Mater. Interfaces* **2016,** *8,* 26002–26007. doi:10.1021/acsami.6b07647
8. Bergmann, V. W.; Guo, Y.; Tanaka, H.; Hermes, I. M.; Li, D.; Klasen, A.; Bretschneider, S. A.; Nakamura, E.; Berger, R.; Weber, S. A. L. *ACS Appl. Mater. Interfaces* **2016,** *8,* 19402–19409. doi:10.1021/acsami.6b04104
9. Garrett, J. L.; Tennyson, E. M.; Hu, M.; Huang, J.; Munday, J. N.; Leite, M. S. *Nano Lett.* **2017,** *17,* 2554–2560. doi:10.1021/acs.nanolett.7b00289
10. Yuan, Y.; Li, T.; Wang, Q.; Xing, J.; Gruverman, A.; Huang, J. *Sci. Adv.* **2017,** *3,* e1602164. doi:10.1126/sciadv.1602164
11. Shi, D.; Adinolfi, V.; Comin, R.; Yuan, M.; Alarousu, E.; Buin, A.; Chen, Y.; Hoogland, S.; Rothenberger, A.; Katsiev, K.; Losovyj, Y.; Zhang, X.; Dowben, P. A.; Mohammed, O. F.; Sargent, E. H.; Bakr, O. M. *Science* **2015,** *347,* 519–522. doi:10.1126/science.aaa2725
12. Saidaminov, M. I.; Abdelhady, L.; Murali, B.; Alarousu, E.; Burlakov, V. M.; Peng, W.; Dursun, I.; Wan, L.; He, Y.; Maculan, G.; Goriely, A.; Wu, T.; Mohammed, O. F.; Bakr, O. M. *Nat. Commun.* **2015,** *6,* 7586. doi:10.1038/ncomms8586
13. Moerman, D.; Eperon, G. E.; Precht, J. T.; Ginger, D. S. *Chem. Mater.* **2017,** *29,* 5484–5492. doi:10.1021/acs.chemmater.7b00235
14. Zhao, P.; Xu, J.; Dong, X.; Wang, L.; Ren, W.; Bian, L.; Chang, A. *J. Phys. Chem. Lett.* **2015,** *6,* 2622–2628. doi:10.1021/acs.jpclett.5b01017
15. Liu, X.; Liu, Y.; Gao, F.; Yang, Z.; Liu, S. F. *Appl. Phys. Lett.* **2016,** *108,* 181604. doi:10.1063/1.4948680
16. Zhou, Y.; You, L.; Wang, S.; Ku, Z.; Fan, H.; Schmidt, D.; Rusydi, A.; Chang, L.; Wang, L.; Ren, P.; Chen, L.; Yuan, G.; Chen, L.; Wang, J. *Nat. Commun.* **2016,** *7,* 11193. doi:10.1038/ncomms11193
17. Wei, T.-C.; Wang, H.-P.; Li, T.-Y.; Lin, C.-H.; Hsieh, Y.-H.; Chu, Y.-H.; He, J.-H. *Adv. Mater.* **2017,** *29,* 1701789. doi:10.1002/adma.201701789
18. Kundys, B. *Appl. Phys. Rev.* **2015,** *2,* 011301. doi:10.1063/1.4905505
19. Fuchs, F.; Caffy, F.; Demadrille, R.; Mélin, T.; Grévin, B. *ACS Nano* **2016,** *10,* 739–746. doi:10.1021/acsnano.5b05810
20. Fernández Garrillo, P. A.; Borowik, Ł.; Caffy, F.; Demadrille, R.; Grévin, B. *ACS Appl. Mater. Interfaces* **2016,** *8,* 31460–31468. doi:10.1021/acsami.6b11423
21. Ding, J.; Zhao, Y.; Du, S.; Sun, Y.; Cui, H.; Zhan, X.; Cheng, X.; Jing, L. *J. Mater. Sci.* **2017,** *52,* 7907–7916. doi:10.1007/s10853-017-0995-8
22. Tan, P.; Deng, Y.; Zhao, Q.; Cheng, W. *Appl. Phys. Lett.* **1999,** *74,* 1818–1820. doi:10.1063/1.123096
23. Mashiyama, H.; Kawamura, Y.; Magome, E.; Kubota, Y. *J. Korean Phys. Soc.* **2003,** *42S,* S1026–S1029.
24. Yang, Y.; Yan, Y.; Yang, M.; Choi, S.; Zhu, K.; Luther, J. M.; Beard, M. C. *Nat. Commun.* **2015,** *6,* 7961. doi:10.1038/ncomms8961
25. Wenger, B.; Nayak, P. K.; Wen, X.; Kesava, S. V.; Noel, N. K.; Snaith, H. J. *Nat. Commun.* **2017,** *8,* 590. doi:10.1038/s41467-017-00567-8
26. Kedem, N.; Kulbak, M.; Brenner, T. M.; Hodes, G.; Cahen, D. *Phys. Chem. Chem. Phys.* **2017,** *19,* 5753–5762. doi:10.1039/c6cp08392g
27. Peng, W.; Wang, L.; Murali, B.; Ho, K.-T.; Bera, A.; Cho, N.; Kang, C.-F.; Burlakov, V. M.; Pan, J.; Sinatra, L.; Ma, C.; Xu, W.; Shi, D.; Alarousu, E.; Goriely, A.; He, J.-H.; Mohammed, O. F.; Wu, T.; Bakr, O. M. *Adv. Mater.* **2016,** *28,* 3383–3390. doi:10.1002/adma.201506292
28. Saidaminov, M. I.; Adinolfi, V.; Comin, R.; Abdelhady, A. L.; Peng, W.; Dursun, I.; Yuan, M.; Hoogland, S.; Sargent, E. H.; Bakr, O. M. *Nat. Commun.* **2015,** *6,* 8724. doi:10.1038/ncomms9724
29. Chen, S.; Wen, X.; Sheng, R.; Huang, S.; Deng, X.; Green, M. A.; Ho-Baillie, A. *ACS Appl. Mater. Interfaces* **2016,** *8,* 5351–5357. doi:10.1021/acsami.5b12376
30. Domanski, K.; Roose, B.; Matsui, T.; Saliba, M.; Turren-Cruz, S.-H.; Correa-Baena, J.-P.; Roldan Carmona, C.; Richardson, G.; Foster, J. M.; De Angelis, F.; Ball, J. M.; Petrozza, A.; Mine, N.; Nazeeruddin, M. K.; Tress, W.; Grätzel, M.; Steiner, U.; Hagfeldtd, A.; Abate, A. *Energy Environ. Sci.* **2017,** *10,* 604–613. doi:10.1039/c6ee03352k
31. Cowan, S. R.; Roy, A.; Heeger, A. J. *Phys. Rev. B* **2010,** *82,* 245207. doi:10.1103/PhysRevB.82.245207
32. Zalar, P.; Kuik, M.; Ran, N. A.; Love, J. A.; Nguyen, T.-Q. *Adv. Energy Mater.* **2014,** *4,* 1400438. doi:10.1002/aenm.201400438
33. Brus, V. V. *Org. Electron.* **2016,** *29,* 1–6. doi:10.1016/j.orgel.2015.11.025
34. Takihara, M.; Takahashi, T.; Ujihara, T. *Appl. Phys. Lett.* **2008,** *93,* 021902. doi:10.1063/1.2957468
35. Borowik, Ł.; Lepage, H.; Chevalier, N.; Mariolle, D.; Renault, O. *Nanotechnology* **2014,** *25,* 265703. doi:10.1088/0957-4484/25/26/265703
36. Shao, G.; Glaz, M. S.; Ma, F.; Ju, H.; Ginger, D. S. *ACS Nano* **2014,** *8,* 10799–10807. doi:10.1021/nn5045867
37. Kiermasch, D.; Rieder, P.; Tvingstedt, K.; Baumann, A.; Dyakonov, V. *Sci. Rep.* **2016,** *6,* 39333. doi:10.1038/srep39333
38. Dong, Q.; Fang, Y.; Shao, Y.; Mulligan, P.; Qiu, J.; Cao, L.; Huang, J. *Science* **2015,** *347,* 967–970. doi:10.1126/science.aaa5760

License and Terms

This is an Open Access article under the terms of the Creative Commons Attribution License (http://creativecommons.org/licenses/by/4.0), which permits unrestricted use, distribution, and reproduction in any medium, provided the original work is properly cited.

The license is subject to the *Beilstein Journal of Nanotechnology* terms and conditions: (https://www.beilstein-journals.org/bjnano)

The definitive version of this article is the electronic one which can be found at: doi:10.3762/bjnano.9.161

BEILSTEIN JOURNAL OF NANOTECHNOLOGY

Direct AFM-based nanoscale mapping and tomography of open-circuit voltages for photovoltaics

Katherine Atamanuk, Justin Luria and Bryan D. Huey*

Full Research Paper

Open Access

Address:
University of Connecticut, Dept. of Materials Science and Engineering, Storrs, Connecticut 06269, USA

Email:
Bryan D. Huey* - bryan.huey@uconn.edu

* Corresponding author

Keywords:
cadmium telluride (CdTe); photo-conductive AFM (pcAFM); PV performance; solar cell; tomographic AFM

Beilstein J. Nanotechnol. **2018,** *9,* 1802–1808.
doi:10.3762/bjnano.9.171

Received: 06 January 2018
Accepted: 25 May 2018
Published: 14 June 2018

This article is part of the Thematic Series "Scanning probe microscopy for energy-related materials".

Guest Editor: P. Leclère

© 2018 Atamanuk et al.; licensee Beilstein-Institut.
License and terms: see end of document.

Abstract

The nanoscale optoelectronic properties of materials can be especially important for polycrystalline photovoltaics including many sensor and solar cell designs. For thin film solar cells such as CdTe, the open-circuit voltage and short-circuit current are especially critical performance indicators, often varying between and even within individual grains. A new method for directly mapping the open-circuit voltage leverages photo-conducting AFM, along with an additional proportional-integral-derivative feedback loop configured to maintain open-circuit conditions while scanning. Alternating with short-circuit current mapping efficiently provides complementary insight into the highly microstructurally sensitive local and ensemble photovoltaic performance. Furthermore, direct open-circuit voltage mapping is compatible with tomographic AFM, which additionally leverages gradual nanoscale milling by the AFM probe essentially for serial sectioning. The two-dimensional and three-dimensional results for CdTe solar cells during in situ illumination reveal local to mesoscale contributions to PV performance based on the order of magnitude variations in photovoltaic properties with distinct grains, at grain boundaries, and for sub-granular planar defects.

Introduction

Cadmium Telluride (CdTe) is an inexpensive thin-film photovoltaic with ca. 5% of the 2017 global market share for solar cells. To optimize the efficiency and reliability of these, or any electronic devices, a thorough understanding of their composition, microstructure, and performance is necessary as a function of device design, processing, and in-service conditions. Atomic force microscopy (AFM) has been a valuable tool for such characterization, especially of materials properties and device performance at the nanoscale. In the case of thin-film solar cells, local photovoltaic (PV) properties such as the open-circuit voltage, photocurrent, and work function have been demonstrated to vary by an order of magnitude, or more, within tens of nanometers [1-3]. Recently, property mapping with high spatial resolution by AFM has been further combined with the

ability to serially mill a surface, in order to reveal underlying surface structures and uniquely develop three-dimensional (3D) nanoscale property maps. The most notable examples are based on pure current detection with the AFM to resolve conduction pathways in filamentary semiconducting devices and interconnects [4,5], and tomographic AFM of photocurrents in polycrystalline solar cells during in situ illumination [6].

Standard photo-conductive AFM (pcAFM) employs a conducting probe, which serves as a positionable top electrode, to map currents upon illumination and/or biasing. With solar cells, the short-circuit current (I_{SC}) can then be directly visualized by simply measuring the photocurrent when there is no potential difference between the sample and the scanning probe. By further sweeping the bias between the sample and the grounded tip, for a single spot or an array of locations, the resulting *I*–*V* curves can be analyzed to interpret several additional performance metrics, which are widely employed by the PV and solar power communities. The open-circuit voltage (V_{OC}), for example, is the probe bias necessary for the photocurrent to pass from positive to negative values, i.e. when the solar cell locally transitions from power generation to power shunting. The similarly crucial maximum-power point and/or fill factor can also be identified from *I*–*V* measurements. These and related PV performance parameters are academically, commercially, and more generally societally important given the complexity, functionality, and widespread benefits of PV devices, such as solar cells.

To extract such PV metrics at the nanoscale, for instance with standard 256 × 256 pixel resolution, over 65000 distinct current–voltage spectra must be acquired and analyzed. We previously developed an efficient, method with high spatial resolution for this purpose, namely photo-conductive AFM spectroscopy (pcAFMs) [1], essentially by collecting an entire array of *I*–*V* spectra in parallel via a series of consecutive pcAFM images. Each image is acquired with a sequentially increased sample bias, tracing through the power generation quadrant of the solar cell specimen for a nano- to micro-scale region, all while preserving a measurement location accuracy at the nanometer scale.

However, despite providing spatial resolution as fine as the tip contact area [4], the voltage resolution for pcAFMs clearly depends on the number of voltage steps and range of biases considered. This is a direct function of the number of stable image frames in an area of interest. But a higher voltage fidelity directly equates to a longer overall acquisition time, necessitating both patience as well as imaging and specimen stability that can be a particular challenge for generally fragile materials systems such as molecular perovskites [7]. Traditional point-by-point measurements are far slower still. Consequently, for AFM-based mapping of solar cell performance parameters that are traditionally derived from *I*–*V* measurements, such as V_{OC}, the spatial and energetic resolution unavoidably conflicts with experimental throughput.

Accordingly, this work presents a new approach for directly mapping V_{OC} with nanoscale resolution, requiring a single, standard-speed AFM scan. This leverages the concept of the proportional-integral-derivative (PID) feedback loop that underpins nearly all AFM topography imaging. Normally, this feedback loop continually updates the AFM probe height in order to maintain a constant AFM tip–sample interaction, which is sensed via the integrated cantilever deflection or amplitude that, of course, changes at surface protrusions or depressions. To simultaneously map V_{OC} directly, the topography is tracked in the same manner, but a secondary PID loop is also configured to continually adjust the sample bias in order to maintain a photocurrent of zero. This is akin to Kelvin probe microscopy or scanning surface potential microscopy, in which a secondary PID loop varies the sample bias to maintain a fixed cantilever amplitude, phase, or frequency. The capacitive and/or coulombic interactions that perturb these signals null when the probe bias equals the ensemble specimen voltage beneath the tip, providing a directly measured map of local surface properties.

There is a particular need for such efficient direct property-mapping routines for computed tomographic AFM (CT-AFM), in which images are serially acquired during progressive surface milling [6,8]. For instance, to investigate the nearly 50% reduction in efficiency for CdTe solar cells compared to their theoretical limits [9-15], it would be beneficial to have through-thickness V_{OC} maps with high spatial and energy resolution. But every V_{OC} map, each comprising tens to hundreds of distinct depths through a sample, necessitates tens of consecutive frames via pcAFMs instead of just one image. Equivalent resolution maps from serially acquired individual *I*–*V* measurements are another hundred times slower. Specifically, for relatively standard AFM scanning at a line rate of 0.5 Hz, direct V_{OC} imaging as proposed herein requires only ca. 8.5 min (for 256 × 256 pixel resolution), compared to 4.3 h if based on pcAFMs (with 30 voltage steps and, hence, image frames), or 18.2 h for traditional point-by-point studies (based on a duration of 1 s to acquire each spectrum, move to the next location, and settle the probe). Of course, high-speed data acquisition can in principle accelerate such measurements of thousands of discrete spectra, as implemented for “peak force” [16] or “fast force” mapping [17,18] where arrays of force–distance curves are acquired during continuous scanning. However, current detection is generally slower than force transduction due to LRC time constants, and in any case tracing full *I*–*V* curves

over a constant range of biases at every location may damage specimens due to occasional high current flow (i.e., heat) or even breakdown. For truly nanoscale tomographic maps of V_{OC} and/or I_{SC} with minimal specimen damage at tens, hundreds, or thousands of distinct depths throughout a specimen, our substantially faster direct approach presented herein (simply requiring one further image per depth) becomes a practical necessity.

Results and Discussion

Figure 1 depicts the system configuration in such a CT-AFM experiment for I_{SC} and direct V_{OC} mapping. The AFM (Asylum Research MFP-3D-IO) is custom-mounted on an optical microscope (Nikon TE-2000) that has a broad-spectrum LED light source (Cree MK-R 12). The LED illuminates an area of ca. $1{\cdot}10^4$ μm^2, including the sample/tip junction, from below through a 40× objective to provide an intensity of ca. 1 equivalent sun. A conducting (B-doped) diamond-coated silicon AFM probe (Nanoworld CDT-NCHR, Soquel, CA, USA), along with a picoampere-resolution current detector (Asylum Research Orca, model 058, 5 V/nA, 1–10 kHz bandwidth), enable either the short-circuit current to be measured or the open-circuit voltage to be directly determined by engaging the secondary feedback loop as previously described. Since the notations I_{SC} and V_{OC} are technically defined for 1 equivalent sun, all results and discussions indicate an effective I_{SC}* and V_{OC}* because the light source is not a true solar simulator. In any case, lateral spatial resolution remains as fine as ca. 20 nm throughout the measurement according to the final topographic features observed. This is compatible with the tip–sample contact radius for a probe apex with a 25–50 nm radius of curvature and an effectively planar substrate. Tomography is achieved directly with the AFM probe simultaneous to the repeated property mapping. Specific settings include a load of ca. 1 μN, a line rate of 0.5 Hz, and a low-deflection feedback gain producing near "open loop" scanning and hence an essentially planar surface milling [8]. Approximately 15 nm in depth are practically removed per image frame, leading to effective 30 nm resolution in the z-direction between consecutive pairs of I_{SC}* and V_{OC}* maps throughout the polycrystalline film thickness.

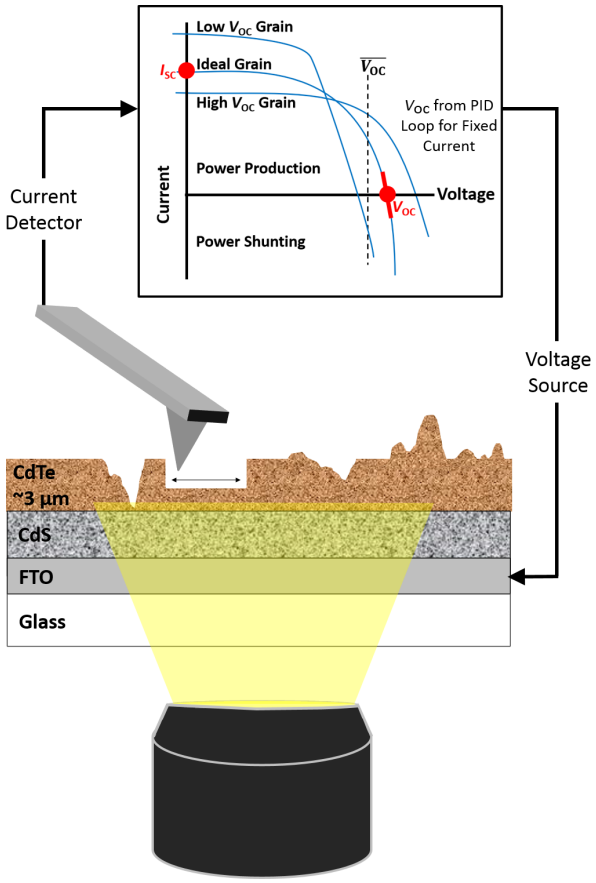


Figure 1: pcAFM measurement of a CdTe/CdS solar cell, during specimen illumination from below through an underlying transparent conducting anode and substrate (FTO/glass). Local currents are detected from above by the AFM probe serving as a positionable cathode. The local photovoltaic properties can vary widely for the heterogeneous microstructure compared to the mean (macroscopic) response. Tomography is achieved by gradually milling the specimen during continuous high-load topographic imaging. Alternating frames toggle between short-circuit current mapping (I_{SC}) based on the photocurrent at zero bias, and direct open-circuit voltage mapping (V_{OC}) via a dedicated PID feedback loop continually adjusting the sample bias to maintain a null photocurrent.

During such progressive imaging some spatial drift is unavoidable, though this is easily accommodated by commercial, free, or custom image analysis routines (respectively Igor Pro, FIJI, and in this case programs written for MATLAB). The necessary drift corrections, typically based on purely rigid registration, cause ca. 10% around the outskirts of the initial property maps to be incomplete for the overall 3D dataset. Accordingly, only pixels with data acquired throughout the depth are considered in the final results. Also, current instead of current density is reported due to the uncertainty about the absolute cross-sectional area.

Figure 2 presents a representative pair of directly detected, effective short-circuit current (Figure 2a) and open-circuit voltage (Figure 2b) images. These signals are uniquely colored for simultaneous visualization when superimposed (Figure 2c), based on a simple 1:1 overlay of the two distinct color images using conventional image processing software (FIJI). Viewed in this manner, most grains present a consistent I_{SC}*, which varies up to three orders of magnitude for adjacent grains (note the log scale). V_{OC}*, on the other hand, is less uniform within a single grain, appearing to vary most strongly at some grain boundaries as well as many seemingly linear features. This type of instant property mapping is especially beneficial for specimens

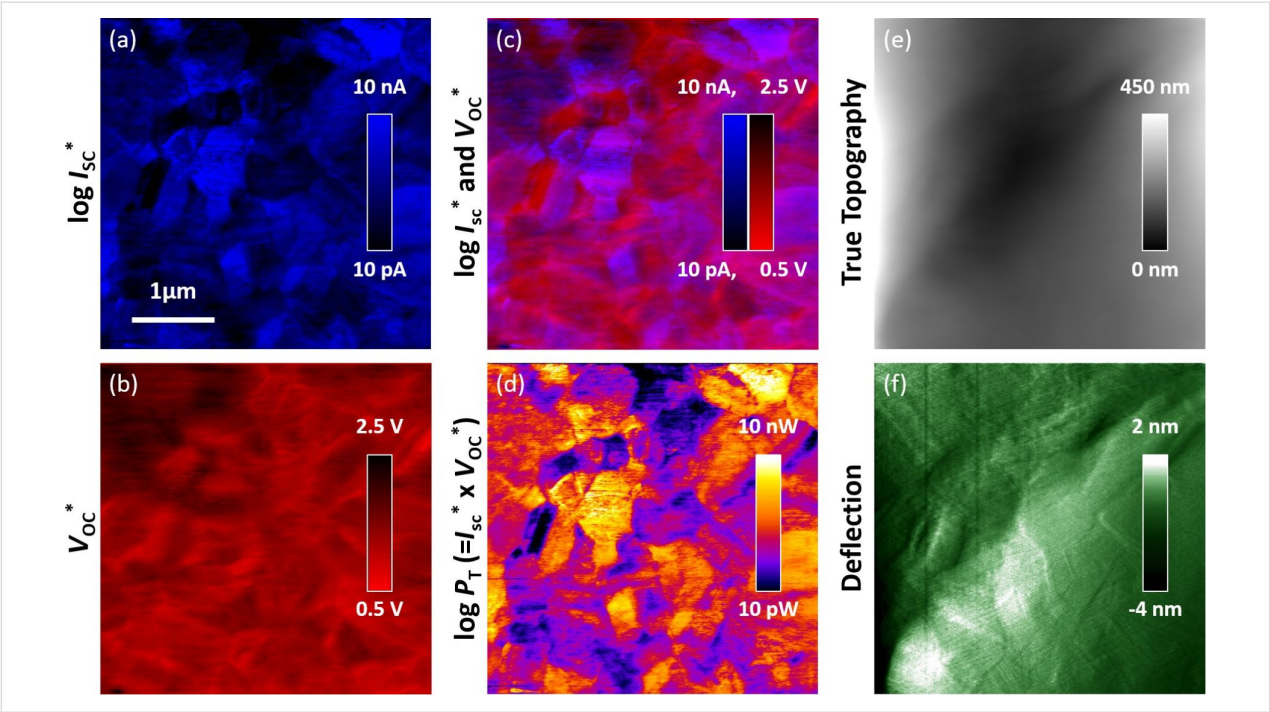


Figure 2: (a) Consecutively acquired I_{SC}* (note the log scale) and (b) directly measured V_{OC}* for a single ca. 4 × 4 µm area. (c) A simple overlay of these distinctly colored images is displayed, demonstrating their sometimes complementary and otherwise uncorrelated behavior. The product of I_{SC}* and V_{OC}* is shown in (d) indicative of the theoretical power (P_T*, log scale). (e) The simultaneously acquired true surface topography and (f) deflection data (essentially an edge-filtered height image to identify any topographic steps or other microstructural boundaries) reveal little correlation with the photovoltaic performance.

sensitive to their environment, as is common for many photovoltaics in the presence of oxygen or humidity [19]. Along these lines, direct measurements of V_{OC}* during exposure to acetic acid are ongoing for Si solar cells to correlate any changes in the local properties with this macroscopically known contributor to the accelerated PV degradation in solar panels [20-23]. Here, the short-circuit current and open-circuit voltage signals are further multiplied in Figure 2d to represent the theoretical power. Distinct from the individual or overlain images of Figure 2a–c, this reveals even more spatially localized variations in photovoltaic performance.

As with every study based on scanning probes, it is important to consider any influence of topography on the results. The as-provided surface of the essentially commercial grade polycrystalline film is relatively rough when considered at the nanometer scale, revealing grains, facets, and grain boundaries with topographic protrusions and depressions as great as ±150 nm. Surface-potential studies of a range of photovoltaics have identified correlations between such features and their measured properties, for example with work function differences of molecular perovskites observed at specific facets [24] or grain boundary interfaces [2]. Topography commonly couples with conductive or photoconductive AFM contrast as well. Routines to test for such associations are therefore increasingly employed [1,24], allowing scientists to focus on or ignore such regions depending on whether they are true local variations or experimental artifacts. In any case, in order to minimize the influence of such topography, our specimens are first partially planarized [8]. This provides a surface morphology with slopes gradually transitioning ±5° over several micrometers according to the true topography [25] (Figure 2e). Local protrusions or depressions are smaller than 6 nm per the edge-identifying deflection signal (Figure 2f) acquired simultaneously with Figure 2a. Compared to the as-received surface profile, the RMS roughness is thus improved up to two orders of magnitude. Notably, there are few correlations between this morphology and the photovoltaic performance.

Figure 3 displays secondary scanning electron microscopy images of the as-provided thin film (Figure 3a, outer regions) and the surface after the initial local planarization (Figure 3a, smooth central area). A corner of this region is depicted in the higher-magnification SEM micrograph (Figure 3b), which also follows ca. 10 nanomilling steps within the square dashed overlay. The sparse bright features around the milled area are clusters of milled material that were not swept out of the field of view during planarization/tomography. The weaker, heterogeneous contrast within results partially from not quite perfect smoothing of the initially high roughness topography.

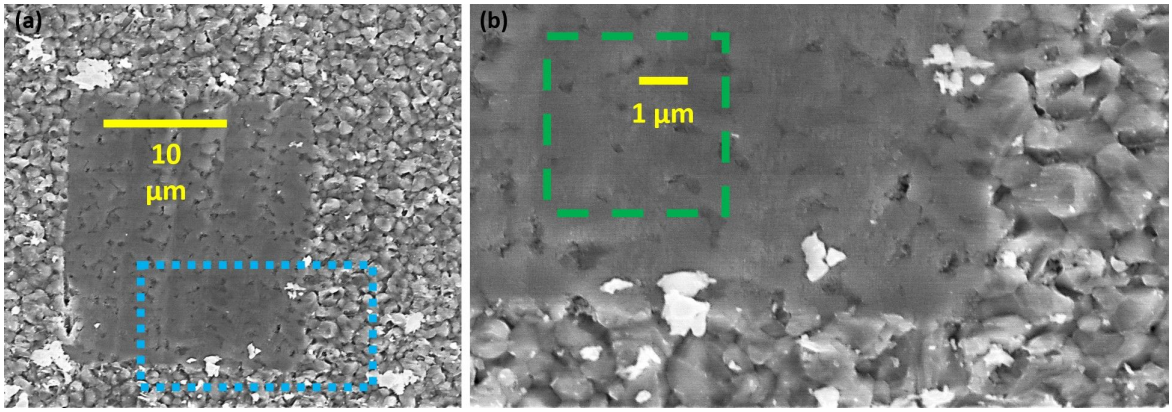


Figure 3: (a) SEM micrograph of a locally planarized polycrystalline CdTe solar cell. The dotted rectangular overlay indicates the location of a higher-magnification SEM image (b) in which the dashed square outline identifies the area studied for Figure 2 and Figure 4.

As already introduced, sequentially repeating I_{SC}* and direct V_{OC}* mapping, with sufficient tip force to continuously remove material, leads to a stack of images that uniquely identify local properties in all three dimensions. For simplicity, a constant milling rate of 15 nm/frame is assumed such that each consecutive tomographic slice represents pairs of I_{SC}* and V_{OC}* in steps of 30 nm along the *z*-direction. Generally, this assumption is consistent with both the uniform SEM contrast of Figure 3, and the clearly linear features resolved in the images of Figure 2, which simply would not appear to be linear without steady milling. It is more specifically supported by the regularly evolving height from consecutive CT-AFM images in separate measurements through an equivalent 2.2 µm thick planarized film [6]. That study required a nearly uniform number of imaging/milling frames to reveal the clearly identifiable highly conducting back electrode throughout a similar field of view, resulting in an estimated average milling rate error better than ±5 nm per image frame. Of course a more sophisticated 3D interpolation, based on the true (*x*, *y*, *z*) coordinates of each acquired pixel, can be implemented for property maps at even more precise depths or cross sections [26]. Such an approach will be especially warranted for initially rough surfaces or island features, instead of an initially planarized and uniformly milling specimen as studied here.

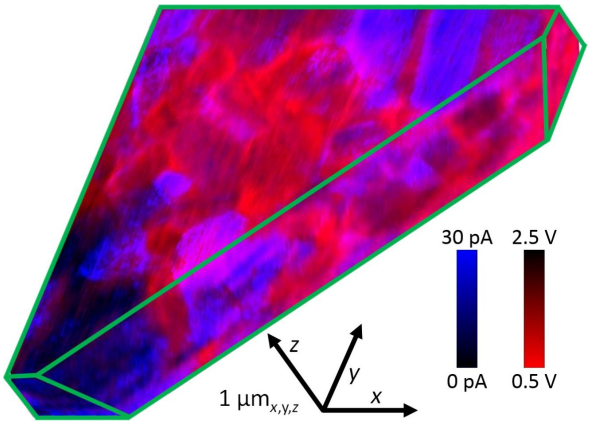


Figure 4: Three-dimensional CT-AFM of the short-circuit current (I_{SC}*, dark to blue contrast) merged with the directly measured open-circuit voltage (V_{OC}*, red to dark) volumetrically rendered to partially reveal an *xy* plane, *xz* and *yz* cross sections, and an oblique *xyz* cut to uniquely expose the nanoscale properties through the specimen thickness. The identified axes also serve as scale bars.

The combined I_{SC}* and V_{OC}* tomography is 3D-rendered in Figure 4, revealing portions of the full rectangular cuboid of acquired 3D data including: the smooth *xy* planar surface; pure *xz* and *yz* cross sections; and an arbitrary oblique *xyz* section. As with Figure 2, bright contrast identifies areas with a strong I_{SC}* (blue), while the contrast for V_{OC}* (red) is flipped to especially highlight the poor V_{OC} at grain boundaries and some sub-granular regions. For any given plane through the specimen it is sometimes difficult to recognize these local properties. This is partially due to convolution with inevitable noise in any SPM-based imaging, but especially results from the stacked and arbitrarily shaped and oriented grains in the microstructure of the thin film. When viewed in 3D, however, the directly acquired photovoltaic properties seem clearly correlated with 3D microstructure.

Specifically, the CdTe thin film exhibits profound (orders of magnitude) heterogeneities in local photovoltaic performance within tens of nanometers of crossing a boundary between three-dimensionally adjacent microstructural features. Some grain boundaries as well as sub-granular planar features appear to reveal relatively poor values of V_{OC}*, supporting prior observations that many interfaces in CdTe may serve as conduits for photoelectrons to move to the underlying n-type CdS layer [6]. Equivalent conclusions have been inferred from complementa-

ry techniques such as simple conductive AFM [27], surface-potential mapping [28], and electron beam induced currents [29], though the fully three-dimensional, directly acquired data of I_{SC}* and now V_{OC}* in Figure 4 is conclusive.

It is noteworthy that qualitatively similar 3D PV data has been reported based on quasi-V_{OC}* imaging and tomography, obtained by simply recording the magnitude and sign of currents when biasing at the mean specimen open-circuit voltage [6] or a similarly suitable bias [30]. According to the schematic in Figure 1, positive currents in these cases imply a locally strong V_{OC}, while negative currents suggest a low V_{OC}, as exemplified by Figure S1 (Supporting Information File 1). But such quasi-V_{OC}* mapping inevitably leads to conjectures based on currents that do not inherently represent actual open circuit conditions, and indeed should be nonlinear near zero current. In fact, non-photovoltaic features such as purely semiconducting, conducting, or resistive regions will appear artificially weak or strong in quasi-V_{OC}* imaging, as in Supporting Information File 1, Figure S1 and [6] for current-shunting grain boundaries. Figure 2 and Figure 4 reveal a more consistent grain boundary response via the direct measurements. Therefore, although quasi-V_{OC}* mapping is simple and efficient, spurious contrast mechanisms can mask the actual local V_{OC} and corresponding statistical and correlative analyses with microstructure and/or other properties. These can only be best revealed by directly measuring V_{OC}*, or for even more sophisticated materials property maps by extension of the straightforward approach presented herein. For instance, with appropriate circuitry that multiplies the instantaneously applied bias and the detected photocurrent, the especially important maximum-power point for a solar cell could be directly imaged in 2D or even 3D in future work. This will only require the additional feedback loop constantly adjusting and recording the probe bias to maintain peak power instead of zero photocurrent.

Conclusion

A new AFM-based method for directly mapping the nanoscale open-circuit potential of photovoltaics is based on a secondary PID feedback loop configured to record local probe biases necessary to constantly maintain open-circuit (zero photocurrent) conditions. In addition to protecting the specimen and probe from high currents as in conventional I/V sweeps, the efficiency of this single-pass approach for direct V_{OC}* mapping is beneficial for measurements sensitive to ambient exposure, thermal drift, or multi-image investigations such as tomographic AFM. This is demonstrated in 2D and 3D with CdTe polycrystalline thin-film solar cells, and correlated with effective short-circuit photocurrent mapping. Grain boundaries are directly observed to possess low open-circuit voltages while grain bulks exhibit widely varying short-circuit currents including sub-granular planar features. Variations in these photovoltaic performance metrics are sometimes complementary but also can be uncorrelated, as uniquely observed by overlaying these signals. When considering their product, equivalent to the theoretical power, profound variations are detected at the nano- and micro-scale. Such novel SPM-based measurements can be crucial to advancing the fundamental understanding, and ultimately performance and reliability, of a wide range of photosensors, photoactivated catalysts, and photovoltaics.

Supporting Information

Supporting Information File 1

Additional experimental data.
[https://www.beilstein-journals.org/bjnano/content/supplementary/2190-4286-9-171-S1.pdf]

Acknowledgements

KA and BDH recognize the Institute of Materials Science for support. JL acknowledges support from the US Department of Energy, Office of Energy, Efficiency and Renewable Energy (EERE) Postdoctoral Research Awards under the SunShot Solar Energy Technologies Program.

ORCID® iDs

Katherine Atamanuk - https://orcid.org/0000-0002-0155-9557
Bryan D. Huey - https://orcid.org/0000-0002-1441-1180

References

1. Kutes, Y.; Aguirre, B. A.; Bosse, J. L.; Cruz-Campa, J. L.; Zubia, D.; Huey, B. D. *Prog. Photovoltaics* **2016,** *24,* 315–325. doi:10.1002/pip.2698
2. Leite, M. S.; Abasin, M.; Lezec, H. J.; Gianfrancesco, A.; Talin, A. A.; Zhitenev, N. B. *ACS Nano* **2014,** *8,* 11883–11890. doi:10.1021/nn5052585
3. Sadewasser, S.; Abou-Ras, D.; Azulay, D.; Baier, R.; Balberg, I.; Cahen, D.; Cohen, S.; Gartsman, K.; Ganesan, K.; Kavalakkatt, J.; Li, W.; Millo, O.; Rissom, T.; Rosenwaks, Y.; Schock, H. W.; Schwarzman, A.; Unold, T. *Thin Solid Films* **2011,** *519,* 7341–7346. doi:10.1016/j.tsf.2010.12.227
4. Celano, U.; Goux, L.; Belmonte, A.; Opsomer, K.; Franquet, A.; Schulze, A.; Detavernier, C.; Richard, O.; Bender, H.; Jurczak, M.; Vandervorst, W. *Nano Lett.* **2014,** *14,* 2401–2406. doi:10.1021/nl500049g
5. Schulze, A.; Hantschel, T.; Dathe, A.; Eyben, P.; Ke, X.; Vandervorst, W. *Nanotechnology* **2012,** *23,* 305707. doi:10.1088/0957-4484/23/30/305707
6. Luria, J.; Kutes, Y.; Moore, A.; Zhang, L.; Stach, E. A.; Huey, B. D. *Nat. Energy* **2016,** *1,* 16150. doi:10.1038/nenergy.2016.150
7. Kutes, Y.; Zhou, Y.; Bosse, J. L.; Steffes, J.; Padture, N. P.; Huey, B. D. *Nano Lett.* **2016,** *16,* 3434–3441. doi:10.1021/acs.nanolett.5b04157

8. Kutes, Y.; Luria, J.; Sun, Y.; Moore, A.; Aguirre, B. A.; Cruz-Campa, J. L.; Aindow, M.; Zubia, D.; Huey, B. D. *Nanotechnology* **2017,** *28,* 185705. doi:10.1088/1361-6528/aa67c2
9. Girish Kumar, S.; Koteswara Rao, K. S. R. *Energy Environ. Sci.* **2014,** *7,* 45–102. doi:10.1039/C3EE41981A
10. Li, H.; Liu, X. X.; Lin, Y. S.; Yang, B.; Du, Z. M. *Phys. Chem. Chem. Phys.* **2015,** *17,* 11150–11155. doi:10.1039/C5CP00564G
11. Al-Jassim, M. M.; Yan, Y.; Moutinho, H. R.; Romero, M. J.; Dhere, R. D.; Jones, K. M. *Thin Solid Films* **2001,** *387,* 246–250. doi:10.1016/S0040-6090(00)01707-7
12. Durose, K.; Boyle, D.; Abken, A.; Ottley, C.; Nollet, P.; Degrave, S.; Burgelman, M.; Wendt, R.; Beier, J.; Bonnet, D. *Phys. Status Solidi B* **2002,** *229,* 1055–1064.
13. Moseley, J.; Metzger, W. K.; Moutinho, H. R.; Paudel, N.; Guthrey, H. L.; Yan, Y.; Ahrenkiel, R. A.; Al-Jassim, M. M. *J. Appl. Phys.* **2015,** *118,* 025702. doi:10.1063/1.4926726
14. Poplawsky, J. D.; Paudel, N. R.; Li, C.; Parish, C. M.; Leonard, D.; Yan, Y.; Pennycook, S. J. *Adv. Energy Mater.* **2014,** *4,* 1400454. doi:10.1002/aenm.201400454
15. Visoly-Fisher, I.; Cohen, S. R.; Ruzin, A.; Cahen, D. *Adv. Mater.* **2004,** *16,* 879–883. doi:10.1002/adma.200306624
16. Ando, T.; Uchihashi, T.; Fukuma, T. *Prog. Surf. Sci.* **2008,** *83,* 337–437. doi:10.1016/j.progsurf.2008.09.001
17. Viani, M. B.; Schäffer, T. E.; Paloczi, G. T.; Pietrasanta, L. I.; Smith, B. L.; Thompson, J. B.; Richter, M.; Rief, M.; Gaub, H. E.; Plaxco, K. W.; Cleland, A. N.; Hansma, H. G.; Hansma, P. K. *Rev. Sci. Instrum.* **1999,** *70,* 4300–4303. doi:10.1063/1.1150069
18. Wahlquist, J. A.; DelRio, F. W.; Randolph, M. A.; Aziz, A. H.; Heveran, C. M.; Bryant, S. J.; Neu, C. P.; Ferguson, V. L. *Acta Biomater.* **2017,** *64,* 41–49. doi:10.1016/j.actbio.2017.10.003
19. Ahn, N.; Kwak, K.; Jang, M. S.; Yoon, H.; Lee, B. Y.; Lee, J.-K.; Pikhitsa, P. V.; Byun, J.; Choi, M. *Nat. Commun.* **2016,** *7,* 13422. doi:10.1038/ncomms13422
20. Kraft, A.; Labusch, L.; Ensslen, T.; Dürr, I.; Bartsch, J.; Glatthaar, M.; Glunz, S.; Reinecke, H. *IEEE J. Photovoltaics* **2015,** *5,* 736–743. doi:10.1109/JPHOTOV.2015.2395146
21. Badiee, A.; Ashcroft, I. A.; Wildman, R. D. *Int. J. Adhes. Adhes.* **2016,** *68,* 212–218. doi:10.1016/j.ijadhadh.2016.03.008
22. French, R. H.; Murray, M. P.; Lin, W.-C.; Shell, K. A.; Brown, S. A.; Schuetz, M. A.; Davis, R. J. Solar radiation durability of materials components and systems for Low Concentration Photovoltaic Systems. In *2011 IEEE Energytech, 2011,* Cleveland, OH, U.S.A., May 25–26, 2011; IEEE: Piscataway, NJ, U.S.A., 2011. doi:10.1109/EnergyTech.2011.5948501
23. Pern, F. J.; Czanderna, A. W. *Sol. Energy Mater. Sol. Cells* **1992,** *25,* 3–23. doi:10.1016/0927-0248(92)90013-F
24. Bergmann, V. W.; Weber, S. A. L.; Ramos, F. J.; Nazeeruddin, M. K.; Grätzel, M.; Li, D.; Domanski, A. L.; Lieberwirth, I.; Ahmad, S.; Berger, R. *Nat. Commun.* **2014,** *5,* 5001. doi:10.1038/ncomms6001
25. Bosse, J. L.; Huey, B. D. *Nanotechnology* **2014,** *25,* 155704. doi:10.1088/0957-4484/25/15/155704
26. Huey, B. D.; Kutes, Y.; Longacre, A.; Atamanuk, K.; Luria, J. *Mater. Today*, in press.
27. Visoly-Fisher, I.; Cohen, S. R.; Gartsman, K.; Ruzin, A.; Cahen, D. *Adv. Funct. Mater.* **2006,** *16,* 649–660. doi:10.1002/adfm.200500396
28. Li, J. B.; Chawla, V.; Clemens, B. M. *Adv. Mater.* **2012,** *24,* 720–723. doi:10.1002/adma.201103470
29. Galloway, S. A.; Edwards, P. R.; Durose, K. *Sol. Energy Mater. Sol. Cells* **1999,** *57,* 61–74. doi:10.1016/S0927-0248(98)00168-8
30. Green, M. A.; Zhao, J.; Wang, A.; Reece, P. J.; Gal, M. *Nature* **2001,** *412,* 805–808. doi:10.1038/35090539

License and Terms

This is an Open Access article under the terms of the Creative Commons Attribution License (http://creativecommons.org/licenses/by/4.0), which permits unrestricted use, distribution, and reproduction in any medium, provided the original work is properly cited.

The license is subject to the *Beilstein Journal of Nanotechnology* terms and conditions: (https://www.beilstein-journals.org/bjnano)

The definitive version of this article is the electronic one which can be found at: doi:10.3762/bjnano.9.171

BEILSTEIN JOURNAL OF NANOTECHNOLOGY

Know your full potential: Quantitative Kelvin probe force microscopy on nanoscale electrical devices

Amelie Axt[1,2], Ilka M. Hermes[1], Victor W. Bergmann[1], Niklas Tausendpfund[2] and Stefan A. L. Weber[*1,2]

Full Research Paper

Open Access

Address:
[1]Max-Planck-Institute for Polymer Research, Ackermannweg 10, 55128 Mainz, Germany and [2]Institute of Physics, Johannes Gutenberg University Mainz, 55099 Mainz, Germany

Email:
Stefan A. L. Weber[*] - webers@mpip-mainz.mpg.de

* Corresponding author

Keywords:
AM-KPFM; AM lift mode; AM off resonance; AM second eigenmode; cross section; crosstalk; field effect transistor; FM-KPFM; frequency modulation heterodyne; frequency modulation sideband; quantitative Kelvin probe force microscopy; solar cells

Beilstein J. Nanotechnol. **2018,** *9,* 1809–1819.
doi:10.3762/bjnano.9.172

Received: 05 January 2018
Accepted: 30 April 2018
Published: 15 June 2018

This article is part of the Thematic Series "Scanning probe microscopy for energy-related materials".

Associate Editor: U. D. Schwarz

© 2018 Axt et al.; licensee Beilstein-Institut.
License and terms: see end of document.

Abstract

In this study we investigate the influence of the operation method in Kelvin probe force microscopy (KPFM) on the measured potential distribution. KPFM is widely used to map the nanoscale potential distribution in operating devices, e.g., in thin film transistors or on cross sections of functional solar cells. Quantitative surface potential measurements are crucial for understanding the operation principles of functional nanostructures in these electronic devices. Nevertheless, KPFM is prone to certain imaging artifacts, such as crosstalk from topography or stray electric fields. Here, we compare different amplitude modulation (AM) and frequency modulation (FM) KPFM methods on a reference structure consisting of an interdigitated electrode array. This structure mimics the sample geometry in device measurements, e.g., on thin film transistors or on solar cell cross sections. In particular, we investigate how quantitative different KPFM methods can measure a predefined externally applied voltage difference between the electrodes. We found that generally, FM-KPFM methods provide more quantitative results that are less affected by the presence of stray electric fields compared to AM-KPFM methods.

Introduction

In this study, we compare the most commonly used amplitude modulation (AM) and frequency modulation (FM) Kelvin probe force microscopy (KPFM) methods under ambient conditions to investigate how these methods can measure quantitative variations in the local contact potential difference (CPD). KPFM is a scanning force microsopcy (SFM) method that correlates the local electric potential landscape with local topographic information. Thus, KPFM is ideally suited to characterize of a variety of nanostructured semiconducting systems such as electronic devices [1] and solar cells [2].

To understand and improve the charge carrier generation and extraction within a solar cell, the local potential distribution needs to be correlated to the constituent layers of the cell. Therefore, a high lateral resolution together with a reliable quantification of the local potential is required. In the past, KPFM measurements have frequently been used to image potential distributions on cross sections of a range of different solar cell devices, including organic [3-5], and inorganic [6] as well as hybrid perovskite solar cells [7-15].

In the course of one of our KPFM studies on a cross section of a perovskite solar cell under operating conditions [7] we observed fundamental differences in the potential distribution when using FM sideband KPFM as compared to AM lift mode KPFM (Figure 1). The cell was under short circuit conditions and could be illuminated with a white light source from the side. Further details on the solar cell, the sample preparation and experimental setup are given in the figure caption and in [7].

The FM- and AM-KPFM data was collected in subsequent measurements with the same cantilever on the same solar cell cross section. However, the resolved potential distributions differed significantly. In dark, the potential drop from FTO to gold measured with FM-KPFM was around −0.55 V, while the potential difference between the electrodes detected with AM-KPFM was only −0.25 V. Furthermore, the absolute potential detected in AM-KPFM had an offset of +1 V. The most fundamental difference in the potential distributions imaged in FM- and AM-KPFM could be observed upon illuminating the sample. While FM-KPFM resolved a +0.35 V increase of the potential within the methylammonium lead iodide (MAPI) capping layer as well as a narrow local minimum featured at the interface of the compact and the mesoscopic TiO_2 layer, AM-KPFM detected only a slightly higher potential in the mesoscopic TiO_2 and the MAPI capping layer. The illumination-induced potential difference resolved by AM-KPFM was less than 50 mV and no local features could be observed. Thus, only using AM lift mode, we likely would have missed the illumination induced changes in the potential distribution, which we assigned to unbalanced charge extraction from the perovskite layer. The absence of local features in the potential distribution imaged with AM lift mode KPFM, the potential offset of +1 V, as well as the reduced potential increase upon illumination suggested that the spatial and quantitative resolution of AM lift mode KPFM was not sufficient to characterize the potential distribution within the solar cell.

For future studies it is therefore important to know the limitations of different KPFM techniques to characterize samples most efficiently by choosing an appropriate operation mode. Since the invention of KPFM, a vast number of studies have investigated differences in lateral and voltage resolution of AM and FM methods. Polak et al. have investigated, how AC coupling between excitation and cantilever deflection signal affects the measured potentials in AM-KPFM [16]. Generally, FM-KPFM is less affected by AC crosstalk artefacts, as excitation and detection are performed at different frequencies. Other influences that have been investigated were the cantilever orientation with respect to a structured sample [17], the tip–sample

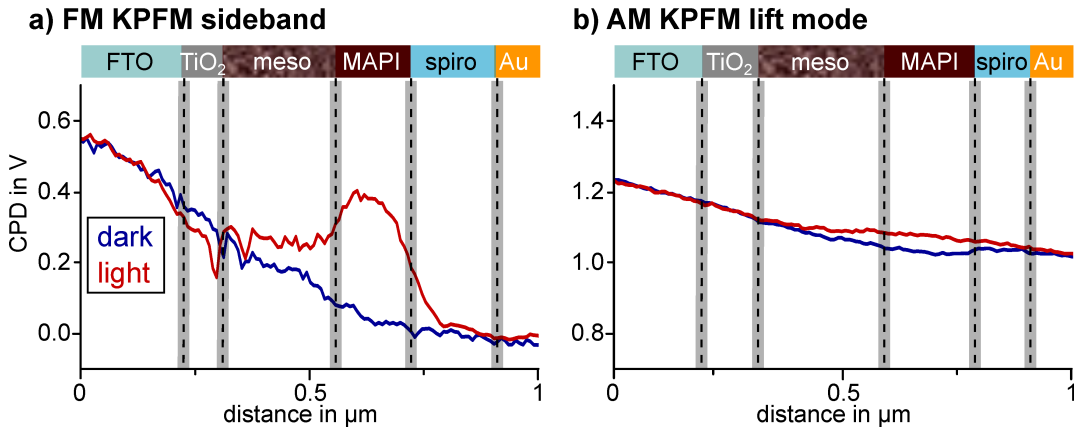


Figure 1: CPD line profiles of two KPFM experiments on the same cross section of a mesoscopic perovskite solar cell under short circuit conditions with and without illumination, visualized by the red and blue line, respectively. The cell consisted of a fluorine-doped tin oxide (FTO) electrode, a compact TiO_2 electron extraction layer and a mesoscopic TiO_2 layer (meso) filled with the perovskite light-absorber methylammonium lead iodide (MAPI). The mesoscopic layer was followed by a compact MAPI capping layer, the hole transport material spiro-OMETAD and a gold electrode. Prior to the measurement the cross section of the solar cell was polished with a focused ion beam (FIB) to minimize topographic crosstalk. The CPD line profiles in a) were extracted from double side band frequency modulation KPFM (FM sideband) scans in single pass with VAC of 3 V [7]. The CPD line profiles in b) were extracted from amplitude modulation KPFM (AM lift mode) scans in lift mode with a tip–sample distance of 10 nm, an oscillation amplitude of ≈80 nm and a tip voltage U_{AC} of 1 V. Each line profile is an average of three adjacent scan lines.

distance [17-20], topographic or capacitive cross talk [19,21,22] and the choice of frequencies. All in all, an overwhelming number of studies have reported a superior lateral resolution, both laterally and in voltage, for FM-KPFM [18,19,23-26]. Li et al. [19] also reported a higher sensitivity for the potential detection.

Until now, most studies comparing AM- to FM-KPFM methods have used samples exhibiting a work function contrast [23,24,27]. For example, Zerweck et al. have observed a superior spatial and quantitative resolution of FM-KPFM as compared to AM-KPFM on a gold and potassium chloride interface in ultra-high vacuum [23]. However, such measurements are difficult to interpret as it is unclear what the expected workfunction contrast is. This is particularly important for measurements under ambient conditions, where adsorption layers can distort the CPD contrast [28].

In our study we follow an idea by Ziegler et al., who investigated the potential resolution of lift mode AM- and FM-KPFM in air [18]. The authors used a microscopic electrode that was set on a defined external bias. Furthermore, the influence of stray electric fields on the measured potential was investigated by varying the background voltage on the silicon substrate. Here, we use an array of micron-scale interdigitated electrodes on glas with a defined potential difference applied between neighboring electrodes. By investigating the pre-defined potential difference between the electrodes, a possible influence of tip- or sample contamination can be minimized. We furthermore investigate the influence of stray electric fields by adding a metal electrode underneath the sample.

The goal of this work is to complement the previous comparative KPFM studies by a comprehensive investigation on the reliability of the potential mapping of five common KPFM techniques under ambient conditions. We compare AM-KPFM in lift mode, on the second eigenmode and off resonance, as well as FM-KPFM with double sideband detection and heterodyne FM-KPFM.

Theory

KPFM [29] utilizes a conductive SFM tip as Kelvin probe [30] to map electrical surface potential variations on a nanometer scale [31]. To quantify the potential difference between the tip and a sample, the electrostatic field is enhanced by additionally applying a voltage between tip and sample. In electrostatic force microscopy [32], an alternating voltage U_{AC} is applied and the response tracked by means of a lock-in amplifier. Thereby, two different detection methods can be used: The amplitude modulation (AM) mode tracks variations in the response amplitude, whereas frequency modulation (FM) mode tracks variations in the cantilever's resonance frequency, e.g., via the phase lag between excitation and response. By applying an additional DC voltage U_{DC} to the tip, the electrostatic force is minimized if $U_{DC} = U_{CPD}$, where U_{CPD} is the contact potential difference between the tip and the sample. This is the basic operation principle of KPFM [31]. This section will introduce the operation principles of the AM- and FM-KPFM detection modes and discuss possible benefits and drawbacks.

Generally, U_{CPD} describes the difference in the Fermi levels

$$U_{CPD} = \left(\varepsilon_{\mathrm{F}}^{\mathrm{tip}} - \varepsilon_{\mathrm{F}}^{\mathrm{sample}}\right)\Big/ e$$

of tip and sample (e: elemental charge), which also contains information about an externally applied bias [18], static charges [27] , or local electronic excitations [33]. In equilibrium, U_{CPD} corresponds to the difference in work functions of the tip and the sample material.

We can calculate the electrostatic force on a SFM tip by considering the capacitance C of the gap between cantilever/tip and the sample. From the capacitor's energy $W = 1/2\ C\ (\Delta U)^2$, we can derive the electrostatic force as

$$F_{\mathrm{E}} = \frac{1}{2}\frac{\partial C}{\partial z}\cdot\left(\Delta U\right)^2, \tag{1}$$

with the tip–sample distance z and the potential difference between the tip and the sample $\Delta U = U_{ext} - U_{CPD}$. Here, U_{ext} is the sum of all externally applied voltages to tip or sample. If we keep the sample grounded and apply an external voltage to the tip with both an alternating AC voltage and a constant bias in the form $U_{ext} = U_{DC} + U_{AC}\sin(\omega_E t)$, the resulting electrostatic force can be divided into one static and two dynamic spectral components [34]:

$$F_{\mathrm{stat.}} = \frac{1}{2}\frac{\partial C}{\partial z}\left(\left(U_{\mathrm{DC}} - U_{\mathrm{CPD}}\right)^2 + \frac{U_{\mathrm{AC}}^2}{2}\right) \tag{2}$$

$$F_{\omega_{\mathrm{E}}} = \frac{\partial C}{\partial z}\left(U_{\mathrm{DC}} - U_{\mathrm{CPD}}\right)U_{\mathrm{AC}}\sin\left(\omega_{\mathrm{E}} t\right) \tag{3}$$

$$F_{2\omega_{\mathrm{E}}} = -\frac{1}{4}\frac{\partial C}{\partial z}U_{\mathrm{AC}}^2\cos\left(2\omega_{\mathrm{E}} t\right) \tag{4}$$

Equation 3 is the fundamental equation describing AM-KPFM: When $U_{DC} = U_{CPD}$, the amplitude of the response at the angular frequency ω_E vanishes. In AM-KPFM, a feedback loop that

minimizes the response amplitude by adjusting U_{DC}. AM detection is ususally more prone to artifacts such cross coupling of the AC drive signal, e.g., into the shaker piezo [21]. Furthermore, Equation 3 shows that the amplitude of the electrostatic force is proportional to the gradient in capacitance. Colchero et al. have shown that for most common tip/cantilever geometries the large surface area of the tip cone and the cantilever yields a significant contribution to the gradient in capacitance, even at tip–sample distances of only a few nanometers [20]. This so-called stray capacitance [35] can decrease the lateral resolution by averaging the surface potential over a larger area.

To reduce the effect of the long-ranged electrostatic interaction of the cantilever, force gradient detection can be used [18,20,23]. The presence of a tip–sample force field $F_{ts}(z)$ causes a shift in the angular resonance frequency ω_0 of the cantilever. For small oscillation amplitudes, the modified angular resonance frequency ω_0' can approximately be described by means of an effective spring constant

$$k_{\text{eff}} = k - \frac{\partial F_{\text{ts}}}{\partial z},$$

where k is the undisturbed spring constant of the cantilever:

$$\omega_0' \approx \sqrt{\frac{1}{m}\left(k - \frac{\partial F_{\text{ts}}}{\partial z}\right)} \tag{5}$$

Thus, an alternating voltage U_{AC} not only causes periodic fluctuations in the electrostatic force (Equation 3), but also in the resonance frequency. The magnitude of this frequency modulation is proportional to the electrostatic force gradient and thereby to the second derivative $\partial^2 C/\partial z^2 = C''$ of the capacitance. Thus, FM detection is more sensitive to the electrostatic interaction of the tip apex with the sample surface [20].

Originally, the peroiodic oscillations in Δf were directly detected by means of a phased-locked loop in non-contact AFM under ultrahigh vacuum conditions. An elegant way of detecting the electrostatic frequency modulation is to use non-linear frequency mixing with a mechanical cantilever oscillation at angular frequency ω_m, such as the tapping oscillation used for the height feedback [36]. As the capacitance gradient monotonically decreases away from the surface, it will also oscillate with frequency ω_m. Thus, the capacitance gradient can be written as a Fourier series

$$\frac{\partial C}{\partial z}(t) = C'(z) = \frac{a_0}{2} + \sum_{n=1}^{\infty} a_n \cos(n\omega_m t),$$

and the electrostatic force (Equation 1) can be written as:

$$\begin{aligned} F_E = &\left[\sum_{n=0}^{\infty} a_n \cos(n\omega_m t)\right]\cdot\left(\frac{1}{2}(U_{DC}-U_{CPD})^2 + \frac{U_{AC}^2}{2}\right) \\ &+\left[\sum_{n=0}^{\infty} a_n \cos(n\omega_m t)\right]\cdot(U_{DC}-U_{CPD})U_{AC}\sin(\omega_E t) \\ &-\left[\sum_{n=0}^{\infty} a_n \cos(n\omega_m t)\right]\cdot\frac{1}{4}\cdot U_{AC}^2\cos(2\omega_E t) \end{aligned} \tag{6}$$

By only considering Fourier coefficients up to $n = 1$, we can again calculate and separate different spectral components of the electrostatic force:

$$F_{\omega_E} = \frac{a_0}{2}(U_{DC}-U_{CPD})U_{AC}\cdot\sin(\omega_E t) \tag{7}$$

$$F_{2\omega_E} = \frac{a_0}{8}U_{AC}^2\cdot\cos(2\omega_E t) \tag{8}$$

$$\begin{aligned} F_{\omega_m\pm\omega_E} = &\frac{1}{2}a_1(U_{DC}-U_{CPD})U_{AC} \\ &\cdot\left[\sin((\omega_E-\omega_m)t)+\sin((\omega_E+\omega_m)t)\right] \end{aligned} \tag{9}$$

$$\begin{aligned} F_{\omega_m\pm2\omega_E} = &-\frac{1}{8}a_1U_{AC}^2 \\ &\cdot\left[\cos(t(2\omega_E-\omega_m))+\cos(t(2\omega_E+\omega_m))\right] \end{aligned} \tag{10}$$

Equation 7 and Equation 8 are equivalent to the AM-KPFM-equations Equation 3 and Equation 4. We can find the connection between the Fourier coefficient and the capacitance gradient as $a_0 = 2C'$ (See Supporting Information File 1 for a formal proof). Equation 9 and Equation 10 show that electrostatic signals can also be detected at the sidebands $F_{\omega_m\pm\omega_E}$ and $F_{\omega_m\pm2\omega_E}$ of the mechanical oscillation at ω_m. In particular, Equation 9 also contains a factor $(U_{DC} - U_{CPD})$ in analogy to Equation 7. This is the fundamental equation describing FM-KPFM. In the Appendix we show that the Fourier coefficient a_1 is proportional to the mechanical oscillation amplitude and to C''.

As C'' is more sensitive to local tip–apex/sample interactions [20], FM-KPFM usually leads to a superior lateral and voltage resolution [18,19,23-26]. On the other hand, the force signal is usually much stronger than the force gradient signal. Thus, higher electrical drive amplitudes are usually required for FM-KPFM that can cause other problems, such as band bending [37].

Methods

An overview and simplified representation of all the KPFM methods used in this study are given in figure Figure 2. AM-KPFM is the most commonly used method on most commercial scanning probe microscopy systems, mainly due to its easy implementation. Nevertheless, there are different ways to operate AM-KPFM. In the simplest form, an AC voltage is applied during normal tapping mode imaging (single scan) at a frequency far below the first resonance $\omega_E << \omega_0$. We refer to this mode as AM-KPFM off resonance (AM off res). This mode is implemented on older AFM systems, where the auxiliary lock-ins were limited in terms of the maximum frequency they could measure. The biggest drawback of this method is the lower signal-to-noise ratio (SNR) resulting from the off-resonance detection. The SNR can be improved by choosing an ω_E at one of the cantilever's eigenmodes. We refer to this mode as AM-KPFM second eigenmode (AM 2 EM), where the topography is measured at the first, and the CPD is measured on the second eigenmode. Finally, in AM-KPFM lift mode (AM Lift mode) the topography and CPD measurements are decoupled: In a first step, a topographic contour line is recorded in tapping mode. In a second step, the mechanical excitation is switched off and the tip follows the same contour line shifted in *z*-direction by a defined lift height, typically 10–100 nm above the sample. AM-KPFM in lift mode has the advantage that in theory the electrostatic response is completely decoupled from any other short-ranged forces that act on the tip during the tapping motion. Furthermore, detecting at the first eigenmode results in an improved SNR. At the same time, the larger tip–sample distance reduces the lateral resolution and the image acquisition time is a factor of two longer, since every line needs to be scanned twice.

In FM-KPFM, the force gradient-sensitive sidebands introduced in Equation 9 are used to measure the CPD. In the mode that we refer to as FM Sideband KPFM, the frequency of electrical excitation is lower than the first resonance $\omega_E << \omega_0$ while the detection is performed at $\omega_m \pm \omega_E$ with the mechanical oscillation frequency ω_m at the first resonance. To decouple the detection of the sidebands from the mechanical carrier signal, ω_m should be sufficiently high. Nevertheless, choosing ω_m too high shifts the sidebands further away from the resonance frequency, decreasing the SNR. Thus, FM sideband KPFM typically has to be performed at higher AC voltages and/or at low detection bandwidths, limiting the speed of the measurement. In FM Heterodyne KPFM [26,38], the electrical excitation is performed at $\omega_E = \omega_1 - \omega_0$, which shifts the sideband frequency to the second eigenmode at ω_1. Here, the big advantage is that resonance amplifies the response without limiting the detection bandwidth, providing an improved SNR and faster imaging speeds [26].

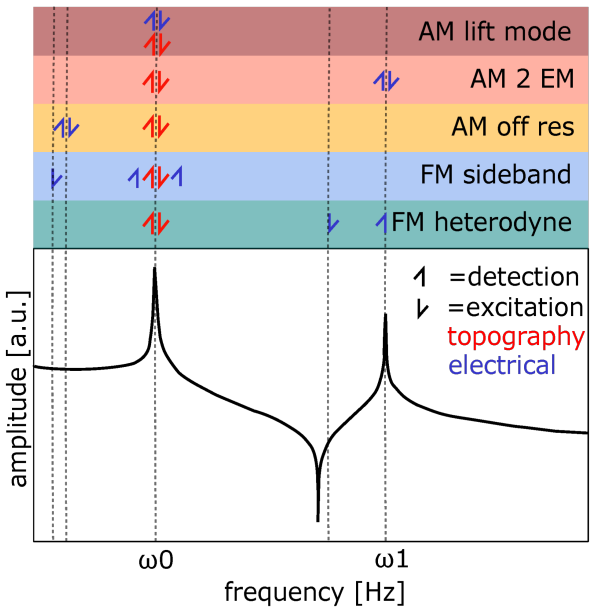


Figure 2: Overview of excitation and detection frequencies for KPFM methods used in this work. The lower part shows the transfer function of the cantilever, amplitude plotted vs frequency. The upper part shows excitation (arrow upwards) and detection (arrow downwards) for the corresponding methods with the respective frequencies. Red color is used for the topography signal and blue for the electrical excitation and detection. The color code in the upper part corresponds to plots in the results. Representation inspired by [26].

Experimental

We used an Asylum research MFP3D SFM in a nitrogen glovebox (level of humidity below 1%) for all experiments. The typical resonance frequency of the cantilevers (Bruker Model:SCM-PIT-V2) was ≈75 kHz, spring constant of 3 N/m, a tip radius of 25 nm and a tip height of 10 to 15 µm. The typical length of the cantilevers was ≈225 µm, the width ≈35 µm. Tip, tip cone and cantilever are coated with PtIr (work function 5.5 eV [39]) on both sides. The topography feedback was performed with amplitude modulation (AM) on the first eigenmode and the oscillation amplitude was kept to approximately 40 nm for all methods. To perform the KPFM feedback, we used a Zurich Instruments HF2LI for all methods except for AM liftmode, where we used the implementation of the Asylum system (NAP mode). On the Asylum system, the CPD signal recorded during the nap scan is applied to the tip during the topography scan. Thereby, electrostatic tip–sample interaction is minimized (Feed-forward compensation [40]). The lift height was set to 10 nm. As we show in the wiring scheme (Figure S14 and Figure S15, Supporting Information File 1) U_{DC} is applied to the tip. We connected the cantilever chip with an external wire to minimizie electrical crosstalk like reported by Polak et al. [16]. The parameters of the measurements can be found in Table 1. The feedback was optimized for $V_P^{ext} = 0.5$ V. The test

Table 1: Overview of methods and parameters, topography carrier in all cases is the first eigenmode of the cantilever $\omega_t = \omega_0$. ω_1 represents the second eigenmode of the cantilever.

Method	electrical excitation	electrical detection	feedback	U_{AC}
AM Lift Mode	$\omega_E = \omega_0$	ω_0	$X(\omega_0) = \min$	1 V
AM 2 EM	$\omega_E = \omega_1$	ω_1	$X(\omega_1) = \min$	1 V
AM Off Res	$\omega_0 >> \omega_E$ = 10 kHz	ω_E	$X(\omega_E) = \min$	1 V
FM Sideband	$\omega_0 >> \omega_E$ = 1.5 kHz	$\omega_0 \pm \omega_E$	$X(\omega_0 + \omega_E) - X(\omega_0 - \omega_E)$	2 V
FM Heterodyne	$\omega_E = \omega_1 - \omega_0$	ω_1	$X(\omega_1) = \min$	1 V

structure was based on an interdigitated electrode array (IDA-Pt 2 µm by ALS, Japan). The pitch of the 90 nm thick platinum electrodes is 4 µm, the width of the electrodes is 2 µm and the length 2 mm. The electrode array consists of 65 pairs of electrodes. According to ALS-Japan the electrodes are made of pure platinum with a work function of 5.7 eV [41]. The electrodes are embedded into the glass substrate and therefore offer a low resistance while keeping the topography variations below ≈50 nm, minimizing the effect of topographic cross talk. To further eliminate the influence of variations in the work function between the electrodes and on the tip, we applied a defined voltage between the electrodes and only considered the potential difference between neighboring electrodes. Thus, the measured potential difference is not influenced by contamination of the surface, the tip or local changes in the materials. To minimize the influence of potential variations along the electrodes we furthermore disabled the slow scan axis during the measurements. To study the effect of stray fields, aluminum foil was placed under the substrate of the electrode array, where we could apply an external voltage of 200 V. To show that KPFM operates in a linear regime (Equation 19) we recorded bias spectroscopy sweeps prior to every measurement (Figure S1 and Figure S2, Supporting Information File 1).

Results and Discussion

We performed the first measurement in the center of the electrode structure (Figure 3) at a position, where the entire length of the cantilever was positioned over the electrode array. The cantilever was placed perpendicular to the electode stripes. This arrangement mimics both the stray field and the potential distribution of flat electronic devices like field effect transistors. Every second electrode on the interdigitated array was grounded (Figure 3) $V_G^{ext} = 0$ V, while on the other electrodes the external potential V_P^{ext} was varied from −3 V to 3 V. Ideally, the KPFM would measure the full potential difference between neighboring electrodes $V_{diff}^{ext} = V_P^{ext} - V_G^{ext}$. To visualize deviations form this ideal outcome, we plotted the deviation of the measured voltage $V_{diff}^{CPD} = V_P^{CPD} - V_G^{CPD}$ from the externally applied voltage $\Delta V = V_{diff}^{ext} - V_{diff}^{CPD}$ as function of V_P^{ext} (Figure 4). Examples for crossectional potential of the interdigitated electrode array can be found in Figure S3, Figure S4,

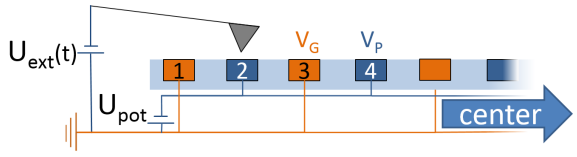


Figure 3: Sketch of the setup as well as marking scheme of electrodes on the edge. U_{ext} represents the electrical excitation applied to the cantilever, U_{pot} the potential applied to the electrodes.

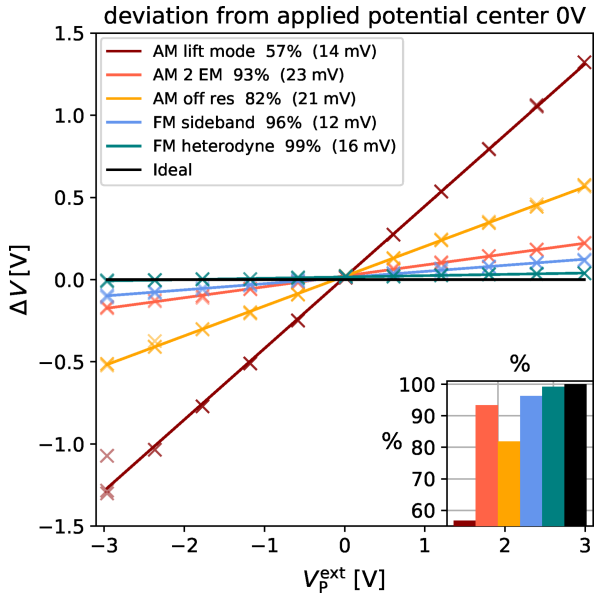


Figure 4: Comparison of the deviation of the measured potential difference from the applied potential plotted against the applied potential for AM (warm colors) and FM (cool colors), black represents an ideal measurement. Inset in the lower right visualizes the fraction of the potential captured by the respective method. Legend in the upper left shows the offset in brackets. Data shown captured in the middle of the electrode structure without an additional electrostatic force.

Figure S5 in Supporting Information File 1. Displayed in black is an ideal curve together with the potentials measured with the three AM-KPFM methods (red, orange and yellow) and the two FM-KPFM methods (blue and turquoise). Any positive slope in these graphs indicates that the measured potential was lower than V_{diff}^{ext}. To which fraction the external voltage was captured

is shown in the inset on the lower right of Figure 4. The offset in the brackets of the legend indicate the offset of the fit.

For the FM Heterodyne KPFM measurement, 99% of the potential difference was captured, which is the closest to the ideal measurement in this set of experiments. With FM Sideband KPFM 96% of the potential difference was captured. AM-KPFM on the second eigenmode captured 87% of the potential difference, which is the most accurate measurement obtained with AM-KPFM. This matches the expectation since this method utilizes the resonance enhancement. AM off resonance captured 82% of the potential difference, while AM lift mode only captured 57% of the potential difference. The huge deviation of AM lift mode could be caused by averaging. Lifting the tip up increases the contribution of the cantilever to the electrostatic force [20]. The large surface area of the cantilever leads to an averaging of the surface potential and therefore the measured potential difference is lower. The small vertical offsets in the fits could be caused by a small offset in the voltage source or by electrostatic cross talk (see discussion later in the manuscript). Nevertheless, with values <20 mV, these offsets are on the order of the experimental error.

The next measurement was performed close to edge of the model electrode structure at a position, where the entire length of the cantilever was over the glas substrate. This geometry is chosen to mimic the experimental situation when measuring on a device cross section. In this geometry, the cantilever is interacting with an insulating surface instead of the electrode structure. Due to this break in symmetry, we observed different results for the first two electrodes (Figure 5 left) as compared to following two electrodes (Figure 5 right).

As in the measurement in the center of the structure, the FM-KPFM methods captured more than 95% of the potential difference. The AM-KPFM modes showed a slightly better performance with AM lift mode capturing 68% of the potential difference. Nevertheless, we noted that the AM 2 EM and AM lift mode curves were vertically shifted by +56 mV and −95 mV, respectively (vertical offsets are given in brackets in the figure legends). The offsets observed with the other KPFM modes and in all measurements at the center of the device were within the experimental error. The offsets measured on the first two electrodes were larger than the offsets on the following two electrodes (Figure 5 right). The observation that this offset only appeared in AM-KPFM modes and that it was stronger closer to the edge of the structure suggests that an additional electrostatic force from the insulating substrate (i.e., a stray field) was acting on the cantilever. This electrostatic force can for example arise from static charges on the glass surface [6].

To test the hypothesis of stray fields causing the offsets, we induced an artificial stray field by placing the substrate on a piece of aluminum foil and applying a voltage of 200 V with respect to the grounded electrode. We then repeated the experiments in the center and at the edge of the electrode structure. The measurement in the center of the electrode structure did not show significant changes compared to the measurement without stray

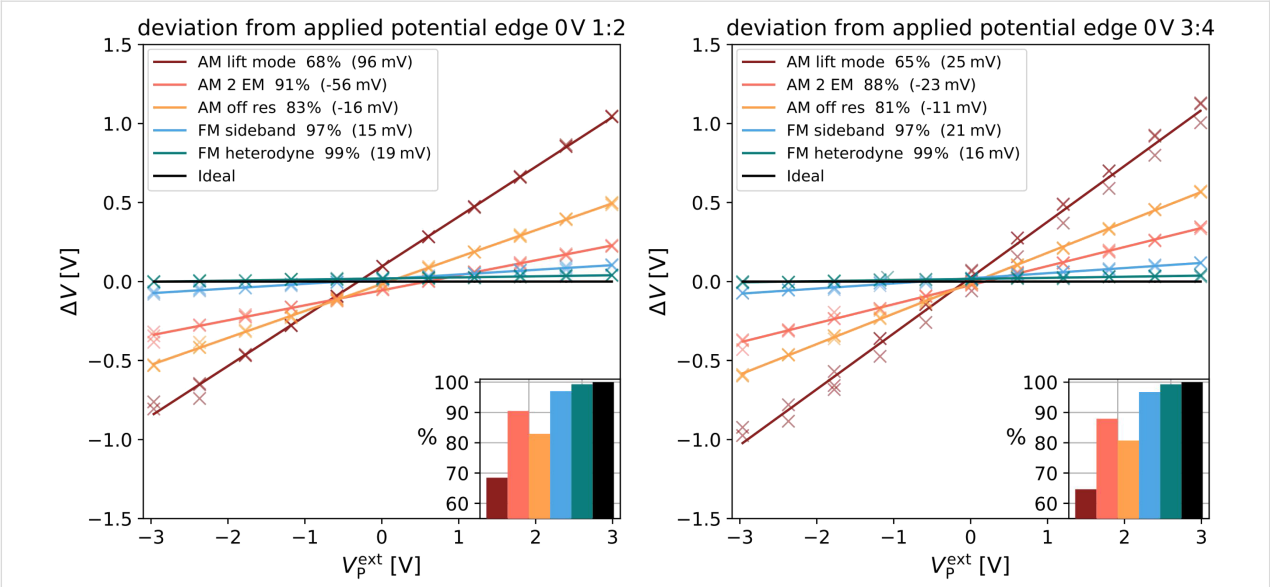


Figure 5: Comparison of the deviation of the measured potential difference from the applied potential plotted against the applied potential for AM (warm colors) and FM (cool colors), black represents an ideal measurement. Insert in the lower right visualizes the fraction of the potential captured by the respective method. Legend in the upper left shows the offset in brackets. Data shown captured on the electrodes 1/2 (left) and 3/4 (right) of the electrode structure without an additional electrostatic force.

field (not shown). However, the measurements at the edge of the electrode showed significant deviations (electrode 1/2: Figure 6 (left) and electrode 3/4: Figure 6 (right)). Whereas the FM modes still measured more than 97% of the applied potential with offsets of less than 25 mV, the AM measurements showed large deviations with offsets of up to 706 mV (AM lift mode). The offsets decreased, e.g., to to 500 mV in AM lift mode, on the next two electrodes 3/4 (Figure 6 (right)).

Since a grounded reference structure is not always available or the work function of the structures is of interest, we investigated the absolute value of the measured potential, as well. The absolute measured potential on the biased electrode is plotted against the applied potential and shown for the most extreme cases: in the center of the structure and on the outer most electrodes. In the center of the structure and in the absence of a stray field, the CPD varied from −220 mV to −148 mV (Figure 7 (left)). Such variations can be due to local changes in the CPD caused by contamination of the tip or variations in the surface as well as remaining charges in the substrate surrounding the electrodes.

On the edge of the electrode structure, the measured CPD increased to up to 840 mV (Figure 7 (right)). These significant deviations are most likely enhanced by stray fields from the glass substrate. In the presence of the artificial stray field caused by the aluminum electrode underneath the substrate, the measured CPD further increased to up to 4.7 V (AM lift mode, Figure 8). Generally, the offsets in CPD were much higher in the AM-KPFM modes compared to the FM-KPFM modes, where the maximum deviation was 250 mV (FM Heterodyne). It is interesting to note that methods operating on the first eigenmode or at frequencies below exhibited a positive offset while for the detection on the second eigenmode, the offset was negative. This could be connected to the way the different motion patterns of the cantilevers fundamental and second eigenmode interact with the substrate [42]. Thereby, a position-dependent sensitivity to stray fields along the cantilever could lead to a changed overall response, depending on which eigenmode is used for the electrostatic detection. The origin of this effect could be elucidated by numerical simulations, which is beyond the scope of this work.

Conclusion

Our results show that generally, FM-KPFM methods provide more quantitative and reliable results. For all experiments, FM-KPFM measured more than 96% of the externally applied potential difference, even in the presence of a strong stray electric field. Due to the stronger contribution of the cantilever on the measured surface potentials in AM-KPFM, the exposure of the cantilever to a stray electric field had a strong impact both on the potential difference and on the absolute potential.

With these new results, we now understand the differences in the potential distributions on the perovskite solar cell cross section that we presented in the introduction: The lower contrast

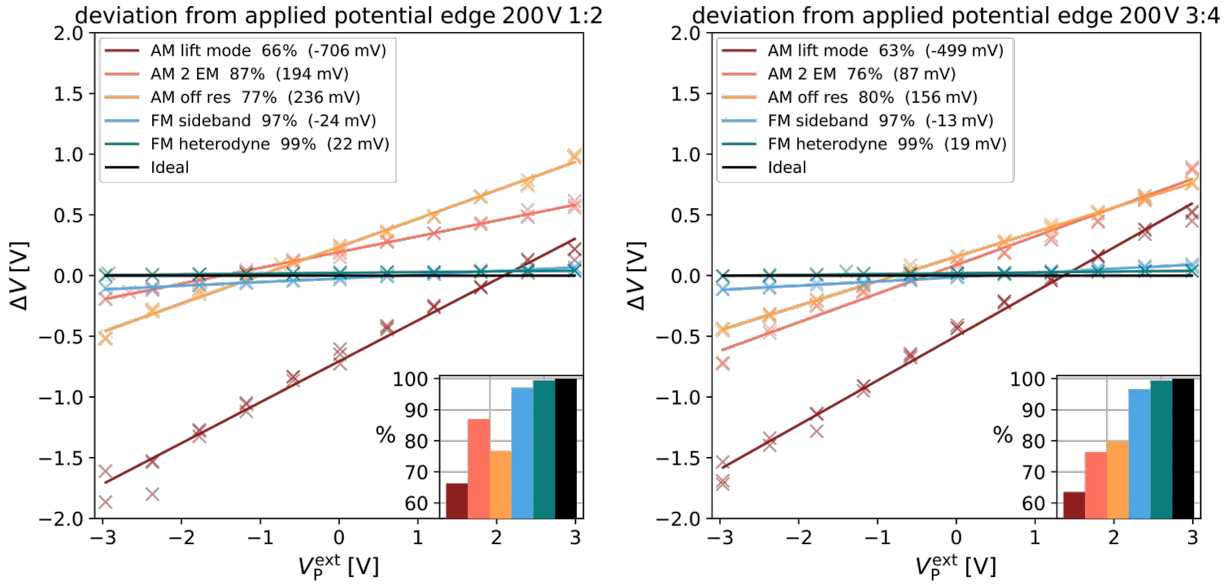


Figure 6: Comparison of the deviation of the measured potential difference from the applied potential plotted against the applied potential for AM (warm colors) and FM (cool colors), black represents an ideal measurement. Insert in the lower right visualizes the fraction of the potential captured by the respective method. Legend in the upper left shows the offset in brackets. Data shown captured on the electrodes 1/2 (left) and 3/4 (right) of the electrode structure with an additional electrostatic force.

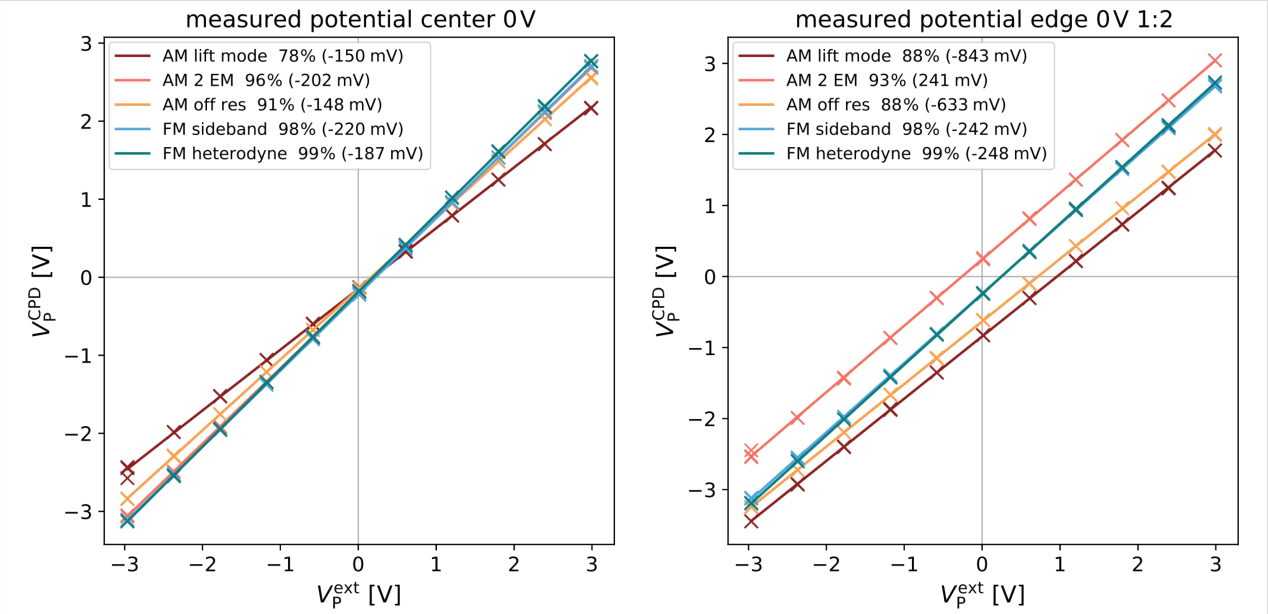


Figure 7: Comparison of the absolute measured potential plotted against the applied potential for AM (warm colors) and FM (cool colors). Legend in the upper left shows the measured CPD at 0 V applied voltage in brackets. Data shown captured in the middle of the electrode structure (left) and on the outer most electrodes (1/2) (right) without an additional electrostatic force.

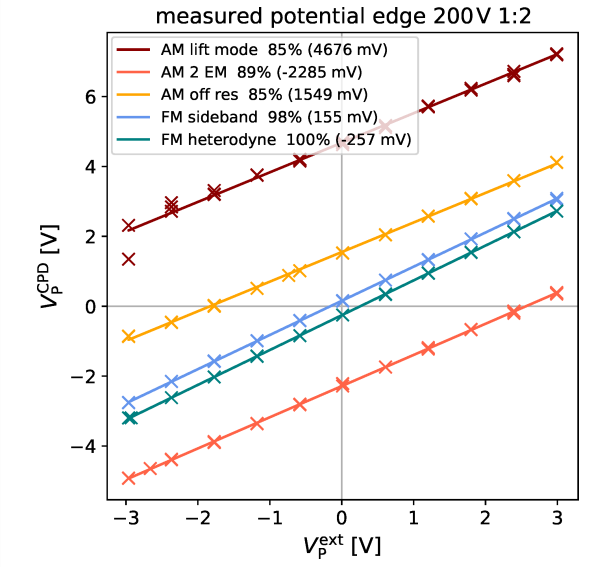


Figure 8: Comparison of the absolute measured potential plotted against the applied potential for AM(warm colors) and FM(cool colors). Legend in the upper left shows the measured CPD at 0 V applied voltage. Data shown captured on the outer most electrodes (1/2) of the electrode structure with an additional electrostatic force.

in the lift mode AM-KPFM image and the shift in the absolute potential as compared to the FM sideband KPFM measurement can be explained by the stronger lateral averaging of the AM-KPFM in lift mode and the presence of a stray electric field. Such a field could originate from gallium ions deposited into the glass substrate during the focused ion beam polishing of the cross section.

Our general recommendation for quantitative device measurements is therefore to use FM-KPFM methods, not only because they gave the most accurate relative potential values but also more reliable absolute potential values. In our study, FM heterodyne KPFM [26] had the best performance, capturing 99% of the potential difference in all measurements even in the presence of strong stray fields. In addition, FM heterodyne measurements can be performed at higher detection bandwidth compared to FM sideband measurements, making the method much faster. If limited to AM methods, we recommend using resonance enhanced detection, such as AM-KPFM on the second eigenmode. AM lift mode, however, is not recommended, since it was the least quantitative method and was most strongly affected by stray electric fields. In any case, when using AM-KPFM, it is crucial to reduce the impact of stray fields and electrostatics e.g. by using a ionizing air blower. These considerations are crucial for reliable quantitative and reproducible device measurements.

Appendix

Connection between sideband amplitudes and force gradient

The Fourier coefficients a_n for the capacitance gradient $\frac{\partial C}{\partial z} = C'$ can be written as

$$a_n = \frac{2}{T_\mathrm{m}} \int_{-T/2}^{+T/2} C'(t) \cos(n\omega_\mathrm{m} t)\,\mathrm{d}t \qquad (11)$$

with the oscillation period $T_m = 2\omega/\omega_m$. Please note that we can use only a cosine term when we phase-shift $z(t)$ in a way that it is symmetric around $t = 0$. Equation 11 is valid for any periodic $z(t)$, so it is also valid for a distorted cantilever motion when the tip is interacting with the surface.

To find the connection between the Fourier coefficients and higher order capacitance derivatives, we can additionally expand C' in a Taylor series around $z_0 = 0$

$$C'(z) = \sum_{k=0}^{\infty} \left.\frac{\partial^k C'(z)}{\partial z^k}\right|_{z=0} \frac{z^k}{k!} \tag{12}$$

By combining the Taylor expansion until $k = 1$ with Equation 11, we can calculate the first Fourier coefficients as:

$$a_0 = \frac{2}{T_m}\left[C'(0)\int_{-T/2}^{+T/2} \mathrm{d}t + C''(0)\int_{-T/2}^{+T/2} z(t)\,\mathrm{d}t + O\left(z^2\right)\right] \tag{13}$$

$$= 2C' \tag{14}$$

The second addend in Equation 13 becomes zero because $z(t)$ is symmetric around $t = 0$. This proves that the AM-KPFM Equation 3 is equivalent to Equation 9. For the second Fourier coefficient we get:

$$a_1 = \frac{2}{T_m}\left[\begin{array}{l} C'(0)\displaystyle\int_{-T/2}^{+T/2} \cos(\omega_m t)\,\mathrm{d}t \\ +C''(0)\displaystyle\int_{-T/2}^{+T/2} z(t)\cos(\omega_m t)\,\mathrm{d}t + O\left(z^2\right)\end{array}\right] \tag{15}$$

$$= \frac{2}{T_m} C' \cdot b \tag{16}$$

With a constant $b \neq 0$. Here, the first addend becomes zero because $\cos(\omega_m t)$ is symmetric around $t = 0$. For a non-distorted cantilever motion with amplitude A_m and $z(t) = A_m \cos(\omega_m t)$, we obtain

$$\begin{aligned} b &= A_m \int_{-T/2}^{+T/2} \cos^2(\omega_m t)\,\mathrm{d}t \\ &= \frac{A_m T_m}{2} \end{aligned} \tag{17}$$

$$a_1 = A_m C'' \tag{18}$$

Thus, the sideband Equation 9 becomes:

$$\begin{aligned} F_{\omega_m \pm \omega_E} = &-A_m C''\left(U_{DC} - U_{CPD}\right)U_{AC} \\ &\cdot\left[\sin\left(\left(\omega_E - \omega_m\right)t\right) + \sin\left(\left(\omega_E + \omega_m\right)t\right)\right] \end{aligned} \tag{19}$$

Thus, the sideband amplitude is proportional to the second derivative of the tip/cantilever-sample capacitance and the carrier amplitude A_m.

Supporting Information

Supporting Information File 1

Additional figures.
[https://www.beilstein-journals.org/bjnano/content/supplementary/2190-4286-9-172-S1.pdf]

ORCID® iDs

Amelie Axt - https://orcid.org/0000-0002-5313-9319
Victor W. Bergmann - https://orcid.org/0000-0002-8093-6057
Stefan A. L. Weber - https://orcid.org/0000-0003-3052-326X

References

1. Bürgi, L.; Sirringhaus, H.; Friend, R. H. *Appl. Phys. Lett.* **2002,** *80,* 2913–2915. doi:10.1063/1.1470702
2. Berger, R.; Domanski, A. L.; Weber, S. A. L. *Eur. Polym. J.* **2013,** *49,* 1907–1915. doi:10.1016/j.eurpolymj.2013.03.005
3. Chen, Q.; Ye, F.; Lai, J.; Dai, P.; Lu, S.; Ma, C.; Zhao, Y.; Xie, Y.; Chen, L. *Nano Energy* **2017,** *40,* 454–461. doi:10.1016/j.nanoen.2017.08.050
4. Saive, R.; Mueller, C.; Schinke, J.; Lovrincic, R.; Kowalsky, W. *Appl. Phys. Lett.* **2013,** *103,* 243303. doi:10.1063/1.4846615
5. Saive, R.; Scherer, M.; Mueller, C.; Daume, D.; Schinke, J.; Kroeger, M.; Kowalsky, W. *Adv. Funct. Mater.* **2013,** *23,* 5854–5860. doi:10.1002/adfm.201301315
6. Jacobs, H. O.; Stemmer, A. *Surf. Interface Anal.* **1999,** *27,* 361–367. doi:10.1002/(SICI)1096-9918(199905/06)27:5/6<361::AID-SIA482>3.0.CO;2-8
7. Bergmann, V. W.; Weber, S. A. L.; Javier Ramos, F.; Nazeeruddin, M. K.; Grätzel, M.; Li, D.; Domanski, A. L.; Lieberwirth, I.; Ahmad, S.; Berger, R. *Nat. Commun.* **2014,** *5,* 5001. doi:10.1038/ncomms6001
8. Lan, F.; Jiang, M.; Tao, Q.; Li, G. *IEEE J. Photovoltaics* **2018,** *8,* 125–131. doi:10.1109/JPHOTOV.2017.2762525
9. Guerrero, A.; Juarez-Perez, E. J.; Bisquert, J.; Mora-Sero, I.; Garcia-Belmonte, G. *Appl. Phys. Lett.* **2014,** *105,* 133902. doi:10.1063/1.4896779
10. Cai, M.; Ishida, N.; Li, X.; Yang, X.; Noda, T.; Wu, Y.; Xie, F.; Naito, H.; Fujita, D.; Han, L. *Joule* **2018,** *2,* 296. doi:10.1016/j.joule.2017.11.015
11. Bergmann, V. W.; Guo, Y.; Tanaka, H.; Hermes, I. M.; Li, D.; Klasen, A.; Bretschneider, S. A.; Nakamura, E.; Berger, R.; Weber, S. A. L. *ACS Appl. Mater. Interfaces* **2016,** *8,* 19402–19409. doi:10.1021/acsami.6b04104

12. Panigrahi, S.; Jana, S.; Calmeiro, T.; Nunes, D.; Martins, R.; Fortunato, E. *ACS Nano* **2017,** *11,* 10214–10221. doi:10.1021/acsnano.7b04762
13. Panigrahi, S.; Calmeiro, T.; Martins, R.; Nunes, D.; Fortunato, E. *ACS Nano* **2016,** *10,* 6139–6146. doi:10.1021/acsnano.6b02090
14. Dymshits, A.; Henning, A.; Segev, G.; Rosenwaks, Y.; Etgar, L. *Sci. Rep.* **2015,** *5,* 8704. doi:10.1038/srep08704
15. Jiang, C.-S.; Yang, M.; Zhou, Y.; To, B.; Nanayakkara, S. U.; Luther, J. M.; Zhou, W.; Berry, J. J.; van de Lagemaat, J.; Padture, N. P.; Zhu, K.; Al-Jassim, M. M. *Nat. Commun.* **2015,** *6,* 8397. doi:10.1038/ncomms9397
16. Polak, L.; de Man, S.; Wijngaarden, R. J. *Rev. Sci. Instrum.* **2014,** *85,* 046111. doi:10.1063/1.4873331
17. Charrier, D. S. H.; Kemerink, M.; Smalbrugge, B. E.; de Vries, T.; Janssen, R. A. J. *ACS Nano* **2008,** *2,* 622–626. doi:10.1021/nn700190t
18. Ziegler, D.; Stemmer, A. *Nanotechnology* **2011,** *22,* 075501. doi:10.1088/0957-4484/22/7/075501
19. Li, G.; Mao, B.; Lan, F.; Liu, L. *Rev. Sci. Instrum.* **2012,** *83,* 113701. doi:10.1063/1.4761922
20. Colchero, J.; Gil, A.; Baró, A. M. *Phys. Rev. B* **2001,** *64,* 245403. doi:10.1103/PhysRevB.64.245403
21. Mélin, T.; Barbet, S.; Diesinger, H.; Théron, D.; Deresmes, D. *Rev. Sci. Instrum.* **2011,** *82,* 036101. doi:10.1063/1.3516046
22. Sadewasser, S.; Leendertz, C.; Streicher, F.; Lux-Steiner, M. C. *Nanotechnology* **2009,** *20,* 505503. doi:10.1088/0957-4484/20/50/505503
23. Zerweck, U.; Loppacher, C.; Otto, T.; Grafström, S.; Eng, L. M. *Phys. Rev. B* **2005,** *71,* 125424. doi:10.1103/PhysRevB.71.125424
24. Moores, B.; Hane, F.; Eng, L.; Leonenko, Z. *Ultramicroscopy* **2010,** *110,* 708–711. doi:10.1016/j.ultramic.2010.02.036
25. Loppacher, C.; Zerweck, U.; Teich, S.; Beyreuther, E.; Otto, T.; Grafström, S.; Eng, L. M. *Nanotechnology* **2005,** *16,* S1–S6. doi:10.1088/0957-4484/16/3/001
26. Garrett, J. L.; Munday, J. N. *Nanotechnology* **2016,** *27,* 245705. doi:10.1088/0957-4484/27/24/245705
27. Jacobs, H. O.; Knapp, H. F.; Stemmer, A. *Rev. Sci. Instrum.* **1999,** *70,* 1756–1760. doi:10.1063/1.1149664
28. Sugimura, H.; Ishida, Y.; Hayashi, K.; Takai, O.; Nakagiri, N. *Appl. Phys. Lett.* **2002,** *80,* 1459–1461. doi:10.1063/1.1455145
29. Nonnenmacher, M.; O'Boyle, M. P.; Wickramasinghe, H. K. *Appl. Phys. Lett.* **1991,** *58,* 2921–2923. doi:10.1063/1.105227
30. Kelvin, L. *Philos. Mag. (1798-1977)* **1898,** *46,* 82–120. doi:10.1080/14786449808621172
31. Weaver, J. M. R.; Abraham, D. W. *J. Vac. Sci. Technol., B: Microelectron. Nanometer Struct.–Process., Meas., Phenom.* **1991,** *9,* 1559. doi:10.1116/1.585423
32. Martin, Y.; Abraham, D. W.; Wickramasinghe, H. K. *Appl. Phys. Lett.* **1988,** *52,* 1103–1105. doi:10.1063/1.99224
33. Zorn, M.; Weber, S. A. L.; Tahir, M. N.; Tremel, W.; Butt, H.-J.; Berger, R.; Zentel, R. *Nano Lett.* **2010,** *10,* 2812–2816. doi:10.1021/nl100741n
34. Hudlet, S.; Saint Jean, M.; Roulet, B.; Berger, J.; Guthmann, C. *J. Appl. Phys.* **1995,** *77,* 3308–3314. doi:10.1063/1.358616
35. Ma, Z. M.; Kou, L.; Naitoh, Y.; Li, Y. J.; Sugawara, Y. *Nanotechnology* **2013,** *24,* 225701. doi:10.1088/0957-4484/24/22/225701
36. Borgani, R.; Forchheimer, D.; Bergqvist, J.; Thorén, P. A.; Inganäs, O.; Haviland, D. B. *Appl. Phys. Lett.* **2014,** *105,* 143113. doi:10.1063/1.4897966
37. Glatzel, T.; Sadewasser, S.; Lux-Steiner, M. C. *Appl. Surf. Sci.* **2003,** *210,* 84–89. doi:10.1016/S0169-4332(02)01484-8
38. Sugawara, Y.; Kou, L.; Ma, Z.; Kamijo, T.; Naitoh, Y.; Jun Li, Y. *Appl. Phys. Lett.* **2012,** *100,* 223104. doi:10.1063/1.4723697
39. Sydam, R.; Kokal, R. K.; Deepa, M. *ChemPhysChem* **2015,** *16,* 1042–1051. doi:10.1002/cphc.201402862
40. Ziegler, D.; Naujoks, N.; Stemmer, A. *Rev. Sci. Instrum.* **2008,** *79,* 063704. doi:10.1063/1.2947740
41. Bouwman, R.; Sachtler, W. M. H. *J. Catal.* **1970,** *19,* 127–139. doi:10.1016/0021-9517(70)90275-7
42. Lozano, J. R.; Kiracofe, D.; Melcher, J.; Garcia, R.; Raman, A. *Nanotechnology* **2010,** *21,* 465502. doi:10.1088/0957-4484/21/46/465502

License and Terms

This is an Open Access article under the terms of the Creative Commons Attribution License (http://creativecommons.org/licenses/by/4.0), which permits unrestricted use, distribution, and reproduction in any medium, provided the original work is properly cited.

The license is subject to the *Beilstein Journal of Nanotechnology* terms and conditions: (https://www.beilstein-journals.org/bjnano)

The definitive version of this article is the electronic one which can be found at: doi:10.3762/bjnano.9.172

BEILSTEIN JOURNAL OF NANOTECHNOLOGY

Numerical analysis of single-point spectroscopy curves used in photo-carrier dynamics measurements by Kelvin probe force microscopy under frequency-modulated excitation

Pablo A. Fernández Garrillo[1], Benjamin Grévin[2] and Łukasz Borowik[*1]

Full Research Paper

Open Access

Address:
[1]Univ. Grenoble Alpes, CEA, LETI, 38000 Grenoble, France and [2]Univ. Grenoble Alpes, CNRS, CEA, INAC, SYMNES, 38000 Grenoble, France

Email:
Łukasz Borowik[*] - lukasz.borowik@cea.fr

* Corresponding author

Keywords:
carrier dynamics; carrier lifetime; carrier recombination; Kelvin probe force microscopy; nanostructured photovoltaics; numerical simulations; photo-carrier dynamics

Beilstein J. Nanotechnol. **2018,** *9,* 1834–1843.
doi:10.3762/bjnano.9.175

Received: 09 February 2018
Accepted: 04 June 2018
Published: 20 June 2018

This article is part of the Thematic Series "Scanning probe microscopy for energy-related materials".

Associate Editor: E. Meyer

© 2018 Fernández Garrillo et al.; licensee Beilstein-Institut.
License and terms: see end of document.

Abstract

In recent years, the investigation of the complex interplay between the nanostructure and photo-transport mechanisms has become of crucial importance for the development of many emerging photovoltaic technologies. In this context, Kelvin probe force microscopy under frequency-modulated excitation has emerged as a useful technique for probing photo-carrier dynamics and gaining access to carrier lifetime at the nanoscale in a wide range of photovoltaic materials. However, some aspects about the data interpretation of techniques based on this approach are still the subject of debate, for example, the plausible presence of capacitance artifacts. Special attention shall also be given to the mathematical model used in the data-fitting process as it constitutes a determining aspect in the calculation of time constants. Here, we propose and demonstrate an automatic numerical simulation routine that enables to predict the behavior of spectroscopy curves of the average surface photovoltage as a function of a frequency-modulated excitation source in photovoltaic materials, enabling to compare simulations and experimental results. We describe the general aspects of this simulation routine and we compare it against experimental results previously obtained using single-point Kelvin probe force microscopy under frequency-modulated excitation over a silicon nanocrystal solar cell, as well as against results obtained by intensity-modulated scanning Kelvin probe microscopy over a polymer/fullerene bulk heterojunction device. Moreover, we show how this simulation routine can complement experimental results as additional information about the photo-carrier dynamics of the sample can be gained via the numerical analysis.

Introduction

In the past decade, the nanoscale investigation of materials properties has captured the attention of the scientific community, partially due to its crucial importance in the improvement of photovoltaic devices [1,2]. Carrier lifetime, or more broadly speaking, photo-carrier dynamics is one of the most interesting parameters to study at the local scale. To date, various ques-

tions regarding the interplay between photo-carrier dynamics and structuration of materials remain unanswered, and it is not clear how it affects performances in some emerging photovoltaic technologies.

In this context, few teams around the world have recently began to develop time-resolved scanning probe microscopies (SPM) techniques, aimed at addressing the photo-carrier dynamics at the local scale in photoactive materials and devices. At this point, Kelvin probe force microscopy (KPFM) emerged as a useful technique that, when implemented under frequency-modulated excitation, can be used to investigate the surface photovoltage decay, thus providing access to the photo-carrier dynamics [3-11].

A common aspect among all KPFM frequency-modulated spectroscopy techniques is that in order to extract time constants associated to photo-physical processes, a mathematical fit procedure is usually implemented. It is evident that the mathematical model used in the fit procedure constitutes a determining aspect in the calculation of time constants. Hence, there is a need to define methods that could check the validity of the mathematical assumptions. This led us to develop a simulation routine that enables to predict the behavior of spectroscopy curves of the average photovoltage as a function of a frequency-modulated excitation source in photovoltaic materials.

In this paper, we describe the general aspects of this simulation routine, and we compare it against experimental results from a previous work were single-point Kelvin probe force microscopy under frequency-modulated illumination (FMI-KPFM) was implemented over a silicon nanocrystal solar cell [3]. Analogously, we compare the simulation routine against the results obtained by intensity-modulated scanning Kelvin probe microscopy on a polymer/fullerene bulk heterojunction device as presented by Shao and co-workers [4]. The outcome of these comparisons did not only provide additional evidence supporting results obtained using the abovementioned techniques as simulations displayed a good agreement with experimental measurements. It also revealed that the simulation routine can complement experimental results as additional information about the photo-carrier dynamics of the sample can be gained through numerical analysis.

Experimental

Photo-carrier generation is a process that takes place in semiconductor materials when electron–hole pairs (positive and negative polarons in the case of organic photovoltaics) are created by exciting an electron from the valence band to the conduction band (π-electrons from the highest occupied molecular orbital to the lowest unoccupied molecular orbital in the case of organic photovoltaics), thus leaving a hole behind that can be considered as a positive charge. Recombination is the opposed process where negative and positive charges recombine and are annihilated.

In both cases, when the system is supplied with additional energy, i.e., through photon absorption, additional carriers are generated. In photovoltaic devices, an open-circuit voltage (V_{OC}) appears when carriers are photo-generated. In the same way, carrier recombination occurs when the extra energy is no longer supplied to the system and V_{OC} decays until the charge equilibrium state is reached.

The surface photovoltage (SPV), which can be seen as a local measurement of V_{OC} in semiconductors [12], has been studied using KPFM under modulated illumination. Indeed, the investigation of the SPV evolution as a function of a frequency-modulated excitation source can be used to access the photo-carrier dynamics in organic, inorganic and hybrid semiconductors [3-9,13]. In short, as depicted in Figure 1, FMI-KPFM consist of the measurement of a surface photovoltage by KPFM (time response between a few milliseconds and a few hundreds of milleseconds) under frequency-modulated excitation (light source, electrical bias), yielding an averaged time-integral value of the instantaneous photovoltage. One can obtain a spectroscopy curve of the average surface photovoltage (SPV_{AV}) by sweeping the excitation source modulation frequency. The spectroscopy curve is then fitted using mathematical models that enable one to determine the time constant(s) associated to the measured SPV dynamics. One of the advantages of FMI-KPFM compared to similar techniques is that in FMI-KPFM, images of

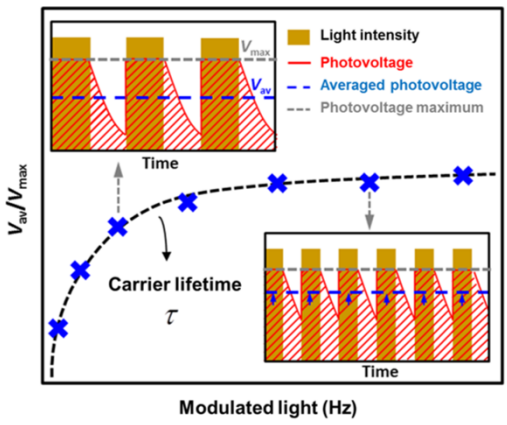


Figure 1: FMI-KPFM working principle: Averaged time-integral values of the instantaneous photovoltage are acquired as a function of the excitation-modulation frequency. SPV decay time constants are calculated upon a mathematical fit of this curve. In FMI-KPFM, images of the SPV decay time constant can be acquired by simultaneously performing this protocol over multiples points on a pre-defined grid area over the sample [3-6].

the SPV decay time constant can be acquired by simultaneously performing the above describe protocol over multiples points on a pre-defined grid area over the sample. However, in the following, the discussion of FMI-KPFM results will turn around single-point measurements.

For the most part, techniques based on this approach do not take into account the built-up time of the SPV, which is the time needed for the surface photovoltage to appear in the first place. This time is associated with the exciton generation, charge dissociation and charge transport along the material so that a photo-generated surface potential can be detected using KPFM. Indeed, in some cases, depending on the material and the excitation intensity, this time can be approximated to zero as the SPV built-up is usually much faster than the SPV decay. However, we will see below that taking into account a non-zero SPV built-up time can modify the interpretation of the spectroscopy curves and, thus, the estimation of the SPV time constants. Here we highlight that the SPV built-up time can be physically interpreted in different ways depending on the sample and the photo-generation mechanism. In inorganic silicon samples for instance, this time constant can be attributed to the effective time needed for exciton generation, dissociation and carrier separation. On the other hand, in the case of some organic photovoltaic (OPV) samples, the SPV built-up time can be attributed to the effective time needed to fill lower energy states (traps). In a more general way, it can be stated that the SPV built-up time is closely related to the carrier diffusion length within each particular material.

In a previous work [1], we implemented a single exponential decay model to fit the spectroscopy curves acquired over a silicon nanocrystal solar cell. In the following, using a novel automated numerical analysis routine, we verify the validity of the model by checking the self-consistency of the previously obtained results via the comparison of measured data, mathematical fit and simulations.

In a first approach, an exponential function can be used to describe the built-up and decay of the SPV in photoactive materials [3-6,8]. Under this premise, we can model the SPV behavior of a photovoltaic material under modulated excitation as a function of the time for both the built-up and decay in the following way for the case of a single SPV built-up and decay time constant (Equation 1 and Equation 2) and for a more general case with *k* build-up and *l* decay time constants (Equation 3 and Equation 4):

$$\mathrm{SPV}_{\text{built-up}} = 1 - \exp\left(-\frac{p}{\tau_\mathrm{b}}\right), \tag{1}$$

$$\mathrm{SPV}_{\text{decay}} = \exp\left[-\frac{(p+i)}{\tau_\mathrm{d}}\right], \tag{2}$$

$$\mathrm{SPV}_{\text{built-up}} = \sum_{1}^{k}\left[1 - \exp\left(-\frac{p}{\tau_{\mathrm{b}_k}}\right)\right], \tag{3}$$

$$\mathrm{SPV}_{\text{decay}} = \sum_{1}^{l}\left(\exp\left[-\frac{(p+i)}{\tau_{\mathrm{d}_l}}\right]\right). \tag{4}$$

Here, p is the time duration of the excitation pulse, i is the duration of time between the pulses, τ_b is the time constant associated to SPV built-up, and τ_d is the time constant associated to SPV decay.

Here, the number of build-up and decay time constants can be determined in advance from accessible literature by taking to account the type and properties of materials, e.g., doping level and type, defects concentration and gap energy. Types of recombination mechanisms for silicon can be found in [14].

Using Equation 1 and Equation 2 we can numerically model the normalized magnitude of the instant SPV as a function of the time for different excitation modulation conditions (Figure 2a). In other words, we can access the normalized magnitude of the instant SPV at any given point in time for any given modulation frequency. Depending on the imposed modulation frequency value, a quasi-steady-state condition is reached after a certain number of excitation pulses, indicating that the equilibrium state of charges was reached. Once this condition is attained, we calculate the average value of the normalized SPV through integration. By performing this calculation at different modulation frequencies we can then plot the evolution of the normalized average surface photovoltage magnitude as a function of the excitation modulation frequency as depicted in Figure 2b. A custom-written software (SPECTY) implementing this routine was separately developed using the SCILAB open source coding tool and the batch processing options of OriginPro software (OriginLab Corp.) yielding the same results.

While both the syntax and the philosophy of the SCILAB open source coding tool and the batch processing options of OriginPro software are different, in both coding environments SPECTY is structured in a similar way. Figure 3 depicts the software flowchart detailing the algorithm used in the performed simulations. As depicted in this figure, upon the introduction of the simulation input parameters (SPV decay and

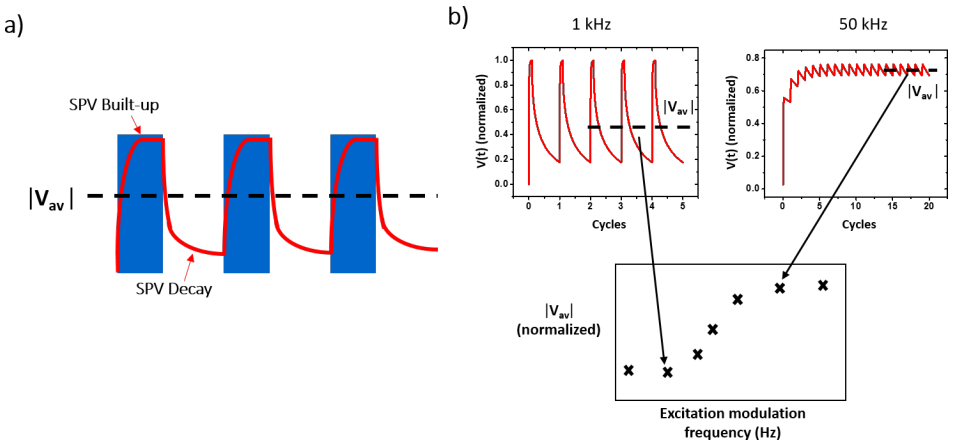


Figure 2: SPECTY working principle: (a) SPV built-up and decay are modeled using Equation 1 and Equation 2 respectively. (b) A quasi-steady-state condition is reached after a certain number of excitation pulses. At this moment the average value of the normalized SPV is calculated. Performing this calculation at different modulation frequencies allows one to plot the evolution of the normalized average surface photovoltage magnitude as a function of the excitation modulation frequency.

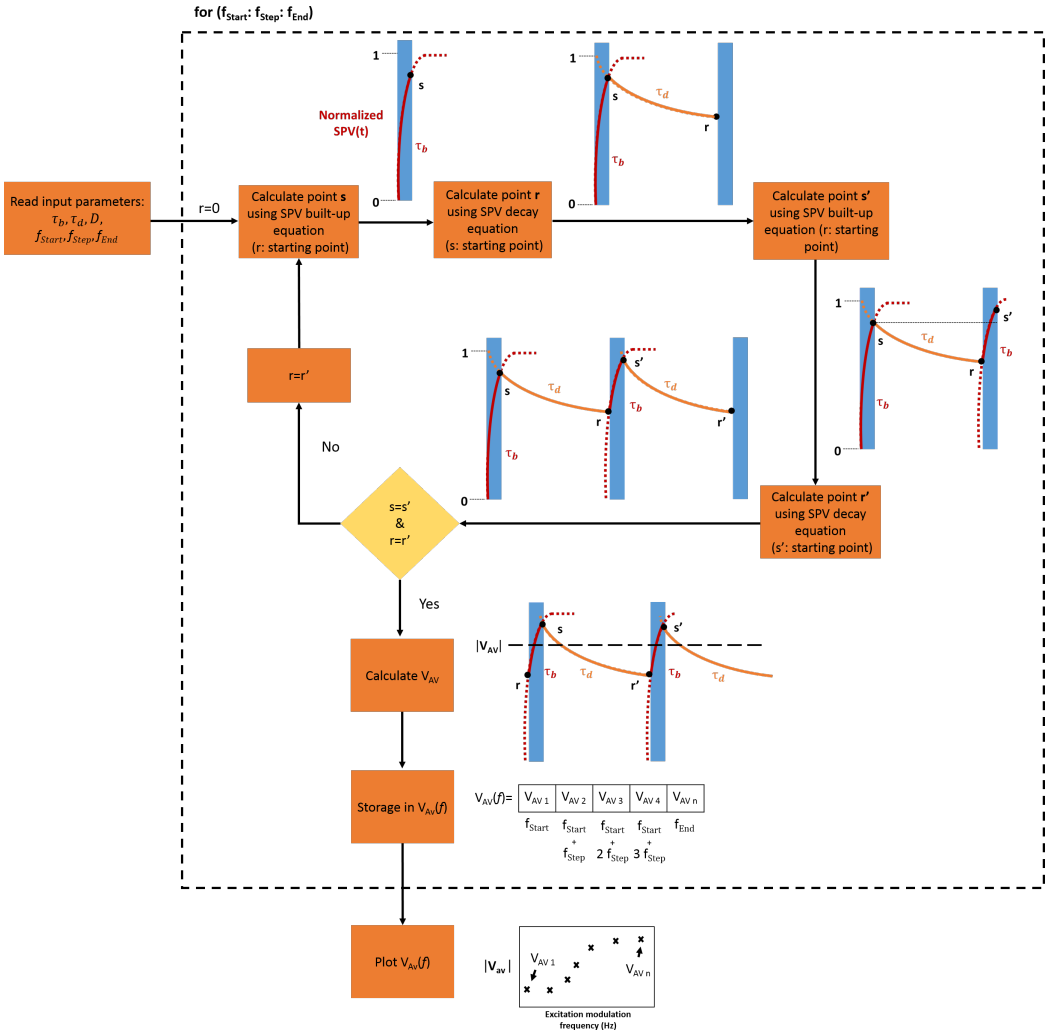


Figure 3: SPECTY's algorithm flowchart. When a quasi-steady-state condition is reached, the average value of the normalized surface potential (V_{AV}) is calculated.

built-up time constants along with the duty ratio and the range of frequencies), the software applies Equation 1 to find the attained value of the surface photovoltage just at the end of the illumination period (called "s" in Figure 3), then in a similar way, the software uses Equation 2 to find the attained value of the surface photovoltage after photo-carrier recombination during the "in-dark" period (called "r" in Figure 3). This process is repeated until two consecutive "s" and "r" points have the same value, which means that the quasi-steady-state condition was reached. Then, the average value of the last two pulses is calculated and stored in the form of a vector. At the end of the for loop, this vector is plotted yielding the spectroscopy curve $V_{AV}(f)$.

Results and Discussion

Using SPECTY we can now verify the validity of the mathematical model used in a previous work, where the minority-carrier lifetime in a silicon nanocrystal solar cell was obtained by KPFM spectroscopy under frequency-modulated light illumination [3]. This can be done by fixing the SPV decay time in the numerical simulation to the value predicted by the mathematical fit used on that occasion and comparing the correspondence between the spectroscopy curve resulting from the mathematical fit and the data points obtained from the numerical simulation.

In [3], minority-carrier lifetime values were calculated through a mathematical fit procedure derived from previous publications [5] using the following expression:

$$\frac{\Delta V_{AV}}{\Delta V_{max}} = D + \tau \cdot f\left[1 - \exp\left(\frac{\alpha - 1}{\tau \cdot f}\right)\right], \qquad (5)$$

where D is the modulation duty ratio, f is the modulation frequency of the light, $(\Delta V_{AV}/\Delta V_{max})$ is the ratio between the time-averaged surface potential and the surface photovoltage at saturation, and τ is the minority-carrier lifetime.

Figure 4 shows the spectroscopy curve resulting from the mathematical fit from which the minority-carrier lifetime was extracted in a silicon nanocrystal solar cell after H-passivation along with the measured data points as presented in [3] together with the simulated data points. For the numerical simulation, τ_d was fixed at 70 µs (to match the value predicted by the mathematical fit), τ_b was fixed at 1 µs, but similar results were obtained using shorter values. On the other hand, the use of $\tau_b > 1$ µs yields simulated data points that no longer follow the mathematical fit curve (green and gray squares in Figure 4). Both p and i were chosen to match the experimental parameters used in [3].

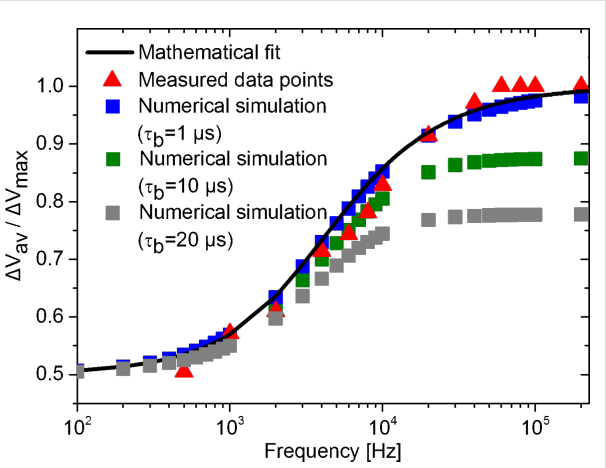


Figure 4: Comparison between spectroscopy curve obtained through the mathematical fit, measured data points and data points obtained by numerical simulations using τ_b = 1, 10 and 20 µs. The data points was taken from Figure 4 of [3].

In Figure 4 we observe a full correspondence between the mathematical fit applied to the minority-carrier lifetime in the silicon nanocrystal solar cell after H-passivation and the numerically simulated data points (τ_b = 1 µs). In addition, this routine provides additional information about the SPV built-up time constant, as it shall be 1 µs at most so that the simulation agrees with the measured data points as shown in Figure 4. This information would not otherwise be accessible solely from the mathematical fit used in our previous paper [3]. Moreover, this time constant value strongly agrees with previous reports of the time scale of photo-generation and electron–hole pair separation in other silicon samples [9,15,16].

Additionally, SPECTY can provide graphic representations of how the SPV as a function of the time evolves with the modulation frequency as shown in Figure 5.

Information about the evolution of SPV_{AV} as a function of the number of excitation cycles can also be accessed via the simulation routine as depicted in Figure 6. In fact, as described above, depending on the value of the imposed modulation frequency, a quasi-steady-state condition is reached after a certain number of excitation pulses (charge equilibrium). In Figure 6 we note that as expected, the higher the modulation frequency is the more illumination cycles are needed to attain the charge-equilibrium state. Nonetheless, we stress that even though more cycles are needed to attain this condition, in terms of time it remains negligible compared to the KPFM integration time.

After having demonstrated how to apply the numerical analysis routine in single-point FMI-KPFM results obtained over a silicon nanocrystal solar cell, we now turn to the analysis of

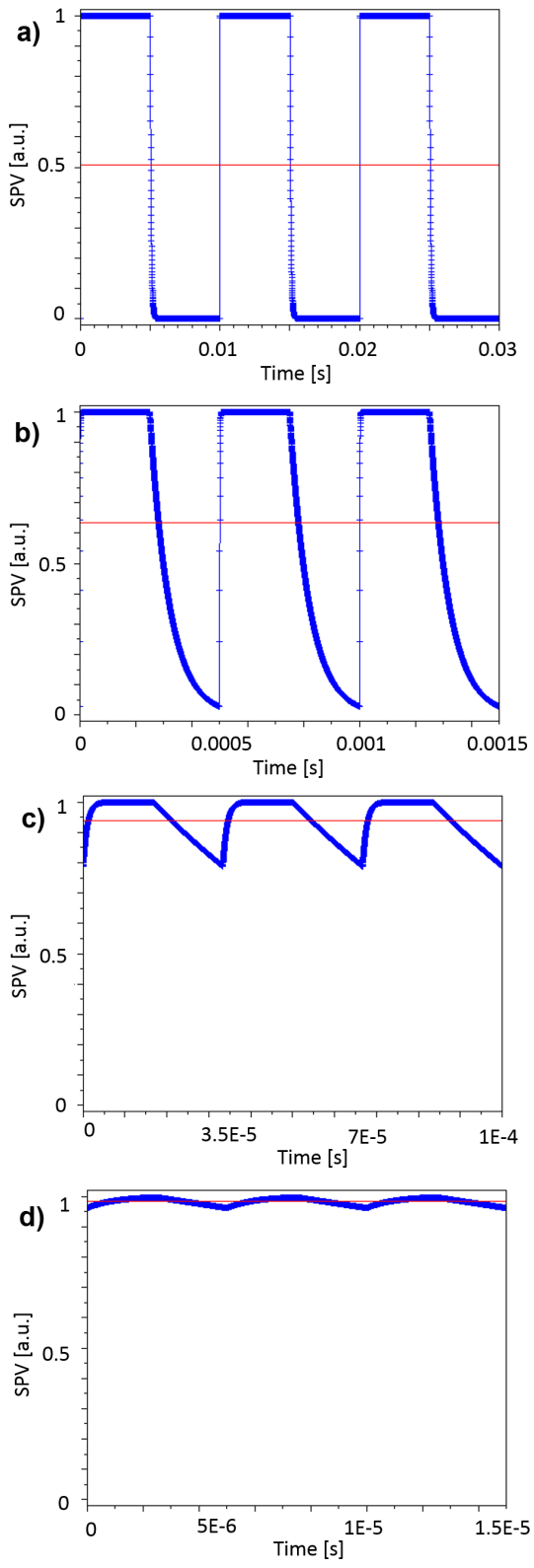


Figure 5: Simulated SPV as a function of the time for different excitation modulation frequencies, the red lines indicate the average SPV value for each modulation condition. Modulation frequencies: a) 100 Hz, b) 2 kHz, c) 30 kHz, and d) 200 kHz.

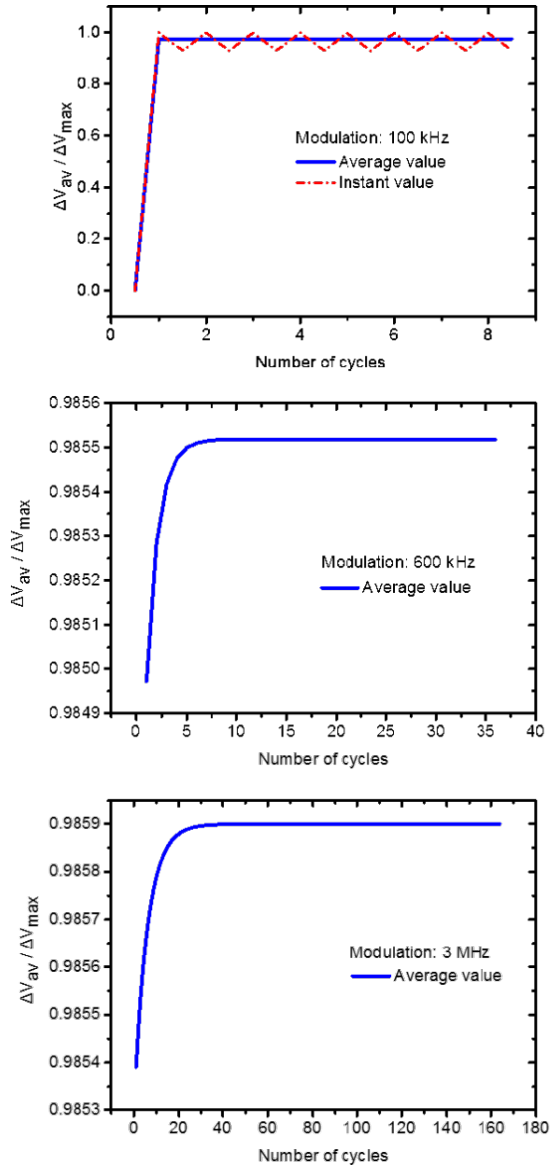


Figure 6: Simulated SPV_{AV} as a function of the number of excitation cycles for different excitation modulation frequencies. From top to bottom: 100 kHz, 600 kHz and 3 MHz. The simulation at 100 kHz includes the SPV instant value oscillation as depicted by the red dashed line. The graphs depicting the results from simulations at 600 kHz and 3 MHz were zoomed-in so that the convergence process can be noticed.

results obtained by intensity-modulated scanning Kelvin probe microscopy over a polymer/fullerene bulk heterojunction device as presented by Shao and co-workers [4].

As stated above, SPECTY can be useful in the analysis of results obtained by several frequency-modulated KPFM techniques. Intensity-modulated scanning Kelvin probe microscopy is a technique that allows one to study the surface photovoltage decay on sub-millisecond time scales in photovoltaic materials.

This technique [4], was used to measure the local photo-carrier lifetime over a region of a PCDTBT/$PC_{71}BM$ bulk heterojunction sample that had either 2,6-difluorobenzylphosphonic acid (oF_2BnPA) or pentafluorobenzylphosphonic acid (F_5BnPA) underneath. In this work it was found that the characteristic photo-carrier lifetime was about two times faster for oF_2BnPA than for F_5BnPA regions at a given light intensity as the characteristic photo-carrier lifetime values extracted from the raw data were 0.51 ms and 1.1 ms, respectively. In the work of Shao and co-workers, a stretched exponential function was used in the fit procedure to describe the dispersive kinetics nature of the SPV decay where the lifetime changes with time.

In the following, using same data, as extracted from Figure 8 of [4], we propose instead, the use of exponential functions including a non-zero SPV built-up time to simulate the resulting average surface photovoltage spectroscopy curves for F_5BnPA and oF_2BnPA regions.

Figure 7 shows different simulated surface photovoltage spectroscopy curves for the F5BnPA region. Based on the analysis of this figure, it can be suggested that the inclusion of a non-zero SPV built-up time demands the use of a shorter SPV decay time as input parameter to the simulation (compared to the 1.1 ms found using a stretched exponential function for fitting purposes), as well as a SPV built-up time ≤2 µs in order to simulate a surface photovoltage spectroscopy curve that passes through the data points with minimum deviation. Similar results were obtained for the oF_2BnPA region (not shown).

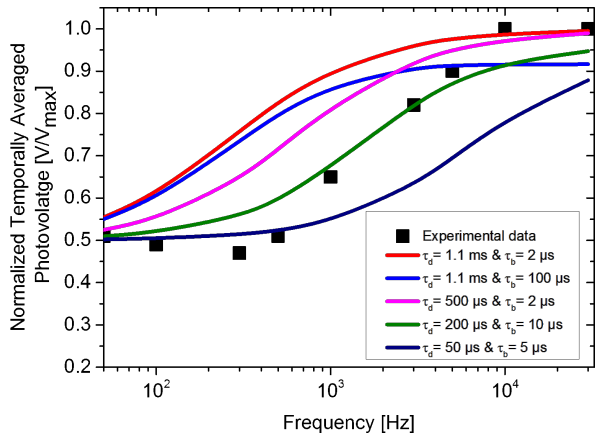


Figure 7: Simulated surface photovoltage spectroscopy curves of the F_5BnPA region for different SPV built-up and decay input parameters. Experimental data was extracted from Figure 8 of [4].

Figure 8 displays the best obtained result of the simulated average surface photovoltage spectroscopy curves and the measured data points for both F_5BnPA and oF_2BnPA regions. The spectroscopy curves presented in Figure 8 were obtained with SPECTY using τ_d = 68.1 µs and τ_b = 1 µs for the oF_2BnPA region, and τ_d = 158.2 µs and τ_b = 2 µs for the F_5BnPA region as input parameters, in both cases *p* and *i* were chosen to match the experimental parameters used in [4].

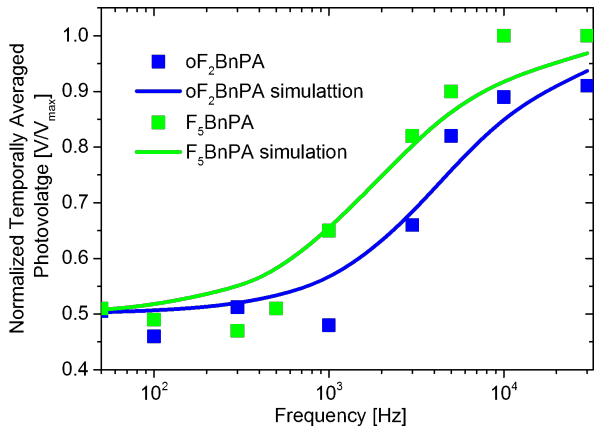


Figure 8: Time-averaged surface photovoltage measured at different modulating frequencies with intensity-modulated scanning Kelvin probe microscopy. Blue and green dots are experimental data for the oF_2BnPA and F_5BnPA areas, respectively. Blue and green lines are best obtained results of the simulated average surface photovoltage spectroscopy curves obtained with SPECTY using τ_d = 68.1 µs and τ_b = 1 µs for the oF_2BnPA region, and τ_d = 158.2 µs and τ_b = 2 µs for the F_5BnPA region as input parameters. Experimental data points were taken from Figure 8 of [4].

While the simulated results presented in Figure 8 resemble those from [4], we nonetheless note that the adjustment level of the simulated curves to the data points does not allow to conclusively claim that estimated SPV time constants are indeed representing the photo-carrier dynamics of the sample. Indeed, it would appear that simulated curves tend to increase even further for higher frequencies while the experimental points reach a plateau, this suggest that more complex photo-carrier dynamics are governing the SPV behavior of the sample, as it is the case for instance for OPV samples exhibiting a high density of low-energy states (traps).

Nonetheless, we stress that even if the calculated photo-carrier lifetime values do not fully agree with those reported in [4], the ratio between the calculated photo-carrier lifetime in F_5BnPA and oF_2BnPA regions remains the same (the characteristic carrier lifetimes of oF_2BnPA are about half than those of F_5BnPA).

Moreover, even if the results in Figure 8 are not entirely conclusive, the measured time scales for the SPV dynamics do seem to agree relatively well with the results of macroscopic transient experiments over similar samples [17]. However, the discrep-

ancy between these results in the microsecond range and those reported previously in the millisecond range, opens a debate around whether the measured intensity-modulated scanning Kelvin probe microscopy data should be analyzed using stretched exponentials with a certain stretching exponent to describe the dispersive kinetics where the lifetime changes with time, or rather use an exponential function that accounts for a non-zero surface photovoltage built-up time.

While there is no short answer to this question, here we highlight that when using stretched exponentials in order to take into account the dispersive kinetics present in the sample, the stretch exponents lie between 0 and 1 [18-21]. However, in [4] the stretching exponent that best fits the results is greater than 1. This inconsistency put some constrains on the interpretation of the calculated photo-carrier time constants.

In order to determine which mathematical model describes best the physical phenomena occurring in the sample upon photo-carrier generation, an experimental protocol is proposed hereafter. Measuring the contact potential difference (CPD) under continuous wave illumination (or DC bias excitation) can give us the magnitude of the average potential that we should detect for the highest modulation frequency if the SPV built-up time can be approximated to zero. In this scenario, data can be fitted assuming $\tau_b = 0$. On the other hand, if the average potential measured for the highest modulation frequency, is below the CPD under continuous wave excitation previously registered, a non-zero SPV built-up time needs to be assumed.

To demonstrate this, a new FMI-KPFM acquisition protocol was developed, in which both the CPD under continuous wave excitation and the SPV_{AV} spectroscopy curve can be simultaneously acquired at each point of the sample. Indeed, by applying a continuous wave excitation pulse to the sample, prior to the acquisition of the SPV_{AV} spectroscopy curve, it becomes possible to measure values of both the CPD in dark conditions and under continuous wave illumination.

Figure 9 shows an example of the obtained result when implementing this protocol over a nano-phase segregated PDBSTQx/$PC_{71}BM$ blend with amplitude modulation FMI-KPFM. In this case, the sample was optically excited using a green (515 nm) PhoxXplus module from OmicronLaserage GmbH (rise and fall times <1.5 ns in digital modulation mode) with a peak output power of 50 mW/cm^2. Modulation frequencies were swept from few tens of hertz to 10 kHz with a 10% duty ratio. We highlight that this sample was previously investigated by our group in an earlier work [6]. However, its photo-physical properties evolved after near 20 months of storage time under UHV conditions.

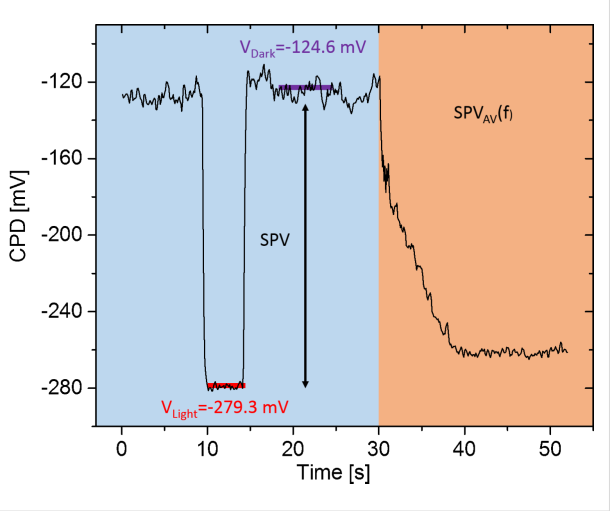


Figure 9: Data obtained from the implementation of the proposed FMI-KPFM protocol for the simultaneous acquisition of the CPD under continuous wave excitation and under dark conditions, along with the SPV_{AV} spectroscopy curve. V_{Dark} corresponds to the in-dark surface potential and V_{Light} is the surface photovoltage measured under continuous wave illumination.

As it can be seen from Figure 9, the magnitude of the CPD measured under continuous wave illumination is higher than the average potential measured at the highest modulation frequency. As mentioned before, in this scenario we propose that a non-zero SPV built-up time shall be accounted for. To do so, firstly the normalized SPV_{AV} spectroscopy curve is extracted as shown in Figure 10. As a first step, we fitted this SPV_{AV} spectroscopy curve using the following equations derived from a previous work to estimate separately the SPV decay time constant τ_d and also τ_d together with a non-zero SPV built-up time constant τ_b [4]:

$$\mathrm{SPV_{AV}}(f) = V_{\mathrm{Dark}} + V_{\mathrm{Light}} \cdot D + \tau_d \cdot f \cdot V_{\mathrm{Light}} \left(1 - \exp\left[\frac{(1-D)}{\tau_d \cdot f}\right]\right), \quad (6)$$

$$\begin{aligned}\mathrm{SPV_{AV}}(f) = {} & V_{\mathrm{Dark}} \\ & + \left(V_{\mathrm{Light}} - V_{\mathrm{Dark}}\right) \\ & \cdot D\left(1 - \exp\left[-\frac{D}{f \cdot \tau_b}\right]\exp\left[-\frac{(1-D)}{f \cdot \tau_d}\right]\right) \\ & + \left(V_{\mathrm{Light}} - V_{\mathrm{Dark}}\right) \cdot \left(f \cdot \tau_d - f \cdot \tau_b\right) \\ & \cdot \left(1 - \exp\left[-\frac{D}{f \cdot \tau_b}\right]\right) \cdot \left(1 - \exp\left[-\frac{(1-D)}{f \cdot \tau_d}\right]\right).\end{aligned} \quad (7)$$

In these expressions V_{Dark} is the in-dark surface potential, V_{Light} the surface photovoltage measured under continuous wave illu-

mination, τ_d the SPV decay time, f is the modulation frequency and D is the illumination duty ratio. Note that Equation 6 does not take into account a non-zero SPV built-up time, in contrast to Equation 7. In both expressions V_{Dark} and V_{Light} are known values that can be set constant in the fit procedure.

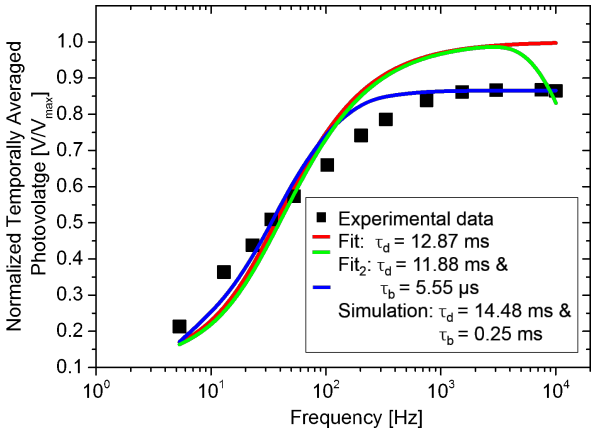


Figure 10: Comparison between curves: Mathematical fit (red and green lines) and simulated SPV_{AV} curve (blue line). The improved adjustment of the simulated SPV_{AV} curve compared to the mathematical fit is attributed to the inclusion of a non-zero SPV built-up time.

In Figure 10, the results of the fit procedures are shown (red and green lines). Although a SPV decay time within the expected range is calculated (ca. 12 ms), the fits exhibit large deviations from the data points. In turn, if we use SPECTY to model the SPV_{AV} spectroscopy curve including the use of a non-zero SPV built-up time, the resulting curve (blue line) presents an improved adjustment to the data points, suggesting that indeed, using SPECTY leads to a more accurate estimation of the SPV photo-carrier dynamics.

As in Figure 8, the blue line in Figure 10 displays the best obtained result of the simulated average surface photovoltage spectroscopy curve over the measured data points using using τ_d = 14.48 ms and τ_b = 0.25 ms. However, it is worth mentioning that while the simulated curve seems to better describe the data set than the mathematical fit, all estimations yield similar SPV decay times.

Conclusion

In summary, we proposed and demonstrated a novel automatic numerical simulation routine that enables the simulation of spectroscopy curves of the average surface photovoltage during the frequency-modulated excitation of photovoltaic materials, provided that the values of the time constants of the SPV dynamics are specified as set-up parameters in the software.

We implemented this routine to check calculated time constants associated to the minority-carrier lifetime obtained with single-point FMI-KPFM on a silicon nanocrystal solar cell. The obtained results were not only confirmed by the numerical analysis, but additional information about the photo-carrier dynamics was found, which otherwise would not be accessible solely from the mathematical fit of the measured data.

We also implemented a numerical simulation routine to check the pertinence of the mathematical model used in intensity-modulated scanning Kelvin probe microscopy measurements of a polymer/fullerene bulk heterojunction device. The output of this analysis led us to propose and demonstrate an experimental protocol for FMI-KPFM and related techniques, intended to help choosing the most adequate mathematical model for a given data set based on the nature of the SPV built-up time.

ORCID® iDs

Pablo A. Fernández Garrillo - https://orcid.org/0000-0003-1452-1707

References

1. Heeger, A. J. *Adv. Mater.* **2014,** *26,* 10–28. doi:10.1002/adma.201304373
2. Beard, M. C.; Luther, J. M.; Nozik, A. J. *Nat. Nanotechnol.* **2014,** *9,* 951–954. doi:10.1038/nnano.2014.292
3. Borowik, Ł.; Lepage, H.; Chevalier, N.; Mariolle, D.; Renault, O. *Nanotechnology* **2014,** *25,* 265703. doi:10.1088/0957-4484/25/26/265703
4. Shao, G.; Glaz, M. S.; Ma, F.; Ju, H.; Ginger, D. S. *ACS Nano* **2014,** *8,* 10799–10807. doi:10.1021/nn5045867
5. Takihara, M.; Takahashi, T.; Ujihara, T. *Appl. Phys. Lett.* **2008,** *93,* 021902. doi:10.1063/1.2957468
6. Fernández Garrillo, P. A.; Borowik, Ł.; Caffy, F.; Demadrille, R.; Grévin, B. *ACS Appl. Mater. Interfaces* **2016,** *8,* 31460–31468. doi:10.1021/acsami.6b11423
7. Almadori, Y.; Bendiab, N.; Grévin, B. *ACS Appl. Mater. Interfaces* **2018,** *10,* 1363–1373. doi:10.1021/acsami.7b14616
8. Narchi, P.; Cariou, R.; Foldyna, M.; Prod'homme, P.; Roca i Cabarrocas, P. *IEEE J. Photovoltaics* **2016,** *6,* 1576–1580. doi:10.1109/JPHOTOV.2016.2598258
9. Fernández Garrillo, P. A.; Narchi, P.; Roca i Cabarrocas, P.; Grévin, B.; Borowik, Ł. *IEEE J. Photovoltaics* **2018,** *8,* 661–663. doi:10.1109/JPHOTOV.2018.2793760
10. Coffey, D. C.; Reid, O. G.; Rodovsky, D. B.; Bartholomew, G. P.; Ginger, D. S. *Nano Lett.* **2007,** *7,* 738–744. doi:10.1021/nl062989e
11. Coffey, D. C.; Ginger, D. S. *Nat. Mater.* **2006,** *5,* 735–740. doi:10.1038/nmat1712
12. Tennyson, E. M.; Garrett, J. L.; Frantz, J. A.; Myers, J. D.; Bekele, R. Y.; Sanghera, J. S.; Munday, J. N.; Leite, M. S. *Adv. Energy Mater.* **2015,** *5,* 1501142. doi:10.1002/aenm.201501142
13. Almadori, Y.; Moerman, D.; Llacer Martinez, J.; Leclère, P.; Grévin, B. *Beilstein J. Nanotechnol.* **2018,** *9,* 1695–1704. doi:10.3762/bjnano.9.161
14. Sinton, R. A.; Swanson, R. M. *IEEE Trans. Electron Devices* **1987,** *34,* 1380–1389. doi:10.1109/T-ED.1987.23095

15. Sinton, R. A.; Cuevas, A. *Appl. Phys. Lett.* **1996,** *69,* 2510–2512. doi:10.1063/1.117723
16. Vu, D. P.; Pfister, J. C. *Appl. Phys. Lett.* **1985,** *47,* 950–952. doi:10.1063/1.95939
17. Elliott, L. C. C.; Basham, J. I.; Pernstich, K. P.; Shrestha, P. R.; Richter, L. J.; DeLongchamp, D. M.; Gundlach, D. J. *Adv. Energy Mater.* **2014,** *4,* 1400356. doi:10.1002/aenm.201400356
18. Freitas, R. J.; Shimakawa, K. *Philos. Mag. Lett.* **2017,** *97,* 257–264. doi:10.1080/09500839.2017.1334133
19. Plonka, A. *Dispersive Kinetics;* Springer, 2001. doi:10.1007/978-94-015-9658-9
20. Krishnan, M. S.; Kol'dyaev, V. Modeling kinetics of gate oxide reliability using stretched exponents. In *International Reliability Physics Symposium. Proceedings. 40th Annual,* Dallas, TX, USA, Aug 7–11, 2002; IEEE , 2002; pp 421–422. doi:10.1109/RELPHY.2002.996676
21. Brosseau, C.-N.; Perrin, M.; Silva, C.; Leonelli, R. *Phys. Rev. B* **2010,** *82,* 085305. doi:10.1103/PhysRevB.82.085305

License and Terms

This is an Open Access article under the terms of the Creative Commons Attribution License (http://creativecommons.org/licenses/by/4.0), which permits unrestricted use, distribution, and reproduction in any medium, provided the original work is properly cited.

The license is subject to the *Beilstein Journal of Nanotechnology* terms and conditions: (https://www.beilstein-journals.org/bjnano)

The definitive version of this article is the electronic one which can be found at: doi:10.3762/bjnano.9.175

BEILSTEIN JOURNAL OF NANOTECHNOLOGY

A scanning probe microscopy study of nanostructured TiO_2/poly(3-hexylthiophene) hybrid heterojunctions for photovoltaic applications

Laurie Letertre[1], Roland Roche[2], Olivier Douhéret[3], Hailu G. Kassa[1], Denis Mariolle[4,5], Nicolas Chevalier[4,5], Łukasz Borowik[4,5], Philippe Dumas[2], Benjamin Grévin[4,6], Roberto Lazzaroni[1,3] and Philippe Leclère[*1]

Full Research Paper

Open Access

Address:
[1]Laboratory for Chemistry of Novel Materials - Center for Innovation and Research in Materials and Polymers - CIRMAP, University of Mons, Mons, Belgium, [2]Aix Marseille Univ, CNRS, Centre Interdisciplinaire de Nanoscience de Marseille (CiNaM), Marseille, France, [3]Materia-Nova R&D Center, Mons, Belgium, [4]Université Grenoble Alpes, F-38000 Grenoble, France, [5]CEA, LETI, Campus MINATEC, F-38054 Grenoble, France and [6]UMR5819 SYMMES CEA-CNRS-UGA, 17 rue des Martyrs F-38054, Grenoble, France

Email:
Philippe Leclère[*] - Philippe.LECLERE@umons.ac.be

* Corresponding author

Keywords:
hybrid heterojunctions; hybrid photovoltaic; Kelvin probe force microscopy; photoconductive-AFM; photo-KPFM; poly(3-hexylthiophene); TiO_2

Beilstein J. Nanotechnol. **2018,** *9,* 2087–2096.
doi:10.3762/bjnano.9.197

Received: 03 April 2018
Accepted: 22 July 2018
Published: 01 August 2018

This article is part of the Thematic Series "Scanning probe microscopy for energy-related materials".

Associate Editor: U. D. Schwarz

© 2018 Letertre et al.; licensee Beilstein-Institut.
License and terms: see end of document.

Abstract

The nanoscale morphology of photoactive hybrid heterojunctions plays a key role in the performances of hybrid solar cells. In this work, the heterojunctions consist of a nanocolumnar TiO_2 surface covalently grafted with a monolayer of poly(3-hexylthiophene) (P3HT) functionalized with carboxylic groups (–COOH). Through a joint analysis of the photovoltaic properties at the nanoscale by photoconductive-AFM (PC-AFM) and surface photovoltage imaging, we investigated the physical mechanisms taking place locally during the photovoltaic process and the correlation to the nanoscale morphology. A down-shift of the vacuum level of the TiO_2 surface upon grafting was measured by Kelvin probe force microscopy (KPFM), evidencing the formation of a dipole at the TiO_2/P3HT-COOH interface. Upon in situ illumination, a positive photovoltage was observed as a result of the accumulation of photogenerated holes in the P3HT layer. A positive photocurrent was recorded in PC-AFM measurements, whose spatial mapping was interpreted consistently with the corresponding KPFM analysis, offering a correlated analysis of interest from both a theoretical and material design perspective.

Introduction

Over the past decades, a large range of photovoltaic (PV) technologies have been developed for the production of renewable energy [1]. Inorganic photovoltaic cells are currently the most employed PV devices with a power efficiency ranging from 20 to 40% [2] and a long-term stability up to 20 years [3]. However, a number of drawbacks affect those technologies. Indeed, in addition to high energy consumption for their fabrication, these devices are deposited on rigid substrates and involve relatively heavy and costly materials of possibly low abundance and/or toxicity [4]. New PV technologies, such as organic photovoltaics (OPV) and hybrid solar cells, are now being developed [2] to cope with such issues. In particular, hybrid solar cells can possibly benefit from the low economic and energy costs of production, high absorbance and tailorable absorption spectrum of the organic materials on the one hand, and from the good stability, absorption and electrical properties of the inorganic materials on the other hand.

Hybrid PV devices include various technologies such as perovskite cells, dye sensitized solar cells (DSSC), with power efficiencies up to 13% [5] and hybrid bulk heterojunctions (HBHJ), which combine an organic matrix and inorganic semiconducting nanostructures such as quantum dots. Among the electron acceptor materials commonly used for DSSC and HBHJ, titanium dioxide (TiO_2) is a well-known metal oxide semiconductor [6-8]. Depending on its nanostructure and its crystalline phase, its conductivity varies from 10^{-4} $\Omega^{-1}\cdot cm^{-1}$ to 10^{-11} $\Omega^{-1}\cdot cm^{-1}$ [9,10]. TiO_2 is very valuable because it can easily form nanostructures, such as nanoporous layers, nanowires or nanocolumns [5,11,12]. Because of its large band gap (3.2 eV [13]), light absorption is carried out by an organic or inorganic dye. The nanostructuration of the acceptor material is crucial for the cell performance [11], as it allows increasing the specific surface of the layer to enhance the amount of grafted dye, and thereby, the photon absorption yield. Nanostructuration is also likely to improve the conductivity of TiO_2 [14]. Because of the influence of the nanostructuration of TiO_2 on the optoelectronic properties of the device, it is of prime interest to study the photovoltaic properties at the nanoscale. Hybrid heterojunction (HHJ) structures are obtained by impregnation of the porous layer with an absorbing dye or a polymer electron donor. Poly(3-hexylthiophene) (P3HT) is often used, because of its strong absorption, its high hole mobility and its donor-like electronic properties [15]. Upon light absorption by the polymer, excitons are generated and they can be dissociated at the interface with TiO_2, the polymer also acting as the hole-transporting layer.

In this work, we investigated nanostructured TiO_2 layers composed of arrays of nanoscale columns, covalently sensitized with a P3HT-COOH monolayer to form hybrid bulk heterojunctions. The grafting of P3HT on the surface of TiO_2, ensured by the COOH groups, was demonstrated to be beneficial for the photoconversion efficiency of the system [16-18]. The vertically aligned nanostructuration of TiO_2 also makes this system attractive, since it ensures direct percolation paths for the photogenerated electrons from the donor–acceptor interface to the cathode, while providing a simple, controlled and ordered architecture. Furthermore, studies are available in literature regarding the photovoltaic response of TiO_2/P3HT blends [16-23] and can be used as a reference for meaningful interpretations of our measurements, both in terms of photocurrent and photovoltage under illumination. The columnar TiO_2/P3HT-COOH HHJs have been studied by photoconductive-AFM (PC-AFM) and photo-assisted Kelvin probe force microscopy (photo-KPFM) to follow the photovoltaic response, i.e., photocurrent and photovoltage, respectively, at the nanoscale under illumination, in order to understand the local physical processes taking place during the photoconversion of energy, and their correlation with the nanoscale morphology of the active layer. A key aspect of this work consists in the joint analysis of these correlated PC-AFM and KPFM measurements, providing a more fundamental understanding of the photovoltaic mechanisms at stake in the systems. To the best of our knowledge, this joint KPFM/PC-AFM study of such a nanostructured array of TiO_2 columns sensitized with functionalized P3HT-COOH constitutes a novel result of interest from both a theoretical and material design perspectives.

Materials and Methods

The TiO_2 layers were synthesized by magnetron sputtering in grazing mode. A thorough description of the fabrication process can be found in the literature [24], which also identified the optimized fabrication parameters for prospective photovoltaic applications. In compliance with these recommendations, the layers were synthesized without any substrate rotation or bias, while fixing the growth temperature to 450 °C and the tilt angle between the substrate and the cathode axis to 60°. Anatase TiO_2 layers with a 200 nm thick nanocolumnar morphology have been deposited on 85 nm-thick ITO-coated glass substrates (Naranjo B.V., sheet resistance of 15 Ω·sq). The average spacing between the columns is (10 ± 3) nm, with an average width of the columns of (19 ± 4) nm, as determined by SEM measurements [24]. The topography of the deposit is shown in the tapping-mode atomic force microscopy (TM-AFM) image of Figure 1d, where the apex of the columns appears as hemispherical protuberances. Regio-regular P3HT-COOH (5400 g/mol, which corresponds to about 30 monomer units, i.e., a total polymer chain length around 130 Å) was synthesized following a reported procedure [24]. A schematic descrip-

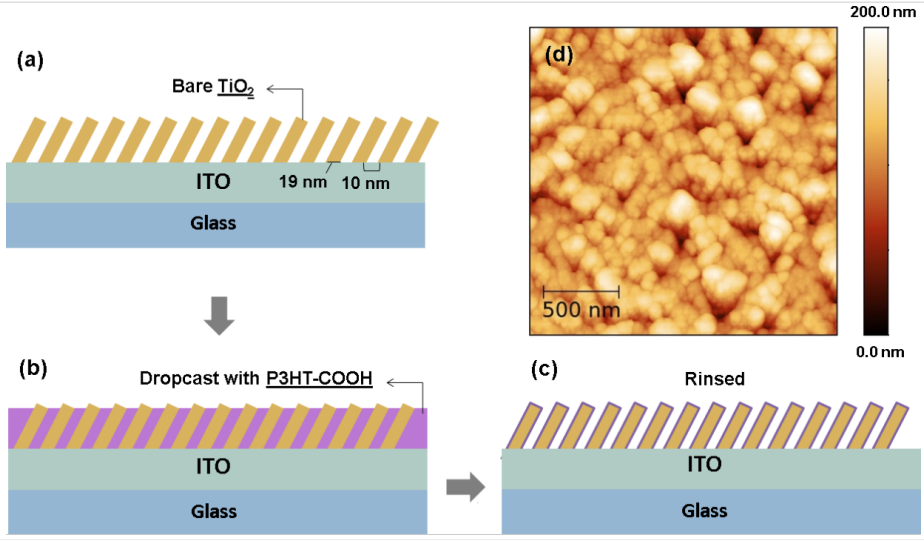


Figure 1: (a–c) Schematic representation of the TiO_2/P3HT-COOH HHJ preparation. (d) 2 × 2 μm^2 TM-AFM height image of a bare nanocolumnar TiO_2 layer.

tion of the grafting protocol is given in Figure 1a–c. The polymer deposit was obtained by dropcasting a 0.5 mg/mL solution of P3HT-COOH in chlorobenzene on the TiO_2 structure. The covalent grafting of the polymer on the nanoporous TiO_2 surface is ensured by the carboxylic –COOH group. Rinsing with chlorobenzene was then carried out to remove the residual ungrafted polymer chains. The success of the polymer grafting is confirmed by UV–visible optical absorption measurement across a 350–800 nm wavelength range, for which an absorption of light higher by one order of magnitude compared to bare TiO_2 was measured [24]. This indicates a good P3HT impregnation along the columns, the interspacing being sufficient for the polymer infiltration.

The photo-KPFM measurements were carried out in a UHV (<10^{-10} Torr) instrument composed of an Omicron Nanotechnology VT-AFM system with a Nanonis controller. The KPFM electrical excitation used a frequency $\omega_{KPFM}/2\pi$ of 958 Hz, with a VAC amplitude of 600 mV. The light source for sample irradiation was a green laser diode (wavelength = 500 nm, power density = 1.45 mW/mm^2). Photo-assisted KPFM measurements were also performed in ambient conditions, with a Bruker multimode microscope controlled by a Nanoscope III unit coupled to a Nanonis control unit (SPECS Zürich). The KPFM electrical excitation was made at a frequency $\omega_{KPFM}/2\pi$ of 80 Hz, with a VAC amplitude of 500 mV. The illumination of the sample for photo-KPFM and photovoltage probing was provided by a white light lamp irradiating the sample surface from the top. In both setups, conductive Nanosensors PPP-EFM tips (PtIr-coated Si probes) were used (resonant frequency around 75 kHz). The sample was grounded while the excitation and regulation biases were applied to the tip. The measured contact potential difference (V_{cpd}) is given by the following expression:

$$|e|\ V_{cpd} = \Phi_{tip} - \Phi_{sample}, \quad (1)$$

where Φ_{tip} and Φ_{sample} are the workfunction of the tip and the sample, respectively. In this work, no calibration of the tip workfunction was necessary, as only the V_{cpd} variations between the materials constituting the photovoltaic blends and their modifications with incoming light were to be measured. These V_{cpd} variations provide relative but quantitative variations of surface potential at the investigated interfaces.

The PC-AFM measurements were carried out in air, using a Bruker Dimension Icon microscope with a Nanoscope V controller. An extended TUNA external module was used for current detection with a detection range within 100 fA to 1 μA. Silicon tips coated with a PtIr conductive alloy (PPP-CONTPt from Nanosensors) were used. The tip and the back-contact were connected while the sample was locally irradiated from the bottom (through the patterned ITO–glass substrates) under AM 1.5 calibrated white light illumination (spot diameter around 200 μm, power density of 100 suns).

Results and Discussion

Photo-KPFM measurements on the TiO_2/P3HT-COOH hybrid heterojunctions

Analysis of the V_{cpd} contrast in the dark

Figure 2a shows a 500 × 500 nm^2 AFM height image obtained in UHV on a nanocolumnar TiO_2 film deposited over a grounded ITO electrode, where the nanocolumns of TiO_2 are

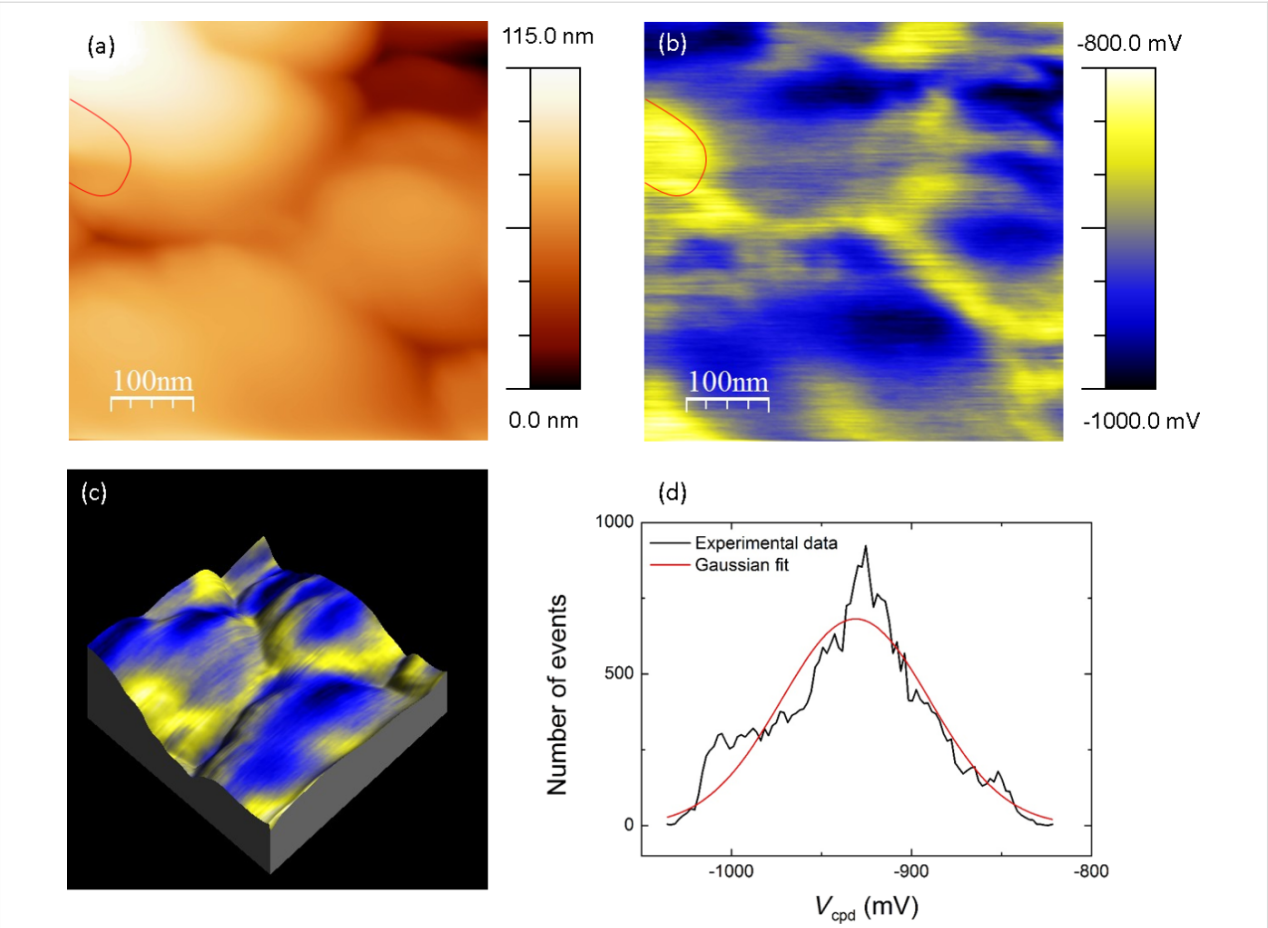


Figure 2: (a) 500 × 500 nm^2 AFM height image of a nanostructured TiO_2 film, obtained in UHV. Height detection parameters: −22 Hz of frequency shift setpoint and 40 mV of amplitude setpoint. (b) Corresponding KPFM V_{cpd} image. V_{cpd} detection parameters: frequency and amplitude of the electrical excitation: 958 Hz and 600 mV. (c) Three-dimensional display of the height image (a), shown with the color scale of the V_{cpd} (b). (d) V_{cpd} histogram extracted from (b) (black line) superimposed with a Gaussian fit (red curve).

assembled in clumps with a width of several hundred nm. Figure 2b shows the corresponding KPFM V_{cpd} image. Figure 2c presents the three-dimensional display of Figure 2a, where the colour scale refers to the V_{cpd} signal of Figure 2b. The distribution of the V_{cpd} values can be fit with a Gaussian distribution centred at −931 mV with a FWHM of 97 mV (Figure 2d).

A direct correlation between the topography and the V_{cpd} signal can be observed, with a higher height corresponding to a more negative V_{cpd}. It is however unlikely that the contrast purely originates from a crosstalk between the topography and the V_{cpd}, as indicated by local mismatching between both contrasts (see red lines in Figure 2a and 2b). Moreover, further measurements (see Figure 3) showed that P3HT grafting barely affects the overall morphology but smooths tremendously the V_{cpd} contrast. Thus, the observed V_{cpd} contrast most probably originates therefore from local variations in the electronic properties of the surface, such as a possibly different free electron density at the top and at the side of the columns. This explanation is further supported by the PC-AFM measurements presented in the last section. As shown in the Supporting Information File 1 (Figure S1), no ungrounded potential is to be detected at the top of the nanocolumnar TiO_2 film. This can therefore not be the origin of the V_{cpd} contrast observed on the bare TiO_2 columns.

Figure 3a displays a KPFM height image obtained in UHV on a TiO_2 deposit grafted with P3HT-COOH. The left part of the image corresponds to a bare area of the ITO electrode, while the right part shows a TiO_2/P3HT-COOH zone. Figure 3b shows the corresponding V_{cpd} image recorded in the dark. A clear difference between the V_{cpd} intensity over the ITO electrode (−614 ± 18 mV in average) and the TiO_2/P3HT-COOH HHJ (−248 ± 49 mV in average) is observed. This V_{cpd} shift clearly appears in the V_{cpd} distributions of Figure 3d. The more negative V_{cpd} value over the ITO electrode reflects consistently a higher corresponding work function (around 4.7 eV in litera-

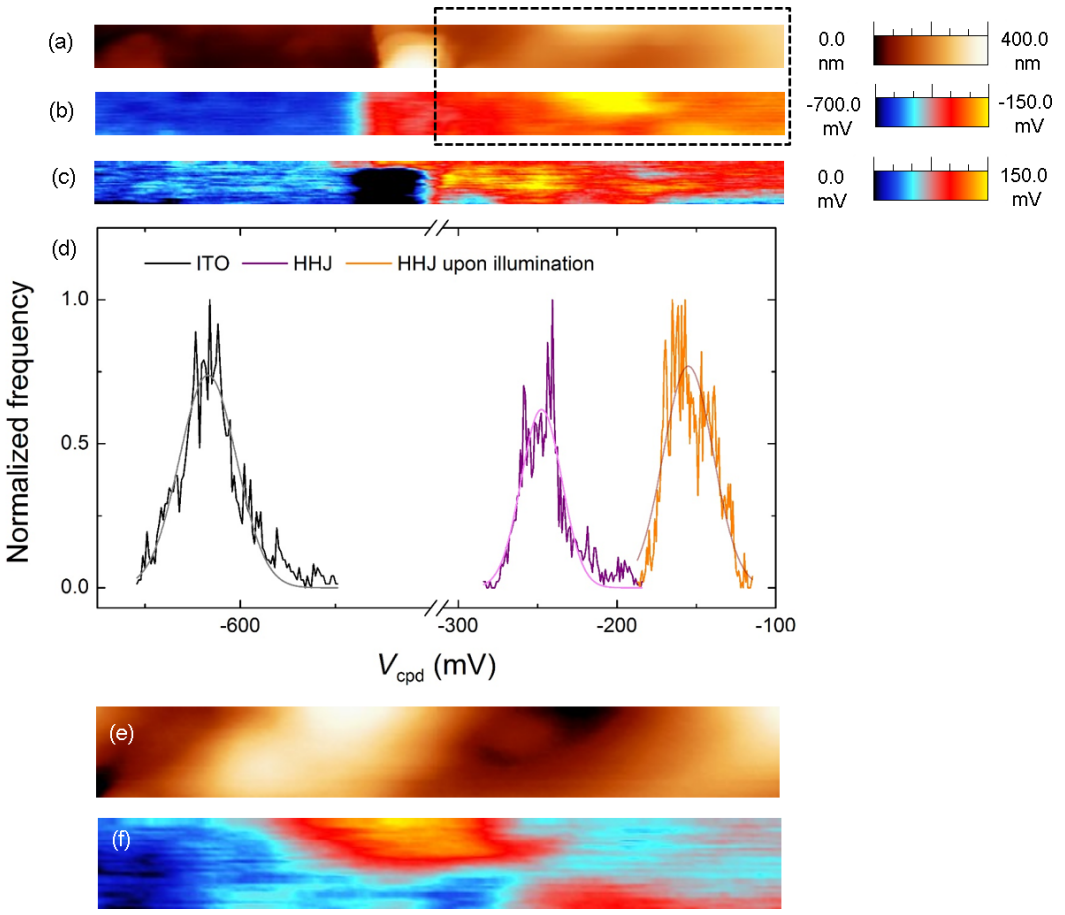


Figure 3: (a) AFM height image obtained in UHV over a 4000 × 270 nm^2 scan area astride the step edge between a TiO_2/P3HT-COOH HHJ (right-part of the image) and the uncovered part of the ITO electrode (left-part of the image). KPFM height detection parameters: −5 Hz of frequency shift setpoint and 50 mV of amplitude setpoint. (b) Corresponding KPFM V_{cpd} image recorded without illumination. KPFM V_{cpd} detection parameters: frequency and amplitude of the electrical excitation: 958 Hz and 600 mV. (c) Corresponding KPFM V_{ph} image obtained by subtracting the V_{cpd} images recorded with and without illumination. (d) V_{cpd} distributions across a 250 × 500 nm^2 surface area in the left (ITO area) and right (HHJ area) part of image (a) and in the right (HHJ area) part of image (c). Gaussian fits have been added for each distribution. (e) and (f) are enlargements of images (a) and (b), respectively, corresponding to the dashed rectangle. The colour scale contrast is enhanced to highlight the main features.

ture [6,15]) compared to that of TiO_2 (around 4.3 eV in literature [7]).

The data of Figure 3 were compared with the images obtained on bare nanocolumnar TiO_2 (Figure 2). In both measurements, the ITO electrode was grounded and the same tip was used. The distribution of V_{cpd} values on the TiO_2/P3HT-COOH area (right part of Figure 3b) is displayed as the purple curve in Figure 3d; the corresponding Gaussian fit is centred at −248 mV, with a FWHM of 30 mV. As seen in Figure 2d, the V_{cpd} is much more negative on bare nanocolumnar TiO_2, This indicates that: (i) the P3HT layer induces an up-shift of the V_{cpd} values, and (ii) this up-shift occurs over the entire surface, since no values typical of bare TiO_2 are recorded on the polymer-grafted surface. This indicates that the P3HT covering is complete, with no bare TiO_2 area left. The fact that the V_{cpd} increases upon P3HT grafting indicates that the surface workfunction of TiO_2/P3HT-COOH is lower than that of bare nanocolumnar TiO_2. This can be understood on the basis of the following discussion, which describes the relative configuration of the electronic levels of the materials within the HHJ.

The covalent bonding between P3HT-COOH and TiO_2 creates a dipole at the interface induced by: (i) the hybridization of the electronic orbitals of the two components, leading to a rearrangement of the charge density at the interface and (ii) the addition of a net dipole intrinsic to the P3HT-COOH molecule itself. The first effect was reported previously [25], evidencing a pinning of the LUMO of P3HT-COOH at the conduction band of the TiO_2 with a net transfer of half an electron per polymer chain from the LUMO of P3HT into the CB of TiO_2. This results in the formation of a dipole at the P3HT-COOH/TiO_2 interface, directed away from TiO_2, where the positive (negative) pole is located in P3HT (TiO_2). Previous KPFM studies

[26-28] confirmed the presence of a dipole directed away from TiO_2 or ITO substrates upon grafting of COOH-containing organic materials. A dipole directed away from the TiO_2 surface (i.e., a negative dipolar moment) means a downshift of the vacuum level upon grafting [29].

The local variations in the V_{cpd} values (the FWHM of the distribution is about 30 mV) are probably due to slightly different densities of grafted P3HT-COOH chains. Indeed, a homogeneous P3HT covering would induce a homogeneous up-shift of the V_{cpd} across the surface, leading to a variation range of V_{cpd} for the TiO_2/P3HT-COOH HHJ having the same origin as that of bare nanocolumnar TiO_2. Yet, unlike what was observed for bare nanocolumnar TiO_2, no correlation between the height and V_{cpd} images can be seen between Figure 3e and Figure 3f. The origin of the contrast is therefore not to be linked to the V_{cpd} variations in the TiO_2 surface, but rather to an inhomogeneous contribution of the grafted P3HT-COOH.

Figure 4 shows a schematic representation of the band diagram of the ITO/TiO_2/P3HT-COOH/tip electronic system (blue lines) in a KPFM measurement configuration, i.e., a grounded ITO electrode and the DC and AC bias applied to the tip. Considering no floating potential at the [ITO/TiO_2/P3HT-COOH] surface (see Supporting Information File 1, Figure S1), a Fermi level alignment can be assumed across the entire ITO/HHJ structure. The dipole pointing away from the TiO_2 at the TiO_2/P3HT-COOH interface, leading to a partial accumulation of e^- (h^+) in the TiO_2 (P3HT), will bend the vacuum level downwards, hence lowering the surface workfunction of the TiO_2 once grafted with P3HT-COOH. The more positive V_{cpd} of TiO_2/P3HT-COOH compared to bare TiO_2 confirms this mechanism.

Figure 5a shows a KPFM height image obtained on a TiO_2/P3HT-COOH deposit in ambient conditions in the dark. While the top of the TiO_2 columns is visible, topographical features cannot be assigned to the presence of P3HT, probably because the nominal thickness of the P3HT-COOH deposit (13 nm) is similar to the roughness of the columnar assembly. No correlation is observed between the columnar topography and the corresponding surface potential image (Figure 5b),

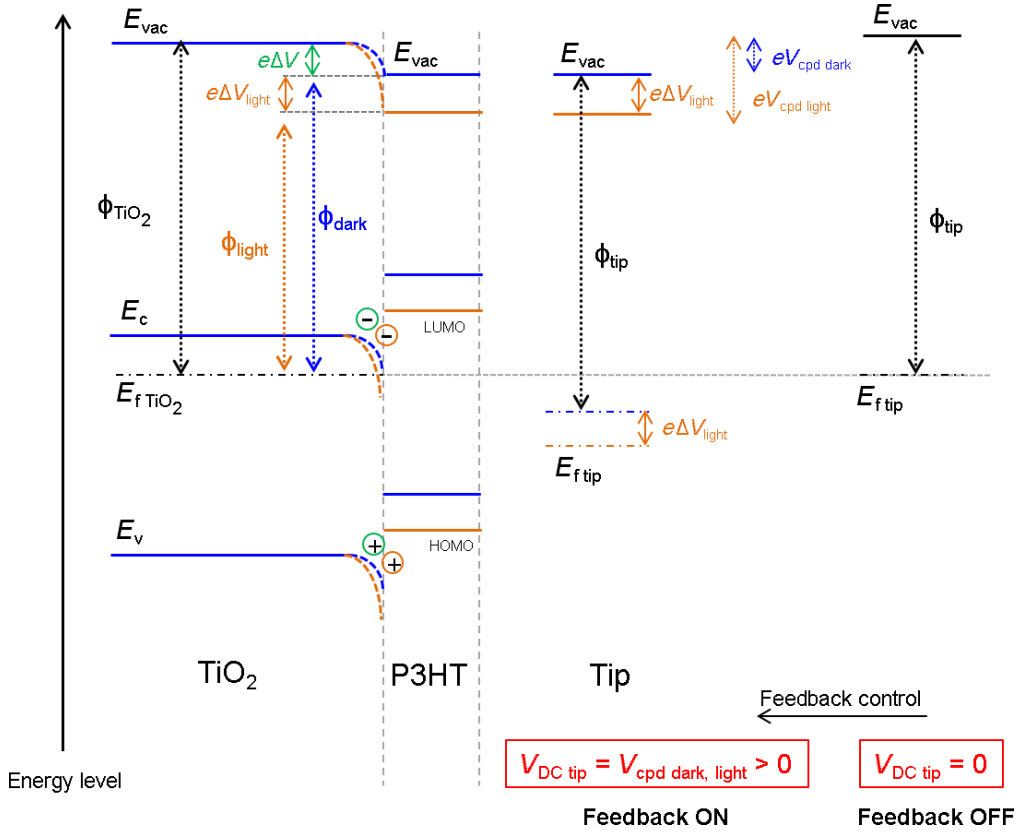


Figure 4: Schematic representation of the electronic band structure of the [TiO_2/P3HT-COOH]–[tip] system in the KPFM measurement configuration considering no feedback control (right part) and feedback control (left part). The blue (orange) lines correspond to the situation in the dark (under illumination). $e\Delta V$ (green color) represents the bond dipole in the dark, while $e\Delta V_{light}$ (orange color) represents the photovoltage under illumination. E_{vac}, E_c, E_v, E_f and Φ stand for vacuum level, conduction band, valence band, Fermi level and workfunction, respectively. HOMO and LUMO mean highest occupied molecular orbital and lowest unoccupied molecular orbital, respectively.

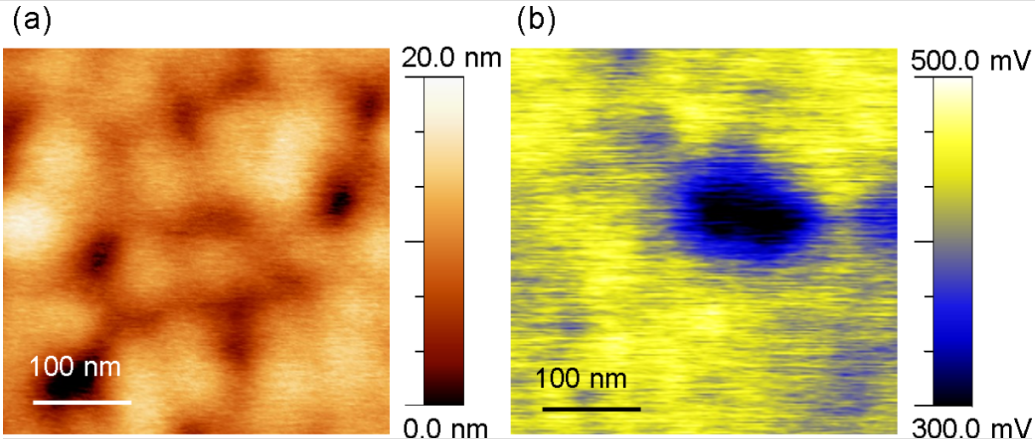


Figure 5: (a) 400 × 400 nm^2 AFM height image obtained in air on a TiO_2/P3HT-COOH HHJ. KPFM height detection parameters: −10 Hz of frequency shift setpoint and 5 nm of amplitude setpoint. (b) Corresponding KPFM V_{cpd} image. KPFM V_{cpd} detection parameters: frequency and amplitude of the electrical excitation: 80 Hz and 500 mV, respectively.

which shows variations within [260; 500] mV. By comparison with the data of Figure 2, this confirms that the V_{cpd} contrast is ruled by the presence of P3HT-COOH at the surface of TiO_2. The V_{cpd} contrast in Figure 5b can be explained on the basis of the bond dipole at the TiO_2/P3HT-COOH interface discussed above. V_{cpd} can then be expressed as $V_{cpd} = V_{cpd\ TiO2} + e\Delta V$, $V_{cpd\ TiO2}$ and $e\Delta V$ being the V_{cpd} of bare TiO_2 and the local bond dipole amplitude, respectively. The lower (higher) V_{cpd} observed in the darker (brighter) zones in Figure 5 (b) corresponds therefore to a lower (higher) $e\Delta V$, which could be related to a lower (higher) P3HT-COOH grafting density.

Variations of V_{cpd} upon illumination

As a preliminary study, KPFM measurements on bare TiO_2 were carried out in the dark and upon illumination (white light). The results are presented in Supporting Information File 1, Figure S2. As expected, no photovoltage is observed, TiO_2 being transparent in the visible spectrum.

Figure 3c shows the KPFM positive photovoltage across the entire TiO_2/P3HT-COOH surface (right-part of the image) upon illumination. This up-shift of V_{cpd} upon illumination is better visualized in the corresponding profiles in Figure 3d. This photovoltage confirms locally a complete P3HT covering over the TiO_2 surface. The positive photovoltage means an increase of the V_{cpd} value, i.e., a decrease of the surface workfunction. This effect can be understood on the basis of Figure 4. Upon grafting, it was previously discussed that a dipole is created at the TiO_2/P3HT-COOH interface, with positive (negative) charges in the P3HT (TiO_2) layer. This leads to a V_{cpd} value denoted $V_{cpd\ dark}$ in Figure 4 and expressed as:

$$eV_{cpd\ dark} = \Phi_{tip} - \Phi_{dark} = \Phi_{tip} - \Phi_{TiO_2} + e\Delta V \qquad (2)$$

where Φ_{tip}, Φ_{TiO2} and Φ_{dark} are the workfunctions of the tip, the TiO_2 layer and the sample surface, respectively. ΔV represents the further voltage compensation needed to cancel the electrostatic forces between the tip and the sample, due to the excess positive charges present in the P3HT layer, i.e., the bond dipole. Upon illumination, it is expected that P3HT-COOH absorbs the incident photons, thus creating excitons. The length of the P3HT-COOH chains being sufficiently small, irrespective of the location where the excitons are generated, they will be able to reach the TiO_2/P3HT-COOH interface, and dissociate by transferring an electron from P3HT into the conduction band of TiO_2. An accumulation of holes in the highest occupied molecular orbital (HOMO) of P3HT and electrons in the conduction band of TiO_2 follows, with the charges remaining close to the interface due to electrostatic attraction. A steady state is then reached between the generation and recombination of charges. The photogeneration of positive charges in the P3HT layer induces an additional V_{DC} that has to be compensated in the KPFM measurement to nullify the tip–sample electrostatic forces. This compensation is denoted ΔV_{light} in Figure 4, and the V_{cpd} value upon illumination, $V_{cpd\ light}$, is now expressed as:

$$\begin{aligned} eV_{cpd\ light} &= \Phi_{tip} - \Phi_{light} \\ &= \Phi_{tip} - \Phi_{TiO_2} + e\Delta V + e\Delta V_{light} \\ &= eV_{cpd\ dark} + e\Delta V_{light} \end{aligned} \qquad (3)$$

This provides the following expression for the photovoltage:

$$V_{ph} = V_{cpd\ light} - V_{cpd\ dark} = \Delta V_{light} \qquad (4)$$

ΔV_{light} is a positive quantity because the DC bias applied to the tip ($V_{DC\ tip}$) (to compensate for positive charges in P3HT) is

necessarily positive. The relation between the surface potential and $V_{DC\ tip}$ is given by $V_{cpd} = V_{DC\ tip}$. This leads to a positive value of the photovoltage, as observed experimentally in Figure 3.

Photoconductive-AFM measurements on the TiO_2/P3HT-COOH hybrid heterojunctions

A 5 × 5 µm^2 height image of a TiO_2/P3HT-COOH HHJ is shown in Figure 6a. The corresponding current image in Figure 6b, obtained in short-circuit configuration upon illumination, shows values of photocurrent up to 25 pA. This confirms light absorption by the P3HT-COOH, followed by the generation of charges at the TiO_2/P3HT-COOH interface. The positive sign of the photocurrent means that the charges collected at the tip are holes. The generation and collection of charges upon illumination can be explained on the basis of Figure 6e, which displays the electronic band structure of the ITO/TiO_2/P3HT-COOH/tip system in short-circuit configuration.

Upon illumination, the photon absorption by P3HT-COOH leads to the creation of excitons in the polymer. The electrons are transferred in the conduction band of TiO_2 at the

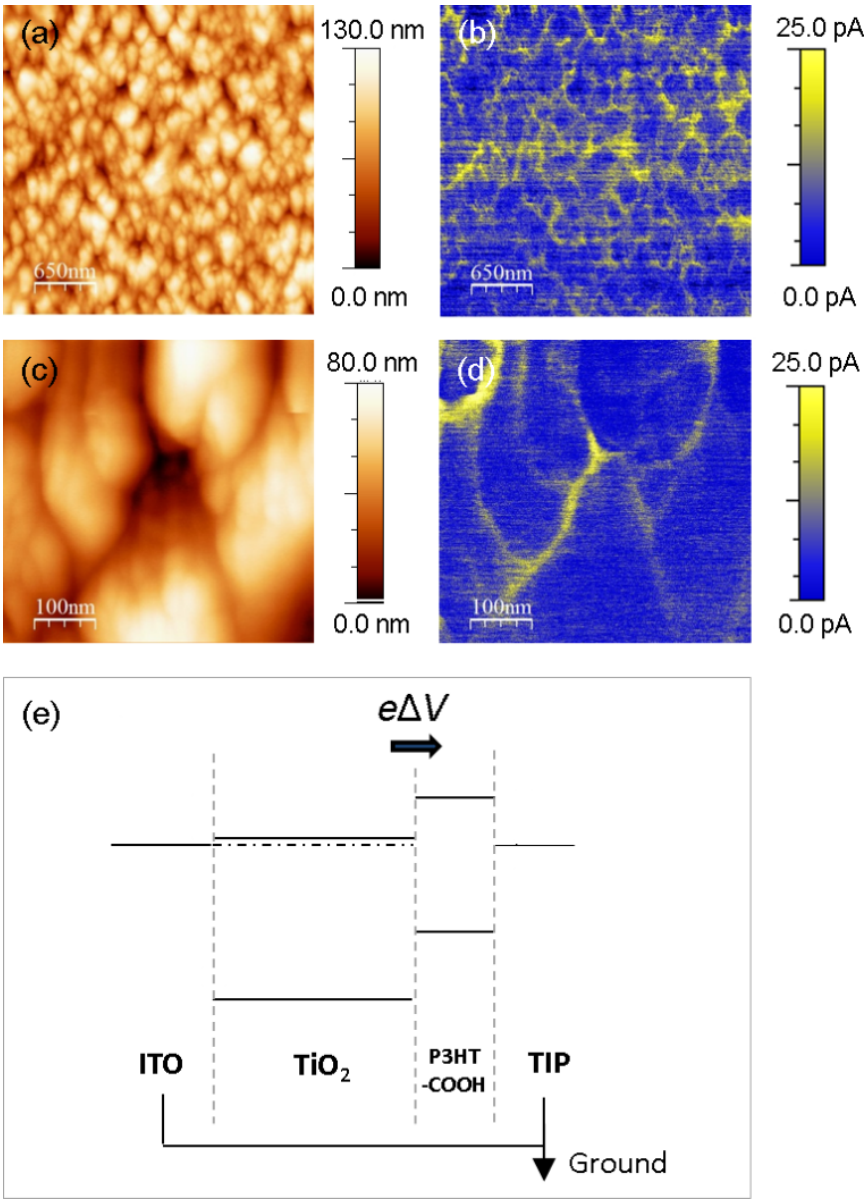


Figure 6: 5 × 5 µm^2 (a,b) and 500 × 500 nm^2 (c,d) PC-AFM height and photocurrent images of a TiO_2/P3HT-COOH HHJ. The images were recorded upon calibrated illumination (AM 1.5, 100 suns), in short-circuit configuration. (e) Schematic representation of the electronic band structure of the ITO/TiO_2/P3HT-COOH/tip system in short-circuit configuration. $e\Delta V$ corresponds to the bond dipole.

TiO_2/P3HT-COOH interface. As the COOH group contributes to the LUMO of P3HT-COOH, the transfer of the electron to the conduction band of TiO_2 is favored compared to unsubstituted P3HT [25]. The photogenerated holes (electrons) are collected at the tip (ITO), and a positive photocurrent is measured when probing the P3HT-COOH layer.

However, the photocurrent map of Figure 6b is far from uniform, with a positive photocurrent reaching 25 pA on the regions corresponding to the inter-columnar spaces, while it is 14 pA over the top of the columns. These local variations are highlighted in Figures 6c and 6d.

The origin of those local variations could be due to the difference in tip–sample contact area between the top of the columns and the intercolumnar zones. However, it is observed in Figure 6a and 6b that, while the topographic variations are of similar amplitude across the entire surface, the intensity of photocurrent in the areas between columns varies, and is therefore not impacted solely by the topographic variations.

We note that the I_{ph} contrast is qualitatively similar to that of the V_{cpd} observed in Figure 2, in which the top of the bare TiO_2 nanocolumns displays more negative V_{cpd} values. I_{ph} and V_{cpd} quantify two different physical mechanisms, being the amount of photogenerated charges flowing in the system for the former, and the sample surface workfunction relatively to that of the tip for the latter. However, both quantities are influenced by the electron density in the conduction band of the TiO_2 and the grafting density of P3HT-COOH. These two properties impact the local conductive properties at the tip–sample contact, thus the resulting photocurrent. Φ_{TiO2} and the P3HT-COOH grafting density are also expected to impact the resulting V_{cpd} since we previously expressed the latter as:

$$V_{cpd} = V_{cpd\ TiO_2} + e\Delta V,$$

where the first and second terms are directly related to Φ_{TiO2} and the P3HT-COOH density, respectively.

Due to the small thickness of the P3HT-COOH layer on top of the TiO_2 columns, the photocurrent contrast recorded with the tip in direct contact with the surface is most probably ruled by the TiO_2 electrical properties. This explains why the I_{ph} contrast shows similarities with the V_{cpd} contrast of bare TiO_2, rather than with that of the TiO_2/P3HT-COOH HHJ. In such a configuration, the similarity of contrast between the I_{ph} (Figure 6b,d and V_{cpd} (Figure 2b,c) images suggests that the lower photocurrent measured on top of the columns might originate from a locally lower initial (i.e., prior to illumination) electron density at the TiO_2 surface. Among various possible factors, this variation of electron density might be due to the presence of different TiO_2 crystal facets, as the latter are shown to influence the electronic properties of the TiO_2 surface [30,31].

Conclusion

Nanocolumnar TiO_2 layers were sensitized with a layer of P3HT-COOH. KPFM surface potential measurements indicate complete covering of the TiO_2 surface by the polymer. A downshift of the vacuum level of the sample upon grafting, i.e., an increase of the surface potential, was measured, due to the formation of a bond dipole at the TiO_2/P3HT-COOH interface. Upon in situ illumination, a positive photovoltage was observed, which is related to the accumulation of photogenerated holes in the P3HT layer. Along with the surface potential shift, a positive photocurrent was measured by PC-AFM measurements over the TiO_2/P3HT-COOH heterojunction upon illumination, corresponding to a hole collection at the tip. Lower photocurrent values measured on top of the TiO_2 columns can be related to the corresponding more negative V_{cpd}, indicating a locally lower electron density pre-existing the illumination.

Supporting Information

Supporting Information File 1

Supporting Information.
Figure S1 shows a FM-AFM height image obtained in UHV astride the step from a nanostructured TiO_2/P3HT-COOH HHJ to the ITO electrode lying below. The applied DC sample bias was varied during the measurement, without illumination. This result aims at demonstrating the absence of floating potential across the layer composing the sample. Figure S2 shows the superimposition of FM-KPFM height and V_{cpd} profiles over a nanostructured TiO_2 film obtained in UHV and recorded with and without illumination. The result aimed at demonstrating the absence of light-induced artefact during the recording of topography, as well as the negligibility of the photovoltaic effect at the TiO_2/ITO interface.
[https://www.beilstein-journals.org/bjnano/content/supplementary/2190-4286-9-197-S1.pdf]

Acknowledgements

The authors are grateful to R. Di Ciuccio (Laboratory of Polymeric and Composite Materials, University of Mons) for the synthesis of P3HT-COOH. The nanoporous TiO_2 layers were synthesized by J. Delvaux (Laboratory of Plasma-Surface Interactions Chemistry, University of Mons). This work was supported by the Action de Recherche Concertée program (MADSSCELLS project), the Science Policy Office of the Belgian Federal Government (BELSPO-PAI VII/5), and the

FRS-FNRS PDR Project 'Hybrid Organic/Inorganic Nanomaterials for Energy COnversion and STOrage Devices on FLEXible and Stretchable Substrates' (ECOSTOFLEX). L.L. is grateful to FRIA and FRS-FNRS for a doctoral fellowship and a travel grant, respectively. Ph.L. is a Senior Research Associate of FRS-FNRS (Belgium).

ORCID® iDs

Denis Mariolle - https://orcid.org/0000-0001-9778-5163
Nicolas Chevalier - https://orcid.org/0000-0002-4011-8746
Łukasz Borowik - https://orcid.org/0000-0002-7472-1105
Roberto Lazzaroni - https://orcid.org/0000-0002-6334-4068
Philippe Leclère - https://orcid.org/0000-0002-5490-0608

References

1. Parida, B.; Iniyan, S.; Goic, R. *Renewable Sustainable Energy Rev.* **2011,** *15,* 1625–1636. doi:10.1016/j.rser.2010.11.032
2. Polman, A.; Knight, M.; Garnett, E. C.; Ehrler, B.; Sinke, W. C. *Science* **2016,** *352,* aad4424. doi:10.1126/science.aad4424
3. Branker, K.; Pathak, M.; Pearce, J. *Renewable Sustainable Energy Rev.* **2011,** *15,* 4470–4482. doi:10.1016/j.rser.2011.07.104
4. Wright, M.; Uddin, A. *Sol. Energy Mater. Sol. Cells* **2012,** *107,* 87–111. doi:10.1016/j.solmat.2012.07.006
5. Mathew, S.; Yella, A.; Gao, P.; Humphry-Baker, R.; Curchod, B. F. E.; Ashari-Astani, N.; Tavernelli, I.; Rothlisberger, U.; Nazeeruddin, M. K.; Grätzel, M. *Nat. Chem.* **2014,** *6,* 242–247. doi:10.1038/nchem.1861
6. Tengstedt, C.; Osikowicz, W.; Salaneck, W. R.; Parker, I. D.; Hsu, C.-H.; Fahlman, M. *Appl. Phys. Lett.* **2006,** *88,* 053502. doi:10.1063/1.2168515
7. Chung, I.; Lee, B.; He, J.; Chang, R. P. H.; Kanatzidis, M. G. *Nature* **2012,** *485,* 486–489. doi:10.1038/nature11067
8. Hagfeldt, A.; Boschloo, G.; Sun, L.; Kloo, L.; Pettersson, H. *Chem. Rev.* **2010,** *110,* 6595–6663. doi:10.1021/cr900356p
9. Othman, M. A.; Amat, N. F.; Ahmad, B. H.; Rajan, J. *J. Phys.: Conf. Ser.* **2014,** *495,* 012027. doi:10.1088/1742-6596/495/1/012027
10. Pomoni, K.; Sofianou, M.; Georgakopoulos, T.; Boukos, N.; Trapalis, C. *J. Alloys Compd.* **2013,** *548,* 194–200. doi:10.1016/j.jallcom.2012.08.136
11. Tian, J.; Zhao, Z.; Kumar, A.; Boughton, R. I.; Liu, H. *Chem. Soc. Rev.* **2014,** *43,* 6920–6937. doi:10.1039/C4CS00180J
12. Weng, Z.; Guo, H.; Liu, X.; Wu, S.; Yeung, K. W. K.; Chu, P. K. *RSC Adv.* **2013,** *3,* 24758–24775. doi:10.1039/c3ra44031a
13. Dette, C.; Pérez-Osorio, M. A.; Kley, C. S.; Punke, P.; Patrick, C. E.; Jacobson, P.; Giustino, F.; Jung, S. J.; Kern, K. *Nano Lett.* **2014,** *14,* 6533–6538. doi:10.1021/nl503131s
14. Reckers, P.; Dimamay, M.; Klett, J.; Trost, S.; Zilberberg, K.; Riedl, T.; Parkinson, B. A.; Brötz, J.; Jaegermann, W.; Mayer, T. *J. Phys. Chem. C* **2015,** *119,* 9890–9898. doi:10.1021/acs.jpcc.5b01264
15. Moerman, D.; Lazzaroni, R.; Douhéret, O. *Appl. Phys. Lett.* **2011,** *99,* 093303. doi:10.1063/1.3628658
16. Weickert, J.; Auras, F.; Bein, T.; Schmidt-Mende, L. *J. Phys. Chem. C* **2011,** *115,* 15081–15088. doi:10.1021/jp203600z
17. Huang, Y.-C.; Yen, W.-C.; Liao, Y.-C.; Yu, Y.-C.; Hsu, C.-C.; Ho, M.-L.; Chou, P.-T.; Su, W.-F. *Appl. Phys. Lett.* **2010,** *96,* 123501. doi:10.1063/1.3357425
18. Wu, M.-C.; Wu, Y.-J.; Yen, W.-C.; Lo, H.-H.; Lin, C.-F.; Su, W.-F. *Nanoscale* **2010,** *2,* 1448–1454. doi:10.1039/b9nr00385a
19. Zeng, T.-W.; Ho, C.-C.; Tu, Y.-C.; Tu, G.-Y.; Wang, L.-Y.; Su, W.-F. *Langmuir* **2011,** *27,* 15255–15260. doi:10.1021/la203533u
20. Phan, H.; Jahnke, J. P.; Chmelka, B. F.; Nguyen, T.-Q. *Appl. Phys. Lett.* **2014,** *104,* 233305. doi:10.1063/1.4883001
21. Batra, Y.; Rai, D.; Mehta, B. R. *Appl. Phys. Express* **2013,** *6,* 041602. doi:10.7567/APEX.6.041602
22. Zeng, T.-W.; Hsu, F.-C.; Tu, Y.-C.; Lin, T.-H.; Su, W.-F. *Chem. Phys. Lett.* **2009,** *479,* 105–108. doi:10.1016/j.cplett.2009.07.104
23. Lin, Y.-Y.; Chu, T.-H.; Li, S.-S.; Chuang, C.-H.; Chang, C.-H.; Su, W.-F.; Chang, C.-P.; Chu, M.-W.; Chen, C.-W. *J. Am. Chem. Soc.* **2009,** *131,* 3644–3649. doi:10.1021/ja8079143
24. Dervaux, J.; Cormier, P.-A.; Konstantinidis, S.; Di Ciuccio, R.; Coulembier, O.; Dubois, P.; Snyders, R. *Vacuum* **2015,** *114,* 213–220. doi:10.1016/j.vacuum.2014.10.016
25. Lasser, L.; Ronca, E.; Pastore, M.; De Angelis, F.; Cornil, J.; Lazzaroni, R.; Beljonne, D. *J. Phys. Chem. C* **2015,** *119,* 9899–9909. doi:10.1021/acs.jpcc.5b01267
26. Nüesch, F.; Carrara, M.; Zuppiroli, L. *Langmuir* **2003,** *19,* 4871–4875. doi:10.1021/la026962w
27. Krüger, J.; Bach, U.; Grätzel, M. *Adv. Mater.* **2000,** *12,* 447–451. doi:10.1002/(SICI)1521-4095(200003)12:6<447::AID-ADMA447>3.0.CO;2-8
28. Henning, A.; Günzburger, G.; Jöhr, R.; Rosenwaks, Y.; Bozic-Weber, B.; Housecroft, C. E.; Constable, E. C.; Meyer, E.; Glatzel, T. *Beilstein J. Nanotechnol.* **2013,** *4,* 418–428. doi:10.3762/bjnano.4.49
29. Goh, C.; Scully, S. R.; McGehee, M. D. *J. Appl. Phys.* **2007,** *101,* 114503. doi:10.1063/1.2737977
30. Wang, X.; Li, T.; Yu, R.; Yu, H.; Yu, J. *J. Mater. Chem. A* **2016,** *4,* 8682–8689. doi:10.1039/C6TA02039A
31. Selçuk, S.; Selloni, A. *J. Phys. D: Appl. Phys.* **2017,** *50,* 273002. doi:10.1088/1361-6463/aa7540

License and Terms

This is an Open Access article under the terms of the Creative Commons Attribution License (http://creativecommons.org/licenses/by/4.0). Please note that the reuse, redistribution and reproduction in particular requires that the authors and source are credited.

The license is subject to the *Beilstein Journal of Nanotechnology* terms and conditions: (https://www.beilstein-journals.org/bjnano)

The definitive version of this article is the electronic one which can be found at: doi:10.3762/bjnano.9.197